



Spatio-Temporal Ultrafast Laser Tailoring for Bulk Functionalization of Transparent Materials

Cyril Maucclair

► To cite this version:

Cyril Maucclair. Spatio-Temporal Ultrafast Laser Tailoring for Bulk Functionalization of Transparent Materials. domain_other. Université Jean Monnet - Saint-Etienne; Freie Universität Berlin, 2010. English. NNT: . tel-00488647v1

HAL Id: tel-00488647

<https://theses.hal.science/tel-00488647v1>

Submitted on 2 Jun 2010 (v1), last revised 21 Feb 2012 (v2)

HAL is a multi-disciplinary open access archive for the deposit and dissemination of scientific research documents, whether they are published or not. The documents may come from teaching and research institutions in France or abroad, or from public or private research centers.

L'archive ouverte pluridisciplinaire **HAL**, est destinée au dépôt et à la diffusion de documents scientifiques de niveau recherche, publiés ou non, émanant des établissements d'enseignement et de recherche français ou étrangers, des laboratoires publics ou privés.

Spatio-Temporal Ultrafast Laser Tailoring for Bulk Functionalization of Transparent Materials

A thesis presented by

Cyril Mauclair

to the Université Jean Monnet, Saint-Etienne, France
and the Freie Universität Berlin, Germany

In partial fulfillment of the requirements for the degree of Dr. Rer. Nat.
in the subject of Experimental Physics

Work realized at the Laboratoire Hubert Curien, Saint-Etienne
and
the Max-Born-Institut für Nichtlinear Optik und Kurzzeitspektroskopie, Berlin

Date of disputation: 27 May 2010

Supervisors:

Prof. E. Audouard	(Université Jean Monnet, Saint-Etienne)
Dr. R. Stoian	(Université Jean Monnet, Saint-Etienne)
Prof. I. V. Hertel	(Freie Universität, Fachbereich Physik, Berlin)
Prof. L. Wöste	(Freie Universität, Fachbereich Physik, Berlin)



*I give unto men weakness
that they may be humble.
(Ether 12:27)*

Abstract

In the past decade, ultrashort laser sources have had a decisive impact on material processing for photonic applications. Since the first demonstration of bulk photowriting of light guides, the control of the irradiation outcome and the machining of more complex devices have been ongoing challenges. However, the technique is usually restricted to the elemental association of an ultrashort source with a focusing lens. It is thus limited in the processing speed and in the achievable bulk modifications. This requires higher flexibility and adaptivity to the material properties.

Accompanying studies of material modifications in space and time, we propose here that automated spatio-temporal tailoring of the laser pulses is an efficient manner to overcome these limitations. More precisely, we demonstrate the generation of multiple processing foci for synchronous photomachining of multiple devices in the bulk. Thus, we report on the parallel photowriting of waveguides, light couplers, light dividers in 2D/3D and wavelength division demultiplexers in fused silica glass. The method relies on laser wavefront dynamic modulation.

As another significant breakthrough, we show that the domain of photowriting can be extended to deep focusing despite of the associated optical distortions. The technique is based on preserving the energy density at arbitrary depths. We indicate that this can be achieved by wavefront shaping or temporal profile tailoring as efficient correction approaches for propagation. The design of the spatial phase mask and of the temporal profile is conducted by an evolutionary optimization loop based on the evaluation of the irradiation outcome in fused silica and borosilicate Crown glass BK7. Additionally, we take advantage of a particular photoinscription regime to machine embedded waveguides with well-defined polarization function in fused silica. We also have unveiled a singular interaction regime where regular structuring takes place before the focal region. We developed a Fresnel propagation code that explains this particular regime. In addition, we evidence a single pulse processing window where a purely spherical void is generated.

For the first time, the dynamics of the energy coupling to the glassy matrix is evaluated for various temporal pulse profiles. Enhanced energy confinement in the case of picosecond pulses is confirmed by characterization of the transient electronic gas and of the subsequent pressure wave in various glasses. We also show that if distinct temporal pulse profiles lead to similar permanent modifications, the transient excitation scenarios can be drastically different. The dynamics of energy deposition in multi-pulse regimes are also investigated. These pump-probe studies were carried out with a self-build time-resolved microscopy system with temporally shaped pump irradiation. We also developed a new method based on the Drude model to differentiate the electronic and matrix contributions to the contrast of the microscopy images allowing to map the free carrier density and lifetime variations and the refractive index changes in the interaction zone.

Zusammenfassung

Im letzten Jahrzehnt wurden Laserquellen mit ultrakurzen Pulsen von entscheidender Bedeutung in der Materialbearbeitung für photonische Anwendungen. Seit den ersten Beispielen für das Schreiben von Lichtleitern im Inneren transparenter Materialien wurde die Kontrolle des Bestrahlungsergebnisses und das Erzeugen von komplexeren Strukturen eine fortwährende Herausforderung. Die Technik ist jedoch für gewöhnlich auf eine elementare Verbindung einer ultrakurzen Lichtquelle und der fokussierenden Linse reduziert. Sie ist daher in der Prozessgeschwindigkeit und der erreichbaren Modifikationsform im Inneren eingeschränkt.

Wir schlagen daher als begleitende Untersuchungen zur Materialbearbeitung in Raum und Zeit, eine automatische raum-zeitliche Anpassung der Laserpulse in einer effizienten Weise vor um diese Einschränkungen zu überwinden. Genauer gesagt, demonstrieren wir die Erzeugung von mehreren Fokussen zur synchronen Photobearbeitung multipler Strukturen im Materialinneren. Dazu gehört die Möglichkeit des parallelen Schreibens von Wellenleitern, Lichtkopplern, Lichtteilern in 2D/3D und Wellenlängen-Demultiplexern in Quarzglas.

Als einen anderen signifikanten Durchbruch in der Bearbeitungstechnik konnten wir die Möglichkeit des Wellenleiterschreibens bei Fokussierungen tief im Materialinneren aufzeigen, trotz der dabei begleitend auftretenden optischen Verzerrungen. Die Technik basiert auf der Erhaltung der Energiedichte in beliebiger Tiefe. Wir konnten zeigen, dass durch eine Wellefrontformung oder eine zeitliche Pulsprofilanpassung eine effektive Korrektur der Lichtausbreitung möglich ist. Das Design der räumlichen Phasenmaske und des zeitlichen Profils wird durch einen evolutionären Optimierungszyklus bestimmt, der auf dem Bestrahlungsergebnis in geschmolzenem Quarz oder in BK7-Glas basiert. Außerdem nutzten wir ein spezielles Bearbeitungsregime um Wellenleiter mit einer wohl definierten Polarisationsfunktion in Quarzglas zu schreiben. Wir konnten zusätzlich ein singuläres Wechselwirkungsregime aufzeigen, das zu einer regelmäßigen Strukturierung vor dem eigentlichen Fokus führt. Dazu bestimmten wir einen Fresnelausbreitungscode, der dieses spezielle Regime erklärt. Darüber hinaus wurde ein Prozessfenster gefunden, in dem eine rein sphärische Struktur entsteht.

Es wurde erstmalig die Dynamik der Energieeinkopplung in glasartige Gitterstrukturen für verschiedene zeitliche Pulsprofile bestimmt. Eine verstärkte Energieeinschränkung bei der Nutzung von Pikosekundenpulsen wird durch die Charakterisierung des transienten Elektronengases und der darauf anschließenden Druckwelle in verschiedenen Gläsern bestätigt. Wir konnten ebenfalls aufzeigen, dass bei unterschiedlichen Pulsprofilen, die zu einer ähnlichen permanenten Modifikation führen, das transiente Anregungsszenario durchaus sehr unterschiedlich sein kann. Die Dynamik des Energieeintrages im Multipulsregime wurde ebenfalls untersucht. Diese Pump-Probe-Untersuchungen wurden mit einem selbst gebauten, zeitaufgelöstem Mikroskopiesystem und mit zeitlich geformten Pumpulsen durchgeführt. Ebenso wurde eine neue Methode entwickelt, die auf dem Drudemodell basiert, um zwischen dem Elektronen- und dem Matrixanteil im Kontrast der Mikroskopiebilder unterscheiden zu können. Das ermöglicht die Abbildung sowohl der Lebensdauänderungen der freien Ladungsträger sowie der Änderungen des Brechungsindex in der bestrahlten Zone.

Résumé

L'arrivée des sources lasers ultracourtes a bouleversé le domaine de la micro-structuration pour l'optique intégrée. La possibilité de photoinscrire des guides d'onde au sein de matériaux transparents a motivé de nombreux efforts pour étendre la technique à la fabrication de systèmes plus complexes et contrôler le résultat de l'interaction laser-matière. Le plus souvent, le procédé se résume à l'utilisation d'une lentille de focalisation sur le trajet du faisceau laser. Cette méthode souffre de limitations intrinsèques sur la vitesse d'usinage et sur le spectre des modifications accessibles. Ces deux problématiques jouent un rôle clef pour valider la solution laser dans un domaine centré sur la flexibilité d'usinage et l'adaptation de l'outil au matériau.

Nous montrons dans ce mémoire que la mise en forme spatio-temporelle des impulsions lasers ultracourtes répond efficacement à ces défis. En particulier, nous indiquons la possibilité de multiplier le nombre de spots lasers pour la fabrication simultanée de plusieurs composants optiques, en répondant ainsi au besoin de rapidité. Cette avancée majeure est illustrée par la photoinscription en parallèle de guides, de diviseurs, de coupleurs ainsi que de démultiplexeurs de lumière en 2D et 3D dans la silice. Cette technique repose sur la modulation dynamique de la phase spatiale du laser.

Il est également reporté ici que le domaine de photoinscription peut être élargi à la focalisation profonde dans les matériaux, malgré les distorsions optiques associées. La modulation du front d'onde ainsi que la mise en forme temporelle de l'impulsion permettent d'ajuster la propagation et ainsi de préserver la densité d'énergie déposée indépendamment de la profondeur de focalisation. La conception du masque de phase et du profil temporel est assurée par une boucle d'optimisation adaptative évolutionnaire basée sur l'évaluation de l'action du laser. Nous utilisons également un régime d'interaction spécifique pour photo-usiner des guides d'onde sensibles à la polarisation dans la silice. De plus, nous dévoilons une nouvelle fenêtre de photoinscription caractérisée par une structuration régulière avant le point de focalisation. Cette topologie est expliquée ici à l'aide d'un code de propagation développé par nos soins. Un autre régime d'irradiation laser mono-impulsion permettant la génération de structures purement sphériques est aussi reporté.

Le couplage d'énergie vers le matériau transparent en fonction de divers profils d'impulsions est étudié à l'échelle femtoseconde. La caractérisation du gaz d'électrons libres ainsi que de l'onde de pression nous permet de mettre en évidence l'efficacité des impulsions picosecondes à déposer l'énergie de manière plus confinée dans différents verres. De même, nous montrons que des profils temporels bien distincts peuvent conduire à une modification optique similaire avec cependant un scénario d'excitation différent. Nous étudions aussi la dynamique énergétique en régime multi-impulsions; proche des conditions d'écriture de guides d'onde. Ces études sont conduites sur un système de microscopie de type pompe-sonde permettant de mettre en forme l'irradiation pompe. Enfin, nous avons développé une méthode basée sur le modèle de Drude permettant d'estimer la densité électronique et la contribution de la matrice vitreuse à partir des images résolues en temps obtenues sur le microscope.

List of publications

Cyril MAUCLAIR

Laboratoire Hubert Curien, Saint Etienne France

Max Born Institut, Berlin Germany

Publications in refereed journals

1. Y. Zhang, G. Cheng, G. Huo, Y. Wang, W. Zhao, **C. Maclair**, R. Stoian, and R. Hui. *The Fabrication of Circular Cross Section Waveguide in Two Dimensions with a Dynamical Slit* Laser Physics **19** 12, 2236-2241 (2009)
2. G. Cheng, K. Mishchik, **C. Maclair** E. Audouard, and R. Stoian. *Ultrafast laser photoinscription of polarization sensitive devices in bulk silica glass* Opt. Express **17** 9515 (2009)
3. **C. Maclair**, G. Cheng, N. Huot, E. Audouard, A. Rosenfeld, I. V. Hertel, and R. Stoian. *Dynamic ultrafast laser beam spatial tailoring for parallel micromachining of photonic devices in bulk transparent materials* Opt. Express **17** 3531 (2009)
Research Highlights of **Nature Photonics** **3** 5/242-243 (May 2009)
4. **C. Maclair**, A. Mermillod-Blondin, N. Huot, E. Audouard, and R. Stoian. *Ultrafast laser writing of homogeneous longitudinal waveguides in glasses using dynamic wavefront correction* Opt. Express **16**, 5841 (2008).
5. A. Mermillod-Blondin, **C. Maclair**, A. Rosenfeld, J. Bonse, I. V. Hertel, E. Audouard, and R. Stoian. *Size correction in ultrafast laser processing of fused silica by temporal pulse shaping* Appl. Phys. Lett. **93** 021921 (2008)
Selected for the August 2008 issue of the **Virtual Journal of Ultrafast Science**
6. R. Stoian, **C. Maclair**, A. Mermillod-Blondin, N. Huot, E. Audouard, J. Bonse, A. Rosenfeld, and I. V. Hertel. *Size corrections during ultrafast laser induced refractive index changes in bulk transparent materials* J. Laser Micro-Nanoengineering **4** 45 (2008)

7. N. Huot, R. Stoian, A. Mermillod-Blondin, **C. Maucclair**, and E. Audouard *Analysis of the effects of spherical aberration during ultrafast laser-induced refractive index variation in optical glasses* Opt. Express **15** 12395 (2007)

Conference proceedings

1. **C. Maucclair**, C. Mishchik, A. Mermillod-Blondin, J. Bonse, A. Rosenfeld, I.V. Hertel, E. Audouard, R. Stoian *Time-resolved observation of energy deposition in fused silica by ultrashort laser pulses in single and cumulative regime* OSA Proceedings, CLEO (2010)
2. **C. Maucclair**, R. Stoian, J. Bonse, A. Mermillod-Blondin, A. Rosenfeld, I. V. Hertel. *Direct time resolved observation of energy deposition by ultrashort laser pulses in fused silica* Proc. LAMP, the 10th International Symposium on Laser Precision Microfabrication (2009)
3. **C. Maucclair**, G. Cheng, , N. Huot, E. Audouard, A. Rosenfeld, I. V. Hertel, and R. Stoian. *Dynamic ultrafast laser beam tailoring for multispot photo-inscription of photonic devices in bulk transparent materials* Proc. SPIE 7205, 720512, Advanced Fabrication Technologies for Micro/Nano Optics and Photonics II, Thomas J. Suleski; Winston V. Schoenfeld; Jian J. Wang, Eds. (2009)
4. R. Stoian, A. Mermillod-Blondin, **C. Maucclair**, N. Huot, E. Audouard, J. Bonse, A. Rosenfeld, I. V. Hertel. *Size corrections during ultrafast laser induced refractive index changes in bulk transparent materials* Proc. LAMP, the 9th International Symposium on Laser Precision Microfabrication (2008)
5. R. Stoian, A. Mermillod-Blondin, **C. Maucclair**, N. Huot, E. Audouard, I. M. Burakov, N. M. Bulgakova, Y. P. Meschecheryakov, A. Rosenfeld, and I. V. Hertel. *Optimizing laser-induced refractive index changes in thermal glasses* Springer Series in Chemical Physics, Ultrafast Phenomena, Eds. P. Corkum, K. Nelson, R. Schoenlein, S. de Silvestri (2008)
6. R. Stoian, A. Mermillod-Blondin, **C. Maucclair**, N. Huot, E. Audouard, I. M. Burakov, N. M. Bulgakova, Y. P. Meschcheryakov, A. Rosenfeld, I. V. Hertel. *Designing laser-induced refractive index changes in thermal glasses* Proc. SPIE 7005, 700518, High-Power Laser Ablation V; Claude R. Phipps; Ed. (2008)

Conference presentations and contributions

1. Contributed talk: *Ultrafast laser spatio temporal forming for bulk photoinscription of photonic devices* Minisymposium on Ultrashort Pulse Sources Grasmere, United Kingdom (2009)

Best student presentation award.

2. Contribution poster: *Ultrafast laser spatial tailoring for local optical functionalization of bulk transparent materials* Journée de la recherche, Université Jean Monnet Saint-Etienne, France (2009)
3. Contributed talk: *Ultrafast photowriting of photonic devices in bulk transparent materials through multispot operation* Canada-France-Germany Young Photonics Researcher Workshop Munich, Germany (2009)
4. Contributed talk: *Dynamic ultrafast laser beam tailoring for multispot photo-inscription of photonic devices in bulk transparent materials* SPIE Photonics West, Micro- and Nanofabricated Electromechanical and Optical Components San Jose, USA (2009)
5. Contribution poster: *Dynamic correction of optical aberrations during ultrafast laser photoinscription of waveguides in bulk transparent materials* École Femto Mittelwahr, France (2008)
6. Contribution poster: *Contrôle de la phase spatiale d'un faisceau laser femtoseconde au moyen d'un algorithme évolutionnaire: Correction des aberrations sphériques pendant la photoinscription de matériaux transparents et mise en forme du spot focal* Journée de la recherche, Telecom Saint-Etienne, France (2007)

Best student poster award.

7. Contributed talk: *Dynamic correction of optical aberrations during ultrafast laser photoinscription of waveguides in bulk transparent materials* LAMP, the 8th International Congress on Laser Precision Microfabrication Wien, Austria (2007)
8. Contributed talk: *Dynamic correction of optical aberrations during ultrafast laser photoinscription of waveguides in bulk transparent materials* Second France-China Workshop on Ultra-short and Ultra intense Lasers and Applications FCILA Lyon, France (2007)

Invited talks and lectures

1. Invited lecture *Spatial Beam Shaping* UltraShort an Intense Laser Technology and Metrology (USIL) intensive program Bordeaux, France (2009)
2. Invited talk *Ultrafast laser tailoring for bulk photoinscription of photonic devices* LASINOF workshop (Laser Interaction and new optical functionality) Bordeaux, France (2009)

Invited seminars

1. Invited seminar *Ultrafast laser tailoring for transparent material bulk functionalization* Fachbereich Physik der Freien Universität Berlin, Institut für Experimentalphysik, Deutschland (2010)
2. Invited seminar *Ultrafast laser writing of homogeneous longitudinal waveguides in glass using dynamic wavefront correction* Fraunhofer Institut für Lasertechnik ILT Aachen, Deutschland (2008)

Book chapter

Results from my research activity have also been reported in the following book chapters:

1. R. Stoian, M. Wollenhaupt, T. Baumert, I. V. Hertel *Pulse shaping in laser material processing in Laser Precision Microfabrication*, Springer Series in Optical Sciences, Sugioka K., Meunier M., Pique A. Eds. (Springer Verlag, Heidelberg, in press 2010)
2. R. Stoian *Spatio-temporal effects in laser photoinscription of embedded waveguides*, Springer (submitted) 2008

Comments

Results from my research activity have also been presented in invited and contributed talks by group colleagues at:

1. The International Congress on Applications of Lasers and Electro-Optics (ICALEO), November 2-5 2009, Orlando USA
2. Frontiers in Optics, Laser Microfabrication, October 11-15 2009, San Jose USA
3. LAMP 2009, The 10th International Symposium on Laser Precision Microfabrication, June 29, July 2 2009, Kobe Japan
4. Symposium on Laser Nanophotonics, 13-17 July 2009, Barcelona, Spain
5. World of Photonics Congress, Laser in Manufacturing, 15-17.06.2009, Munich, Germany
6. Ecole Femto 2008, 29.09-3.10. 2008, Mittelwihr, France
7. Journée modélisation "Interaction rayonnement-matière: du solide au plasma" 24-26.09.2008 Paris, France

8. Advanced Laser Technologies ALT08, 13-18.09.2008 Siofok, Hungary
9. The Fifth International Symposium Modern Problems of Laser Physics (MPLP 2008), 24-30.08.2008, Novosibirsk, Russia
10. SiO2-2008 Conference, 30.06-2.07.2008 Saint Etienne, France
11. The 9th International Congress on Laser Precision Microfabrication LPM 2008 16-20.06.2008, Quebec City, Canada
12. Ultrafast Phenomena 2008, 9-13.06.2008, Stresa, Italy
13. MRS Strasbourg 2008, 26-30.05.2008
14. High-Power Laser Ablation Conference, HPLA 2008, 20-24.05.2008, Taos, USA
15. Gordon Conference on Photoacoustic and Photothermal Phenomena: Photoinduced Processes and Applications, 10.02-15.02. 2008, Ventura, California, USA
16. SPIE Photonics West08 Laser Microprocessing, 01.2008 San Jose, USA
17. 9th International Conference on Laser Ablation COLA 07, 24-28.09.2007 Tenerife, Spain
18. Second France-China Workshop on Ultra-short and Ultra intense Lasers and Applications FCILA 2007, 6-8.06.2007 Lyon, France
19. The 8th International Congress on Laser Precision Microfabrication 24-28.05.2007, Wien, Austria
20. Workshop Modélisation et procédés laser ultra brefs, 26-28.03.2007 Carry le Rouet, France

Contents

1	Introduction	1
2	Focusing of ultrashort laser pulses	5
2.1	Definitions	6
2.1.1	Mathematical model of ultrashort laser pulses	6
2.1.2	Spatial beam profile	6
2.1.3	Temporal pulse profile	7
2.2	Linear propagation	9
2.2.1	Spatial effects	9
2.2.2	Temporal effects	22
2.3	Nonlinear propagation	23
2.3.1	Self-focusing	25
2.3.2	Self-phase modulation	25
2.4	Conclusion	26
3	Light interaction with dielectrics	28
3.1	Nonlinear ionization	28
3.1.1	First photoionization mechanisms	28
3.1.2	Impact ionization and photoionization	30
3.2	Optical properties	32
3.2.1	Free electrons without damping in vacuum	32
3.2.2	Free electrons with damping in materials	34
3.3	From the transient electronic gas to the refractive index modification	37
3.3.1	Color centers	37
3.3.2	Lattice re-organization	39
3.3.3	Thermomechanical effects	40
3.4	Conclusion	40

4	Experimental set up	41
4.1	Laser sources	41
4.2	Temporal pulse shaping	43
4.2.1	Generalities	43
4.2.2	Temporal shaping apparatus	46
4.3	Spatial beam shaping	46
4.3.1	Beam controllers	47
4.3.2	The optical valve	48
4.3.3	Designing the wavefront modulation	50
4.4	Experimental details	56
4.4.1	Generalities	56
4.4.2	Observation microscope	57
4.4.3	Beam characterization instruments	59
4.4.4	Beam delivery	59
4.4.5	Samples and sample displacement	59
5	Static observations of permanent modifications	61
5.1	Characterization techniques overview	62
5.1.1	Microscopy-based methods	62
5.1.2	Indirect techniques	66
5.2	Analysis of permanent laser-induced traces in glass	68
5.2.1	Main regimes of photoinscription	69
5.2.2	Full characterization of BK7 glass irradiations	71
5.2.3	A new single pulse photoinscription regime: formation of regular pre-dots	76
5.2.4	Spherical voids with single pulse in borosilicate glass (D263)	82
5.2.5	Application of laser-induced birefringence in fused silica	85
5.3	Conclusion	88
6	Time-resolved imaging of transient bulk modifications	90
6.1	Introduction	91
6.1.1	State of the art	91
6.1.2	Experimental details	92
6.2	Method for mapping the free electronic density and of the ionic contribution	93
6.2.1	Calculation of the free electronic density from OTM images	93
6.2.2	Method to unveil the transient matrix state	94
6.3	Influence of the pulse length on the free carrier generation above the modification threshold	96

6.4	Mapping of the transient free electronic density and the matrix phase in BK7 and fused silica	100
6.4.1	Topology of the free carrier density and lifetime in BK7 glass	100
6.4.2	matrix dynamics after ultrashort irradiation in BK7 glass	103
6.4.3	Free carrier density and matrix changes in SiO ₂ glass	105
6.5	Pressure wave characterization in glass	106
6.5.1	The pressure wave as an energy transfer indicator in fused silica	107
6.5.2	Double pressure wave generated in fused silica	108
6.5.3	Morphology of pressure waves in other glasses	109
6.6	Time-resolved investigations of temporally shaped pulses	109
6.7	Pump-probe picturing in type II waveguide writing regime in fused silica	112
6.8	Conclusion	116
7	Spatio-temporal laser beam control for bulk functionalization	117
7.1	Temporal tailoring for improved energy deposition	117
7.1.1	Experimental details	118
7.1.2	Results and discussion	118
7.2	Aberration counteraction in longitudinal waveguide writing in BK7 glass	122
7.2.1	Wavefront aberrations in longitudinal writing	122
7.2.2	Experimental details	125
7.2.3	Results and discussion	126
7.3	Wavefront modulation for parallel photoinscription	132
7.3.1	Description of dynamic multispot operation	133
7.3.2	Experimental precisions	134
7.3.3	Results and discussion	135
7.4	Conclusion	145
8	Conclusion and perspectives	146

List of Figures

2.1	General scheme of light focusing of a collimated laser beam.	5
2.2	Propagation of a Gaussian beam around the waist: The normalized intensity profile is plotted along the z axis. The beam waist w_0 , Rayleigh range z_R and wavefront radius of curvature $R(z)$ are indicated.	8
2.3	General propagation scheme for an electromagnetic wave.	10
2.4	Simulated focal fluence map in air for 3 simple beam truncation situations concentrated by a 4 mm focal length focusing objective (FO) for a $1 \mu\text{J}$ light pulse (after the lens). Left: Intensity distribution in the lens plane (x, y) . Center: Fluence distribution around the focal plane (x', y') at which $z_f = 0$. Right: Fluence distribution in the x, y plane of higher light concentration. a) Pure Gaussian focusing without any truncation. b) Uniform illumination of a 1 mm radius pupil. c) Gaussian illumination of a 1 mm radius pupil with the $\frac{1}{e^2}$ intensity drop matching the pupil radius. The focal map possess a cylindrical symmetry with respect to the propagation axis z and laser arrives from left. Note the transformation from a Gaussian distribution towards an Airy pattern when beam truncation takes place.	12
2.5	Temporal broadening estimation due to pulse front distortions from a fused silica lens in air adapted from [Bor88]. a) Geometrical scheme for pulse front calculations. The pulse front travels at the speed of light c in the air and at the group velocity v_G in the lens. b) Pulse front shape and position around F following [Bor88] in the discussed focusing conditions at different moments $t = -30, -15$ and -1 fs before the marginal rays reach the focal plane ($t = 0$) . The marginal portions of the pulse front meet the focal area before the paraxial components, leading to a signal temporal stretching of ΔT at the focal point. As explained in the text, this temporal elongation is independent of the light pulse temporal properties.	15

2.6	Optical microscopy pictures of the pulse front tilt effect in transverse bulk machining of fused silica from [YKS ⁺ 08a]. k is the wave vector of the writing laser. the blue arrows stand for the sample scanning direction. The pulse front tilt is managed by the used of two a) or three b) mirrors and is schematically represented in red. Dark-background pictures were obtained with the addition of crossed polarizers.	17
2.7	Scheme for chromatic aberration estimation when light is focused in the bulk of a glass sample. d_b (d_r) is the penetration depth of the bluer (redder) part of the laser spectrum, d_{foc} is the focusing depth, i.e the penetration depth if the sample had a refractive index $n = 1$.	18
2.8	Examples of common wavefront aberrations in radians described by Zernike polynomials. a) Tilt. b) Defocus. c) Coma. d) Astigmatism. e) First order spherical aberration. f) Second order spherical aberration	20
2.9	Simulated fluence map around the focal spot in presence of various optical aberration for a 4 mm focal length lens ad a 1 μ J light pulse. Left: Fluence distribution around the focal plane (x', y') at which $z_f = 0$. Right: Intensity distribution in the focal plane (x', y'). a) Astigmatism. b) Coma. c) Spherical aberration.	21
2.10	Calculated pulse elongation (FWHM) due to both SOD and TOD after propagation in glass. a) FWHM dependency on the propagation distance. Open symbols: fused silica, solid symbols: BK7 glass. Triangles: 50 fs pulse, circles: 150 fs. Right: Calculated pulse shape after 1 m of glass with b) only the TOD effect, and c) d) with both SOD and TOD. The blued area stands for the secure propagation window visited in this report, where negligible SOD and TOD pulse stretching takes place for the 150 fs pulse.	22
2.11	Illustration of nonlinear spatio-temporal propagation effects in a glass with $n_2 > 0$ adapted from [Sch01]. a) Spatial effect: self-focusing of a collimated beam. b) Temporal effect: blue frequency shift due to self-phase-modulation.	24
2.12	Comparison of calculated fluence and intensity maps assuming pure linear Gaussian propagation a), c) and taking into account non linear effects solving the NLSE b), d) which considers self-focusing, self phase modulation, plasma defocusing, self-steepening and energy absorption due to photoionization (see [BBS ⁺ 07]). The z-scale is logarithmic.	27

3.1	Schematic representation of the main photoionization mechanisms in dielectric depending on the Keldysh parameter γ . a) Multiphotonic ionization ($\gamma > 1.5$). b) Intermediate situation where both MPI and TI mechanisms take place. c) Tunneling ionization ($\gamma < 1.5$). d) Ionization from intermediate energy levels associated with material impurities.	29
3.2	Reflectivity and transmission of $1\ \mu\text{m}$ thick free electronic cloud according to the Drude model without damping with respect to the ratio $\frac{N}{N_{cr}}$ for 800 nm and 400 nm optical radiation. For 400 nm light, N_{cr} is $7 \times 10^{21}\ \text{cm}^3$ and for 800 nm light, N_{cr} is $1.74 \times 10^{21}\ \text{cm}^3$ in vacuum.	34
3.3	Reflectivity and transmission of $1\ \mu\text{m}$ thick free electronic cloud in fused silica according to the Drude model with damping with respect to the ratio $\frac{N}{N_{cr}}$ for 800 nm and 400 nm optical radiation. In fused silica, for 400 nm light, N_{cr} is $1.5 \times 10^{22}\ \text{cm}^3$ and for 800 nm light, N_{cr} is $3.7 \times 10^{21}\ \text{cm}^3$. The solid curves assume a constant Drude damping time τ whereas the dashed plots include a inverse proportionality to $\frac{N}{N_{cr}}$, taking into account the screening effect.	36
3.4	Refractive index of a free electronic cloud in fused silica according to the Drude model with damping with respect to the ratio $\frac{N}{N_{cr}}$ for 800 nm and 400 nm optical radiation.	37
3.5	Schematic illustration of exciton and intrinsic defect energy levels in fused silica. Exciton self trapping energy relaxation into permanent or transient defects is represented by the violet arrows. The absorption band of each type of defects is also reported on the left energy scale (adapted from [MQG ⁺ 04, SW96])	38
4.1	Schematic representation of high repetition rate amplified femtosecond laser source from Coherent. The green arrow represents the pump beam and the red arrow the seeded and amplified femtosecond pulses.	42
4.2	Schematic illustration of temporal femtosecond pulse through spectral components manipulation extracted from [Tra07].	43
4.3	Temporal shaper unit employed in this report. CM: Curved mirror. LC-SLM: Liquid-crystal spatial light modulator allowing for phase manipulation of the pulse spectral components. In the absence of the LC-SLM, this set up is called a zero dispersion stretcher unit because the exit pulse is then exactly recomposed as the initial pulse without any distortion.	44
4.4	General scheme of spatial beam shaping which implies amplitude wavefront modulation to obtain user defined focal spot.	46

4.5	LC-SLM employed for spatial beam shaping on the HRR laser system (extracted from [San05]). Left: Principle of working of the optically-addressed optical valve. Right: Photography of the component (yellow).	49
4.6	Global search optimization illustration. a) Illustration of a the space search associated with an phase addressing point with examples of optimization progress. HC stands for hill climbing and and SA for simulated annealing. HC steps 1 to 3 shows local maximum trapping whereas SA steps 1 to 3 shows global maximum finding. b) Iteration steps of the HC optimization loop. c) Iteration steps of the SA optimization loop.	53
4.7	Iterative steps of the evolutionary optimization strategy.	54
4.8	Scheme of the experimental set up associated with the HRR laser system. TS: temporal shaper as presented in Sec. 4.2. WS: wavefront sensor. HeNe-WL: Helium Neon laser source (emitting at 633 nm) and white light source for waveguide characterization. OTM-PCM: Optical transmission and phase contrast microscopy for sample modification investigation. T1: Telescope enlarging the femtosecond laser beam before the LC-SLM. SP: Spatial shaping unit composed of an optically addressed 2D LC-SLM. T2: Demagnifying telescope imaging the LC-SLM plane on the focusing objective (FO) entrance pupil. The setup enables spatio-temporal optimization of the femtosecond laser pulses according to a desired bulk modification.	57
4.9	Illustration of the experimental set up associated with the LRR laser system. TS: temporal shaper illustrated in the top inset and presented in Sec. 4.2. FO: focusing objective. OTM-PCM: Optical transmission and phase contrast microscopy for sample modification investigation. χ^2 : Frequency doubling crystal. PD: Photodiode. CC: Cross-correlation apparatus. DL: delay line. T1: Telescope reducing the femtosecond laser beam size before second frequency doubling crystal. T2: Telescope magnifying the beam before entering the microscope illumination path. The setup permits temporal pulse optimization of laser induced bulk modification and time-resolved side picturing of the focal volume area upon temporally shaped femtosecond irradiations.	58

5.1	Schematic representation of the light trains in phase contrast microscopy. C. A.:circular annulus, C: condenser, D: diffracted wave, B: background or non-diffracted wave, Obj.: microscope objective, Ph. P.: circular phase plate, Oc.: ocular. The sample is supposed to be a phase only object. The circular annulus is optically conjugated with the phase plate implying that all non-diffracted rays traverse the circular phase plate with an associated artificial retardation. The delay is tuned to achieve constructive (resp. destructive) interferences with the diffracted waves thus yielding bright (resp. dark) zones in the image.	63
5.2	Illustration of the principle of differential contrast microscopy. Pol.: polarizer, Wol. P.: Wollaston Prism, C: condenser, Obj.: microscope objective, Anal.: analyzer. The sample is supposed to be a phase only object with to regions of different refractive index ($n_1 > n_2$). The pair of Wollaston bi-prisms allows for transformation of the optical index gradient into intensity variations thanks to their birefringent properties. The technique is sensitive to refractive index gradients only. More details are provided in the text.	64
5.3	Mach Zender Microscopy principle. C: condenser, O: microscope objective, S: sample with phase object, R: reference sample. a) Illustration of the light pathway in the interferometric set up. The Mach Zender configuration splits the source light into two arms (object and reference arm) whose only difference relies in the phase object to be analyzed. The fringes distortions in the image formed by the recombined beam are directly related to the refractive index modulation to be measured. b) MZM image of two bulk photowritten waveguides in BK7 glass. The deviation of the fringes is clearly observable in the core of the waveguide.	65
5.4	Principle of local refractive index increase of a bulk photowritten waveguide from the measurement of its numerical aperture $NA = \sin \left[\arctan \left(\frac{r}{d} \right) \right]$. FO: focusing objective. The inset shows a typical far field pattern of a longitudinal photowritten waveguide in fused silica glass.	67
5.5	Photoinscription regime overview in fused silica (left) and BK7 (right) in PCM for 150 fs pulses. a) and b) Effect of the accumulation of pulses at 166 Hz in static conditions. c) and d) Structures obtained upon longitudinal sample scanning at $50 \mu\text{m/s}$ and 100 kHz repetition rate.	70

5.6	Femtosecond irradiation outcome in BK7 glass (10^5 pulses (100 kHz) at $200\text{ }\mu\text{m}$ deep with $\text{NA} = 0.45$ and $\text{NA}_{eff} = 0.41$. The laser comes from the left. a) Static irradiation b) Scanning at $1\text{ }\mu\text{m/s}$ along the laser propagation axis; the spot moving towards the laser source. The same structure is pictured using various microscopy techniques: OTM: Optical transmission microscopy, PCM: Phase contrast microscopy, DIC: Differential interference microscopy, MZM: Mach Zender microscopy, QPM: Quantitative phase microscopy.	72
5.7	Refractive index profile cross section of longitudinal waveguides in BK7 glass measured with QPM and MZM.	74
5.8	QPM refractive index profile cross section of static traces (first column) and longitudinal waveguides (second column) in BK7 glass without inverse Abel transform a) and with the inverse transform b). Transverse cross-sections indicated by the dotted lines occupy the bottom row. As the Abel transform requires a cylindrical symmetry for the projected data, the images were numerically mirrored with respect to the optical axis.	75
5.9	Pictures of single pulse irradiation outcome in the bulk of fused silica and BK7 glass under phase contrast microscopy (PCM) and optical transmission microscopy (OTM). The laser pulse comes from left and its energy was varied from the first detectable modification regime to the higher available energy. The latter case shows a novel photowriting regime where very regularly spaced dots are formed up to $200\text{ }\mu\text{m}$ before the focal area upon single pulse irradiation. $\text{NA} = 0.45$ and $\text{NA}_{eff} = 0.42$	77
5.10	Comparison between a) PCM pictures of single pulse irradiation in fused silica and BK7 glass with the b) Fresnel propagation results in both glasses. The vertical dashed lines shows the correspondence between the position of the dots before the region of main focus and the the fluence peaks predicted by the propagation code. c) displays an horizontal cross section of the PCM picture (solid) and the the numerical results (square)	79
5.11	Example of an array of dots written in fused silica in the depicted photowriting regime. Each line was written from a single pulse irradiation. The main damage is situated on the right and is not shown.	81
5.12	Successive write/erase/write... operation in BK7 glass illustrated by PCM pictures. The morphology of the femtosecond (fs) and picosecond (ps) structures is preserved in the previously erased zone.	82

5.13	PCM pictures of single pulse irradiation in D263 borosilicate glass for various pulse energy and duration. The laser comes from left and the focusing objective associated with an index-matching oil provided a numerical aperture of 1.25. The inset shows a quasi-spherical voxel where the no elongation along the laser propagation axis takes place. the depth of the structures is $130\text{ }\mu\text{m}$ with respect to the surface.	83
5.14	Cumulative study in fused silica at $200\text{ }\mu\text{m}$ deep observed with optical transmission microscopy (OTM), phase contrast microscopy (PCM) and cross polarizers microscopy (CPM). The appearance of birefringent structures after a few hundreds of pulses is denoted by the bright area in CPM. $\text{NA} = 0.45$ and $\text{NA}_{eff} = 0.42$. . .	85
5.15	Polarization dependent optical guiding in various types of longitudinal waveguides in a-SiO ₂ written by linearly polarized 800 nm femtosecond laser radiation with $\text{NA} = 0.42$ and $\text{NA}_{eff} = 0.31$. Images in the left frame show top view PCM pictures of photowritten waveguides with a linear polarization indicated on the left side. The upper part depicts a type I trace while a type II is represented in the bottom part. The right frame shows near-field modes for injected 800 nm radiation; the polarization of the injection laser is depicted on the top of the right frame. All the structures are written by 33 mW (type I) and 195 mW (type II), 100 kHz laser pulses at the speed of $10\text{ }\mu\text{m}$. The length of all waveguides is 7.3 mm	87
5.16	Morphological details on the type II waveguide: a) PCM pictures of the extremities of type II structure written at 150 mW , 50 kHz and $10\text{ }\mu\text{m}$ compared with a static trace (1 s irradiation), b) scanning electron microscopy picture of the waveguide cross section after transverse cutting, polishing and etching showing the nano-gratings perpendicular to the writing laser polarization.	87
6.1	Illustration of the experimental set up for time-resolved studies. TS: temporal shaper. FO: focusing objective. OTM-PCM: Optical transmission and phase contrast microscopy for sample modification investigation. χ^2 : Frequency doubling crystal. DL: delay line. T1: Telescope reducing the femtosecond laser beam size before second frequency doubling crystal. T2: Telescope magnifying the beam before entering the microscope illumination path. the additional laser source labeled Nd:Yag emits nanosecond pulses at 532 nm	92

6.2	Illustration of the steps of the proposed calculation method to extract the matrix phase variations from time-resolved pictures of BK7 glass at various delays in the high energetic regime of photoinscription (4.3 μ J, 150 fs pulse focused at NA= 0.45 and NA _{eff} = 0.42). The maximum detectable absorption under OTM was found at 1 ps. From left to right: OTM picture; calculated $\frac{N_e}{N_c}$; PCM picture; subtraction of the PCM picture with the $\Delta n_{x,z}$ calculated from the $\frac{N_e}{N_c}$ map. See text for details.	96
6.3	Intensity dependence of the transient electronic density N_e normalized to N_{cr} for femtosecond and picosecond pulse at NA= 0.45 and NA _{eff} = 0.38. a) Side $\frac{N_e}{N_{cr}}$ mapping from optical transmission microscopy pictures following Eq. 6.3. The laser comes from left. b) Averaged $\frac{N_e}{N_{cr}}$ versus the pulse energy over an identical volume for picosecond and femtosecond cases on logarithmic scales.	97
6.4	Intensity dependence of the electronic density map N_e normalized to N_{cr} for femtosecond and picosecond pulse in fused silica. a) Examples of transient $\frac{N_e}{N_{cr}}$ with indication of the estimated focal plane (dashed line) for femtosecond (bottom) and picosecond (top) irradiation. $\frac{N_e}{N_{cr}}$ was averaged on the left (empty) and on the right (solid) of the focal plane for femtosecond (circles) and picosecond (squares) and plotted vs the pulse energy in b). An overall saturation of the electronic density is clearly observable for the shorter pulse, whereas the picosecond irradiation permits a significant increase of the electronic density before the focal plane.	99
6.5	Selected time-resolved images with OTM and PCM in fused silica and BK7 glass in the energetic regime of photoinscription, 4.3 μ J, 150 fs, NA= 0.45 and NA _{eff} = 0.42.	101
6.6	Electronic densities as a function of the optical delay for various regions of the irradiation volume in BK7. The conditions are the same as Fig. 6.2. a) $\frac{N_e}{N_c}$ map at 1 ps (top) with a PCM picture of the permanent modification (bottom) at the same scale. Areas of interest are designated by the letter B,C,D,F for which the decay is plotted in b). The dashed line represents the estimated geometrical focus.	102
6.7	Electronic densities and free carrier lifetime along the laser propagation axis in BK7 . The PCM picture of the corresponding permanent modification is shown to scale in background. Irradiation conditions: 4.3 μ J, 150 fs, NA= 0.45 and NA _{eff} = 0.42	103

6.8	BK7 matrix qualitative phase mapping of the interaction region on ultrashort time scales. a) matrix map at 30 ps (top) with a PCM picture of the permanent modification (bottom) at the same scale. Areas of interest are designated by the letters D and F for which the transient variations are plotted in b). The horizontal line in b) shows the background level.	104
6.9	Electronic density and matrix variations in fused silica. a) Free carrier lifetime along the laser propagation axis in fused silica. The PCM picture of the corresponding permanent modification is shown in background. b) matrix map at 30 ps (top) with a PCM picture of the permanent modification (bottom) at the same scale. Areas of interest are designated by the letters D and F for which the transient variations are plotted in c). The horizontal line in c) shows the background level. Irradiation conditions: $4.3 \mu\text{J}$, 150 fs, $\text{NA} = 0.45$ and $\text{NA}_{eff} = 0.42$	105
6.10	Pressure wave picturing from PCM images for various pulse duration in fused silica at constant pulse energy. ($4.3 \mu\text{J}$, 150 fs, $\text{NA} = 0.45$ and $\text{NA}_{eff} = 0.42$) . . .	106
6.11	Comparison of the $\frac{N_e}{N_c}$ and the PW amplitude for femtosecond to picosecond pulse durations in fused silica. a) $\frac{N_e}{N_c}$ map calculated from OTM pictures. b) Comparison of the $\frac{N_e}{N_c}$ (triangles) and the PW amplitude (squares). Pulse energy: $4.3 \mu\text{J}$, $\text{NA} = 0.45$ and $\text{NA}_{eff} = 0.42$	107
6.12	Evidence of two pressure waves from a single femtosecond pulse irradiation in fused silica from a transient PCM picture a). b) Determination of the traveling speed. c) Amplitude decay of PW1 as a function of radius. Pulse energy: $40 \mu\text{J}$, $\text{NA} = 0.45$ and $\text{NA}_{eff} = 0.42$	108
6.13	PCM pictures of the pressure wave of (left to right) fused silica, BK7, SF57 and TeO_2 glass resulting from a femtosecond pulse irradiation at $\text{NA} = 0.45$ and $\text{NA}_{eff} = 0.42$	109
6.14	PCM pictures of permanent modifications in fused silica associated with a) picosecond irradiation with various pulse length and b) double pulse sequence with various temporal separation. The total pulse energy is $20 \mu\text{J}$ and $\text{NA} = 0.45$ and $\text{NA}_{eff} = 0.42$	110
6.15	Calculated transient $\frac{N_e}{N_c}$ for single irradiation with a) a 150 fs pulse, b) a 3 ps and two pulses separated by 3 ps. Each irradiation sequence carries an energy of $6 \mu\text{J}$. Left column: example of the $\frac{N_e}{N_c}$ 2D map corresponding to the delay of maximum free carrier generation. Right column, Temporal evolution of the maximum $\frac{N_e}{N_c}$ with indication of the irradiation envelope. Picosecond and double pulse sequences generate a $\frac{N_e}{N_c}$ three times higher than the femtosecond case. $\text{NA} = 0.45$ and $\text{NA}_{eff} = 0.38$	111

6.16	Time-resolved OTM (left) and PCM (right) pictures in single and cumulative regime corresponding to type II waveguide writing i.e 180 fs, 1000 pulses, 1.5 μ J at NA= 0.45 and NA _{eff} = 0.42.. 'Perm.' refers to permanent modification.	113
6.17	Details of the temporal evolution of the laser modification after 1000 pulses from OTM a) and PCM b) pictures. The mean gray level of the head (square) and the tail (triangle) of the trace is plotted versus time delay.	115
7.1	a) PCM images of static permanent structures and transient plasma observations induced by single short pulse in bulk irradiated α -SiO ₂ for various depths. Irradiation parameters: 160 fs and 1 μ J. The laser pulse is coming from left. The plasma images are taken 1 ps after the pulse excitation. b) Schematic view of spherical aberration.	119
7.2	a) Short pulse (SP) and optimal pulse (OP) induced structures at a depth of 500 μ m and 1 μ J input energy. b) The corresponding axial cross-sections. The inset shows the optimal pulse shape.	120
7.3	Structures induced by pulses with different pulse durations a) or double pulse sequences with various pulse separations b) at 1 μ J. Energy effects for pulses with selected durations; short 0.16 ps pulse c), 2 ps pulse d), and 6 ps pulse e). All structures are induced at a depth of 500 μ m.	121
7.4	Illustration of longitudinal waveguide writing with the associated wavefront distortions upon deep focusing [HTS ⁺ 05]. Insert: Description of spherical aberration due to refraction at air-dielectric interfaces and the subsequent elongation of the focal area. The longitudinal aberration depends on the index contrast between the two media and increases with the numerical aperture and the focusing depth. . . .	124
7.5	The feedback loop diagram. a) Schematic representation of the optimization procedure, emphasizing the main steps of the self-improvement approach. The strategy involves applying, testing and comparing each phase mask according to its ability to achieve user-defined bulk modification, (here restricted axial elongation of the structure). b) Phase-mask fitness attribution sub-steps: irradiation of the sample with the tested phase mask, estimation of the corresponding trace length and ranking of the phase mask.	125

7.6	Static (left, (a,b)) and dynamic, longitudinally-written (right, (c,d)) material modifications induced in BK7 by ultrafast laser radiation at different input powers with $NA = 0.45$ and $NA_{eff} = 0.41$. The static irradiation corresponds to 10^5 pulses/site while the dynamic structures are made at a scanning speed of $1 \mu\text{m/s}$. Laser pulses are incident from the left and scanned towards the laser source. The structures are localized at $200 \mu\text{m}$ depth with respect to the air-dielectric interface. Waveguide writing conditions are achieved only at high powers (see text for details). e) Axial cross-section through the laser written structures in conditions a) and b). The axial cross-sections correspond to the relative change in the refractive index.	127
7.7	Evolution of the trace fitness during the optimization run at the depth of $2500 \mu\text{m}$. Example of traces and corresponding gray-level phase masks at different moments of optimization are given as well.	129
7.8	a) Non-corrected (left) and spatially-corrected (right) static structures induced at different depths with respect to the sample surface $NA_{eff} = 0.41$. The working depth was defined in Fig. 7.4 as the position of the paraxial focus. The structures are induced by 10^5 pulses of 150 fs duration at 100 kHz and 125 mW average power. b) Axial cross-sections through some laser written structures. Note the discrepancies in the spatial scales in a) and b).	130
7.9	Comparison between the effect of theoretical and optimized correction phase masks for 125 mW input power. Static laser structures induced at $2000 \mu\text{m}$ depth without correction (1), with theoretical correction (2), with adaptive correction (3). $NA = 0.45$ and $NA_{eff} = 0.41$	130
7.10	Longitudinal structures at different working depths in corrected (top) and non-corrected (bottom) cases. The corrections enable a positive refractive index change over a distance of 3 mm . Scanning speed is $1 \mu\text{m}$ at 125 mW average power. Right, far-field pattern of the guided mode at 633 nm for the corrected guide.	131
7.11	Scheme of double spot operation. BPM: Binary phase mask. Insert: Double spot intensity profile inside the sample at the focus of the objective generated by a simple step grating phase at very low power captured by direct imaging on a CCD camera. The blue arrow shows the direction of motion of the sample for longitudinal photoinscription.	133

7.12	Comparison between single and double spot longitudinal photoinscription of waveguides in fused silica. Up: Single spot operation, down double spot operation. a) Side view PCM picture of SSO photowritten waveguides written at different translation speeds at 10 kHz, 8 mW, superposed with transversal cross section of the relative gray scale decrease indicating a positive change of the refractive index (see text body). b) corresponding nearfield profile of 633 nm injected guide written at $5 \mu\text{m/s}$, 10 kHz, 8 mW in single spot operation. c) PCM picture of two simultaneously photowritten waveguides through double spot operation at $5 \mu\text{m/s}$, 10 kHz, 24 mW. d) Optical transmission microscope picture of the cross section of one of the waveguides in c) in white light illumination. e) nearfield profile of one of the waveguides pictured in c) at 633 nm. $\text{NA} = 0.32$ and $\text{NA}_{\text{eff}} = 0.21$	136
7.13	Illustration of the main steps of the photowriting of a light divider based on evanescent coupling in a single sample scan. The period of the binary grating is increased at a certain moment during photoinscription in order to draw closer the two processing foci, thus machining the light divider according to the desired shape.	140
7.14	Bulk photowritten light divider based on evanescent coupling of injected waves in partial arrays achieved through double spot operation at 24 mW total power and $5 \mu\text{m/s}$ scan velocity: a) schematic view of the structure: The conditions followed by l_c and l_{c2} enabling evanescent coupling from the central to the external guides are given in the text. b) Assemblage of PCM side-pictures of the device, its total length is 8.2 mm and the lateral separation between tracks is $9 \mu\text{m}$. c) Nearfield profile under HeNe injection at 633 nm.	140
7.15	Bulk photowritten WDD device achieved through double spot operation at 24 mW total power and $5 \mu\text{m/s}$ scan velocity. a) Schematic view of the structure (condition followed by l_o is given in the text). b) Nearfield profile under 633 nm (solid) and 800 nm (dashed) simultaneous injection in the top arm. c) PCM side-image of the overlapping region. d) Theoretical prediction of the 633 nm (solid) and 800 nm (dashed) intensity variations in the excited waveguide according to [Sny72, MS74] taking into account the wavelength dependance of the coupling coefficient. The total length of the structure is 7.4 mm.	142
7.16	a) Schematic view of a bulk photowritten twisted X coupler achieved through DMSO in a single scan. b) Optical transmission microscopy pictures of the central region, showing 90° rotation. c) Nearfield profile at the output of the top arm under 633 nm injection in the bottom waveguide.	143

7.17	Schematic view of bulk photowritten 3D light dividers achieved through DMSO.	
	a) One to four light divider. b) One to seven hexagonal light divider. The conditions followed by l_{c4} and l_{c6} are given in the text. Inserts: Nearfield profile under 633 nm injection in the central waveguide	
	Schematic view of a bulk photowritten 3D hexagonal light divider achieved through DMSO. Inserts: Nearfield profile under 633 nm injection in the central waveguide.	144

List of Tables

2.1	Examples of Zernike polynomials describing common geometrical aberrations. . .	19
4.1	Laser sources characteristics	42
4.2	Common spectral phase masks and their effect on the output pulse temporal profile	45
4.3	Main characteristics of the optical valve employed on the HRR system for spatial beam shaping.	49
4.4	Basic iteration of the IFTA or Gerchberg-Saxton algorithm [GS72].	51
5.1	Main refractive index evaluation techniques. PCM: Phase contrast microscopy, DIC: Differential interference microscopy, MZM: Mach Zender microscopy, QPM: Quantitative phase microscopy, NAD: Numerical aperture determination, NFPA: Near field profile analysis, LM: Lloyd's mirage, RNF: Refracted near field profilometry.	69
6.1	Proposed method to unveil the matrix dynamics by canceling the free electronic contribution	95

Chapter 1

Introduction

Optical functionalization of bulk transparent materials is a growing field of expertise constantly fed by market demands of various integrated optical devices. While planar techniques for fabricating such components constitute an efficient and available industrial solution, it is now more and more confronted to inherent limitations intimately linked to the planar processing strategy unadapted for three-dimensional (3D) devices.

On this particular point, the laser processing techniques bear substantial arguments, peculiarly when ultrashort pulses are employed [MJ06].

A significant aspect of the nonlinear interaction of the infrared femtosecond pulses with dielectric media is the possibility to trigger material properties alterations on a restricted volume. When tightly focused into a transparent media, irradiances of several TW/cm^2 are generated in a few micrometers size focal volume [TSZ⁺06]. This tremendous electric field approaching the bounding strength of matter has immediate effects of the electronic population of the material. Multiphotonic electronic excitation along with tunneling ionization feed the conduction band with new carriers during the very first moments of interaction, then accompanied by a collisional multiplication process. For sufficiently tight focusing, electronic densities up to $10^{21-22} \text{ cm}^{-3}$ are produced in a few tens of femtosecond [HBT⁺07]. Such a cloud strongly modifies the transient and permanent optical properties of the media. After the femtosecond pulse passage, various energy relaxation paths lead the system back to a thermodynamical equilibrium. When the excitation efficiency is enough, optically driven permanent material transformations are induced. The material's behavior under femtosecond illumination as well as the laser pulse spatio-temporal properties determine the nature of the laser-induced local variations. These structural modifications may change several optical characteristics such as birefringence, absorption, and refractive index. This last feature opens the door to the achievement of more complex photonic devices as a translation of the single laser spot permits three dimensional photo-drawing of light-guiding components.

This application of great interest has been demonstrated thirteen years ago where ultrashort

pulses were employed in order to trigger local increase of the refractive index and produce embedded waveguides upon laser spot translation [DMSH96]. These promising results triggered a great interest in the research community, as the 3D available processing axis offered by the laser machining technique presented the immediate potential to push away the acquainted planar limitations. Significant efforts were carried out to unveil the physical processes governing the interaction identifying several competitive absorption channels (multiphotonic [TSZ⁺06], tunneling [JLS⁺03] and impact ionization [SFH⁺96a]) and energy relaxation pathways (defect generation, densification [MQG⁺04]) with the help of time-resolved investigations. If this fundamental aspect is still widely investigated, the engineering facet has attracted numerous research groups demonstrating the bulk machining potential in achieving more and more complex embedded photonic structures in a few-steps process. For instance, in fused silica glass, a growing plethora of optical circuits unceasingly alimments the literature (waveguides , light couplers, light dividers, Bragg gratings, Fresnel lenses, microfluidic channels, optical storage... see [IWNS06, Kro08, BSB05] and references therein). When the dielectric material is carefully chosen and/or conceived (e.g with the addition of dopants) , active optical components are possibly envisaged. In that frame, recent reports confirmed this extent of the bulk femtosecond writing technique fabricating gain waveguides [SSB⁺00], frequency-doubling waveguides [CTH⁺07] and femtosecond-written waveguide lasers [VTO⁺07].

For most of those realizations, a rather straightforward experimental set-up is employed as it generally resumes to a femtosecond laser source whose radiation is focused inside a polished sample. The specimen is then translated longitudinally or transversally with respect to the laser propagation axis to draw the entire device, both techniques having inherent limitations [IWNS06]. More precisely, longitudinal writing is usually restricted to relatively short photonic circuits, in shallow focusing conditions in order to maintain air/glass wavefront distortions at a low level. The case of transverse writing also requires shallow writing to prevent the machined structures from ellipticity if no additional beam manipulation is employed. With strategies to withdraw these limitations, the perspectives of the field largely meet the level to stand as a preferred solution for the challenges of integrated optics where 3D processing access at any bulk depths is obviously a inevitable step towards versatile embedded photonic components.

In this very thriving field of expertise, we intend to point out an innovative and more general approach to the question of femtosecond bulk machining which is demonstrated to overcome the above-mentioned limitations. As a recurrent strain, this report revolves around this simple assertion, that *spatio-temporal modulation of the laser ultrashort pulses significantly extents the potential offered by femtosecond bulk machining*. For instance, this method has the potential to withdraw the above-mentioned limitations, allowing to judiciously adapt the laser irradiation to the material reaction or to the form to inscribe in a flexible manner. In addition, spatio-temporal shaping also

permits deeper understanding of the laser-matter interaction as it reveals the conditions for optimal energy coupling from the laser pulse to the glassy lattice.

Consequently, in this report, spatial wavefront modulation is shown to enable deep bulk focusing for longitudinal femtosecond machining of waveguides. A demonstration of parallel processing for bulk photowriting is presented as well and also relies on spatial phase control of ultrashort pulses. Also, the effect of temporal tailoring of femtosecond pulses on the photowriting outcome is investigated both from time-resolved picturing of the interaction and from the morphology of the permanent bulk modifications. Unambiguous conclusions regarding the rate of coupled energy with respect to pulse duration are indicated. As these observations imply the use of advanced detection techniques, a special care is taken to briefly introduce the various microscopy techniques utilized. The results are obtained in glasses with contrasted response to the standard ultrafast laser solicitation in order to underline the flexibility of the technique and to better unveil the physical processes leading to bulk modifications.

This thesis is organized as follows. The following chapter (Ch. 2) is dedicated to draw a clear picture of femtosecond laser focusing with a detailed analysis regarding the energy spatial distribution. It is composed of two parts dealing successively with linear and nonlinear behaviors of light. In the first part, critical concepts such as beam truncation, Gouy phase, pulse front distortions, wavefront aberrations and dispersion-related phenomena are presented with their significant effect on the focal distribution of intensity, a determinant parameter for bulk processing. Those relatively simple concepts are of great significance to us as their influence is too often underestimated if not simply forgotten even in refereed literature dealing with experimental results from laser machining; forbidding the reader to fully comprehend the irradiation conditions. Nonlinear effects are taken into account in the second part, namely the self-focusing and the self phase modulation effects with estimation of their impact on the focal intensity distribution in given conditions.

The third chapter reviews the physics of ultrashort light pulses interaction with dielectrics in bulk machining conditions, from the generation of a hot electronic plasma to the production of permanent modifications. A review of the main identified photoionization mechanisms is provided. The excited solid transient state is mathematically treated using the well-known Drude model with emphasis on the effect of the critical electronic density. Energy relaxation pathways leading to various permanent modifications (punctual defects, lattice reorganization and stress accumulation) are indicated.

Ch. 4 describes equipment details regarding the ultrashort light sources employed, as well as the beam manipulation apparatus dedicated to spatial wavefront tailoring and temporal pulse shaping. A delineation of the pump-probe experimental set-up devoted to time-resolved picturing (Ch. 6) occupies a few lines there. The chapter also briefly presents the optimization algorithms at the core of the self-learning feedback loop successfully employed to tune the irradiating pulse

spatial or temporal properties according to desired bulk modification(see Ch. 7).

In Ch. 5 we present a detailed experimental investigation of permanent bulk modifications and photoinscription regimes preceded by an overview of refractive index characterization techniques. A comparison of the available methods (*optical transmission (OTM)*, *phase contrast (PCM)*, *Mach Zender Microscopy (MZM)* and *quantitative phase contrast microscopy (QPM)*) is conducted on a well-defined femtosecond damage in borosilicate crown (BK7) glass in order to form the two-dimensional mapping of the local refractive index modulation, the Abel inversion is discussed in that frame. Various femtosecond irradiation outcomes in different glasses complete the chapter as an illustration of the tremendous diversity of bulk local change available upon varied exposure conditions (numerical aperture, pulse accumulation, polarization...) with a peculiar emphasis on longitudinal waveguide writing windows in fused silica.

After static investigations, time-resolved side-imaging of the transient properties of the material before permanent damage occupies Ch. 6. A new method for separation of the free electronic and lattice contributions on the OTM and PCM pictures is presented. The transient electronic density temporal evolution is studied for femtosecond and picosecond pulse in fused silica above the modification threshold. For the first time, the density topology of the transient electronic gas around the focus is evaluated for both pulse durations, showing the more dense and confined character of the picosecond-generated plasma. The microscopic topology of the bulk free carrier density and lifetime is also investigated. A set of investigations is thus conducted in fused silica and BK7 glass, revealing the axial modulation of the free carrier lifetime which lasts longer in the zones of permanent modification. The pressure wave is characterized for various glasses (fused silica, BK7, TeO₂ and SF57 heavy metal oxide glass). We also investigate on an ultra-short time scale two photoinscription regimes producing similar permanent modifications but implying very contrasted dynamics, namely picosecond and double pulses. Finally, time-resolved measurements are conducted in a regime close to the type II waveguide writing regime.

Ch. 7 introduces experimental results showing that spatio-temporal tailoring extends significantly possibilities offered by ultrashort sources in bulk machining. Deep waveguides in BK7 glass photowritten with dynamic wavefront control are presented at first. They are followed by demonstration of parallel bulk waveguide writing in fused silica. Various photonic components (light couplers, dividers and WDD) designed from evanescent coupling considerations are achieved using the technique. Besides, successful optimizations of temporal pulse shapes according to a user-defined bulk modification in fused silica are presented.

Finally, Ch. 8 sets forth the main experimental results discussing the perspectives with an emphasis on their expected impact on industrial solutions and on fundamental research as well.

Chapter 2

Focusing of ultrashort laser pulses

As energy density is critical for processing purposes, the aim of the present chapter is to revisit basic notions pertaining to the focal distribution of light intensity, particularly when ultrashort pulses are involved. When lasers are used as machining tool, an apparatus aiming at concentrating the electromagnetic field in a well defined spatial position is usually employed to attain adequate intensities (see Fig. 2.1). This operation can be achieved with curved mirrors or with converging lenses. While geometrical optics predict an idealistic light 'point' in the image plane in the case of an aberration-free system, it is obvious that a more general formalism has to be undertaken to understand what happens in the processing plane. It is also the first step to take in order to draw closer to the smallest and shortest light spot available; maybe the most determinant parameter when light is utilized as a machining or an investigating process.

The chapter treats linear and nonlinear effects in two separated parts. It appeared indispensable to us to dedicate a section to the too-often dismissed or taken for granted linear phenomena accompanying light propagation and focusing. Their influence on the spatio-temporal focal intensity distribution and, as a consequence, on the energy deposition and the subsequent irradiation outcome is dramatic. A Fourier-based ([Goo05]) numerical propagation code written in the LabView 6.1 © environment is employed all along the chapter as an illustrative mean to emphasis the impact of the various light properties. After a brief presentation of the theoretical frame with essential definitions, some linear properties of light propagation are reviewed, namely the consequences of



Figure 2.1: General scheme of light focusing of a collimated laser beam.

beam truncation, the Gouy phase, optical aberrations and dispersion. Insights concerning temporal effects are associated with the discussion.

The third part of the chapter relates to the nonlinear aspects of light propagation in the case of ultrashort focusing. Self-focusing and self-phase-modulation are addressed, both having a direct impact on the pulse duration and on the spatial light distribution.

2.1 Definitions

2.1.1 Mathematical model of ultrashort laser pulses

Representation of light as a propagative vibration of an electromagnetic field finds its root in the 19th century and succeeds in explaining numerous physical phenomena. For the purpose of this chapter, this formalism is sufficient. When light travels through a given medium, the properties of the electromagnetic field can be described by the well-known Maxwell equations from which the scalar wave equation on the electric field E can be derived under a few assumptions [GST03]:

$$\vec{\nabla}^2 \vec{E}(x, y, z, t) = \frac{1}{c^2} \frac{\partial^2 \vec{E}(x, y, z, t)}{\partial t^2} \quad (2.1)$$

z being the propagation axis, x, y correspond to the Cartesian coordinates in a transverse plane with respect to the propagation axis, t is the time variable and c the speed of light in vacuum. Therefore, the mathematical model taken for our laser radiation must be a solution to this equation. Under these circumstances, the light wave can be fully characterized by the knowledge of its electric field amplitude $E(x, y, z, t)$ denoted by the complex quantity [DR06]:

$$E = E(x, y, z, t) = \frac{1}{2} \tilde{u}(x, y, z) \tilde{\epsilon}(t) \exp[i(\omega t - kz)] \quad (2.2)$$

k is the wave vector supposing a quasi-monochromatic radiation linearly polarized. It is related to the wavelength in vacuum λ by $k = \frac{2\pi n}{\lambda}$ with n the refractive index of the medium at this wavelength and ω the carrier frequency. The scalar $\tilde{u}(x, y, z)$ denotes the transverse beam profile and $\tilde{\epsilon}(t)$ is the slowly varying complex envelope comprehending the oscillations of the electric field which is described by the exponential term. The contra-propagative term is omitted for simplicity.

2.1.2 Spatial beam profile

When handling a light beam emitted from a stable laser cavity, the spatial intensity repartition of the fundamental mode detected in a given plane $I(x, y)$ is most of the time represented by a Gaussian distribution. In the frame of the paraxial approximation (i.e the transverse beam dimensions remain small enough compared to propagating distances), a quite famous solution to the scalar

wave equation designed to represent laser emission is the Gaussian beam [Sie90]. $\tilde{u}(x, y, z)$ takes then the form:

$$\tilde{u}(x, y, z) = \frac{u_0}{q(z)} \exp \left(-ik \frac{x^2 + y^2}{2q(z)} \right) \quad (2.3)$$

where

$$\frac{1}{q(z)} = \frac{1}{R(z)} - \frac{i\lambda}{\pi w^2(z)} = \frac{1}{q_0 + z} \quad (2.4)$$

$R(z)$ is the wavefront radius of curvature, it is worth noting its z dependency. $w(z)$ is the beam radius at $\frac{1}{e^2}$ of the intensity profile $I(x, y)$. $q(z)$ is the complex beam parameter. This quantity allows complete spatial definition of the Gaussian beam with the relation $q(z) = q_0 + z$. Taking the origin of the z -axis at $z = 0$ at the waist position $w(z) = w_0$ we have $R(z) = \infty$ meaning that at this point the wavefront is a plane orthogonal to the propagation axis (although not to be confused with a plane wave [DR06]). Using Eq. 2.4, the complex beam parameter then writes:

$$q(0) = q_0 = \frac{\pi w_0^2(z)}{i\lambda} \quad (2.5)$$

Substituting q_0 from Eq. 2.5 to Eq. 2.4 and taking the imaginary and the real parts respectively yields the evolution of the beam radius and the radius of curvature along the z -axis [Sie90]:

$$w(z) = w_0 \sqrt{1 + \frac{z^2}{z_R^2}} \quad (2.6)$$

$$R(z) = z + \frac{z_r^2}{z} \quad (2.7)$$

$z_r = \frac{\pi w_0^2}{\lambda}$ is the length over which the beam radius remains below $\sqrt{2}w_0$ which also defines the confocal parameter ($2z_r$). In relation to the limited spatial extent of the Gaussian beam, diffraction involves a certain divergence of the radiation with an gradual increase of the beam radius $w(z)$ and of the wavefront radius of curvature $R(z)$. Fig. 2.2 summarizes the situation with a plot of the intensity profile around the waist position.

The expression of the electric field in Eq. 2.2 solution to the wave equation possess a time-dependent envelope term $\tilde{e}(t)$ which carries the temporal characteristics of the laser pulses. The next section reviews basic definitions relative to the pulse envelope.

2.1.3 Temporal pulse profile

One can readily conceive an mental picture of what a light pulse is. If a fixed point-like detector with a response capable of resolving the oscillation of the electric field associated with visible

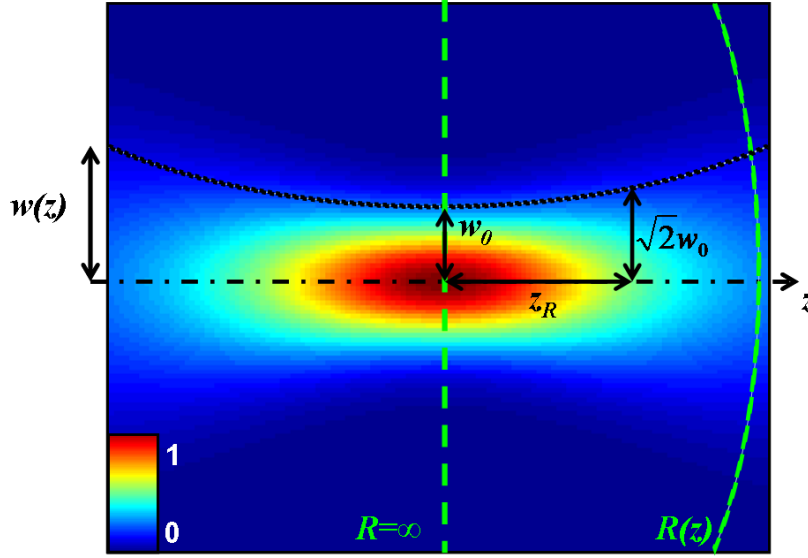


Figure 2.2: Propagation of a Gaussian beam around the waist: The normalized intensity profile is plotted along the z axis. The beam waist w_0 , Rayleigh range z_R and wavefront radius of curvature $R(z)$ are indicated.

light (less than 2 fs) was targeted by a linearly polarized femtosecond pulse, it would measure an fast oscillating electric field enveloped in a temporal amplitude function which can be written as [Tra07]:

$$E(t) = \tilde{\epsilon}(t) \exp[i(\omega t)] = \epsilon(t) \exp[i\omega t + i\varphi(t) + \varphi_0] \quad (2.8)$$

φ_0 is the carrier to envelope phase term and can be neglected for 'long' pulse durations (more than 100 fs). $\varphi(t)$ is the time-dependent phase. The instantaneous frequency [DR06] is the first derivative of the phase term in Eq. 2.8 $f(t) = \omega + \frac{d\varphi(t)}{dt}$. The corresponding intensity distribution reads:

$$I(t) = \frac{1}{2} c n_0 \epsilon_0 \tilde{\epsilon}(t) \tilde{\epsilon}(t)^* \quad (2.9)$$

The output of common femtosecond oscillators may deliver various type of temporal profile such as Lorentz, Hyperbolic secant or Gaussian distribution. However, for analytical convenience, the Gaussian shape is frequently assumed [DR06]. In that case, the temporal intensity distribution writes:

$$I(t) = I_0 \exp\left(-2 \frac{t^2}{\tau_G^2}\right) \quad (2.10)$$

where τ_G is half of the pulse duration taken at the $\frac{1}{e^2}$ intensity drop. When the temporal shape is more complicated, momentum theorems are employed [DR06]. More conveniently, the full

width half maximum is usually employed $\tau_{1/2} = \tau_G \sqrt{2 \ln 2}$. This relation also holds in the spatial domain, yielding the connection between the waist w and the full width half maximum beam transverse dimension $d_{1/2}$. Therefore, for a given pulse energy E_{pulse} with measured pulse duration and beam waist, the peak intensity I_{peak} can be expressed as

$$I_{peak} = \frac{2E_{pulse}}{\pi w^2 \tau_G} \quad (2.11)$$

The spectral properties are available through a simple Fourier transform of $\varepsilon(t)$:

$$\varepsilon(\omega) = \mathcal{F}\{\varepsilon(t)\} = \int_{-\infty}^{+\infty} \varepsilon(t) e^{i\omega t} dt = \bar{\varepsilon}(\omega) e^{-i\phi(\omega)} \quad (2.12)$$

where $\bar{\varepsilon}(\omega)$ denotes the spectral amplitude and $\phi(\omega)$ the spectral phase. When all spectral components are in phase, the shortest pulse duration $\tau_{1/2}$ is attained, resulting in a Fourier-limited optical pulse. This lower limit is reported by the time-bandwidth product for Gaussian pulses [Tra07]:

$$\Delta\omega \tau_{1/2} \geq 2\pi \times 0.441 \quad (2.13)$$

where $\Delta\omega$ is the full width half maximum of the laser spectrum. The instantaneous frequency reports for dephasing between spectral components or 'chirp'. For $f(t) = at$, the pulse is said to be linearly chirped which corresponds to a simple pulse broadening from the Fourier limit. The spectral phase $\phi(\omega)$ is often expanded in Taylor series:

$$\phi(\omega) = \sum_{j=0}^{\infty} \frac{1}{j!} \left. \frac{\partial^j \phi(\omega)}{\partial \omega^j} \right|_{\omega_0} \times (\omega - \omega_0)^j \quad (2.14)$$

where ω_0 is the carrier frequency. The zeroth order term denotes the time domain absolute phase. Applying the Fourier-shift theorem with the first order term $\phi'(\omega_0)(\omega - \omega_0)$ in Eq. 2.12, it appears that this term accounts for a temporal translation of the laser pulse which do not have any consequence in 'unusual' laser processing. The second and third orders have direct effect on the electric field and are related to second and third order dispersion (SOD and TOD). Their influence is discussed in Sec. 2.2.2.

2.2 Linear propagation

2.2.1 Spatial effects

Focal distribution of intensity

Gaussian propagation laws summarized in Fig. 2.2 are very useful to get a rapid idea of the fluence distribution when ultrashort light is focused in the bulk of transparent materials [Sch01]. However,

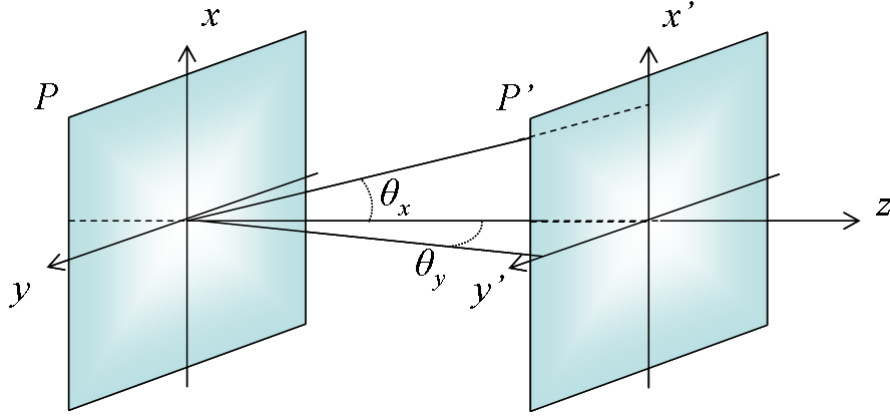


Figure 2.3: General propagation scheme for an electromagnetic wave.

a more general mathematical frame has to be exploited in order to weigh linear effects such as beam iris and wavefront distortions. Here, we employ the Fourier propagation law under the scalar approximation in a paraxial frame [Goo05] which is particularly suited for calculation around focal regions [FZT05]. The complex electric amplitude $\tilde{A}'(x', y')$ after propagation in air over a distance D from a plane $P(x, y)$ to a plane $P'(x', y')$ (see Fig. 2.3) of an electromagnetic wave $\tilde{A}(x, y) = A(x, y) \exp[\varphi(x, y)]$ writes:

$$\tilde{A}'(x', y') = \frac{1}{i\lambda D} \exp\left(i\frac{2\pi}{\lambda}D\right) \exp\left[i\frac{\pi}{\lambda D}(x'^2 + y'^2)\right] \times \mathcal{F}_{f_{x'}, f_{y'}} \left\{ \tilde{A}(x, y) \exp\left[i\frac{\pi}{\lambda D}(x^2 + y^2)\right] \right\} \quad (2.15)$$

where $f_{x'} = \frac{x'}{\lambda D}$ and $f_{y'} = \frac{y'}{\lambda D}$ represent spatial frequencies. With this equation, the complex amplitude is easily predictable numerically after known propagation. Moreover, it holds not only for Gaussian intensity profile but also for any intensity transverse distribution and spatial phase. This propagation equation has to be completed with the effect of a lens of focal length f under the same paraxial approximation. Consequently, before propagation calculations, the incident amplitude $\tilde{A}(x, y)$ is multiplied by a phase factor $\exp(\varphi_l)$ defined by:

$$\exp(i\varphi_l) = \exp\left[-\frac{i\pi}{\lambda f}(x^2 + y^2)\right] \quad (2.16)$$

Therefore, given the amplitude and the wavefront profile on a focusing lens, the intensity distribution of the focal region can be explored in two dimensions x' and y' for propagation distances around the focal plane ($d = f \pm \delta$) following:

$$I(x', y') \propto \frac{1}{\lambda^2 d^2} \left\| \mathcal{F}_{f_{x'}, f_{y'}} \left\{ \tilde{A}(x, y) \exp\left[-\frac{i\pi}{\lambda f}(x^2 + y^2)\right] \exp\left[i\frac{\pi}{\lambda d}(x^2 + y^2)\right] \right\} \right\|^2 \quad (2.17)$$

which reduces to:

$$I(x', y') \propto \frac{1}{\lambda^2 d^2} \left\| \mathcal{F}_{f_{x'}, f_{y'}} \left\{ \tilde{A}(x, y) \exp \left[-\frac{i\pi}{\lambda} (x^2 + y^2) \left(\frac{1}{d} - \frac{1}{f} \right) \right] \right\} \right\|^2 \quad (2.18)$$

Assuming a collimated laser beam ($R(z) = \infty$) carrying a pulse of $1 \mu\text{J}$ with a Gaussian beam profile of radius $w_0 = 1 \text{ mm}$ arriving on a borderless lens of focal length $f = 4 \text{ mm}$, we plot the focal intensity fluence map in air using the previous equation as shown on Fig. 2.4 a). As expected, we retrieve precisely the focal waist $w = 1 \mu\text{m}$, Rayleigh length and peak fluence $F = 61 \text{ J.cm}^{-2}$ as predicted by the Gaussian beam propagation law (see Eq. 2.6) using $z = f$.

This situation is quite far from usual experimental conditions as the focusing element, being either a lens, microscope objective or mirror, has a finite spatial extent. For uniform illumination of such a pupil with a radius $r = 1 \text{ mm}$, the same formalism permits to draw again the focal region as represented on Fig. 2.4 b). The corresponding numerical aperture $NA = \frac{r}{\sqrt{r^2 + f^2}}$ becomes $NA \approx 0.24$. The awaited square of the cardinal sinus is clearly observable on the figure at $z = f$ (or $z_f = 0$). The spatial dimensions are in perfect harmony with the diffraction limit law in air concerning the radius r' at which the focal distribution (Airy pattern) first drops to zero:

$$r' = 1.22 \frac{\lambda f}{2r} = 1.22 \frac{\lambda \sqrt{1 - NA^2}}{2NA} \quad (2.19)$$

yielding $r' = 1.95 \mu\text{m}$. If a Gaussian function is fitted to the result, the corresponding $\frac{1}{e^2}$ intensity drop radius increases to $w = 1.32 \mu\text{m}$ as compared to the preceding $w = 1 \mu\text{m}$. In that case, the peak fluence drops by a factor 2 ($F = 30 \text{ J.cm}^{-2}$) and the focal volume spreads out significantly. We also underline here the appearance of light spots before the main focal zone which, in the case of sufficient pulse energy, inevitably lead to bulk modifications (see Chap.5).

Real experimental conditions usually lie in an intermediate state, a compound between the two former situations. Addressing a converging lens or microscope objective with the Gaussian radiation emitted from a femtosecond laser inevitably results in beam truncation, strong or slight, with the consequences summarized in Fig. 2.4 c). The Fourier formalism is general enough to consider these circumstances. Here, truncation is set to match the $\frac{1}{e^2}$ intensity drop. Since 86.5% of the power is carried within those boundaries, one could expect very little effect of this truncation on the focal distribution. Following that idea, formulas yielding focal waist w' only from the numerical aperture of the lens were recently discussed [Ash03]:

$$w' = \frac{\lambda}{\pi} \frac{\sqrt{1 - NA^2}}{NA} \quad (2.20)$$

This relation supposes a perfect match between the pupil radius and the beam size on the lens, which corresponds to a truncation. In that case the NA is simply expressed by:

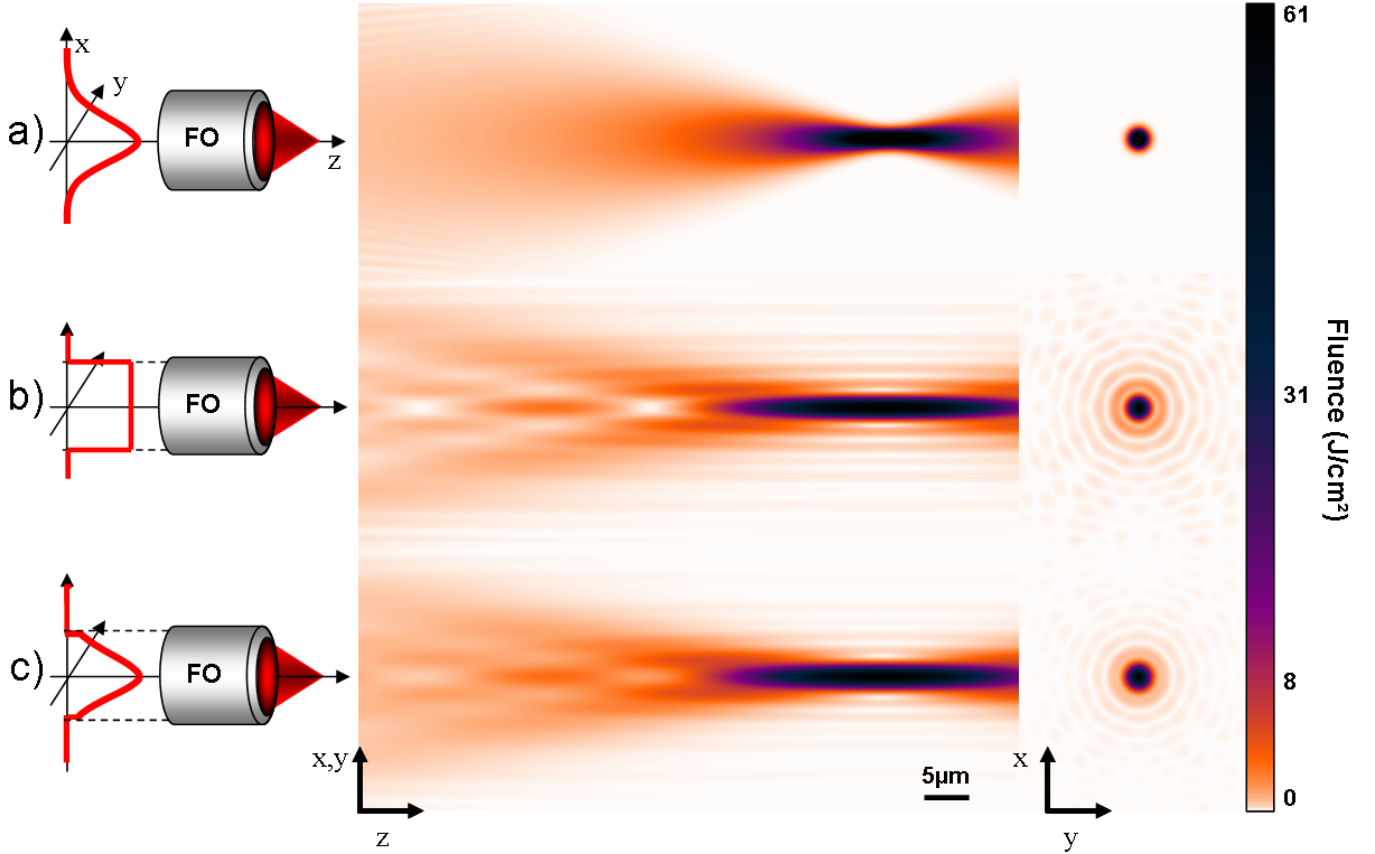


Figure 2.4: Simulated focal fluence map in air for 3 simple beam truncation situations concentrated by a 4 mm focal length focusing objective (FO) for a $1 \mu\text{J}$ light pulse (after the lens). Left: Intensity distribution in the lens plane (x, y). Center: Fluence distribution around the focal plane (x', y') at which $z_f = 0$. Right: Fluence distribution in the x, y plane of higher light concentration. a) Pure Gaussian focusing without any truncation. b) Uniform illumination of a 1 mm radius pupil. c) Gaussian illumination of a 1 mm radius pupil with the $\frac{1}{e^2}$ intensity drop matching the pupil radius. The focal map possess a cylindrical symmetry with respect to the propagation axis z and laser arrives from left. Note the transformation from a Gaussian distribution towards an Airy pattern when beam truncation takes place.

$$NA = \sin \theta = \frac{w}{\sqrt{w^2 + f^2}} \quad (2.21)$$

Consequently, applying these formulas to our case, the focal waist is $w' = 1 \mu\text{m}$ which is in agreement with the pure Gaussian case and therefore completely disregards the truncation effect (the aperture is considered infinite). This simplified point of view leads to a wrong idea of the focal volume dimensions.

The complete picture to be drawn necessitates the Fourier numerical simulations comprehending the beam truncation at the entrance of the lens. The calculated focal map presented in Fig. 2.4 c) undoubtedly demonstrates the strong effect of truncation and the large difference on the focal plane distribution and fluence as compared to the pure Gaussian case in a). An intermediate intensity repartition between the squared cardinal sinus of the uniform illumination and the Gaussian function occupies the focal plane. Ahead, a regular scheme of interferences forming pre-spots which are situated exactly as in the uniform illumination case. The focal waist is close to the uniform illumination case $w = 1.48 \mu\text{m}$ and the peak fluence is $F = 28 \text{ J.cm}^{-2}$. It is worth noting that a quicker calculation mean for focal distribution size in beam truncation cases is provided from a lens manufacturer ¹. There, the focal spot size at $\frac{1}{e^2} w'$ reads:

$$w' = K \frac{\lambda f}{2r} = K \frac{\lambda \sqrt{1 - NA^2}}{2NA} \quad (2.22)$$

where K is a fitting parameter depending on the truncation ratio $T = \frac{w_0}{r}$. In our last case, $T = 1$ which implies $K = 0.915$ yielding $w' = 1.48 \mu\text{m}$ in perfect agreement with our numerical simulations. As a general remark, it is obvious that the information of the nominal numerical aperture NA only is not sufficient to have a precise estimate of the focal spot dimension. A possible solution is to provide the truncation factor T but in order to offer a quicker idea of the experimental focusing conditions, we prefer to mention the 'effective' numerical aperture NA_{eff} . It is defined as the numerical aperture uniformly illuminated ($K = 0.82$) that yields the same spot size as the experimental truncated case. To preserve sufficient pulse energy, we employed most of the time rather low truncation ratio, resulting in NA_{eff} quite lower than the nominal NA . Therefore, NA_{eff} is indicated along with the nominal NA for the experimental results presented throughout this report. Nevertheless, precise knowledge of the fluence mapping around the focusing plane is highly desirable when analyzing bulk irradiation outcomes, making the Fourier propagation simulations a preferred tool to discuss the topology of bulk changes (see Chap. 5).

¹see for example <http://www.cvimellesgriot.com>

Gouy phase

When spherical waves with finite spatial extent are focused, the electromagnetic field experiences a phase shift known as the Gouy phase [Gou90], this phenomenon is present for material waves as well. For Gaussian beams, this phase shift writes:

$$\varphi_G = \arctan \left(\frac{z_f}{z_r} \right) \quad (2.23)$$

and is equal to π after a waist position [KL66]. A very intuitive explanation of the Gouy phase based on simple geometrical considerations is reported by Boyd *et al.* [Boy80], another approach involving spatial confinement limitations can also account for this phase shift [RRW⁺99]. While Finite Difference Time Domain (FDTD) simulations implying the full Maxwell equation verify the Gouy phase ², experimental evidences with spherical pressure waves in crystal were quite recently announced [FSWN02]. The consequences on this absolute phase shift are most of the time transparent for 'usual' applications of ultrashort lasers, especially when the pulse duration remains long compared to an oscillation of the electric field or slowly varying envelope approximation SVEA [DR06]. Yet, the growing field of high harmonic generation and attosecond physics is largely indebted to ultrashort laser with controlled absolute phase [QTM⁺06, CK07]. For situations revoking the SVEA, where the light pulse is brief enough to comprehend just a few electromagnetic oscillations (e.g 5 fs at 800 nm), one has to differentiate sine and cosine pulses (see [DR06, Tra07]) for which the absolute phase difference equals π . In the THz domain, where electronic detectors can follow the electromagnetic oscillations, Ruffin *et al.* experimentally showed the switch from cosine to sine pulses due to the Gouy phase [RRW⁺99].

Pulse front distortion

The pulse front is defined as the surface coinciding with the intensity peak of the light pulse. Its propagates with the group velocity $v_G = c \left(n - \lambda \frac{dn}{d\lambda} \right)^{-1}$ whereas the wavefront travels at the phase velocity $v_\varphi = \frac{c}{n}$. If in vacuum, these two paces are identical, they differ for any medium presenting dispersion ($\frac{dn}{d\lambda} \neq 0$) as in the glass of a lens. The well-known Sellmeier equations give the chromatic dependency of the refractive index for fused silica glass [Mal65]. The difference between group and phase velocity does not lead to temporal broadening for a traveling electromagnetic pulse in fused silica. One has to consider the second and higher derivative orders of the refractive index with respect to the wavelength; which is the object of a coming paragraph. However, due to the particular spatial shape of a lens, the difference $v_G \neq v_\varphi$ leads to temporal broadening in the focus region [Bor88]. The pulse front propagation time T from the plane A to the focal plane F (see Fig. 2.5) can be readily calculated from simple geometrical considerations:

²J. H. Bergervoet, Gouy phase shift with FDTD. <http://home.iae.nl/users/bergervo/gouy/gouy.html>.

$$T = \frac{L_1 + L_3 + L_4}{c} + \frac{L_2}{v_G} \quad (2.24)$$

The temporal delay ΔT between marginal and paraxial rays accumulated from the plane A to F obviously depends on r and is expressed by [Bor88]:

$$\Delta T = \frac{r_0^2 - r}{2cf(n-1)} \left(-\lambda \frac{dn}{d\lambda} \right) \quad (2.25)$$

The pulse front can be then plotted following the equations:

$$\begin{aligned} z &= c(t - \Delta T(r)) \cos \left(\arctan \frac{r}{f} \right) \\ x &= c(t - \Delta T(r)) \sin \left(\arctan \frac{r}{f} \right) \end{aligned} \quad (2.26)$$

where $t = 0$ corresponds to the moment when the marginal rays first reach F and $x, z = 0$ the F position. Fig. 2.5 depicts the pulse front for the focusing conditions employed in the discussion ($f = 4$ mm, $r = 1$ mm). Following Eq. 2.25, the delay ΔT between marginal and paraxial rays in F is found to be 11 fs would measure a signal of duration $\Delta T = 11$ fs. We insist on the fact that this temporal broadening is a linear effect and relies on the first derivative of the glass refractive index and therefore, does not have any connections with the initial pulse duration. Experimental evidences of pulse front distortions were reported in lenses and telescopes showing precise agreement with the predictions [Bor89]. We also mention here, that if non purely spherical pulse fronts are presented here as a drawback, pulse front engineering starts to interest researchers as it offers an additional adjustable parameter potentially augmenting the processing flexibility. In particular, while research efforts are carried out to precisely measure the pulse front tilt associated with dispersive elements often met in CPA system [AGZT04, SMD01], artificial pulse front tilt has been recently successfully exploited to show pulse front tilt dependent bulk processing [YKS⁺08a, YKS08b]. In particular, fused silica transverse bulk machining with pulse front tilt is shown to produce birefringent structures in one direction and isotropic structures in the other, resembling the effect of quill writing. In anisotropic media (LNb crystals) non-reciprocal photoinscription was demonstrated by anisotropically enhancing the current flow. It is also experimentally verified that reverting the pulse front tilt or the scanning direction produce equivalent structures (see Fig. 2.6). Whereas the phenomenon appears only on restricted depths in fused silica and for transverse photowriting, the associated symmetry rupture of the in-volume modification is evidently heavy in consequences for bulk machining. The use of advanced ultrashort pulse characterization tool such as frequency resolved optical gating (FROG) and is modification (GRENOUILLE) can precisely quantify pulse front distortions [AKOT03].

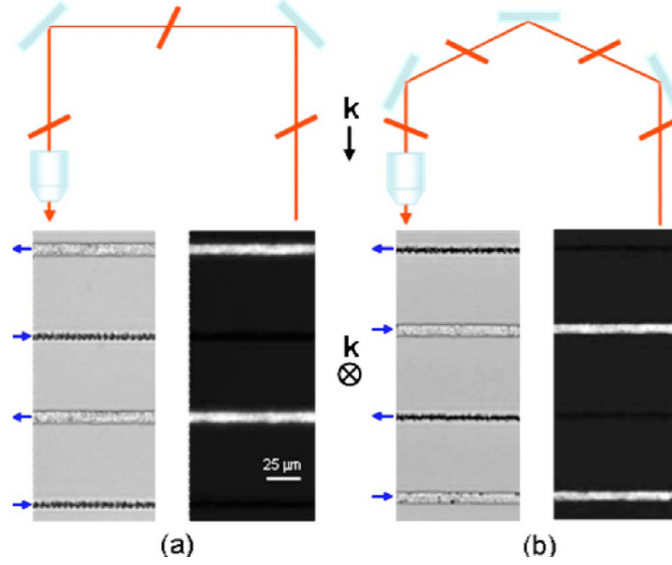


Figure 2.6: Optical microscopy pictures of the pulse front tilt effect in transverse bulk machining of fused silica from [YKS⁺08a]. k is the wave vector of the writing laser. the blue arrows stand for the sample scanning direction. The pulse front tilt is managed by the used of two a) or three b) mirrors and is schematically represented in red. Dark-background pictures were obtained with the addition of crossed polarizers.

For ease of explanation, we based our discussion assuming a simple fused silica lens. Naturally, when focusing ultrashort pulses, more elaborated focusing components are usually employed, such as achromatic doublets or dedicated microscope objective, thus being free of temporal broadening due to pulse front distortions [Bor88]. However, when manipulating ultrashort pulses, the need of resizing or collimating the beam inevitably leads to the use of various lenses which possibly have detrimental effects on the pulse if care is not taken to evaluate pulse front distortions.

Chromatic aberrations

When a simple converging lens is employed on the path of light radiation with a given spectrum bandwidth, rays associated with the bluer part of the spectrum are focused further than the redder ones, a phenomenon known as the chromatic aberration³. Given the focal length f of a lens of refractive index n , the axial spreading Δf around F along the propagation axis writes:

$$\frac{\Delta f}{f} = \frac{\Delta \lambda}{\lambda} \frac{\Delta n}{n - 1} \quad (2.27)$$

with $\Delta \lambda \approx 10$ nm being the laser source relatively narrow spectral bandwidth centered on $\lambda = 800$ nm and Δn the refractive index difference for the boundary wavelength of the laser spectrum obtained from the Sellmeier relations [Mal65]. For a fused silica lens, $\frac{\Delta f}{f} = 4.8 \times 10^{-6}$,

³well-illustrated at <http://www.microscopyu.com/>

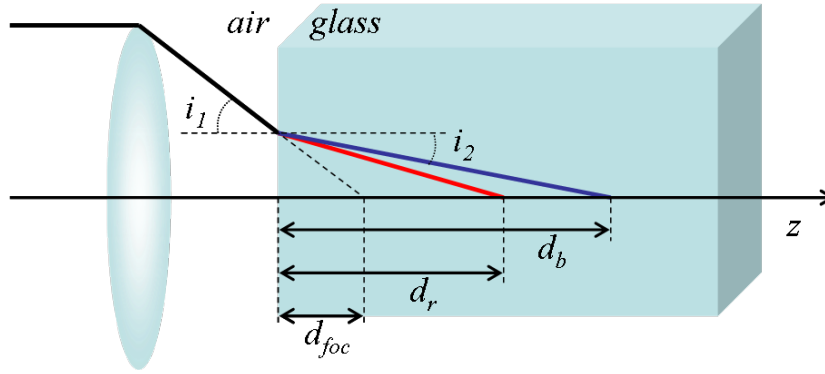


Figure 2.7: Scheme for chromatic aberration estimation when light is focused in the bulk of a glass sample. d_b (d_r) is the penetration depth of the bluer (redder) part of the laser spectrum, d_{foc} is the focusing depth, i.e the penetration depth if the sample had a refractive index $n = 1$.

corresponding to a few nanometers in the case of a focal length of $f = 4$ mm which is clearly negligible compared to the dimensions of the focal intensity distribution (see Fig. 2.4). If the effect from the lens is insignificant, when focusing light in the bulk of a glass sample through an air-glass interface, the refraction angles at the interface have to be considered for the wavelengths contained in the laser spectrum. These angles determine the depth of light penetration in the bulk before reaching the optical axis. This depth is indicated on Fig. 2.7 with d_b (d_r) standing for the penetration depth of the bluer (redder) part of the laser spectrum. Those distances depend on the incident angle i_1 and the focusing depth d_{foc} and can be calculated using the Snell-Descartes refraction law along with simple geometrical analysis:

$$d_{b,r} = d_{foc} \tan(i_1) \left\{ \tan \left[\sin^{-1} \left(\frac{1}{n_{b,r}} \sin(i_1) \right) \right] \right\}^{-1} \quad (2.28)$$

with $n_{b,r}$ the refractive index of the glass for the bluer (redder) part of the laser spectrum. It is straightforward to see that for small incidence angles the previous relation reduces to $d_{b,r} = n_{b,r} d_{foc}$. Evaluating the difference $\Delta = d_b - d_r$ yields the z-axial spreading of irradiance due to chromatic aberration. In our case, for a focusing depth of $d_{foc} = 137 \mu\text{m}$ (the real depth of the spot is then $200 \mu\text{m}$), Δ is on the order of 29 nm for incidence angle up to 30° (i.e $NA = 0.45$). Therefore, this aspect of chromatic aberration is also negligible in our conditions. A rapid look at the corresponding temporal stretching between the bluer and the redder part of the pulse indicates a pulse broadening of less than 2 fs for both lens and interface chromatic effects, which is also insignificant compared to the typical pulse duration ($\approx 150 \text{ fs}$) employed in this report. Nevertheless it has to be kept in mind when dealing with wide spectrum, strong and deep focusing and with transparent materials showing important dispersion.

Table 2.1: Examples of Zernike polynomials describing common geometrical aberrations.

Tilt	$\Delta\varphi = 2\rho \cos \theta$
Defocus	$\Delta\varphi = \sqrt{3}(2\rho^2 - 1)$
Astigmatism	$\Delta\varphi = \sqrt{6}\rho^2(2 \cos^2 \theta - 1)$
Coma	$\Delta\varphi = \sqrt{8}(3\rho^3 - 2\rho) \cos \theta$
First order spherical aberration	$\Delta\varphi = \sqrt{5}(6\rho^4 - 6\rho^2 + 1)$
Second order spherical aberration	$\Delta\varphi = \sqrt{7}(20\rho^6 - 30\rho^4 + 12\rho^2 - 1)$

Wavefront aberrations

This paragraph does not aim at unrolling an exhaustive list of all the non-chromatic wavefront distortions. Instead it recalls the main aberrations to be aware of in femtosecond laser bulk processing. It is well-known that the spatial phase function associated with any geometrical aberrations can be decomposed on the orthogonal basis of Zernike polynomials defined on the normalized circular pupil (ρ, θ) [Zer34]. Table 2.1 presents a few examples of the primary polynomials illustrated on Fig. 2.8.

In order to estimate the effect of some aberrations on the focal intensity distribution in the bulk, the phase function $\Delta\varphi$ of a given Zernike polynomial can simply be added to the spatial phase of the incident complex amplitude in the Fourier propagation calculations already mentioned. Since the tilt and defocus components do not alter the intensity repartition but only its position in the air, they are disregarded in the following discussion. However, in the case of bulk processing, wavefront tilts influence the refraction at the air glass interface (see Chap. 5). Fig. 2.9 gathers fluence maps around the focal plane under the successive influence of coma, astigmatism and spherical aberration as defined in Table 2.1 without additional coefficient. For comparison the non-aberrated results are presented in Fig. 2.4 c).

A widespread wavefront degradation when manipulating solid state lasers is astigmatism [SSS99, Koe06] whose effect is considered in Fig. 2.9 a). The z-rotational symmetry is lost and the focal volume presents two particular planes surrounding the focus called the meridional and the sagittal focal planes where the (x', y') intensity repartition degenerates into two perpendicular lines [Tra07] as retrieved in our simulations (not shown). As clearly observable on Fig. 2.9 b), comatic aberration also breaks the rotational symmetry of the focal distribution mimicking the shape of a comet in the (x', y') plane. This kind of wavefront distortions is frequently met in optical system suffering from lens misalignment as shown for a microscope objective in [Tra07].

Additionally, spherical aberrations play a major role as their origin can be found either in the focusing lens or objective [BW99], in the non-uniform heating of the solid gain medium [Sie93, HW93], or in the air-medium interface when focusing in the bulk of transparent materials [HTS⁺05].

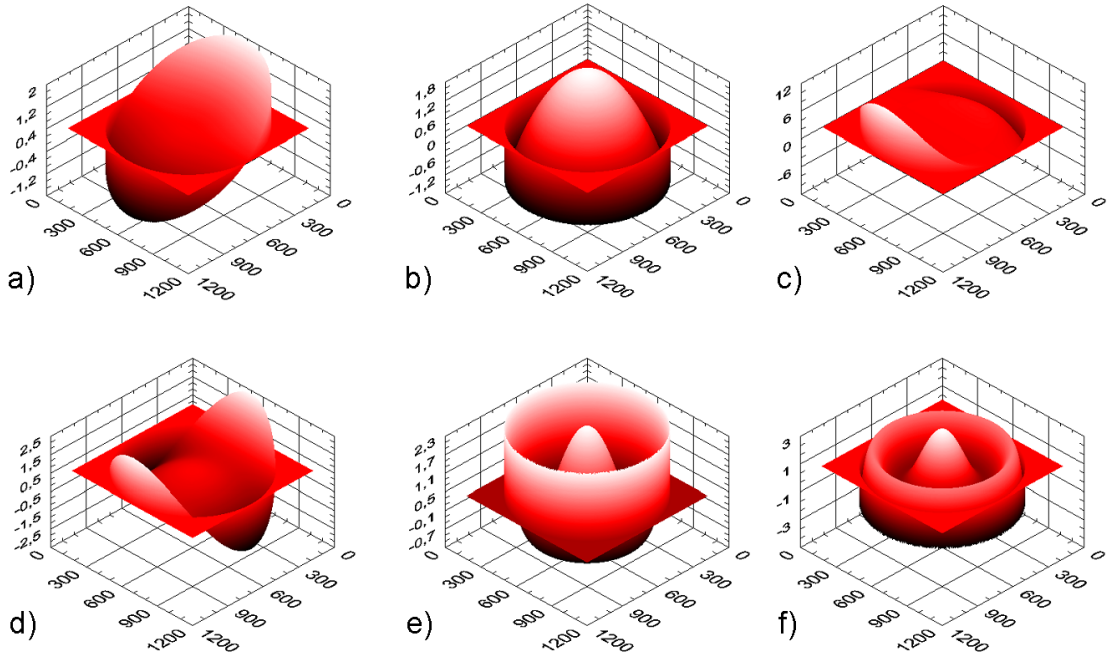


Figure 2.8: Examples of common wavefront aberrations in radians described by Zernike polynomials. a) Tilt. b) Defocus. c) Coma. d) Astigmatism. e) First order spherical aberration. f) Second order spherical aberration

On a geometrical point of view, spherical aberration is related to the difference of intersection on the z -axis of marginal rays and the paraxial rays (clear ray tracing results are reported in [Ash03]. When paraxial rays are focused sooner on the z -axis than the marginal rays as in the case of a single lens, the spherical aberration is said positive. The inverse situation (as met with air-glass interfaces [HTS⁺05]) is simply called negative. Consequently, the above-mentioned contributions to spherical aberrations can counteract each other. Fig. 2.9 c) illustrates the axial spreading of intensity due to spherical aberration as defined in Table 2.1. The fluence drops significantly and the focal volume is elongated along the z -axis. A detailed study of the wavefront distortions associated with deep focusing through an air-glass interface is provided in Chap. 5.

Undoubtedly, focusing laser beams is not a straightforward operation. The preceding discussion, although intentionally restricted to linear effect with spatial dependence, made clear the extraordinary sensitivity of the focal volume to any degradation of the focusing conditions (beam truncation, pulse front distortions, aberrations). In the following, the pulse duration subordination to linear and nonlinear temporal effects is presented to complete the focal intensity distribution of concentrated ultrashort light pulses.

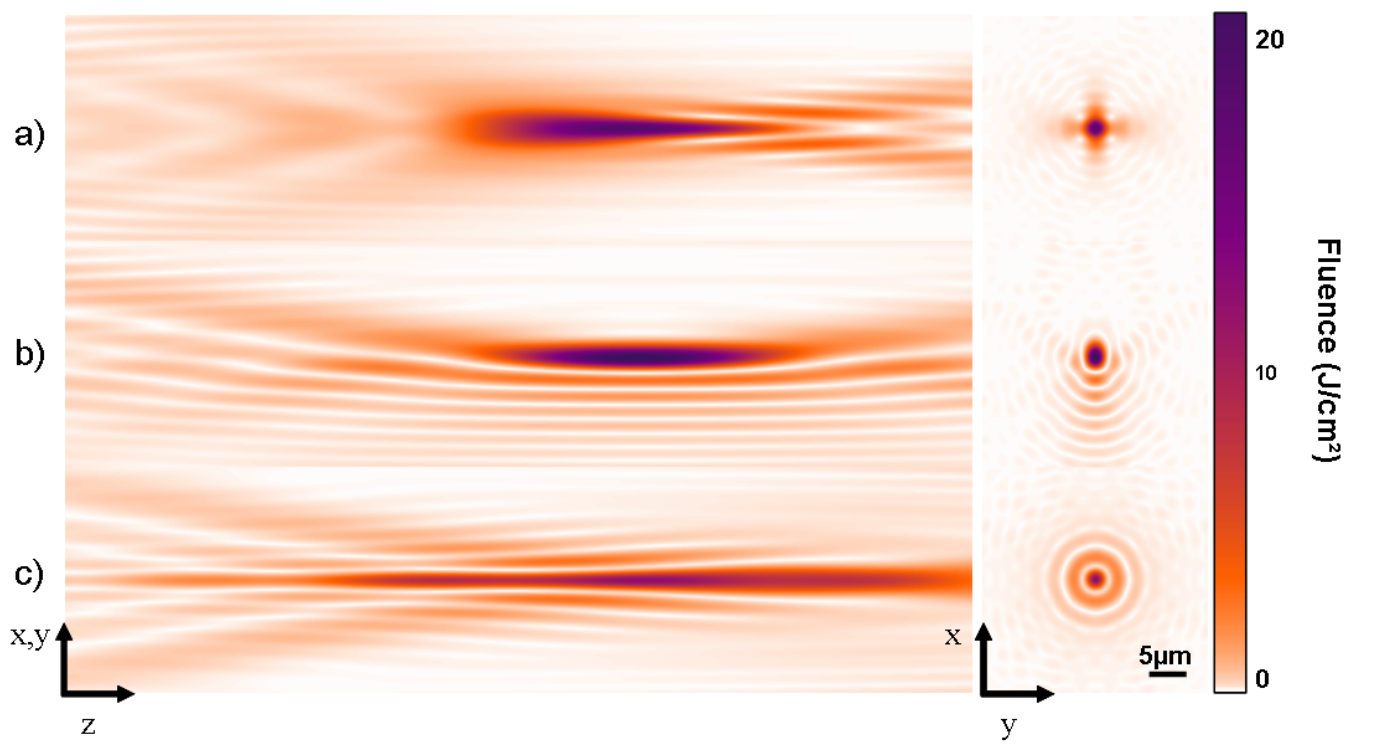


Figure 2.9: Simulated fluence map around the focal spot in presence of various optical aberration for a 4 mm focal length lens and a $1 \mu\text{J}$ light pulse. Left: Fluence distribution around the focal plane (x', y') at which $z_f = 0$. Right: Intensity distribution in the focal plane (x', y') . a) Astigmatism. b) Coma. c) Spherical aberration.

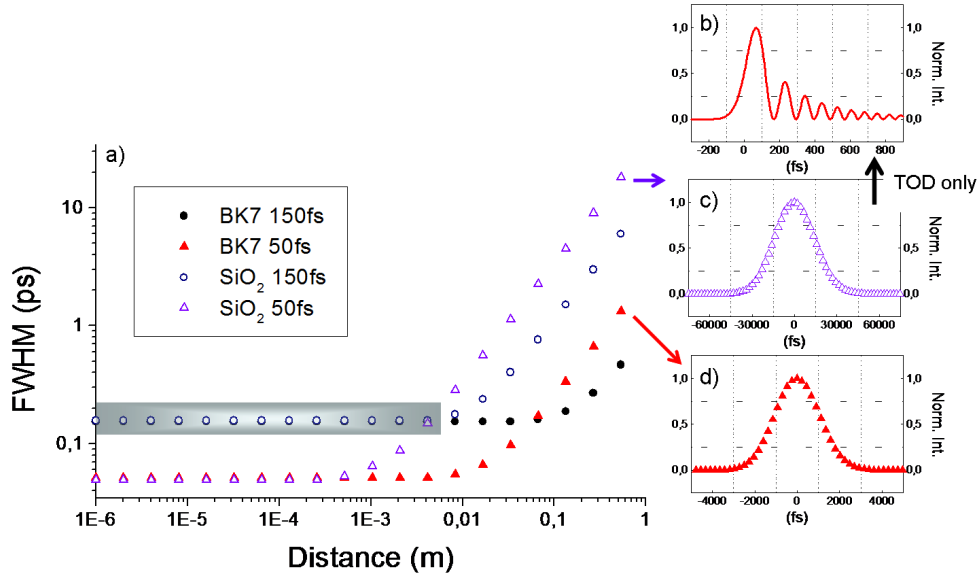


Figure 2.10: Calculated pulse elongation (FWHM) due to both SOD and TOD after propagation in glass. a) FWHM dependency on the propagation distance. Open symbols: fused silica, solid symbols: BK7 glass. Triangles: 50 fs pulse, circles: 150 fs. Right: Calculated pulse shape after 1 m of glass with b) only the TOD effect, and c) d) with both SOD and TOD. The blue area stands for the secure propagation window visited in this report, where negligible SOD and TOD pulse stretching takes place for the 150 fs pulse.

2.2.2 Temporal effects

Chromatic dependence of the refractive index $n(\omega)$ has direct consequences on the spectral phase $\phi(\omega)$ of light pulse traveling in glass. After a distance L , the accumulated spectral phase $\phi_m(\omega)$ reads [Tra07]:

$$\phi_m(\omega) = k(\omega)L = \frac{\omega}{c}n(\omega)L \quad (2.29)$$

The first derivative of this expression yields the group delay with respect to the phase velocity. We saw in Sec. 2.2.1 that in a uniform medium, this does not lead to pulse broadening, but stands for the retardation between the phase and the pulse front. The second derivative permits to define the group velocity dispersion (GVD) also called the group delay dispersion (GDD):

$$\text{GVD} = \frac{d^2\phi_m(\omega)}{d\omega^2} = \phi'' = \frac{\lambda^3 L}{2\pi c^2} \frac{d^2n}{d\lambda^2} \quad (2.30)$$

This phenomena is related to the various velocities of the pulse spectral components in the medium. Replacing ϕ'' in Eq. 2.14 and then Eq. 2.14 in Eq. 2.12 permits to numerically evaluate the temporal broadening associated with GVD. A positive SOD ϕ'' leads to a linear up-chirped

pulse [Tra07] where the redder spectral components travel faster (e.g in optical glass in the visible range). The duration stretching is also derivable analytically. In that case, a bandwidth-limited Gaussian pulse lasting $\tau_{1/2}$ (FWHM) remains Gaussian and stretches to:

$$\tau_L = \sqrt{\tau_{1/2}^2 + \left(4 \ln 2 \frac{\phi''}{\tau_{1/2}}\right)} \quad (2.31)$$

Turning to the third derivative of Eq. 2.29, the definition of the third order dispersion (TOD) arises:

$$\text{TOD} = \frac{d^3 \phi_m(\omega)}{d\omega^3} = \phi''' = \frac{-\lambda^4 L}{4\pi^2 c^3} \left(3 \frac{d^2 n}{d\lambda^2} + \lambda \frac{d^3 n}{d\lambda^3}\right) \quad (2.32)$$

In contrast to GVD, the cubic spectral phase distortion associated with TOD can not only elongate the pulse but also alter the pulse shape as the central frequency arrives before frequencies on either side causing beating in the temporal domain. Again, the effect on the temporal pulse profile can be numerically drawn using Eq. 2.14 and Eq. 2.12. An analytical expression is derived in [Tra07]. Third order dispersion can rapidly appear in series of dispersive elements (gratings, prisms) usually associated with CPA amplifiers [HKY⁺06]. The laser sources mentioned in this report, under careful tuning, were exempt of such artifacts. Inevitably SOD and TOD are simultaneously present when light pulses travels in glass which is unavoidable in bulk machining.

In order to quantify their respective effect, calculations were carried out for pulses of 50 fs and 150 fs (FWHM) for increasing traveling distance in BK7 glass and fused silica glass. Both SOD and TOD are taken into account. We briefly mention here that, if the pulse distortion associated with TOD usually requires a more general definition of the pulse length based on the second order moment [Tra07], its contribution when compared to the SOD remains very restricted (this is clearly observable on the pulse shapes in Fig. 2.10 which stay symmetric even after 1 m propagation in fused silica or BK7 glass). Therefore, we employ the standard FWHM definition. Calculations show that for a 150 fs light pulse and up to 1 cm propagation in BK7 or fused silica glass, SOD and TOD pulse stretching is negligible (blue area in Fig. 2.10). This result secures our discussion as this distance corresponds to the deepest bulk irradiation spot visited in this work.

2.3 Nonlinear propagation

Ultrashort pulses traveling in dielectric media induce microscopic displacements of the bound charges. In the simplified scenario of electrons elastically bound to the atomic core, when the light energy remains negligible before the electron-core bound, the system answers in a linear way. In that case, the association of the oscillating dipoles forming the macroscopic polarization

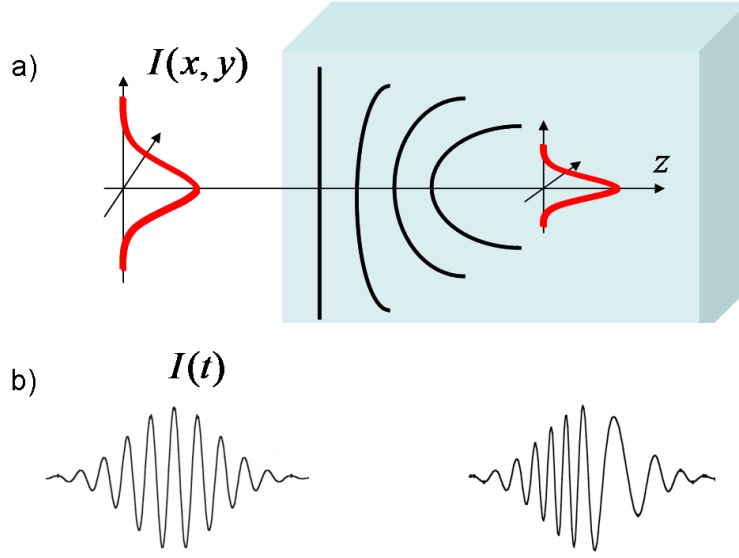


Figure 2.11: Illustration of nonlinear spatio-temporal propagation effects in a glass with $n_2 > 0$ adapted from [Sch01]. a) Spatial effect: self-focusing of a collimated beam. b) Temporal effect: blue frequency shift due to self-phase-modulation.

P is proportional to the laser electric field amplitude ε . At higher intensities, the material response departs from the linear behavior and in first approximation, it is useful to consider the square of the electric field as well [She02]. Consequently, the refractive index follows a more general expression involving both first and second order of the electric field:

$$n = \sqrt{1 + \chi^{(1)} + \frac{3}{4}\chi^{(3)}|\varepsilon|^2} \quad (2.33)$$

where $\chi^{(m)}$ is the m -th order susceptibility of the material here assumed to accept an inversion symmetry ($\chi^{(2)} = 0$ as for glasses in general). Writing n_0 as the linear refractive index ($n_0 = \sqrt{1 + \chi^{(1)}}$) and assuming that the nonlinear contribution stays slight, the refractive index takes the simpler form:

$$n = n_0 + n_2 I \quad (2.34)$$

where $n_2 = \frac{3\chi^{(3)}}{4\varepsilon_0 c n_0^2}$. The corresponding spatio-temporal dependency of the refractive index with the laser intensity (Kerr effect) has dramatic consequences on the pulse propagation.

For instance, $n_2 = 2.48 \times 10^{-16} \text{ cm}^2/\text{W}$ in fused silica [TRC96] making the effect negligible at low intensities. In our experimental conditions however, the Kerr effect modulates the refractive index seen by the pulse following its spatial and temporal intensity profile.

2.3.1 Self-focusing

The spatial intensity profile of the beam triggers a spatially-dependent response of the material. Simply saying, the Gaussian irradiance induces a Gaussian refractive index distribution which acts as lens and collapses the beam as illustrated in Fig. 2.11 a). The catastrophic effect occurs above a critical power P_{cr} given by [MQG⁺04]

$$P_{cr} = 3.77 \left(\frac{\lambda^2}{8\pi n_0 n_2} \right) \quad (2.35)$$

A power threshold rather than a intensity threshold can be explained considering a collimated flat top beam [Boy08] of diameter d . In that case, the index modulation due the spatial Kerr effect leads to a step index waveguide if n_2 is positive. The total reflection condition for an internal ray then writes $\theta_r^2 \approx 2n_2 I / n_0$. When this angle is equal or superior to the diffraction angle given by $\theta_d \approx n_0 / d$, it yields the condition for self-focusing to overcome diffraction $P_{cr} \propto d^2 I \geq \lambda^2 / (2n_0 n_2)$. Refinements including the Gaussian beam profile yields Eq. 2.35 [HUA⁺92]. In fused silica at 800 nm, the power threshold for self-focusing is $P_{cr} = 2.2$ MW which corresponds to a pulse energy of 0.2 J which is usually overpassed in the context of bulk femtosecond writing, therefore we must apprehend its influence. If self-focusing forces a collimated beam to focus, it enhances the convergence of focused laser and consequently moves the focal spot towards the laser [SFPM01, FSL02]. Self-focusing considered alone predicts a overall collapse of the beam leading to a non-physical object where the laser energy would be gathered on a infinitely small scale. The electron-core bound nonlinear response being at the origin of this phenomena plays also a counteracting role. Self-focusing leads to higher and higher intensities, thus the bound force is eventually overcome by the light electric field, providing detached electrons (see Chap. 3). From a imaged point of view, the consecutive electronic gas plays a immunological role because of the associated decrease of the local refractive index (evaluated in Sec. 3.2.2) which causes the laser beam to diverge. The repetition of this scenario alternating self-focusing and plasma defocalisation is at the origin of the filaments [SNCV04, CCK⁺08].

2.3.2 Self-phase modulation

Eq. 2.34 implies a dependency of the refractive index on the intensity profile in the temporal domain as well. Simply considering the phase velocity, the peak sees a stronger refractive index than the edges of the pulse and is delayed with respect to them resulting in a compaction of the electric field towards its trailing edge [Sch01]. More accurately, the phase accumulated after propagation over a distance L reads

$$\varphi = kL - \omega_0 t = \frac{\omega L}{c} [n_0 + n_2 I(t)] - \omega_0 t \quad (2.36)$$

The negative time derivative of this expression leads to the instantaneous frequency

$$\omega(t) = \omega_0 - \frac{n_2 \omega L}{c} \frac{d(I)}{dt} \quad (2.37)$$

On the leading edge of the pulse, $\frac{d(I)}{dt} > 0$ which diminishes the instantaneous frequency towards redder wavelengths. The trailing edge knows the inverse phenomena yielding a symmetric pulse broadening. Additionally, the propagating pulse is influenced by the onset of free carriers generated through various photoionization processes discussed in the next chapter. Briefly, the free electronic plasma has optical properties potentially responsible for a defocusing effect as well as a blue shifting on the temporal profile. Self focusing and self phase modulation can be taken into account to draw the focal distribution with help of the Non Linear Schrödinger Equation (NLSE). Previous calculations ([BBS⁺07]) based on the NLSE considering also plasma defocusing, self-steepening and energy absorption due to photoionization are reported on Fig. 2.12b) and compared with pure Gaussian beam (Fig. 2.12ba)). Both simulations suppose a $w = 0.9 \mu\text{m}$ beam waist. Even if NLSE calculations exceed the scope of the present discussion, the effect of self focusing is well observable as the high fluence area forms earlier in the pulse propagation (Fig. 2.12b)). The shielding role played by plasma defocusing is mainly at the origin of the C-shaped high fluence zone and of the dramatic drop of energy concentration estimation from 60 J.cm^{-2} assuming pure Gaussian focusing to 2.3 J.cm^{-2} taking into account the major nonlinear effects on the light propagation. The maximum irradiance values are respectively $40 \times 10^{13} \text{ W.cm}^{-2}$ and $2 \times 10^{13} \text{ W.cm}^{-2}$.

2.4 Conclusion

Arriving at the end of this chapter, it seems necessary to draw a quick summary in the light of the purpose of the discussion. Simple mathematical and simulation tools were presented in order to render possible quick and precise simulations of the focal irradiance map associated with femtosecond bulk machining; taking into account common linear effects (beam truncation, aberrations...) with an estimation of nonlinear contributions. This simulation instrument has a decisive impact in understanding the morphology of transient and permanent bulk optical modification consecutive to femtosecond irradiation. Thence, simulations results are confronted to experimental bulk modification pictures all along this report to enlighten the correlations as well as the shortcomings of the simulations.

The discussed detrimental effect of propagation non linearities on the success of the achieved concentration of energy tends to show that the main challenge to sufficiently localize the energy deposition is related to the reduction of this non linear effects. Thus, we indicate in the following that employing a more suited temporal pulse envelope can meet this requirement, an additional

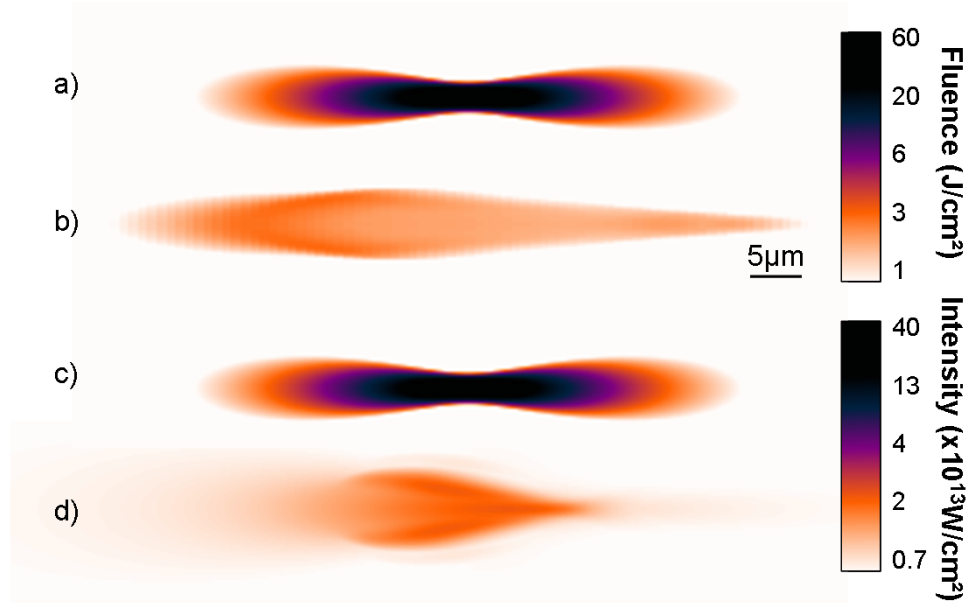


Figure 2.12: Comparison of calculated fluence and intensity maps assuming pure linear Gaussian propagation a), c) and taking into account non linear effects solving the NLSE b), d) which considers self-focusing, self phase modulation, plasma defocusing, self-steepening and energy absorption due to photoionization (see [BBS⁺07]). The z-scale is logarithmic.

proof of the processing flexibility offered by temporal pulse shaping. More precisely, we present laser-induced permanent modifications indicating a better efficiency of the energy coupling in the case of picosecond pulse envelopes (see Chap. 5 and 7). Time resolved characterization of the transient electronic cloud reported in Chap. 6 also confirm this possibility with carefully chosen double pulses sequence. Before, the next chapter details the mechanisms leading to the formation of transient and permanent changes in the material optical properties and their influence of the energy deposition rate.

Chapter 3

Light interaction with dielectrics

This chapter presents the mechanisms leading to permanent modifications induced by ultrashort irradiations. We first describe the main photoionization mechanisms responsible for the formation of a transient free electronic cloud. Its optical properties are discussed in the frame of the Drude model including damping. The obtained plasma optical properties are characterized by absorptive and dephasing effects upon which the time-resolved images presented in Chap. 6 are numerically treated. The chapter ends with a review of the energy relaxation pathways from the transient electronic gas to a permanent local change.

3.1 Nonlinear ionization

Linear absorption of light in dielectric occurs at wavelengths energetic enough to surpass the electronic bandgap thus promoting electrons from the valence band (VB) to the conduction band (CB). At 800 nm, most common glasses such as fused silica or BK7 glass are transparent, their bandgap being well above the energy carried by a 800 nm photon. This is where the nonlinear aspect of the interaction takes its significance, rendering possible the absorption of multiple photons where the laser irradiance is high enough. Two well-known mechanisms are identified in seeding the first electrons from the valence band to the conduction band, namely the multiphotonic ionization and the tunneling ionization.

3.1.1 First photoionization mechanisms

Multiphotonic ionization (MPI)

At high laser frequencies (but still beneath single photon absorption), the simultaneous absorption of several photons can exceed the energy gap E_G of the dielectric and withdraw electrons from the

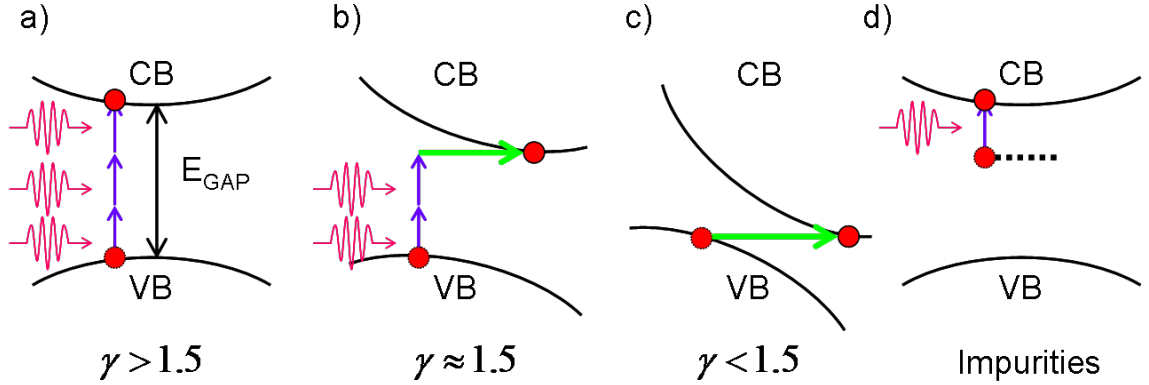


Figure 3.1: Schematic representation of the main photoionization mechanisms in dielectric depending on the Keldysh parameter γ . a) Multiphotonic ionization ($\gamma > 1.5$). b) Intermediate situation where both MPI and TI mechanisms take place. c) Tunneling ionization ($\gamma < 1.5$). d) Ionization from intermediate energy levels associated with material impurities.

valence band to the conduction band as illustrated on Fig. 3.1 a). The probability per time unit that a bound electron absorbs K photons at the same instant is given by:

$$P_{MPI}(I) = \sigma_K \left(\frac{I}{\hbar\omega} \right)^K \quad (3.1)$$

where I is the laser intensity and σ_K is the absorption coefficient for K photons [JBC⁺89]. For example, in fused silica where $E_G = 9$ eV, at least six photons at 800 nm (1.55 eV) are necessary for MPI to happen. The scaling of the MPI rate with the K-power of the intensity and stands as an clear experimental signature of the process (verified in fused silica and sapphire under 50 fs pulse irradiation [TSZ⁺06, MQG⁺04]). Deviations from this simple model should be expected from the onset of ponderomotive effects associated with the non-uniform electromagnetic field [ML74], the start of free electron heating with the subsequent collision multiplication and the rarefaction of electrons candidates as MPI takes place.

Tunneling ionization (TI)

For very strong laser intensities and lower frequencies, the local electric field potentially disturbs the band structure of the transparent material. As illustrated on Fig. 3.1 c), the conduction and the valence band can undergo potential bending making possible the transfer of one electron from the valence to the conduction band by the tunnel effect. As this mechanisms can accompany MPI, a more general frame has been proposed by Keldysh to account for the interplay of the two phenomena [Kel65] which is briefly presented hereafter.

The Keldysh model

As an estimation of the interplay between MPI and TI, the adiabatic parameter also known as the Keldysh parameter γ permits to have a rapid idea of the predominance of one or the other mechanism. This quantity reads [Kel65]:

$$\gamma = \frac{\omega}{e} \sqrt{\frac{mc n \varepsilon_0 E_g}{I}} \quad (3.2)$$

where e and m are the reduced electronic charge and mass respectively. Transition from TI dominated regime to MPI occurs at $\gamma \approx 1.5$ [SBM01] (see Fig. 3.1 b)) where the electronic excitation is operated with both mechanisms. In fused silica ($E_G = 9 \text{ eV}$), under 800 nm illumination, this shift corresponds to a laser intensity of $I \approx 5.10^{13} \text{ W/cm}^2$, which is related to a fluence of approximately 7 J/cm^2 for a 150 fs pulse (FWHM). In our focusing conditions, this condition is met for a pulse energy of $0.25 \mu\text{J}$ when neglecting non linear effects. However, we saw in Chap. 2 that their influence drops the irradiance by an order of magnitude, leading to a pulse energy of a few microjoules for $\gamma \approx 1.5$. As the irradiation conditions explored in this report are in this range, it is reasonable to expect both TI and MPI as the main mechanisms providing the first free electrons. The Keldysh model is still under a relatively long-lasting scientific debate as many research groups dispute its prediction in ultrashort irradiations experiments [CSF⁺05, LKS⁺98, SFH⁺96a, DLK⁺94, TBK⁺99]. As a main issue, the plethora of experimental strategies for the determination of the ionization threshold plays a significant role which partly explains the discrepancy [SUB⁺09].

Other mechanisms can contribute to the first electronic seeds in the conduction band. The presence of defects in the glassy matrix generates intermediate energy levels within the material's bandgap, which require less photons to populate the conduction band (see Fig. 3.1 d). However, this contribution remains restricted as the typical impurity density in transparent solids is about 10^8 cm^{-3} [SBM01]. When compared to the focal volume, less than one electron is expected to be available within the interaction region. However, repetitive irradiations may drastically increase this number and provide more seed electrons via an incubation effect.

3.1.2 Impact ionization and photoionization

As soon as the bottom of the conduction band populates, the free electrons absorb light due to inverse bremsstrahlung. When their kinetic energy surpasses the material's bandgap, a valence band electron can be promoted to the conduction band by collisional ionization. The repetition of this process leads to the well-known electronic avalanche. The avalanche ionization rate β links the free electron density with the amount of seed electrons $N_e(t)$:

$$\frac{dN_e}{dt} = \beta N_e(t) \quad (3.3)$$

The relation of the avalanche ionization rate with the laser intensity is still not treated as an unanimous matter in the scientific community. As some researchers predict a square root dependence [DLK⁺94, Tho81], a linear relationship $\beta = \alpha I$, α being the avalanche coefficient as proposed by Stuart *et al.* [SFH⁺96a] seems to prevail as it is still vastly employed [HBT⁺07]. Briefly, two assumptions accompany the linear dependence, namely the flux doubling approximation (as soon as one electron has accumulated enough kinetic energy, it triggers an impact ionization) and the constant shape of the CB electronic energetic distribution regardless of the electronic density.

In situations where tunneling is negligible ($\gamma > 1.5$), the transient free electronic density under subpicosecond irradiation can be described by a simple rate equation involving MPI and avalanche carrier multiplication [SFH⁺96a]:

$$\frac{dN_e}{dt} = \alpha I N_e(t) + P_{MPI}(I)(N_0 - N_e) - \frac{N_e}{\tau_{rec}} \quad (3.4)$$

where N_0 is the density of atoms (assuming one available free electron per atom site) and τ_{rec} is the radiative recombination time accounting for a diminution of the carrier density within the pulse duration [ADS⁺94]. Experimental studies concerning Eq. 3.4 have either underlined [LKS⁺98, TBK⁺99, SFH⁺96a] or controverted [JBC⁺89, QGM01] the role of avalanche ionization. In the effort of providing a unified model, refinements of Eq. 3.4 has been recently proposed by B. Rethfeld [Ret04, Ret06] in the form of a multiple rate equation (MRE). Concisely, this model takes into account the avalanche coefficient dependency not only on N_e but also on the electronic energetic state, as an electron in the bottom of the CB will need a non negligible time to acquire sufficient kinetic energy to generate impact ionization than an already excited CB electron. Eq. 3.4 disregards this 'loading' time and appears as a special case of the MRE [Ret04].

As a drastic summary, one can state that around the modification threshold in fused silica, MPI tends to clearly dominate the whole ionization process in the case of short pulses (< 150 fs). In that case, the free electronic density scaling with the laser intensity to the K-power stands as an irrevocable experimental signature of MPI [TSZ⁺06, HBT⁺07]. For longer pulses (> 800 fs), the observed independence of the damage threshold with respect to the laser polarization state pleads for a reduced responsibility of the MPI compared to the avalanche contribution [JLS⁺03].

3.2 Optical properties

Once electrons are promoted to a conductive state, the optical properties of the solid vary in a dynamic way. The purpose of this section is not only to give a brief introduction to the optical properties of a material locally bearing a certain amount of free electrons, but also to show that basing ourselves on simple results from the Drude theory [Dru06], it is possible to quantitatively estimate electronic densities from microscopy absorption pictures under limited hypothesis. The resulting estimation of the free carrier population then leads to the knowledge of the phase retardation experienced by the light probing the electronic cloud. With this precious information, phase contrast microscopy pictures can be corrected from the electronic contribution to the contrast, thus providing the lattice phase picturing under a few assumptions. After briefly recalling the simplest free electron in vacuum model from Drude, we refine it taking into account damping of the electronic motion in dielectrics with the lattice influence. Reflectivity, transmission and phase retardation are evaluated along the discussion.

3.2.1 Free electrons without damping in vacuum

We start our discussion with the simplest hypothesis regarding the properties of an free electronic gas in vacuum. While damping is thought to be collisions between electrons and atoms of non ideal lattice [Hum04], we neglect at first the influence of lattice defects. The analysis is conducted on a one dimensional frame of reference supposing a plane light wave linearly polarized. The field strength associated with such a radiation wave writes $\varepsilon = \varepsilon_0 \exp(i\omega t)$ with the same notations as in Ch. 2. Since we consider here that the light is the only force applied to the electron, its acceleration can be readily defined using Newton's second law, yielding the motion equation:

$$m \frac{d^2 x}{dt^2} = e\varepsilon = e\varepsilon_0 \exp(i\omega t) \quad (3.5)$$

where e and m are the electronic charge and mass respectively. This simple differential equation abides this well known trial solution $x = x_0 \exp(i\omega t)$ which, associated with the motion equation 3.5 permits to express the momentary displacement x as $x = -\frac{e\varepsilon}{\omega^2}$. The polarization $P = exN$ denotes the sum of the electric dipole momenta $\mu = x \times e$ per volume unity with N referring to the density of free electrons. The complex dielectric constant $\tilde{\epsilon}$ is related to the polarization by [GST03] $\tilde{\epsilon} = 1 + \frac{P}{\epsilon_0 \varepsilon}$. Using the three last equations, we obtain a very intuitive relation underlining the material's optical behavior (denoted by its dielectric constant) with respect to the free electronic density N .

$$\tilde{\epsilon} = 1 - \frac{e^2 N}{\epsilon_0 m \omega^2} \quad (3.6)$$

The dielectric constant corresponds to the square of the complex refractive index $\tilde{n} = n + ik$, with k known as the damping constant (or extinction coefficient). From this relation, it is possible to delineate the material's optical properties for different light frequencies ω and for various free carrier densities N . For example, assuming a perpendicular incidence, the reflection coefficient R is defined following Fresnel formula:

$$R = \frac{(n - 1)^2 + k^2}{(n + 1)^2 + k^2} \quad (3.7)$$

It is also possible to evaluate the absorption properties of the electronic gas with the help of the extinction coefficient k , simply related to the absorbance α by $\alpha = \frac{4\pi k}{\lambda}$. Associating this result with the well-known Beer-Lambert law,

$$I = I_0 \exp(-\alpha L) \quad (3.8)$$

where L is the length of material traversed by the optical wave and I its intensity, we are able to calculate the reflectivity R and the transmission $T = \frac{I}{I_0}$ for light propagating through a free electronic gas for different electronic densities and at various wavelengths. In the frame of this simplified model, the gas acts like a high-pass optical frequency filter [BS96] with the particularity that the cut-off frequency augments with the electronic density. The consequences on the expression of R in Eq. 3.7 are respectively $R = 1$ and $R = \frac{(n-1)^2}{(n+1)^2}$. The cut-off frequency associated with this sharp change of behavior is a manifestation of the plasma frequency ω_P corresponding to the annulment of \tilde{n}^2 (see Eq. 3.6):

$$\omega_P = e \sqrt{\frac{N}{m\epsilon_0}} \quad (3.9)$$

The related plasma oscillation implies the ensemble of the electron gas in a fluidlike collective undulation [Hum04]. Interestingly enough, the previous definition of the plasma frequency in Eq. 3.9 reveals a square root dependence with respect to the electronic density N . As our investigations of the electronic plasma subsequent to laser irradiations were carried out at a fixed wavelength, (400 nm), it is practical to define a critical electronic density N_{cr} for which the plasma oscillation synchronizes with the light frequency that traverses it:

$$N_{cr} = \frac{\omega^2 \epsilon_0 m}{e^2} \quad (3.10)$$

During the laser irradiation, the electronic density N varies as electrons are promoted from the valence band to the conduction band through various mechanisms [SFH⁺96a] detailed in the former section. Therefore, it is riveting to see the reflectivity and transmission dependence on the ratio $\frac{N}{N_{cr}}$. In order to do so, the dielectric constant $\tilde{\epsilon}$ in Eq. 3.6 maybe simply rewritten including N_{cr} :

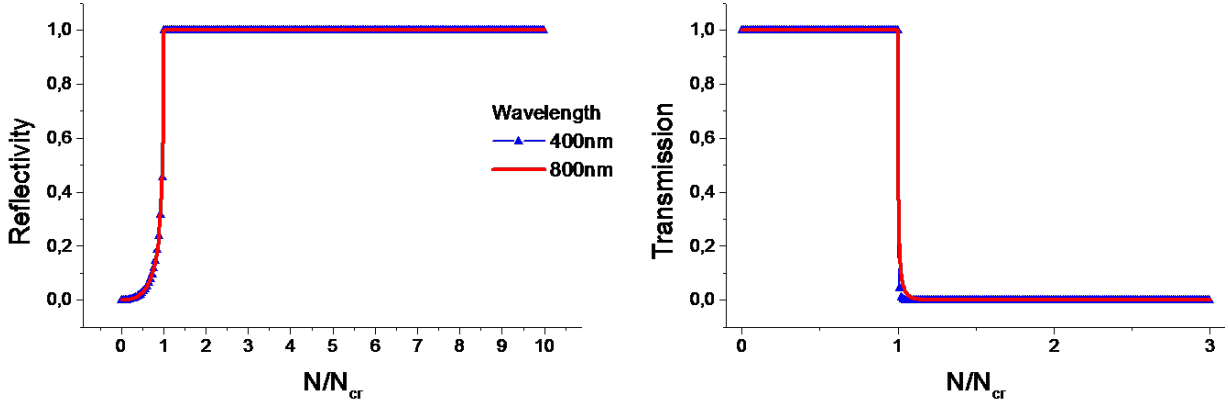


Figure 3.2: Reflectivity and transmission of 1 μm thick free electronic cloud according to the Drude model without damping with respect to the ratio $\frac{N}{N_{cr}}$ for 800 nm and 400 nm optical radiation. For 400 nm light, N_{cr} is $7 \times 10^{21} \text{ cm}^3$ and for 800 nm light, N_{cr} is $1.74 \times 10^{21} \text{ cm}^3$ in vacuum.

$$\tilde{\epsilon} = 1 - \frac{N}{N_{cr}} \quad (3.11)$$

Then, using Eq. 3.7 and Eq. 3.8, one can plot the evolution of transmission and reflectivity for an increasing electronic density N as reported in Fig. 3.2.

The model employed here is the simplest we can imagine. However, starting for basic assumptions, it succeeds in explaining the sharp increase of reflectivity with the free electronic density and helps introducing in a very intuitive way the notion of plasma resonance and matches quite finely reflectivity properties of various metals [Hum04]. On the other hand, the transmission predictions are not in harmony with experimental evidences, in particular, the plateau showing full transmission for electronic densities inferior to the critical density is not realistic for electronic gas in materials (for example in metals). Consequently, refinements of this model are proposed in the following, taking into account the lattice of the medium and its interaction with the electrons.

3.2.2 Free electrons with damping in materials

The following model is still widely used to understand transient optical properties associated with ultrashort laser dielectric irradiation [TSZ⁺06, HBT⁺07, SFH⁺96a, SvdL00, MQG⁺04]. Collisions involving electrons and atoms of a non ideal lattice, i.e containing lattice defects. The resulting motion damping translates into an additional term in the electronic motion equation Eq. 3.5:

$$m \frac{d^2 x}{dt^2} + \gamma \frac{dx}{dt} = e \epsilon_0 \exp(i\omega t) \quad (3.12)$$

Following the same considerations involving the solution of equation Eq. 3.12 and the polarization $P = exN$ as in the previous subsection 3.2.1, we obtain again the free-electron contribution to the dielectric constant which implies the damping factor γ :

$$\tilde{\epsilon} = 1 - \left(\frac{e^2 N}{\epsilon_0 m} \right) \frac{1}{\omega^2 + i\gamma\omega} \quad (3.13)$$

The damping factor γ is related to the Drude damping time or scattering time $\tau_D = \frac{1}{\gamma}$ which can be assimilated to the average time between electronic collisions implying momentum scattering (e.g with the lattice). It is usually on the order of a femtosecond in fused silica [SFH⁺96a]. We now consider the electronic plasma in the bulk of a dielectric. Therefore, the above-mentioned dielectric constant $\tilde{\epsilon}$ comes as a variation the dielectric constant $\tilde{\epsilon}_{material}$ of the host material. We mention briefly that it is also possible to take into account the depletion of electrons from the optical valence to populate the free electronic cloud as well as band-structure renormalization. However, as those two latter contributions remains negligible compared to a pure Drude model (see [SvdL00] for silicon which has a thinner bandgap), we dwell in this simplified frame. The total dielectric constant then reads:

$$\tilde{\epsilon}_{tot} = \tilde{\epsilon}_{SiO_2} - \left(\frac{e^2 N}{\epsilon_0 m_{opt}^* m} \right) \frac{1}{\omega^2 + i\gamma\omega} \quad (3.14)$$

which rewrites:

$$\tilde{\epsilon}_{tot} = \tilde{n}^2 = \tilde{\epsilon}_{SiO_2} - \left(\frac{Ne^2}{\epsilon_0 m_{opt}^* m \omega^2} \right) \frac{1}{1 + (\omega\tau)^{-2}} + i \left(\frac{Ne^2}{\epsilon_0 m_{opt}^* m \omega^2} \right) \frac{(\omega\tau)^{-1}}{1 + (\omega\tau)^{-2}} \quad (3.15)$$

Inserting the critical density $N_{cr} = \frac{\omega^2 \epsilon_0 \tilde{\epsilon}_{SiO_2} m}{e^2}$ (for ease of understanding, we consider the N_c of a collisionless plasma in fused silica), we obtain:

$$\tilde{\epsilon}_{tot} = \tilde{n}^2 = \tilde{\epsilon}_{SiO_2} \left[1 - \left(\frac{N}{N_{cr}} \right) \frac{1}{1 + (\omega\tau)^{-2}} + i \left(\frac{N}{N_{cr}} \right) \frac{(\omega\tau)^{-1}}{1 + (\omega\tau)^{-2}} \right] \quad (3.16)$$

where m_{opt}^* is the effective optical mass of a free electron given by $m_{opt}^* = (m_e^{*-1} + m_h^{*-1})^{-1}$ where m_e^* and m_h^* are the mobility effective masses of electrons and holes. Here m_{opt}^* is assumed to be equal to unity [HBT⁺07, SFH⁺96a, Ret04]. Now that the complex refractive index $\tilde{n} = n + ik$ is defined, we can evaluate again the reflectivity R and transmission T with respect to the electronic density divided by the critical density utilizing Eq. 3.7 and Eq. 3.8. The corresponding curves are reported in Fig. 3.3. Contrary to the previous damping model, absorption is expected to occur as soon as one electron is freed from its valence situation thus being able to absorb light by inverse bremsstrahlung where the associated energetic losses are due to its interaction with the neighboring environmental. Note also the evolution of reflectivity which now knows a minimum at the critical

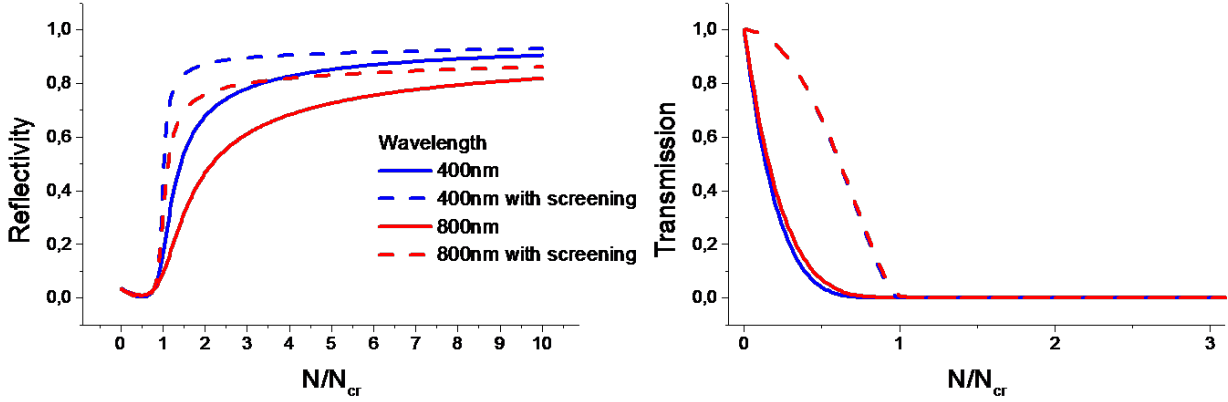


Figure 3.3: Reflectivity and transmission of 1 μm thick free electronic cloud in fused silica according to the Drude model with damping with respect to the ratio $\frac{N}{N_{cr}}$ for 800 nm and 400 nm optical radiation. In fused silica, for 400 nm light, N_{cr} is $1.5 \times 10^{22} \text{ cm}^3$ and for 800 nm light, N_{cr} is $3.7 \times 10^{21} \text{ cm}^3$. The solid curves assume a constant Drude damping time τ whereas the dashed plots include a inverse proportionality to $\frac{N}{N_{cr}}$, taking into account the screening effect.

density (or equivalently at the plasma frequency) and a dramatic increase for larger electronic densities.

The scattering time τ is also expected to shorten as the electronic density augments following a phenomenological law given by $\tau = \tau_1 \times \frac{N_{cr}}{N} + \tau_0$ [QHA⁺00]. From time-resolved surface reflectivity on fused silica, Siegel *et al.* found $\tau_1 = 3.7 \text{ fs}$ [SPG⁺07]. This latter expression of the scattering time must be completed with an additional constant τ_0 , that is the shortest duration between two collisions as this quantity cannot be zero. We take this delay to be below the femtosecond [Ash03]. Fig. 3.3 takes into account this density dependence of the Drude damping time in the dashed curves. The so-called screening effect associated with this relation is clearly noticeable for densities lower than the critical density. Intuitively speaking, the growing free electronic cloud weakens the ionic field moderating the electronic collisions rate. This results in an reduced absorption power and an increased reflectivity for densities below plasma oscillations (dashed curves). Naturally, for stronger densities, the behavior remains similar.

These latter evaluations clearly enable the electronic density quantitative calculation from optical transmission microscopy pictures under careful estimation of the thickness of the electronic cloud. Moreover, it is straightforward to deduce the optical retardation associated with the electronic cloud as its refractive index n_{plasma} is simply calculable following $n_{plasma} = \Re(\tilde{n})$ associated with Eq. 3.16. The corresponding results are shown on Fig. 3.4. Using those latter calculations, phase contrast microscopy pictures were corrected from the electronic contribution in absorption and in phase, revealing the lattice transient optical properties which are discussed in

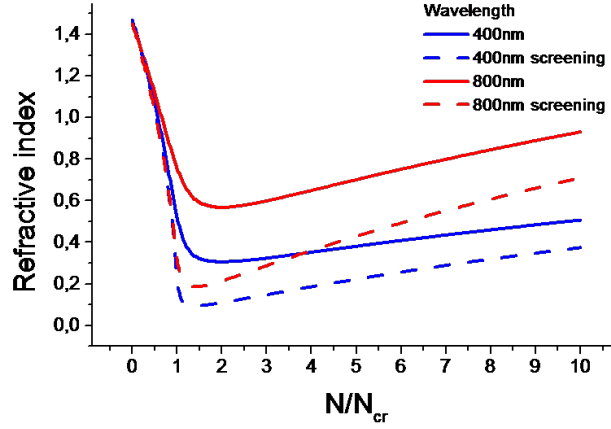


Figure 3.4: Refractive index of a free electronic cloud in fused silica according to the Drude model with damping with respect to the ratio $\frac{N}{N_{cr}}$ for 800 nm and 400 nm optical radiation.

Ch. 6.

3.3 From the transient electronic gas to the refractive index modification

The mechanisms (MPI, TI, impurities and avalanche) leading to the constitution of the local free electronic cloud subsequent to femtosecond insulation and the optical properties (absorbance, refractive index) of the transient gas were reviewed in the two preceding sections. Once the free carrier ensemble is formed, the material finds itself in a very unusual situation where a dense and hot electronic plasma coexists with the cold ions of the dielectric lattice. Various thermodynamic paths then redistribute the energy surplus in order to retrieve a thermodynamic equilibrium. This energy relaxation leads to local structural deformations with consequences on the permanent optical, chemical and mechanical properties. In short, the bulk modifications can be cataloged in two general classes: color centers and lattice re-organization. As a consequence on the irradiated region, both processes lead to an alteration of the local properties which naturally propagates to the local refractive index [AH88].

3.3.1 Color centers

Through various nonlinear mechanisms (see Sec. 3.1), femtosecond irradiation in wide bandgap materials can promote electrons from the valence band to the conduction band, leaving a hole in the valence band. The Coulomb attraction may bind the couple formed by an electron and a hole

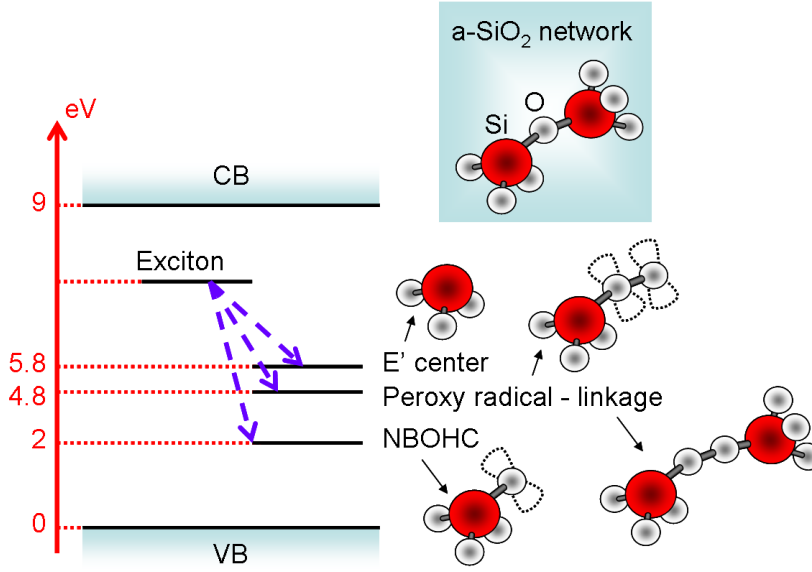


Figure 3.5: Schematic illustration of exciton and intrinsic defect energy levels in fused silica. Exciton self trapping energy relaxation into permanent or transient defects is represented by the violet arrows. The absorption band of each type of defects is also reported on the left energy scale (adapted from [MQG⁺04, SW96])

which is then called an exciton [SW96]. In fused silica, the electron-hole binding is strong and localized near a single atom [MQG⁺04]. Excitons can relax through delocalized and localized channels with a higher probability for the latter in wide bandgap materials as fused silica. A significant relaxation mechanisms relates to the localization of the energy contained in the exciton which creates a self-trapped exciton (STE) in 150 fs [ADS⁺94]. Therefore, this mean of energy deposition generates localized lattice rearrangements or in other words defect generation. In fused silica, constituted of SiO_4 tetrahedrals with a silicon atom at the center and oxygen atoms at the four corners (see Fig. 3.5), STE strongly weakens the Si-O-Si bond, moving the oxygen atom out of its equilibrium position [MQG⁺04]. The consecutive alteration of the SiO_4 tetrahedrals entails the creation of a variety of transient or permanent point defects such as E' centers, non bridging hole centers (NBOHC), peroxy radicals and peroxy linkages (see Fig. 3.5 for illustration) whose experimental signatures can be detected using photoluminescence and Raman scattering spectroscopies [SW96, SSK⁺03, KD03]. For example, a large fluorescence band was observed around 630 nm corresponding to the presence of NBOHC after femtosecond irradiation in fused silica [CHRK01].

Petite *et al.* [PDGM97] showed that the permanent local refractive index associated with these defects can be estimated with the help of the Lorentz model [Hum04] for the bound electronic contribution. From this model, it appears that the local refractive index increase is higher for defects

situated deeper in the bandgap (e.g NBOHC). As a rapid estimation, for a defect concentration of 1% of the SiO_4 tetrahedrals, the resulting refractive index change Δn is about 0.1%. Experimentally [SB02], a permanent defect (E' and NBOHC) concentration of 3.10^{19} is accompanied with a $\Delta n = 0.1\%$. However, it is pointed out that the thermal stability of the defects and the index of refraction are uncorrelated [SB02]. In particular, the index of refraction remains unchanged beyond 500°C whereas the characteristic defect fluorescence vanishes after 400°C which seems to exclude defects as the unique responsible of the increase of the refractive index. In BK7 glass, the chemical and structural changes are dominated by the presence of the boron oxygen hole center [SB02]. Ab-initio molecular dynamics studies [SD03] have also shown the appearance of persistent E' centers and NBOHC after femtosecond irradiation in fused silica. Those defects give rise to an increase of the refractive index through Kramers-Kronig mechanism [SD03].

3.3.2 Lattice re-organization

If the previous ventilation takes a so-to-say atomistic point of view, the present paragraph consider the material from a farther point. In a extremely simplistic summary, the energy transfer from the excited electronic cloud to the cold ions of the lattice leads to an uncommon temperature and pressure elevation inducing local glass melting associated with densification upon cooling. If in the pure fused silica network, silicon atoms form five or six member rings, the presence of three and four member rings after femtosecond irradiation is readily detectable from their respective Raman peaks (490 cm^{-1} and 605 cm^{-1} [CHRK01, PC98]). The associated decrease of the Si-O-Si bond angle implies a local densification. The origin of this matrix re-organization is not unique.

For example, a strong strain field surrounding the focal area has been observed in quartz after single and multiple pulse irradiation [GWN⁺03]. Permanent stress fields dependent on the laser scanning direction are also reported in fused silica [PSF⁺03] with unique application for bulk processing (scissor or chiral effect [PLPA08]).

In borosilicate glasses, thermal phenomena in regimes of multiple pulses accumulation has been studied [GM97]. Transition from a thermal diffusion regime to a heat accumulation regime with the irradiation repetition rate is shown to have a predictable impact on the dimensions and properties of the bulk modification [EZN⁺08]. In tight connection with the local heat flow in high repetition rate regime, laser-induced ion migration accompanied with densification was recently observed from the elemental redistribution subsequent to the ultrafast irradiations [KMH08].

As a broader point of view, the Douillard-Duraud point defect model draws a strong relation between lattice re-organization and defects in fused silica [DD96]. Molecular dynamics simulations of fused silica with a increasing concentration of vacancies have shown a correlated increase of densification [Tan98]. Having in mind these various channels leading to local modification of the

material properties, it is instructive to attempt to delineate photoinscription regimes even though most of the above mentioned mechanisms might occur simultaneously.

3.3.3 Thermomechanical effects

At rather low intensities under multiple irradiations, incubative effects associated with the gradual accumulation of defects dominate the material's response and are typical of a 'soft' photoinscription regime. At moderate and higher incident powers, the onset of thermo-mechanical effects rule the modification mechanisms [SWBH10] (see also Chap. 5). For instance, NLSE simulations connected to a dynamic thermal elastoplastic model can qualitatively account for the laser-induced bulk modification in BK7 glass and fused silica [MBM⁺08, MBR⁺09]. In BK7, the ultrashort irradiation leads to the formation of a hot region, where, due to rapid thermal expansion, the material is quenched in a low-density phase depending on the heating and relaxation rates [EKW⁺04]. For higher energy densities, compressive shock waves are generated and determine the formation of a strongly compacted region around the low density core. In fused silica, time-resolved observations tend to confirm that the refractive index change and particularly the void formation is mostly driven by a thermo-mechanical phenomena [MBR⁺09, ST05]. There, the temperature elevation results in a strong mechanical constraint leading to a deformation beyond the elastic limit at the origin of the void.

3.4 Conclusion

After identifying the main photoionization mechanisms feeding the transient electronic gas, we analyzed its optical properties in the frame of the Drude model. More precisely, we indicated that its transmittance and refractive index at both the pump and the probe wavelengths (resp. 800 nm and 400 nm) significantly drop when the electronic density augments close to the critical density. This result is at the basis of the numerical treatment of the time-resolved microscopy images which permit to obtain the 2D electronic density and matrix index changes (see Chap. 6). The chapter also identified strong and soft interactions generated by non linear effects leading to permanent modifications.

Chapter 4

Experimental set up

As the aim of the present report is to demonstrate the flexibility offered by ultrafast laser tailoring in the field of in-volume machining of transparent materials, a precise description of the involved equipment seems indispensable. Naturally, femtosecond bulk machining with the capacity to tailor spatially and temporally the irradiation sequence require several experimental apparatus which are presented in the following. We first review rapidly the main characteristics of the ultrashort laser sources mentioned in this report. Then, a section is dedicated to temporal pulse shaping providing a general description of this widespread technique with details on the actual systems equipping the laser sources. Then, spatial beam shaping is discussed with a review of various beam controlling solutions comprehending precisions on the optical valve employed within this report. The discussion is completed with the description of phase mask designing algorithms based on iterative Fourier transform loops and on global optimization strategies. Lastly, schematic illustrations of the irradiation set ups are reported with explanations on their specificities and particulars regarding sample handling and investigation means.

4.1 Laser sources

Two distinct femtosecond laser sources were employed along this thesis. While both sources are based on Ti:Sapphire Chirped Pulse Amplification (CPA), one provides relatively high repetition rate (up to 250 kHz) to the detriment of pulse energy and is referred to as HRR system. The second system offers higher pulse energy with lower repetition rate (LRR) (up to 1 kHz).

The high repetition rate laser is schematically represented on Fig. 4.1. It includes a Vitesse oscillator (Coherent) and a RegA amplifier (Coherent) and produce pulses with 13 nm FWHM spectra centered around 800 nm. Both are pumped by a continuous wave laser (Verdi) which is a continuous laser constituted of two power diodes (808 nm) pumping a Nd:YVO₄ crystal with a intra-cavity frequency doubling LBO crystal to match the Ti:Sapphire absorption spectrum. The

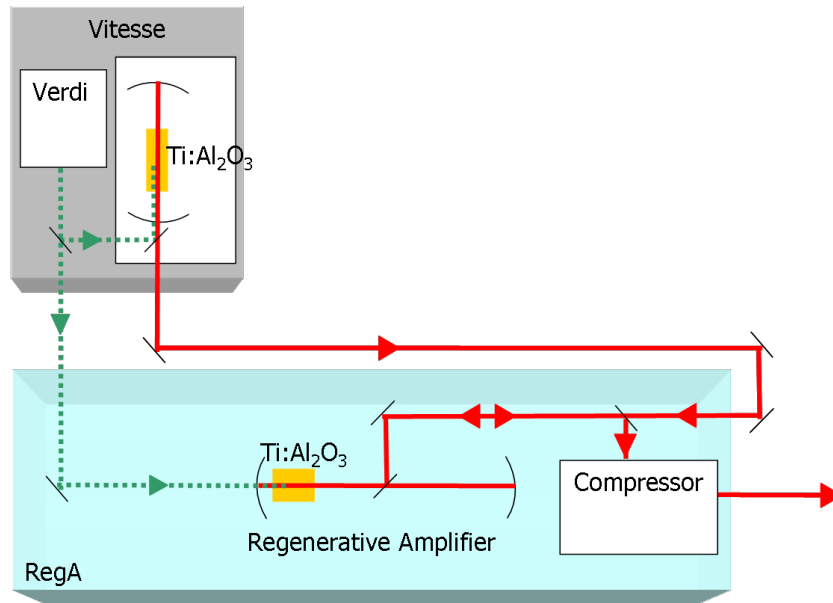


Figure 4.1: Schematic representation of high repetition rate amplified femtosecond laser source from Coherent. The green arrow represents the pump beam and the red arrow the seeded and amplified femtosecond pulses.

system delivers 130 fs (FWHM) pulses with an energy approaching $4 \mu\text{J}$, and the output beam has a $1/e^2$ diameter of about 5 mm with a FWHM spectral bandwidth of 10 nm centered at 800 nm. This HRR system was preferably employed for bulk photoinscription of photonic devices taking advantage of the flexibility offered by its high repetition rate and its most-of-the-time sufficient pulse energy. This system is equipped with a spatial shaping apparatus and a temporal shaping system too.

The LRR system (Clark OCR-1000) provides a higher pulse energy and is consequently dedicated to static and dynamic investigations as the high pulse energy enables bulk irradiation and

Table 4.1: Laser sources characteristics

Laser system	HRR	LRR
Maximum pulse energy	$4 \mu\text{J}$	$600 \mu\text{J}$
Repetition rate	10 kHz to 250 kHz	166 Hz to 1 kHz
Pulse duration (FWHM)	130 fs	100 fs
Output beam diameter ($1/e^2$)	5 mm	6 mm
Spectral bandwidth (FWHM)	10 nm	8 nm
Spatial shaper	Yes	No
Temporal shaper	Yes (before amplification)	Yes (after amplification)

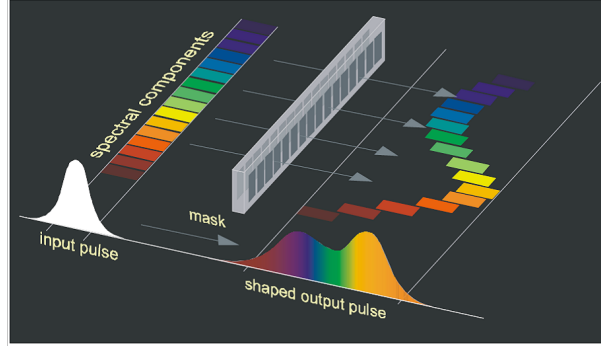


Figure 4.2: Schematic illustration of temporal femtosecond pulse through spectral components manipulation extracted from [Tra07].

probing of the affected zone with satisfactory illumination conditions. Again, both amplifier and oscillator use a Ti:Sapphire as an active medium, delivering femtosecond light wave packets with a spectral bandwidth of 8 nm around 800 nm and a FWHM pulse duration of 100 fs. The optical pulses are stretched up to 100 ps in a homemade diffraction-grating-based stretching unit and seed a regenerative amplifier. The repetition rate is controllable via the Pockels cell driving from 166 Hz to 1 kHz. The lowest repetition rate allows to use an additional electromechanical shutter in order to pick up single pulses. The available amount of energy per pulse is about $600 \mu\text{J}$ with a beam diameter at $1/e^2$ of 6 mm. This laser system is completed with a temporal shaping unit.

A summary of the HRR and LRR laser sources main characteristics are reported in Tab. 4.1.

4.2 Temporal pulse shaping

Following the leitmotiv of this report, we detail here the technique of temporal tailoring of ultra-short light pulses which we show to widen the application field of femtosecond bulk processing (see Chap. 7). After a brief review of general principles regarding femtosecond temporal pulse shaping, the apparatus deployed on the HRR and LRR laser system is described.

4.2.1 Generalities

Detailed discussions regarding femtosecond temporal shaping through Fourier synthesis can be found in [Tra07, Wei00], the present paragraph outlines the main general points in order to properly introduce the temporal shapers in use on the two laser systems. Naturally, direct manipulation of frequency components in the time domain would require yet nonexistent devices with the capacity to control the light intensity on a femtosecond scale. A powerful way to bypass this difficulty is found in manipulating the pulse in the spectral domain. We emphasized in Sec. 2.2.2 the in-

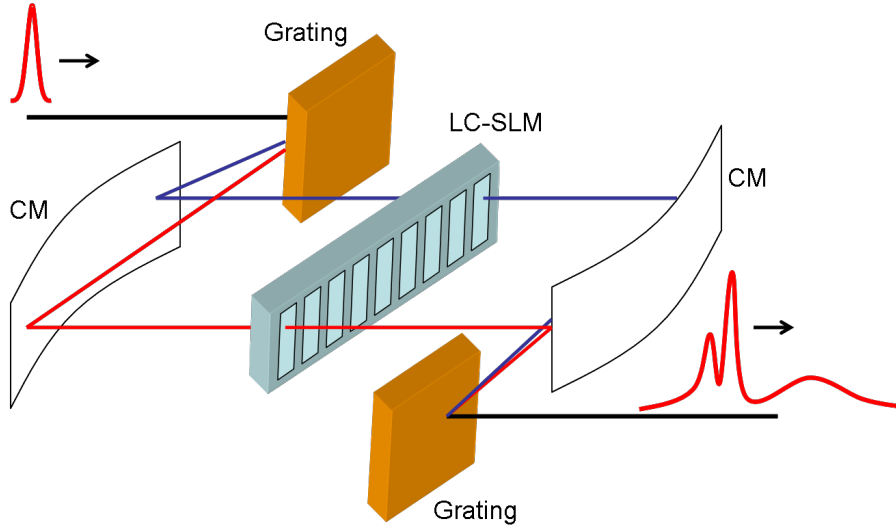



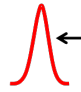





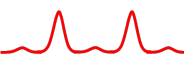
Figure 4.3: Temporal shaper unit employed in this report. CM: Curved mirror. LC-SLM: Liquid-crystal spatial light modulator allowing for phase manipulation of the pulse spectral components. In the absence of the LC-SLM, this set up is called a zero dispersion stretcher unit because the exit pulse is then exactly recomposed as the initial pulse without any distortion.

fluence of dispersion (SOD and TOD) on the temporal pulse form upon propagation in dispersive media. The refractive index spectral dependency has consequences on the temporal pulse shape (see Eq. 2.12). Therefore, an efficient manner to control the pulse shape lies in a phase modulation on the spectral components as schematically illustrated on Fig. 4.2.

In order to have access to the femtosecond pulse spectral components, Fourier transformations can be optically achieved allowing the passage from the time domain to the spectral domain. Fig. 4.3 illustrates the following explanation. An incoming ultrashort laser pulse is dispersed by a grating and its spectral components are focused by a curved mirror (CM) in the plane of a liquid crystal spatial light modulator (LC-SLM) placed in the CM Fourier plane thus realizing an optical Fourier operation from to the spectral domain. In this plane, the spectral components are discriminated by their respective beam waist and different diffraction angle. If no phase modulation is operated by the LC-SLM, a mirrored association of alike optical elements reforms the pulse to its original shape; the set up is then referred to as zero dispersion unit. If a phase and/or amplitude mask is applied by the LC-SLM, the temporal pulse shape can be controlled. It is therefore convenient to characterize the apparatus with its linear transfer function $h(t)$ in the temporal domain [Tra07]. Supposing a light pulse $e(t)$ entering the apparatus, the output $s(t)$ follows $s(t) = e(t) \otimes h(t)$ where \otimes denotes the convolution product. In the spectral domain, the same relation reads

$$S(\omega) = E(\omega)H(\omega) \quad (4.1)$$

Table 4.2: Common spectral phase masks and their effect on the output pulse temporal profile

Phase mask	$\phi(\omega)$	Temporal profile $I(t)$
Ramp		
Parabolic		
Cubic		
Phase grating		

Generally, the transfer function is complex : $H(\omega) = R(\omega)e^{i\psi(\omega)}$. Its real and imaginary parts respectively correspond to the mask transmission and phase modulations along the direction where the spectral components are dispersed [Tra07]. For energy conservation reasons, phase-only modulation was employed in our experiments. Therefore, the temporal envelope $s(t)$ of the outcoming light is obtained from the inverse Fourier transform of Eq. 4.1 with $R(\omega) = 1$

$$s(t) = \frac{1}{2\pi} \int S(\omega)e^{i\omega t} d\omega = \frac{1}{2\pi} \int E(\omega)e^{-i\psi(\omega)}e^{i\omega t} d\omega. \quad (4.2)$$

The measurable envelope of the pulse corresponds to the real part of $s(t)$ while the imaginary part gives the residual chirp. The effect of common phase masks is presented in Tab. 4.2 giving an illustration of usual pulse shapes. Similarities to the spatial domain (at the Fourier plane of a lens) are clearly noticeable [DR06]. It is noteworthy to point out that if Fig. 4.2 is very intuitive, one should be prudent when considering it. As an example, a ramp phase mask does not elongate the pulse as expected from Fig. 4.2, but simply shifts it temporally without altering its form (see Tab. 4.2). Parabolic and cubic phase masks correspond to SOD and TOD, respectively (see Sec 2.2.2). Phase-only masks can be designed to closely approach user-defined temporal profile from iterative algorithms. Such algorithms are also employed in the spatial domain and are presented in Sec. 4.3.3.

Another temporal pulse shaping technique has to be mentioned here, namely the Acousto-Optic Programmable Dispersive Filter (AOPDF) [VLC⁺00]. The basic principle relies on a programmable radio frequency (RF) signal traversing a birefringent crystal. Under phase matching condition, optical frequencies from the laser pulse can be diffracted from the crystal fast axis to the slow axis reproducing the RF signal (static on the femtosecond scale) thus allowing arbitrary pulse shaping. This compact device is quite straightforward to utilize, however it cannot withstand high laser fluences $< MW/cm^2$ and generates up to 60% losses [VLC⁺00].

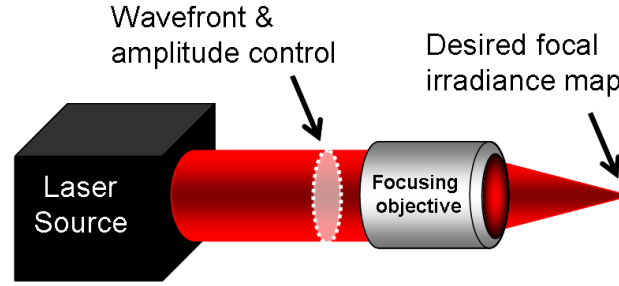


Figure 4.4: General scheme of spatial beam shaping which implies amplitude wavefront modulation to obtain user defined focal spot.

4.2.2 Temporal shaping apparatus

Fig. 4.3 portrays the system present on both lasers (HRR and LRR). Cylindrical mirrors are employed both to avoid chromatic aberrations and to minimize the density of energy on the LC-SLM [PWA⁺03]. The phase-only mask is a one-dimensional array of liquid crystals (Jenoptik) comprising 640 pixels electrically addressable. For the HRR laser system, the pulse shaping unit is inserted between the oscillator and the regenerative amplifier. In this way, the cavity of the regenerative amplifier plays the role of a spatial filter, allowing the delivery of a TEM_{00} beam only. This configuration notably prevents problems of beam distortion that may occur when modifying the spectrum of the beam [BKK⁺05]. For the LRR laser system dedicated notably to the dynamic investigations, preserving the shortest pulse duration for the probe with sufficient energy for illumination was a necessity. Therefore, the temporal pulse shaper is placed on the pump arm, after the output of the amplifier with a spatial care to avoid any spatial chirp and pulse front distortions [AKOT03].

4.3 Spatial beam shaping

In relation with the demand of higher flexibility for femtosecond bulk machining, tuning the beam wavefront is a decisive controlling parameter that can not only overcome propagation artifacts but also push the technique to higher efficiency (see Chap. 7). This section first draws a quick review of the most widespread solutions to achieve spatial beam tailoring before introducing the optical valve installed on the HRR laser system. Phase masks designing strategies are then described with insights on the interest and limitations of global optimization algorithms in this field.

4.3.1 Beam controllers

The general principle of spatial beam shaping concerns the beam amplitude and/or wavefront modulation with the scope of attaining a user-defined focal irradiance map as depicted on Fig. 4.4. This quite wide definition comprehends technique of wavefront 'cleaning' to reach the smallest focal spot for diffraction limited processing or observation. In order to achieve amplitude or wavefront tuning, several techniques may be employed. Naturally, before going to that advanced level of focusing light, one has to be familiar with the influence of several parameters which always accompany femtosecond laser processing such beam truncation, aberrations and so on (see Chap. 2).

Static modulators

The simplest system one can think of consist in simply positioning an aperture in the form of the desired irradiance map in front of the focusing element and then working at the image plane of the aperture (e.g for surface processing). If this method is very robust and yields satisfactory results, it carries intrinsic limitations. As the processing plane is not the focal lens plane, the maximum fluence is not obtainable and the static aperture remains a limitation when dynamic reconfigurability is needed [San05]. In the same order of ideas, slit beam shaping knows a quite recent gain of interest in the bulk photowriting of transversal waveguides (i.e laser spot is translated perpendicularly to the laser propagation axis). The technique permits long depth-of-field photoinscription of guides with circular cross section compensating by an asymmetry in the section plane the elongation along the confocal region [CSM⁺03, AMSW05].

Pertaining with static beam formers, the well-known family of Diffractive Optical Elements can modulate the phase and/or the amplitude of the processing laser [LCW94]. Thanks to their design based on Iterative Fourier Transform Algorithms or advanced optimization algorithms, they enable efficient arbitrary beam shaping with the advantage of offering the highest available fluence [Cor93].

Dynamic modulators

Entering in the world of phase and/or amplitude modulators with dynamic reconfigurability, the devices take the name of Spatial Light Modulators (SLM). A complete review of the matter is available in [Efr94]). Here, we briefly evoke deformable mirrors and liquid-crystal SLM. Deformable mirrors (DM) are phase-only SLM and are constituted with a reflective surface which is locally displaced through mechanical, piezoelectrical or electrostatic force. The surface can be either an assemblage of numerous miniature consecutive mirrors or a flexible membrane [Efr94]). The main advantages of DM are a rather extended modulation course (up to 10 μm), a big size, a good resistance to high fluences, the absence of pixels (in the case of contiguous membrane) and

achromaticity (since the wavefront modulation is based on reflection). However, the spatial resolution is usually restricted to 1 mm and the refreshing rate is rather low (≈ 0.1 s). Their interest finds its significance when DM are consecrated to simple phase functions with low spatial frequencies (tilt, phase curvature and other first Zernike polynomials). However, we must not ignore DM based on Micro-Electro-Mechanical Systems MEMS whose specificities tend to push away the historical DM limitations (pitch reduced by a factor of ten and the response time under $100 \mu\text{s}$) while keeping the advantage of achromaticity at the cost of slightly reduced stroke ¹.

Liquid crystal based spatial modulators (LC-SLM) take advantage of the liquid crystal molecules properties. These molecules have a ellipsoidal shape with a certain polarity associated with the capacity to rotate under an external electric field with geometrical organizational constraints [Goo05]. The various types of molecule assemblage (nematic, smectic...) within the liquid crystal layer have consequences on their physical properties. The oblong form of the molecules implies birefringent properties, i.e the refractive index seen by a traversing beam varies between the ordinary and extraordinary index (n_o and n_e) depending on the molecules orientation with respect to the beam polarization. Based on this principle, amplitude and/or wavefront modulation is achievable provided that an electric field locally controls the LC molecules orientation. An electrodes network generates the local electric field with the detrimental pixelization (and the associated diffraction effects [Cor93, Efr94]). To overcome this impediment, LC-SLM equipped with optical addressing through a photoconducting layer were developped [AHHM82]. The main limitations of LC-SLM's concern their limited phase modulation range (up to $4 \mu\text{m}$), a lower resistance to high fluences than DM, a smaller maximum size and a limited spectral bandwidth. Nevertheless, they offer a quicker answer and a higher spatial resolution (under $100 \mu\text{m}$) with an increased number of addressing points (800×600). The optical valve utilized on the HRR laser system belongs to this LC-SLM family. The wide field of applications of SLMs includes light beam correction/shaping for material processing, microscopic or astronomic observation [Goo05] and more recently for coherent beam combining [LSK⁺10].

4.3.2 The optical valve

The optical valve disposed on the HRR system is composed of a thin parallel nematic LC layer [Goo05] and a photoconducting crystal (Bismuth and Silicium oxyde $\text{B}_{12}\text{SiO}_{20}$ or BSO) surrounded by two transparent (ITO) electrodes. As compared to the electrically addressed LC-SLM, the valve is optically controlled. The addressing beam is adjusted with a interferometric filter at 450 nm to meet the BSO absorption window. According to the addressing beam irradiance, the BSO crystal generates a varying number of carriers thus modulating the local electric field and the

¹see for example <http://www.bostonmicromachines.com/>

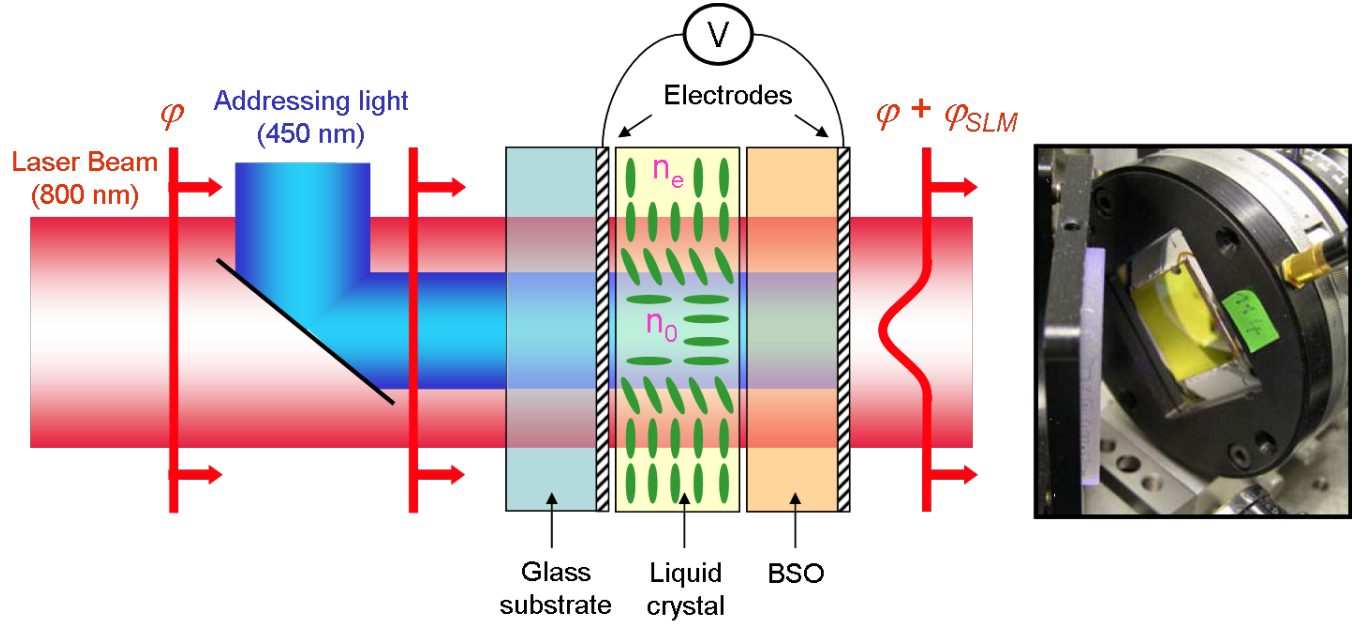


Figure 4.5: LC-SLM employed for spatial beam shaping on the HRR laser system (extracted from [San05]). Left: Principle of working of the optically-addressed optical valve. Right: Photography of the component (yellow).

Table 4.3: Main characteristics of the optical valve employed on the HRR system for spatial beam shaping.

Modulation area size	$10 \times 10 \text{ mm}^2$
Maximum birefringence	$\Delta n = 0.2$ at 800 nm
LC layer thickness	$14 \mu\text{m}$
Phase modulation range	up to 6π at 800 nm
Response time	100 to 500 ms
Spatial resolution	$100 \mu\text{m}$
Measured transmission	80%

LC molecules orientation and consequently the local refractive index (see Fig. 4.5). The main characteristics of the device are summarized in Tab. 4.3 and a detailed description of the component is found in [San05]. Although not pixelized, the optical valve offers a finite spatial resolution of 100 nm due to the circumscribed mobility of consecutive LC molecules. The device is coupled to a Shack-Hartmann wavefront sensor (HASO 32 from Imagine Optics) with the help of a imaging telescope to verify the applied spatial phase modulation.

4.3.3 Designing the wavefront modulation

The proper wavefront modulation obviously depends on the user's scope regarding the beam form at given position. The core of spatial beam shaping lies in the the design of the phase mask that enables user-defined beam shape after known propagation. An overview of the main solutions in the domain is presented hereafter.

Iterative Fourier Transform Algorithm (IFTA)

The most widespread solutions responding to this need take their roots in the Gerchberg-Saxton algorithm or, Iterative Fourier Transform Algorithm (IFTA) [GS72]. This deterministic optimization loop yields the adequate wavefront modulation in a plane P to achieve a desired beam intensity distribution in a farther plane P' . Its principle is briefly summarized hereafter [GS72, LT02]. A light beam characterized in the plane P by its spatial phase $\varphi(x, y)$ and its amplitude $A(x, y)$ propagates to a plane P' where the aimed intensity distribution I_T lies (defining the target amplitude $A_T(x', y')$).

The first iteration of the algorithm simply numerically propagates $A(x, y)$ and $\varphi(x, y)$ to P' to obtain $A'(x', y')$ and $\varphi'(x', y')$ (see Tab. 4.4). Subsequently, the difference between the target and the actual intensity distribution is calculated (e.g the root mean square error or RMS). The inverse propagation is then accomplished with the care taken to replace $A'(x', y')$ by $A_T(x', y')$ yielding $A_1(x, y)$ and $\varphi_1(x, y)$ in P . The actual beam amplitude $A(x, y)$ in P replaces $A_1(x, y)$ and the process reiterates until the algorithms converges to a stable wavefront $\varphi_n(x, y)$ in P producing a small enough RMS error in P' . It is important to note that if the wavefront in P' is obviously affected by the iterations, the loop does not manage its final state, meaning that the spatial phase in the processing plane is not necessary flat. In fact, a strong parabolic component is usually obtained, moving the processing plane out of the focusing plane [HSA07]. In our case, the propagation operation takes into account the passage from the LC-SLM plane to the focal image plane of the focusing objective. Experimentally, the optical valve is imaged onto the entrance pupil of the objective through a demagnifying telescope. Consequently, the propagation from P to P' simply reduces to a Fourier transform (see Eq. 2.18 with $f = d$).

Table 4.4: Basic iteration of the IFTA or Gerchberg-Saxton algorithm [GS72].

Phase modulation plane	Propagation (FT)	Target plane
$A(x, y) \exp \varphi_{(0,n)}(x, y)$	\Rightarrow	$A'(x', y') \exp \varphi'(x', y')$
\uparrow		\downarrow
$A_1(x, y) \exp \varphi_1(x, y)$	\Leftarrow	$A_T(x', y') \exp \varphi'(x', y')$

$$A'(x', y') \exp [\varphi'(x', y')] = \frac{i}{\lambda d} \mathcal{F}_{f_{x'}, f_{y'}} \{A(x, y) \exp [\varphi(x, y)]\} \quad (4.3)$$

This result renders this IFTA implementation relatively straightforward. As often however, the passage from the computer to the real experimental life is cruel. We pointed out that the wavefront in the target plane remains an uncontrolled parameter. If this were not the case, the IFTA would be useless since the beam amplitude and phase definition in one plane is sufficient to define the beam everywhere. However, we look for a phase only solution to approximate the target while keeping sufficient energy. This comment is significant as if the constraint on the spatial amplitude in the processing plane is well respected, there is absolutely no guarantee that the target plane is actually a focusing plane (i.e with a flat wavefront).

In fact, a strong parabolic contribution can accompany IFTA-generated phase masks and implies the presence of hot spots in front or after the target plane. For surface machining, a simple bypass consists in positioning the sample surface in the proper plane [SHA⁺05]. For bulk machining however, they obviously pose a problem which can be overcome with the use of an additional phase modulator and defined 3D field distribution [HSA07].

Other optimization algorithms may be employed to design a phase mask in order to achieve arbitrary beam shapes at the focus of the lens. For example, calculations based on discrete phase levels (e.g π) as widely employed in the design of DOE [Goo05]. However, the resulting spatial phase discontinuities may be at the origin of energy losses and additional undesired diffraction.

Feedback loop

In the light of the preceding discussion, the necessity of a more flexible and reliable optimization guide than the theoretical intensity distribution emerges. While the design of an user-defined irradiance is already a strong step towards an increased processing flexibility, the laser-induced modification topology may not follow the desired irradiance map. Indeed, it has only little chances given the strong nonlinear propagation effects which obviously take place in the energetic conditions required for bulk processing (see for instance the fluence maps deteriorated by nonlinear propagation effects in Chap. 2). Hence, the use of a quantity relying more on the laser action constitutes a step further for guiding the optimization. By directly evaluating the result of the laser

irradiation to orientate the design of the phase mask, the nonlinear propagation effects, interaction specificities, optical distortions and any other known or unknown artifacts are taken into account during the iterative process. This strategy ensures the respect of the user-defined aim despite of any unexpected phenomena within the limits of achievable changes.

Nevertheless, the challenge to be faced when adopting this optimization philosophy is the drastic increase of the space search size and complexness accompanied by the fact that the nature of the possible laser outcomes is most of the time not predictable. This non-deterministic characteristic has direct consequences on the choice of an adapted optimization strategy to drive the optimization procedure. Thus, the need of a powerful searching strategy capable of efficiently exploring a vast domain in a reduced amount of iterations becomes evident. Moreover, the procedure requires a self-improving capability to successfully drive the automated loop towards the desired irradiation outcome. Natural candidates for this challenging problematic are the global optimization algorithms which we briefly review hereafter.

Global optimization algorithms

Global optimization algorithms can also be employed, for example simulated annealing [EBGR05], hill climbing (or simplex) and evolutionary approaches [WBP⁺05]. It is important to note that those strategies are not restricted to spatial shaping but can concern any other problematic (with a particular interest for temporal pulse shaping).

The general principle of this wide class of algorithms is to stochastically investigate a space search with the scope of finding the best or a close-to-the-best solution to a given problem. Their interest dominates when testing all available solutions (brute-force or exhaustive search) becomes inadequate in terms of computing resources. In the frame of spatial phase shaping, the space search comprehends all the possible phase value combinations (or phase masks) on the 2D area covered by the optical valve i.e an array of 256×256 addressing points whose phase value is encoded on 12 bits. The corresponding space search size is $(2^{12})^{65536}$ which manifestly casts away the idea of performing a brute force search. Here, an additional difficulty resides in the fact that small changes on the phase mask to be optimized generate strong alterations on the intensity envelope.

Detailed description of the hill climbing, simulated annealing and evolutionary strategies are respectively presented in [RN09, KGV83, ES03]. We attempt here to quickly give a general feeling of the matter. First, the adequacy of the wavefront modulation with the user-defined scope must be a calculable or measurable quantity describing the merit of the specific irradiation profile and is termed *fitness* throughout this report. For example, in the case of beam shaping, an effective solution is to define the fitness as the inverse of the RMS error between the target intensity and the intensity obtained with the phase mask under evaluation. However, any other experimental parameter can play this evaluation role. For each addressing point of the phase mask, the reachable phase

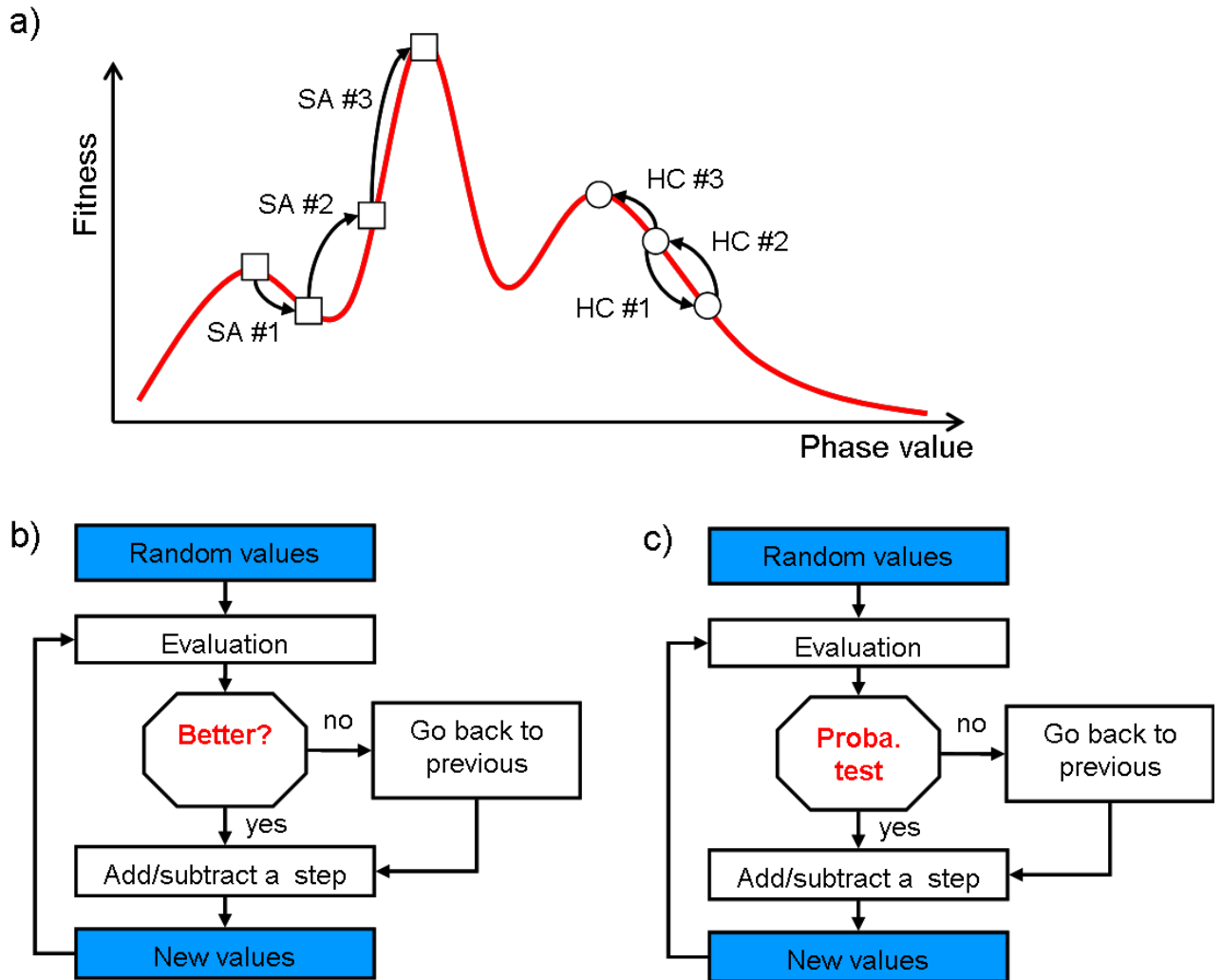


Figure 4.6: Global search optimization illustration. a) Illustration of a the space search associated with an phase addressing point with examples of optimization progress. HC stands for hill climbing and and SA for simulated annealing. HC steps 1 to 3 shows local maximum trapping whereas SA steps 1 to 3 shows global maximum finding. b) Iteration steps of the HC optimization loop. c) Iteration steps of the SA optimization loop.

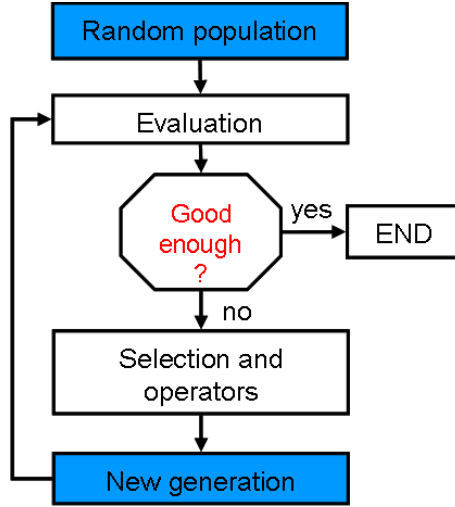


Figure 4.7: Iterative steps of the evolutionary optimization strategy.

values have a positive or negative impact on the fitness drawing a space search curve as illustrated on Fig. 4.6 a) with presumably local optimal (maximal) points and a single global maximum. In order to encounter as quickly as possible the global maximum, the hill climbing philosophy consists in performing successive positive or negative step-variations on the phase addressing points following the iteration scheme on Fig. 4.6 b). When the step induces a better fitness, the new value is kept and a new cycle starts, otherwise the opposite step is taken. If this strategy assures an unceasing increase of the fitness, it potentially remains trapped in local maxima as illustrated on Fig. 4.6 a).

Stochastic Hill Climbing tends to overcome this limit with the addition of a probabilistic test on the decision to follow or not a change. In other words, a change leading to a worse fitness is not necessarily rejected (see Fig. 4.6 c)) with the consequence of possibly bypassing minima to attain more global maxima (illustrated in Fig. 4.6 a)). When the probability to accept a bad choice reduces with the algorithm's iterations, the strategy is referred to as Simulated Annealing; a technique originally inspired by metallurgy annealing where the controlled decrease of temperature (i.e probability) is employed to reduce defects and increase the size of crystals (i.e finding states of lower internal energy).

Evolutionary strategies also mimics a natural phenomena to perform the non-exhaustive exploration of the search space. At first, a population of random phase mask is created and evaluated, each individual (or phase mask) being labeled with a fitness (see Fig. 4.7). The phase mask pixels are assimilated to the genes of the individuals. The elites of this very first generation are then employed to give rise to a new generation through operators called mutation and crossover. Mutations simply add a noise to some randomly chosen genes (i.e pixels) and crossover mixes the gens of two elites to create new individuals. The new generation experiences evaluation and selection as their

parents and the process reiterates. A significant particularity of these optimizations is that they deal with a group of items instead of a single subject, ensuring a efficient exploration of the space search. Evolutionary strategies were very soon employed on ultrafast laser system for temporal shaping with the scope of controlling molecular states [JR92] proven to be effective for a large field of processes based on controlled laser-matter interaction ranging from designing molecular states to photochemical reaction or more recently material processing strategies [MBM⁺08, MMR⁺08] and see Chap.7.

Many other exciting approaches can also be employed (ants colony, tabu search, harmony optimization...). We underline soundly here that such probabilistic optimizations are extremely slow when compared to IFTA and never guarantee the finding of the best solution. However, they offer a much wider frame of application since the evaluating parameter can not only be the laser intensity distribution [EBGR05] but any measurable physical parameter such as surface modification aspect [CTE⁺07], bulk modification aspect [MMH⁺08] or ions yield from surface ablation [SMB⁺05].

The riveting work of Booth *et al.* has to be mentioned here. Especially dedicated to the field of microscopy, aberration correction was demonstrated without the use of a wavefront sensor. The principle relies on an exhaustive search on the orthogonal basis formed by the Zernike polynomials [Boo06] with very quick convergence to achieve wavefront cleaning. Very recently, this work was successfully extended to fused silica aberration-free bulk processing with the plasma emission as the feedback parameter [JMWB10].

Ready-to-use phase masks

In many situations, the design of the spatial phase masks with the help of more or less complex algorithms is not indispensable. Straightforward examples are naturally the correction of measured or calculated aberrations. Most of the time, the user-defined processing scope can be reached only under particular conditions influencing the physics of the interaction. For example, waveguide writing regimes may require sufficient energy confinement that may be lost under propagation artifacts linked with aberrations (see Chap. 7. In the case of transverse waveguide writing, these distortions may lead to a loss of symmetry towards unwanted ellipticity of the processing spot and thus on the photowritten waveguide. An sound illustration of the interest of ready-to-use phase mask is found in the recently demonstrated response to these propagation impediments. More precisely, it was shown that a particular aberration (astigmatism) can be purposely imprinted on the beam wavefront to enable the transverse writing of waveguides with improved cylindrical symmetry [TBR⁺08, dICFG⁺09].

The quickly growing field of non-diffractive laser beams for laser processing [CLJ⁺09] and optical manipulation [CKT⁺08] and has to be mentioned here. The adjective 'non-diffractive' stands for a non-physical solution to the wave equation which has the particularity to show no

diffraction upon propagation. A well-known example of these kind of beams has its central part surrounded by oscillating rings in the form of a Bessel function. These so-called Bessel beams can be experimentally approached with simple circular truncation on a Gaussian beam or the use of a dedicated phase modulation element called an axicon. The main effect is a strong increase of the longitudinal extent where the beam radius remains constant as compared to the Gaussian case (see experimental images in [CLJ⁺09]) while the transverse spot size slightly increases. Indeed, this elongation is observable on Fig. 2.4 a) and b) dealing with the effect of beam truncation. The interest of a longer Rayleigh length lies in the possibility to photoinscribe long structures without sample displacement. Another thriving kind of non-diffractive radiations is the class of Airy beams characterized by a transverse acceleration property translating in a 'curved' intrinsic propagation [SBDC07]. To obtain this fascinating light behavior, a cubic phase modulation has to be applied with either a SLM [SC07], a continuous transparent phase mask [PKM⁺09] or a binary phase mask [DSLL09]. Applications of this beam were shown in optical manipulation [BHS⁺09] and curved plasma generation [PKM⁺09].

Another very significant instance is found in the vast field of optical tweezers. Without entering into details, optical tweezing permits the trapping of a micrometer-size sphere or micro-organism in a laser field in a fluid using light gradient forces [NB04]. For a single sphere or cell to be trapped and displaced, the single laser spot at the focus of an objective can be moved using parabolic and tilted wavefront modulations (for movements along the laser propagation axis and in the plane perpendicular to this axis respectively). When dealing with numerous particles, these phase masks can be associated with phase grating modulations thus generating multiple laser spots readily in the focal area of the objective [PRG05]. In the same order of ideas, phase masks based on multiplexed Fresnel lenses have recently permitted femtosecond laser processing with multiple spots [HHN06]. We also demonstrated dynamic multispot femtosecond bulk waveguide writing with the help of a grating-type phase masks (see Chap. 7 and [MCH⁺09]).

4.4 Experimental details

4.4.1 Generalities

The HRR laser system is particularly suitable for the photowriting of guiding structures. The set up around it was thought to render quite easy their characterization. The focusing objective not only focuses the femtosecond laser but also permits white light illumination and HeNe laser injection for straightforward characterization of longitudinal photowritten guide(see Fig. 4.8). The set up is also equipped with a home-made cross-correlator (not shown on Fig. 4.8). The reference pulse is obtained by deriving a fraction of the oscillator beam before spectral phase modulation, delayed

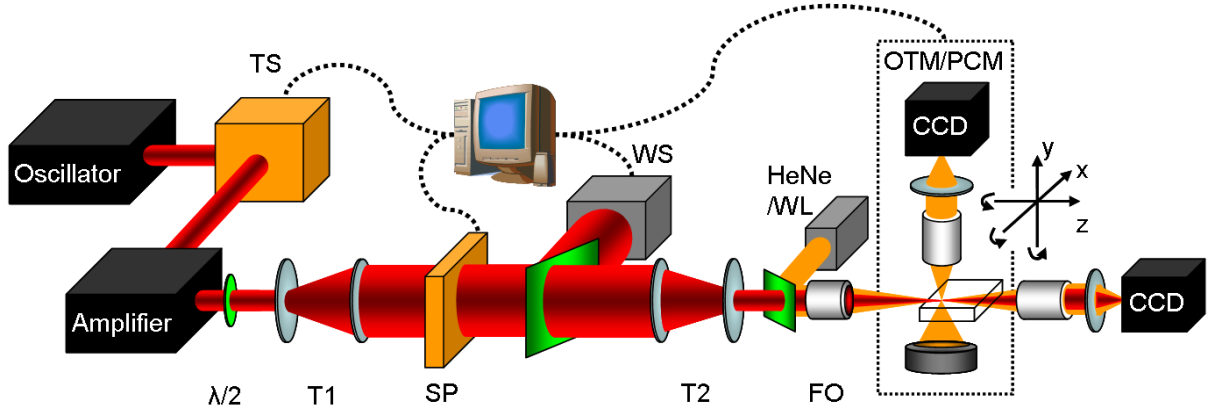


Figure 4.8: Scheme of the experimental set up associated with the HRR laser system. TS: temporal shaper as presented in Sec. 4.2. WS: wavefront sensor. HeNe-WL: Helium Neon laser source (emitting at 633 nm) and white light source for waveguide characterization. OTM-PCM: Optical transmission and phase contrast microscopy for sample modification investigation. T1: Telescope enlarging the femtosecond laser beam before the LC-SLM. SP: Spatial shaping unit composed of an optically addressed 2D LC-SLM. T2: Demagnifying telescope imaging the LC-SLM plane on the focusing objective (FO) entrance pupil. The setup enables spatio-temporal optimization of the femtosecond laser pulses according to a desired bulk modification.

by approximately 0.5 ns and amplified. The reference pulse is thus amplified on the same trail as the main pulse while remaining as short as the standard output of the laser system.

The LRR laser system is a bit more complex (see Fig. 4.9). Several mirrors and other optical components were omitted for clarity. Since the temporal beam shaping unit is positioned after amplification, the beam is divided into a reference beam avoiding temporal shaping and a pump beam. A home made cross-correlator permits enables measurements of the temporal pump pulse shape. The reference beam is frequency doubled and conducted to the observation microscope to achieve pump-probe side-imaging of the laser-matter interaction area. The time overlapping for cross-correlations and pump-probe experiments is managed with the help of dedicated delay lines.

4.4.2 Observation microscope

Most of the experimental pictures presented in this report were obtained with the help of a microscope Olympus BX41 utilized in transmission for both laser systems. Classic optical transmission and positive phase contrast mode were mainly employed to investigate the sample permanent and transient modifications. For the latter, the illumination light source was replaced by the femtosecond probe completed with diffusers to wash out speckle artifacts. On the HRR, a Sony CCD camera XCLU1000 enables the image acquisition with a CCD array of 1600×1200 pixels whose size are $4.4 \times 4.4 \mu\text{m}$. On the LRR laser system a more sophisticated camera from Andor (iXon^{EM} + 885

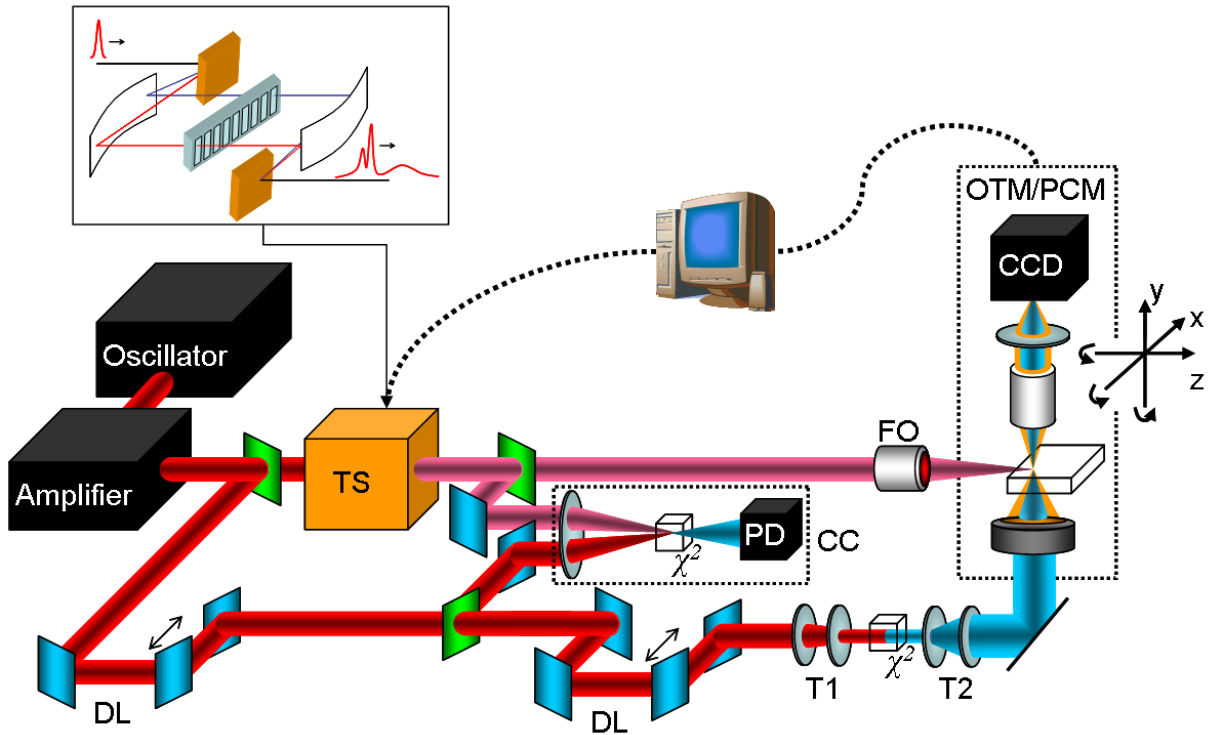


Figure 4.9: Illustration of the experimental set up associated with the LRR laser system. TS: temporal shaper illustrated in the top inset and presented in Sec. 4.2. FO: focusing objective. OTM-PCM: Optical transmission and phase contrast microscopy for sample modification investigation. χ^2 : Frequency doubling crystal. PD: Photodiode. CC: Cross-correlation apparatus. DL: delay line. T1: Telescope reducing the femtosecond laser beam size before second frequency doubling crystal. T2: Telescope magnifying the beam before entering the microscope illumination path. The setup permits temporal pulse optimization of laser induced bulk modification and time-resolved side picturing of the focal volume area upon temporally shaped femtosecond irradiations.

EMCCD, 1004×1002 and pixel size $8 \times 8 \mu\text{m}$) with an image intensifier especially dedicated time-resolved picturing in low illumination conditions. Both systems are utilized with LabView.

4.4.3 Beam characterization instruments

To insure the femtosecond laser beam quality, a beam profiler (LBA-USB, Spiricon) is regularly employed at various positions on the optical path. That way, accidental beam clipping and other artifacts are detected and taken care of. The spectrum of the femtosecond irradiation is checked with a fiber spectrometer from Ocean Optic and the pulse duration is evaluated with the help of the home made cross-correlators. We also intensively use a portable autocorrelator (PulseCheck from APE) in diverse points of the laser path even after the focusing objective to vouch the short pulse duration.

4.4.4 Beam delivery

For both laser systems, we use an electro-mechanical shutter commercialized by Uniblitz (LS6). The shutter allows simple pulse picking on the LRR system via a synchronized connection to the output of the Pockels cell. The signal corresponding to the delivery of a pulse N is electronically delayed in order to synchronize the shutter aperture with the arrival of the pulse $N + 1$ double-checked with the help of a fast photodiode. On the LRR, the shutter permits the delivery of burst of pulses whose size depend on the shutter opening time easily controlled with LabView.

The femtosecond laser pulses are focused with the help of a super long working distance (17 mm) microscope objective (Nikon SLWD 50 \times). Its numerical aperture (NA) is 0.45 and working distance equals 17 mm. That way sufficient room is left for the observation objective from the phase contrast microscope. The choice of the numerical aperture corresponds to a trade off between the need of large working distance while achieving sufficient light concentration with limited elongation of the focal volume along the propagation axis (as in the case of lower NA).

4.4.5 Samples and sample displacement

The glass samples employed in this work are parallelepipeds of $3 \times 20 \times 10$ mm polished on all faces of greater area. The main materials studied here are pure amorphous silica (a-SiO₂) and N-BK7. The employed fused silica is a wet silica glass (Corning 7980-5F). BK7 is a borosilicate crown glass manufactured by Schott, widely used as technical optical glass for applications in the visible region. The chemical composition of BK7 as specified by Schott is the following: silica(70 – 80), boron oxide(10 – 20), sodium oxide (1 – 10), potassium oxide(1 – 10), barium oxide(1 – 10), titanium oxide, calcium oxide and antimony trioxide in small quantities (≤ 1) in

percentage by weight. Samples are fixed on a homemade sample holder allowing side-imaging of the irradiation area and mounted on two motorized translation stages (Physik Instrumente model M-126.DG) in the horizontal plane while the vertical positioning is ensured by a manual translation stage. The motorized stages are connected to a PC and are compatible with LabView. They allow a positioning of the sample with a precision on the order of 100 nm.

Chapter 5

Static observations of permanent modifications

The aim of this chapter is to present some laser induced permanent bulk modifications which have a particular interest for photonic application. Having in mind that the local refractive index change is of prime interest for waveguiding applications, we firstly review several local refractive index characterization techniques completing optical transmission microscopy. We conducted a detailed comparison of the experimentally available methods (phase contrast microscopy, Mach Zender Microscopy and quantitative phase contrast microscopy) on a well-defined femtosecond permanent modification in borosilicate crown (BK7) glass. For this trace, the two-dimensional mapping of the local refractive index modulation is formed with each of the available techniques which are thus compared. Considering the symmetry of the laser-induced modification, the interest of the Abel inversion for refractive index measurement is discussed in that frame. Various processing windows are verified corresponding to low energy soft index changes or more energetic domains. We unveil a new photoinscription regime in high energetic conditions in fused silica and BK7 where thermo-mechanical paths of material transformation prevail. We show that the specific topology of the corresponding irradiation outcome can unambiguously be explained by considering the laser linear propagation in the focal area and we illustrate the interest of this regime for simultaneous photowriting of multiple structures. We also report for the first time on the formation of purely spherical voids under single pulse irradiation in borosilicate D263 glass in tight focusing conditions. Finally, a study of pulse accumulation in fused silica is conducted with an emphasis on the presence of laser-induced nano-arrangements and the associated birefringence. Taking advantage of this effect, we demonstrate the possibility to induce polarization-sensitive waveguides.

5.1 Characterization techniques overview

A brief account for the main refractive index detection methods is given in the following with the distinction of microscopy-based techniques and indirect techniques.

5.1.1 Microscopy-based methods

Having in mind the age of optical microscopy¹, it is quite impressive to note that the method remains most of the time the preferred tool for observation of minute absorptive features. With a resolution possibly in the order of the illumination wavelength and a possibly large field of view [PBW05], the method is non-destructive, allows for surface and bulk investigations, does not require post-calculations and present an unequaled acquisition rapidity only limited by the electronic detection devices. However, when confronted to the observation of bulk laser-induced objects, the technique reaches an intrinsic limitation in the sense that such objects usually present hardly detectable absorption properties. On the other hand, they are most of the time accompanied by local optical index variations. The problematic was first met in biology where the need for observation of quasi-transparent objects (e.g epithelial cells) triggered research efforts to reveal optical path variations and dedicated microscopy techniques emerged since the first half of the 20th century. Here, we briefly review some of these techniques, i.e phase contrast microscopy, differential interference contrast microscopy, Mach Zender microscopy and more recent, quantitative phase microscopy.

Phase Contrast Microscopy (PCM)

The phase microscopy technique was first proposed in 1934 by Zernike [Zer34]. If detailed descriptions are readily available in literature and in abundance on the Internet ², we introduce here its main principles in order to enlighten the major advantages and limitations. Fig. 5.1 illustrates the following explanation. The technique relies on a classic microscope with Koehler illumination. A annulus aperture is placed in front of the condenser and is optically conjugated with a phase plate of the same geometry positioned after the objective (in nowadays systems, the phase annulus is build within the objective). Consequently and in the absence of sample, all the light gets through the phase annulus only, and is referred to as the background light (B) (see Fig. 5.1). With the presence of a phase object of small refractive index variations, the wave passing through the phase object (termed 'O') knows a slight optical retardation. This wave can be decomposed into the sum of a wave emerging from the background with a diffracted wave, referred to as (D) which is optically delayed by a quantity of approximately $\frac{\pi}{2}$ (easily verifiable when subtracting

¹Usually attributed to the lens grinders Hans and Zacharias Janssen in the 1590s

²see for instance <http://www.microscopyu.com/>

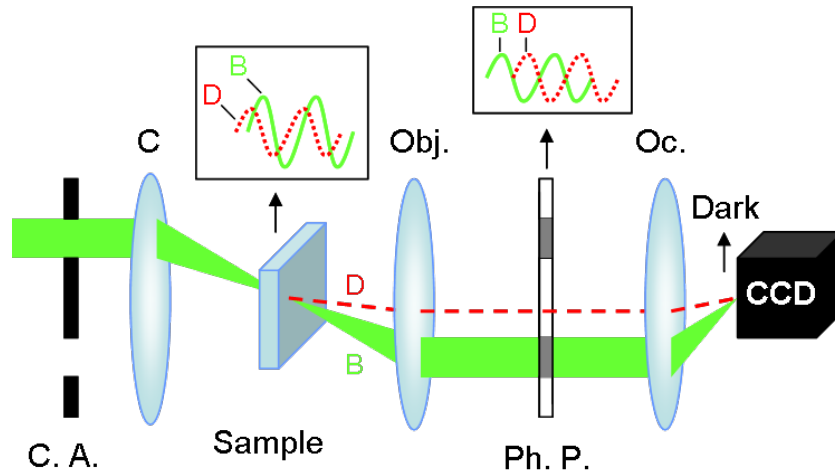


Figure 5.1: Schematic representation of the light trains in phase contrast microscopy. C. A.:circular annulus, C: condenser, D: diffracted wave, B: background or non-diffracted wave, Obj.: microscope objective, Ph. P.: circular phase plate, Oc.: ocular. The sample is supposed to be a phase only object. The circular annulus is optically conjugated with the phase plate implying that all non-diffracted rays traverse the circular phase plate with an associated artificial retardation. The delay is tuned to achieve constructive (resp. destructive) interferences with the diffracted waves thus yielding bright (resp. dark) zones in the image.

B to O). By appropriately setting the artificial retardation of the background light, constructive or destructive interferences between B and D are achievable, translating the optical index variations into intensity modulation. PCM is termed positive (resp. negative) when the phase plate delay is adjusted to produce darker (resp. bright) regions for the higher (resp. lower) refractive index zones of the sample. The positive technique used here throughout all the text offers a instantaneous qualitative mapping of the local refractive index with a resolution close to the limit of diffraction of the microscope.

Differential Interference or Nomarski Microscopy (DIC)

The technique was first proposed by Georges Nomarski in the mid-1950s as a contrast enhancing technique. The birefringent properties of uniaxial crystals are employed to translate phase retardations in constructive or destructive interferences. Fig. 5.2 presents the optical elements of interest that complete classic transmission microscopy to form the Nomarski apparatus. The incoming light is linearly polarized and enters the first Wollaston-Nomarski bi-prism. This birefringent optical component divides each linearly polarized incoming ray into two orthogonally polarized quasi-parallel rays (1) and (2) with well-defined relative retardation. If the two rays encounter identical optical index in the sample, they are recombined by second identical Wollaston bi-prism to generate the original linear polarization state following the back-propagating light

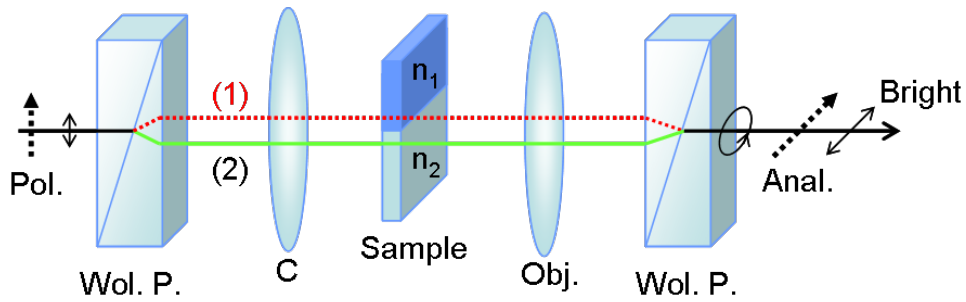


Figure 5.2: Illustration of the principle of differential contrast microscopy. Pol.: polarizer, Wol. P.: Wollaston Prism, C: condenser, Obj.: microscope objective, Anal.: analyzer. The sample is supposed to be a phase only object with two regions of different refractive index ($n_1 > n_2$). The pair of Wollaston bi-prisms allows for transformation of the optical index gradient into intensity variations thanks to their birefringent properties. The technique is sensitive to refractive index gradients only. More details are provided in the text.

principle. The analyzer is turned to extinct the corresponding polarization state. Consequently, all the regions of uniform refractive index appear dark in the image. However, if the rays (1) and (2) meet different optical index in the sample, the additional variation in their respective retardation does not allow for recombination to the original linearly polarization state by the second prism. Instead, an elliptical polarization is obtained. Since the analyzer cannot extinct this polarization state, the outgoing ray reveals the refractive index gradient only. A detailed comparison of DIC with PCM is available on the Internet³. Due to the restricted illumination pupil, a halo shows up around objects visualized in PCM which can be diminished by apodization techniques. However, PCM exhibits a higher sensitivity compared to DIC, which reveals refractive index gradients only, making difficult the relative discrimination of regions of different index. Furthermore, phase contrast microscopes do not comprehend thick optical elements, contrary to DIC whose biprisms pair potentially lead to dispersion; unadapted for time-resolved imaging on ultrafast scales (see Ch.6).

As a general comment on the two preceding methods, we point out that the absorption properties of the investigated area always accompany the contrast of the PCM or DIC images. Methods for canceling the absorption contribution were developed requiring additional calculation steps [NK92].

Mach Zender or interferometric Microscopy (MZM)

The two above-mentioned microscopy methods have known a wide interest particularly for biological imaging since they drastically ease the detection of phase-only or quasi-phase-only objects. However, both methods fail in providing a quantitative measurement of the local refractive index

³<http://micro.magnet.fsu.edu/primer/techniques/dic/dicphasecomparison.html>

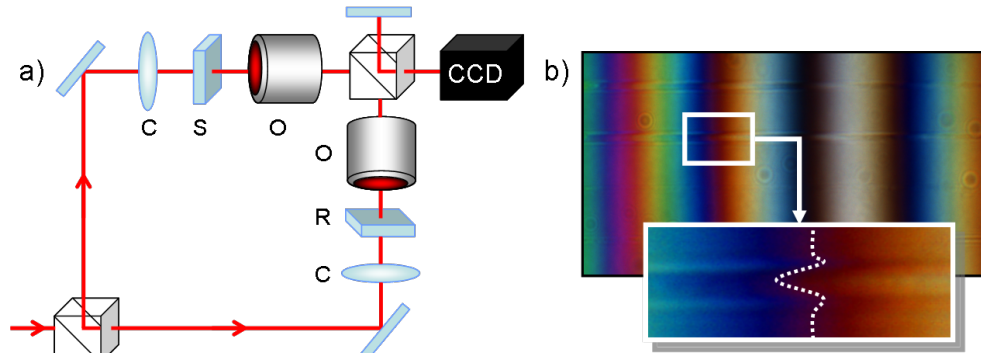


Figure 5.3: Mach Zender Microscopy principle. C: condenser, O: microscope objective, S: sample with phase object, R: reference sample. a) Illustration of the light pathway in the interferometric set up. The Mach Zender configuration splits the source light into two arms (object and reference arm) whose only difference relies in the phase object to be analyzed. The fringes distortions in the image formed by the recombined beam are directly related to the refractive index modulation to be measured. b) MZM image of two bulk photowritten waveguides in BK7 glass. The deviation of the fringes is clearly observable in the core of the waveguide.

[BBN02]. It has to be noticed that this feature is most of the time dispensable in biological or medical micro-imaging where the detection of given objects (cells, tissues...) is usually the main scope. Nevertheless, in the case of physical characterization of laser-induced phase objects, the quantitative measurement of the local optical index is highly desirable because of its direct impact on the possibility to photowrite guiding elements in the bulk. One of the first interferometric microscope was proposed in 1950 [Dys50]. If the principle is quite straightforward, it is certainly one of the most powerful method for quantitative phase object imaging. Each of the two arms of the Mach Zender interferometer comprehends a microscopic imaging system with the investigated sample in the object arm and an identical virgin sample in the reference arm to ensure overlapping of the coherent wavefields after recombination (see Fig.5.3a)). The fringes are captured in the image plane and their distortions are proportional to the refractive index modulation (see an example of a photowritten waveguide in Fig.5.3b) ⁴). Various declinations based on interferometric measurements have raised employing for example the confocal configuration and a Michelson-type interferometer [KNKL08], optical diffraction tomographic systems [KKK09] and a liquid cell shearing interferometer [EGA02].

The method of phase-shifting microscopy belongs as well to the family of interferometric microscopy. Again, interferences are formed in the image plane with the insertion of a biprism in front of the image plane to form an interference pattern [ECK⁺02]. In the same order of ideas, the technique of digital holography microscopy (DHM) relies on numerically analyzing the interfer-

⁴obtained at the ILT-Fraunhofer

ence pattern from the overlapping reference and object beams without the restriction of capturing the information in the image plane [CBD99, RCD⁺08]. The procedure requires two successive acquisitions of the hologram with and without the phase object to be analyzed and was successfully employed to precisely characterize photowritten waveguides [OCM⁺05]. The technique of Fourier phase microscopy (FPM) [PDV⁺04] combines the principles of PCM and phase-shifting interferometry where a spatial light modulator assures the phase shift, however the measurement is carried point by point. An advanced technique combining FPM with single 2D interferogram recording was recently demonstrated [PIDF06]. For all these methods, the quantitative information of the optical index change is at the expense of additional numerical treatment and/or picture acquisition leading to a higher measurement time demand. As the need of a rapid mean is decisive for the optimization loops and the time resolved studies employed in this work, our choice remained on PCM. However, considering the increasing calculation speed offered by modern desk computers, the perspective of turning to a quantitative phase detection technique is now envisaged.

Quantitative phase contrast microscopy (QPM)

The principle relies on the fact that a refractive index variation has measurable consequences on the light propagation which is described by the intensity transport equation. Following that idea, quantitative phase contrast microscopy is based on a post analysis of an ensemble of three optical transmission images of the region of interest [BNPR98]. While one picture corresponds to the in-focus imaging, the two others are taken below and above the focusing plane at a distance equaling the microscope objective depth of field. As a quite imposing numerical step, the intensity transport equation is solved to determine the medium refractive index mapping corresponding to the measured planes. It was demonstrated that the measurement could be performed without sample displacement provided the simultaneous use of three cameras [HMG⁺08]. If the post analysis software is commercially available ⁵, the method was found to generate unexpected results and requires calibration with a well-defined phase object (see next section).

5.1.2 Indirect techniques

A plethora of various methods for retrieving the refractive index value of embedded laser-induced structures were exploited since the birth of femtosecond waveguide writing [DMSH96]. As an exhaustive review of the question would surpass the scope of the current discussion, we intend to give a broad view on the main available solutions. Therefore, we review here the techniques of numerical aperture determination, near field profile analysis, Lloyd's mirage and refracted near field profilometry.

⁵<http://www.iatia.com.au/products/lifeSciences/quantitative.asp>

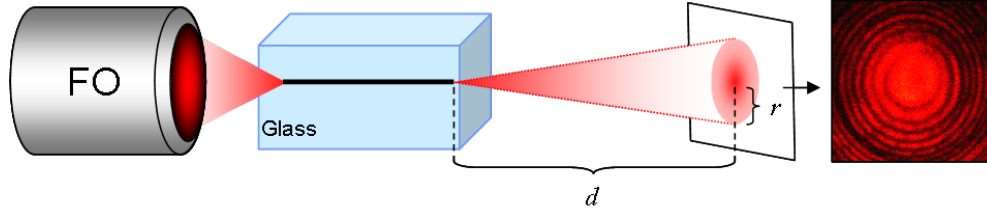


Figure 5.4: Principle of local refractive index increase of a bulk photowritten waveguide from the measurement of its numerical aperture $NA = \sin \left[\arctan \left(\frac{r}{d} \right) \right]$. FO: focusing objective. The inset shows a typical far field pattern of a longitudinal photowritten waveguide in fused silica glass.

Numerical aperture determination (NAD)

This widespread technique concerns the characterization of waveguides and consists of injecting the structure with a monochromatic radiation and measuring the numerical aperture (NA) associated with the far field of the outcoming beam (see Fig.5.4). The method assumes a step index profile whose amplitude Δn given by:

$$\Delta n \approx \frac{NA^2}{2n} \quad (5.1)$$

n being the refractive index of the surrounding medium. The technique offers a reliable estimate of the local refractive index provided that the NA is correctly measured. If this last remark seems obvious, experimentally the question is not trivial as the far field distribution is rarely a uniform disk. On the contrary, a set of concentric circles are usually present when injecting a bulk written guide (see inset of Fig.5.4). Their origin is attributed to interferences between the guide outcoming light and uncoupled radiation [HWG⁺99] or to the overlap of higher orders guiding modes [MQI⁺97]. However, the second proposition seems incorrect as those fringes are also present in monomode guides [San05]. Evidently, these circles complicate the determination of r as the question of where the far field extremity is situated is difficult [Mer07]. However, the problematic of refractive index determination from far field distribution has already been thoroughly addressed in the field of optical fibers [AP83]. Basing ourselves on these results, the radius corresponds to the $\frac{1}{e^2}$ intensity drop of a careful Gaussian fit to the far field distribution. Therefore, this robust and reliable method was intensively employed for the present work. The focusing method [Mar79] relies on a somewhat similar principle. Here, the core of the guide is illuminated transversally by a parallel beam and his lens-like action is analyzed from the outcoming power distribution, requiring additional numerical steps. We also mention here the technique employed by Sudrie *et al.* in [SFPM01] which consists in photowriting a set of 100 structures forming a diffraction grating working in transmission. The analysis of the diffraction pattern yields the averaged refractive index.

Near field profile analysis (NFPA)

Capturing the fundamental mode near field intensity distribution, the refractive index profile of an embedded waveguide can be reconstructed from the Helmholtz equation in the TE mode associated with the Poynting theorem [MB83]. Improvements of the technique involve taking into account the microscope objective transfer function and desensitization of the calculations to price of additional assumptions on the refractive index profile [YNC96]. The calculation costs and the sensitivity of the method to noise from the experimentally measured near field profiles made us prefer the NAD method.

Lloyd's mirage (LM)

Again dedicated to the characterization of guiding structures, the technique is based on a generalization of the experiment of Lloyds mirror. An interference pattern formed by a point source and its mirage induced by the investigated structure. The pattern is analyzed to retrieve the refractive index modulation with diffraction limited resolution [AKNO94].

Refracted near field profilometry (RNF)

The RNF has been developed to measure the refractive index profile in standard telecom fibers but can also be applied to embedded waveguides. A tightly focused beam producing a small enough focal spot is injected into the guide. The refracted rays quitting the guiding region are collected by an annular detector as the spot transversally scans the guide. The measured intensity is proportional to the difference between the guide core index and the surrounding index [CDG⁺96]. The method provides a diffraction limited resolution and is non-invasive.

Table. 5.1 summarizes the main advantages and drawbacks of the above-mentioned methods. Considering the need of a non destructive method capable of providing a reliable refractive index map at a pace allowing for optimization and dynmai picturing, our choice naturally retained PCM and DIC with a preference to PCM for the reasons mentioned in its dedicated paragraph. However, other techniques were employed for better characterization and comparison with PCM. In the next section, we hence report on refractive index picturing of a well-defined laser-induced modification employing OTM, PCM, QPM, MZM and NA measurement.

5.2 Analysis of permanent laser-induced traces in glass

Taking advantages of efficient characterization techniques, we aim at presenting the variety of ultrashort irradiation outcomes finely depending on the photoinscription conditions and the material properties. We first describe 'strong' and 'soft' photoinscription regimes in fused silica and BK7.

Table 5.1: Main refractive index evaluation techniques. PCM: Phase contrast microscopy, DIC: Differential interference microscopy, MZM: Mach Zender microscopy, QPM: Quantitative phase microscopy, NAD: Numerical aperture determination, NFPA: Near field profile analysis, LM: Lloyd’s mirage, RNF: Refracted near field profilometry.

Technique	Δn estimation	resolution	post-analysis	speed
PCM	qual.	diff. limit	no	instant.
DIC	qual. (gradient)	diff. limit	no	instant.
MZM	quant.	diff. limit	little	quick
QPM	quant.	diff. limit	significant	slow
NAD	quant.	area average	little	quick
NFPA	quant.	diff. limit	significant	slow
LM	quant.	diff. limit	little	quick
RNF	quant.	diff. limit	little	slow

Then, after characterizing an efficient waveguide writing regime in BK7, we consider high energy irradiations outcomes in various glasses and explains their unusual topology with propagation calculations from the model presented in Chap. 2. Then, the flexibility offered by tight focusing is underlined in another borosilicate glass. Finally, the accumulation of numerous pulses in fused silica glass is investigated. The associated appearance of self-organized nanostructures is exploited to draw polarization-sensitive waveguides in fused silica.

5.2.1 Main regimes of photoinscription

As a function of the irradiation regime, different photoinscription regimes can be identified based on the corresponding structural morphologies in fused silica and BK7 glasses. The choice of fused silica as a model material is motivated by its well-known physical properties, its predisposition for femtosecond waveguide writing and the long-lasting scientific effort regarding the femtosecond interaction in this glass for both fundamental and applicative perspectives. To a certain extent, BK7 glass plays the testing role of optimization procedure presented in the last chapter. While being a good candidate for integrated optics applications, its ‘natural’ reluctance to refractive index increase under ultrashort irradiation [BSC⁺05] is the opportunity to demonstrate the robustness of the self-improving loops in triggering user-defined bulk modifications (see Chap. 7).

Fig. 5.5 presents static and dynamic irradiations in both glasses with nominal NA= 0.45 (a), b), d)) and NA= 0.42 (c)). NA_{eff} is respectively 0.42 and 0.31. While a more detailed comparison between the two glasses is available in [Mer07], we briefly emphasize the key points useful for the rest of this report. On Fig. 5.5 a) b), the alteration of regions of positive and negative index tends

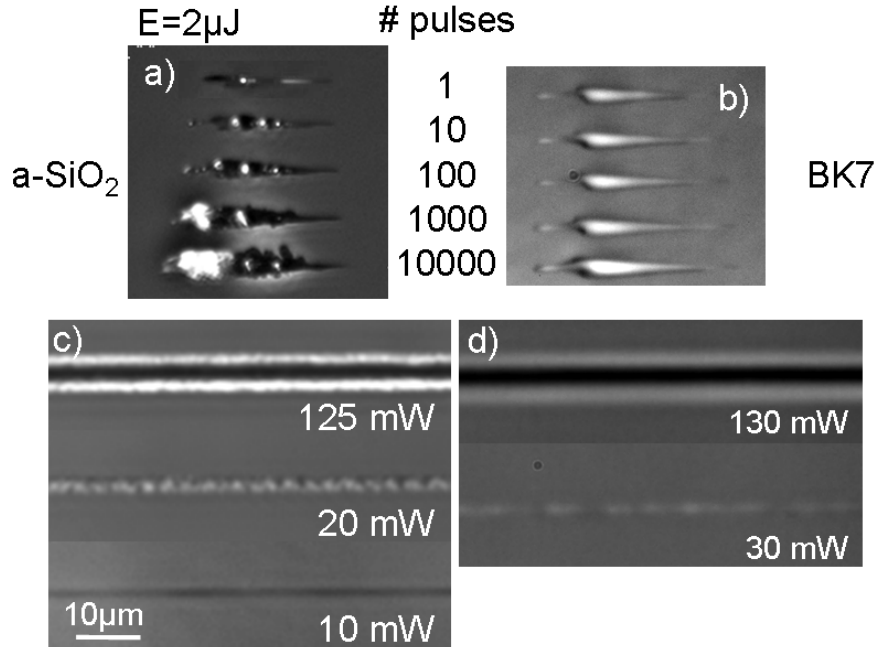


Figure 5.5: Photoinscription regime overview in fused silica (left) and BK7 (right) in PCM for 150 fs pulses. a) and b) Effect of the accumulation of pulses at 166 Hz in static conditions. c) and d) Structures obtained upon longitudinal sample scanning at 50 $\mu\text{m/s}$ and 100 kHz repetition rate.

to confirm the onset of thermomechanical effects. At this moderate energy and taking into account the relatively low softening point of BK7 (560°C), its response appears to be dominated by thermal expansion resulting in the onset of a low density material. While the number of accumulated pulses does not seem to influence the permanent change, the repetition rate is the critical parameter, suggesting that thermal effects play a dominant role [Mer07].

Regarding fused silica, the permanent traces indicate a refractive index modulation which is generated by an axial variation of excitation in terms of plasma density and temperature. This modulation derives from a dynamic filamentation balance between dispersion, nonlinear focusing, and ionization. This results in a longitudinally-varying refractive index structure along the propagation axis, with a central positive (dark) index change bordered by white regions of decreased density (see Fig. 5.5 a)). The white domains were previously identified with regions of maximum energy deposition,[BBS⁺07, SJM04] where material is likely to suffer expansion. The black, positive index region involves a complex mixture of thermomechanical phenomena and defect generation. A noticeable difference between BK7 and a-SiO₂ is their response to a multipulse irradiation sequence. Incubation effects clearly appear in a-SiO₂ contrary to BK7.

Turning to longitudinally photowritten structures in Fig. 5.5 c) d), one can note for the both glasses that the photoinscription character varies from an incubative type at low intensities, relying on electronic effects, to the onset of thermo-mechanical effects at moderate and higher incident

powers. In borosilicate BK7, most observable features are rarefaction and compaction effects. From a broad point of view, the photoinscription regimes are related to the amount of energy deposition and can be divided in two categories.

First, a strong *thermo-mechanical regime* associated with a high index contrast via repeated expansion or compaction cycles [SB02, CHRK01] appears in energetic irradiation conditions (> 20 mW) in fused silica and BK7. Second, a *smoother regime* capable of triggering soft electronic alterations produced by under-dense plasmas and weak index changes can be observed at low irradiation doses in fused silica at the bottom of Fig. 5.5 c). Quite interestingly, this low energetic regime is slightly below the single pulse energy threshold for detectable changes under PCM. Moreover the corresponding permanent modification shows a smooth black only area (i.e refractive index increase) and appears only in the case of pulse accumulation emphasizing the concept of smooth and gradual change. Recent experimental results in BK7 (not shown) indicate the existence of this regime in this glass as well [Sol09].

5.2.2 Full characterization of BK7 glass irradiations

In this section, a efficient waveguide writing regime in BK7 is identified and physical insights are discussed. The corresponding laser-induced structures are pictured employing the main microscopy techniques described in the previous paragraph. A quantitative mapping of the refractive index is thus provided, putting in light the advantages and the shortcomings of the techniques in the frame of laser induced traces characterization.

Picturing of the structures

Employing the HRR laser system (see Chap. 4), BK7 glass samples were irradiated with 10^5 pulses (100 kHz) at a processing depth of $200\text{ }\mu\text{m}$ with $\text{NA} = 0.45$ in conditions of negligible wave front distortions [HTS⁺05]. For sufficient energy per pulses ($> 1\text{ }\mu\text{J}$), a well-identified relatively strong regime of photoinscription mostly governed by thermomechanical mechanisms is obtained and was discussed above. Fig. 5.6 presents the irradiation outcome for static a) and scanning b) conditions observed with optical transmission microscopy (OTM), PCM, DIC, MZM and QPM ⁶.

The contrast of the OTM photography has been enhanced as the structure is hardly detectable in this configuration. We recall here that the contrast in OTM is not necessary linked to absorptive features. The presence of optical path variations in the sample can deviate the illumination rays upon refraction, leading to contrast in the OTM image corresponding to the zones of refractive index gradients. Naturally this contribution to the contrast remains poor in comparison to the contrast

⁶The MZM and QPM images were obtained at the ILT Fraunhofer with the kind help of Dr. I. Mingareev, Dr. D. Wortmann, Dr. J. Gottmann and Dr. D. Mahlmann.

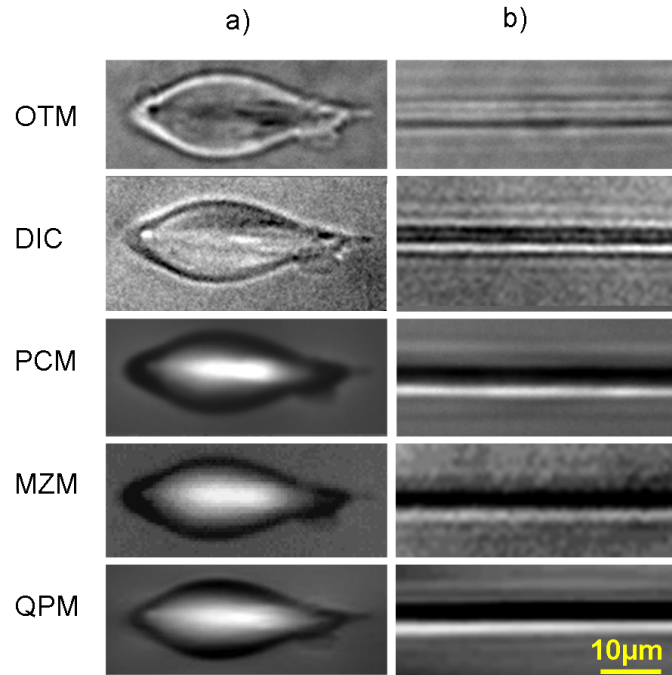


Figure 5.6: Femtosecond irradiation outcome in BK7 glass (10^5 pulses (100 kHz) at $200 \mu\text{m}$ deep with $\text{NA} = 0.45$ and $\text{NA}_{\text{eff}} = 0.41$. The laser comes from the left. a) Static irradiation b) Scanning at $1 \mu\text{m/s}$ along the laser propagation axis; the spot moving towards the laser source. The same structure is pictured using various microscopy techniques: OTM: Optical transmission microscopy, PCM: Phase contrast microscopy, DIC: Differential interference microscopy, MZM: Mach Zender microscopy, QPM: Quantitative phase microscopy.

from absorptive features⁷. DIC being sensitive to optical index gradients, we remark that refractive index variations are well transcribed, however, refractive index comparison between homogeneous regions (e.g between the interior and the surrounding of the trace) is not straightforward. For ease of comparison, the gray scale of the PCM, MZM and QPM images are identical with the white zones denoting negative index variations and the black zones an increase of the optical index. As evident when comparing PCM, MZM and QPM pictures, the topology of the modification is similarly reported from a qualitative point of view for both static and scanning irradiation. The static photography reveals a central core of lower refractive index (in white with PCM MZM and QPM) surrounded by a darker shell associated with a higher optical index. This particular distribution is discussed in the following.

Laser excitation in BK7

Here, we qualitatively estimate some of the consequences of the nonlinear propagation to better support the experimental observations of the laser-induced modification in fig.5.6.

At 800 nm, three photon absorption in BK7 (energy gap 4.2 eV) are necessary to trigger the formation of an electron-hole plasma. We indicate here that the measured average power threshold above which a detectable bulk modification under the described microscopy system (see Chap. 4) with unaberrated tight focusing is around 7 mW. In the light of the critical power threshold for self focusing in BK7 (1.96 MW, corresponding to 30 mW average power) and knowing that $n_2 = 3.45 \times 10^{-16} \text{ cm}^2/\text{W}$ we can securely state that material transformation takes place before strong nonlinearity develops. A main consequence emerges. Under tight focusing conditions, efficient plasma generation occurs in the early stages of the pulse, well before the activation of the self-focusing mechanisms. The generated plasma introduces a negative phase shift, peaked on the axis, acting as a divergent lens. Most of the incoming pulse energy is then spread around the focal region. In these conditions, self-focusing plays a secondary role. However, once the focusing point advances into the bulk, the input threshold power for visible modification increases significantly.

This specific topology can presumably be connected to a strong expansion of the irradiated volume. In glasses characterized by high thermal expansion such as BK7, energy density plays a paramount role in establishing a positive index change. Under regular irradiation conditions, the refractive index change in BK7 is dominantly negative [BSC⁺05] and explained by strong radial thermal expansion. After the initial laser heating, the material expands while cooling, which, in turn, inhibits the backward relaxation and quenches the material in a low density phase. However, high energy densities generate compressive shock waves [STS⁺07] and determine the formation of a strongly compacted region around the low density core. These provide the prerequisites for axial

⁷In fact, PCM and DIC are build upon this idea, i.e to enhance the contrast linked to the optical path variations.

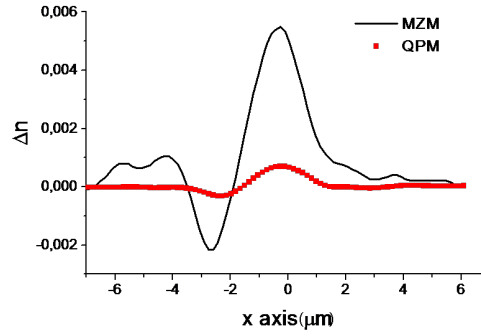


Figure 5.7: Refractive index profile cross section of longitudinal waveguides in BK7 glass measured with QPM and MZM.

positive change in the refractive index at the structure tip. Upon longitudinal photoinscription, if the energy concentration stays sufficient, the high density positive index phase can be replicated during the scan, leading to the formation of a waveguide (see Fig. 5.6b).

Refractive index measurement

For photonic applications, a precise control of the refractive index change permits to precisely design waveguides and more complex components. Therefore, its quantitative measurement in the case of the longitudinal photowritten structures of Fig. 5.6b) is performed with the help of MZM, QPM and numerical aperture determination (NAD). The cross-sectional refractive index profiles of the longitudinal waveguide in Fig. 5.6b) measured with QPM and MZM are reported in Fig. 5.7. The maximum refractive index increase with respect to the background reported by the MZM technique is 0.0055 whereas the QPM method gives an increase of 0.0007. Repeated NAD measurements yielded an increase of 0.005, thus confirming the MZM result. We show in the following that the strong discrepancy with the QPM may be partly explained by the necessity to take into account the cylindrical symmetry of the photowritten structure with respect to the propagation axis z . This symmetry was experimentally verified. Since the QPM technique involves capturing three different planes around the focal plane and solving the intensity transport equation, the refractive index profile of the pictured waveguide is projected on the observing plane. In other words, placing ourselves in the cylindrical system r, θ along z , the refractive index profile of the guide $f(r)$ is projected on the observing plane x, z . This exact mathematical operation is called the Abel direct transform [Zen03] and yields the projected function $p(x)$ following:

$$p(x) = 2 \int_x^{+\infty} \frac{r f(r)}{\sqrt{r^2 - x^2}} dr \quad (5.2)$$

Having the projected data from the QPM picture, the inverse Abel transform permits to retrieve

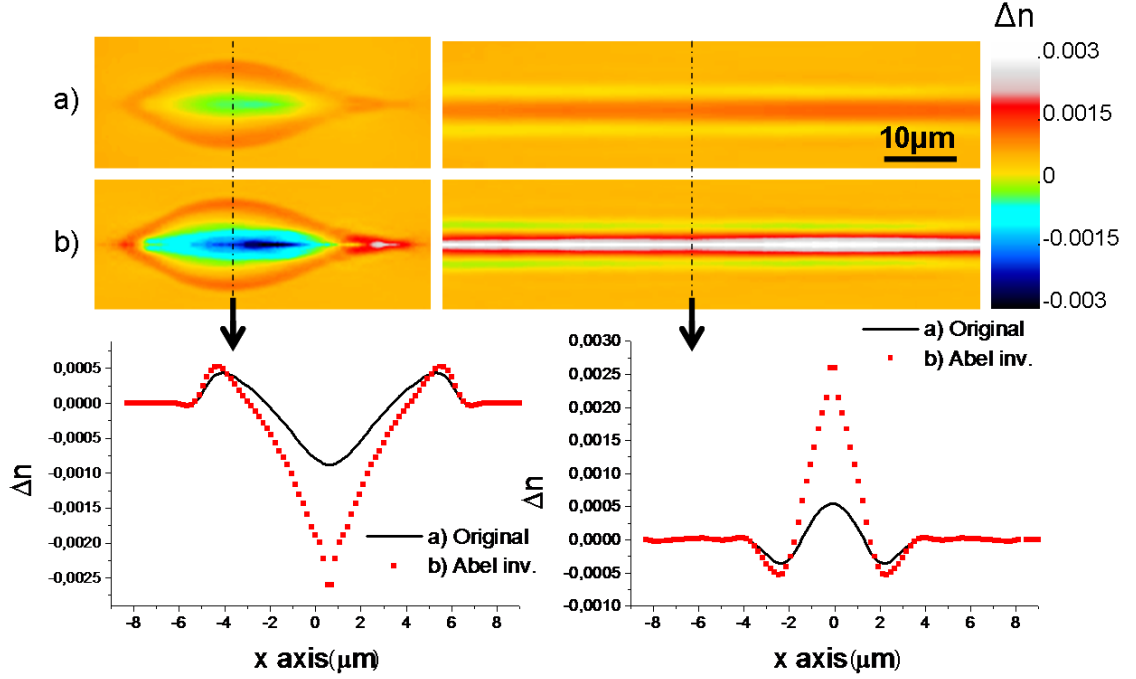


Figure 5.8: QPM refractive index profile cross section of static traces (first column) and longitudinal waveguides (second column) in BK7 glass without inverse Abel transform a) and with the inverse transform b). Transverse cross-sections indicated by the dotted lines occupy the bottom row. As the Abel transform requires a cylindrical symmetry for the projected data, the images were numerically mirrored with respect to the optical axis.

the waveguide index profile $f(r)$:

$$f(r) = \frac{-1}{\pi} \int_r^{+\infty} \frac{p'(x)}{\sqrt{x^2 - r^2}} dx \quad (5.3)$$

Following recent results of optical fiber characterization employing QPM [RAB⁺02], we carefully computed the inverse Abel transform under Labview and applied it to correct our QPM measurements. The results are presented in Fig. 5.8. For the longitudinal wave guide, the measured refractive index increase attains 0.003 which is in the range of the MZM and NAD results. However, the dependency and sensitivity of QPM to numerical calculations is strong.

If for QPM of cylindrical objects, the Abel inversion is indispensable, the question is more subject to discussion in the case of 'classic' microscopy (OTM, PCM, DIC and MZM). More precisely, when using high magnification, the modern microscopic systems provide a fine depth of field (on the order of the micrometer). This distance corresponds to the thickness of the projected data on the observing plane. Naturally, the Abel inversion is of importance when this quantity surpasses the imaged object diameter. However, considering the lateral size of the laser-induced modifications presented in this report (a few tens of micrometers), the fine micrometric slicing

offered by the microscope at the employed magnifications makes the need of a Abel reconstruction questionable. Therefore, unless specified otherwise, we did not perform any Abel inversion on the microscopy images in this report.

Considering the advantages and drawbacks of the refractive index characterization technique and having in mind the need of a rapid and reliable imaging method, we preferred the PCM technique as a quick mean of evaluation and comparison. We completed the corresponding qualitative index mapping with quantitative measurements from NAD (and MZM when possible) to further characterize the laser-induced structures when necessary.

In conclusion, we measured a refractive index increase of 0.0055 in the core of the longitudinal waveguide photowritten in BK7 in this mostly thermo-mechanical processing window and an index decrease of 0.002 around the core.

5.2.3 A new single pulse photoinscription regime: formation of regular pre-dots

Background and experimental conditions

Increasing the pulse energy naturally complicates the interaction picture. We indicate here a specific photoinscription regime where a ensemble of very regularly spaced and aligned modifications appear *before* the main focusing area in fused silica and BK7. To the best of our knowledge, this particular processing regime was not yet identified in the literature. Usually, under femtosecond single pulse bulk irradiation with sufficiently tight focusing, a unique modification takes place in a well defined area situated at or close to the focal plane [BSC⁺05, Mer07]. However, it was recently shown that under tighter focusing conditions, the modified area can extent after the focal plane in the form of consecutive voids with quite regular spacing if the nonlinear propagation and filamentation are supposed.[TKO05, KSQ⁺05]. This exotic photoinscription regime depends widely on the number of pulses, self focusing and spherical aberration. Using this processing window, arrays and waveguides were machined as an illustration of the applicative potential.

The photowriting regime we unveiled is drastically different in many aspects and presents significant advantages for bulk processing applications. Fig.5.9 presents the bulk modifications in fused silica and BK7 glass subsequent to single femtosecond pulse irradiation (160 fs FWHM) for a wide range of pulse energies. The laser geometrical focus is situated 200 μm beneath the material's surface; in conditions of negligible spherical aberrations [HSM⁺07]. We point out here that Fig.5.9 is a nice illustration of the interest of the phase contrast microscopy technique (PCM) when imaging laser-induced modifications (see the beginning of this chapter). Indeed, these minute changes can be invisible with optical transmission microscopy only (OTM) (see Fig.5.9 where the low energy traces are detectable only in PCM).

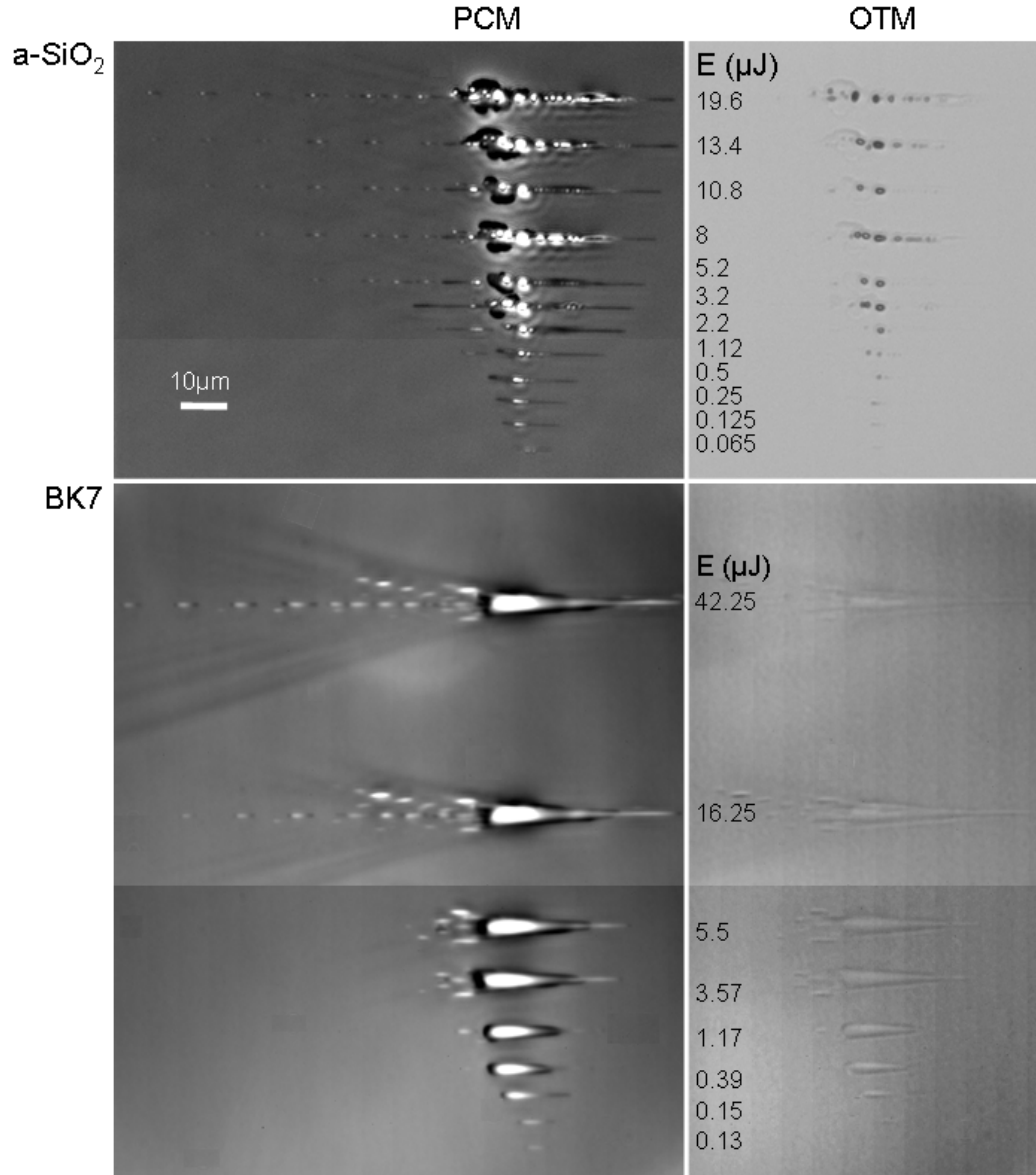


Figure 5.9: Pictures of single pulse irradiation outcome in the bulk of fused silica and BK7 glass under phase contrast microscopy (PCM) and optical transmission microscopy (OTM). The laser pulse comes from left and its energy was varied from the first detectable modification regime to the higher available energy. The latter case shows a novel photowriting regime where very regularly spaced dots are formed up to $200\mu\text{m}$ before the focal area upon single pulse irradiation. $\text{NA} = 0.45$ and $\text{NA}_{\text{eff}} = 0.42$

Let us first consider the moderate energetic regimes below $2\ \mu\text{J}$. As already reported in the literature [Mer07, BBS⁺07, BSC⁺05], we note a drastic difference in the response of BK7 and a-SiO₂ under laser irradiation. While the response of BK7 is dominated by thermal expansion in a large region resulting in the onset of a low density material, the response of a-SiO₂ is characterized by the appearance of a reduced white region under PCM which corresponds to a void [GM97], and a filament of higher refractive index (black area under PCM) than the pristine bulk. It was shown by using a formalism of nonlinear propagation that the void region corresponds to the highest energy exposure [BBS⁺07]. Time-resolved investigations also associated this zone with the region of stronger absorption of the transient electronic plasma [MBR⁺09].

When turning to higher energies ($< 10\ \mu\text{J}$), the area of main light focusing is left into an extreme thermodynamic state after the energy transfer from the electronic bath to the lattice. The corresponding intense levels of pressure exceed the bulk modulus and the energy dissipates in the form of a pressure wave (pictured and characterized in Chap. 6), with dramatic consequences on the local structure of the material [JNT⁺06].

The new photoinscription regime is clearly observable on the traces obtained at the highest available energy in Fig.5.9. One can notice from the PCM pictures that, in both BK7 and fused silica glass, a particular regime of interaction takes place when the pulse energy is above approximately $15\ \mu\text{J}$ for BK7 and $8\ \mu\text{J}$ for fused silica. A very regular succession of dots perfectly aligned on the laser propagation axis precedes the area of main focusing in both BK7 and fused silica. We observed that this line extends to the sample surface when the highest pulse energy is employed. The topology of these pre-dots is quasi-identical in both glasses which can be surprising since those glasses are known to behave very differently under femtosecond exposure [Mer07].

Origin of the pre-dots

In the context of femtosecond processing, it is tempting to assign the topology of these structures to non-linear propagation in the form of a regular alternation of self-focusing and plasma defocusing (each plasma being at the origin of a dot). In fact, it was shown that loose focusing conditions favoring filamentary propagation permit the photowriting of various permanent structures [YWL⁺04]. As filaments position and length are very sensitive to the temporal characteristic of the pulses [HSL06], we conducted investigations varying the pulse duration to validate the filament hypothesis (not shown). Investigations with longer pulses revealed that the position of the dots remains perfectly identical for pulse duration under the picosecond. For longer pulses, the dots simply disappear. These observations do not speak in favor of a filamentary propagation.

Interestingly enough, the distance separating two consecutive dots is slightly smaller in fused silica ($\approx 11.1\ \mu\text{m}$) than in BK7 ($\approx 12.3\ \mu\text{m}$), following the tendency of their respective refractive index at 800 nm ($n_{a\text{-SiO}_2} \approx 1.453$ and $n_{\text{BK7}} \approx 1.509$). This observation motivated us to precisely

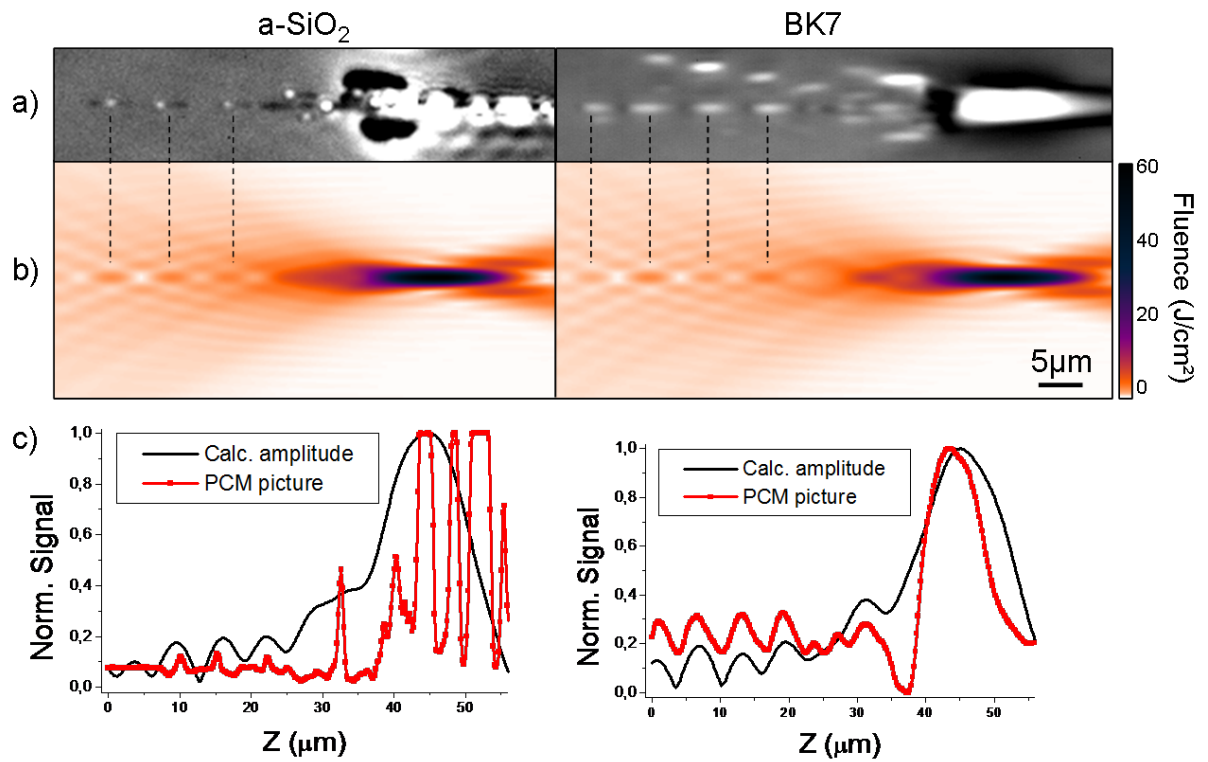


Figure 5.10: Comparison between a) PCM pictures of single pulse irradiation in fused silica and BK7 glass with the b) Fresnel propagation results in both glasses. The vertical dashed lines shows the correspondence between the position of the dots before the region of main focus and the the fluence peaks predicted by the propagation code. c) displays an horizontal cross section of the PCM picture (solid) and the the numerical results (square)

calculate the laser beam linear propagation using the Fresnel propagation code we developed (see Chap. 2). The experimental beam radius on the focusing objective as well as the truncation value were taken into account. We calculated the phase and amplitude of the laser beam after propagation from the lens until the air-glass interface. Then a phase term was added to the laser spatial phase to take into account the phase distortion due to the refraction. The analytical expression of this additional phase term $\psi(\rho)$ is easily obtained from geometrical considerations [BNW98] and reads:

$$\psi(\rho) = d [n_2 \cos(\theta_2) - n_1 \cos(\theta_1)] \quad (5.4)$$

where n_1 and n_2 are the optical indices of the air and the glass respectively. d is called the focusing depth in [HTS⁺05] and corresponds to the distance between the sample surface and the geometrical focus when $n_2 = n_1$. θ_1 is linked to the lens numerical aperture (NA) and to the normalized pupil radius ρ by $\rho = \frac{\sin \theta_1}{NA}$. θ_2 is defined from the Snell-DesCartes law $n_1 \sin \theta_1 = n_2 \sin \theta_2$. The propagation through the air glass interface is also accompanied by a certain amount of reflection depending on the incidence angle and the beam polarization. We took into account the corresponding variation of amplitude transmission following the Fresnel reflection formulae. We precise here that the beam polarization is in the incidence plane which is parallel to the microscopy images found throughout this report. The propagation calculation were then carried out for an ensemble of planes comprising the focal area. Fig. 5.10 b) presents the calculated focal fluence maps for fused silica and BK7 glasses and compare them with the PCM pictures of the bulk modification (Fig. 5.10 a)). Horizontal cross sections along the optical axis of the PCM pictures and the simulations are reported in Fig. 5.10 c). The specific topology of the on-axis dots is unambiguously predicted by the Fresnel propagation results. We underline here that these regular regions of higher fluence are mainly linked with the truncation of the beam as showed in Chap. 2. It is therefore extremely important to correctly take into account the linear effects when trying to understand the morphology of laser induced modification i.e to go beyond the the pure Gaussian model to estimate the focal intensity distribution.

Application: multi-dots photowriting

As an illustration of the potential applications of this photowriting regime, an array of dots is presented on fig. 5.11. The 70 shown dots were written with only 14 single pulse irradiations, evidencing the interest of this regime to write many structures in a reduced amount of time. The concerned modification could be used as data points or arrays of transverse waveguides (i.e with a continuous irradiation sequence under transversal displacement of the sample). Naturally, the challenge is to control the dots position and number to render this photowriting regime appealing for data storage and multi-waveguide writing. Given that the dots position rely on easily calculable

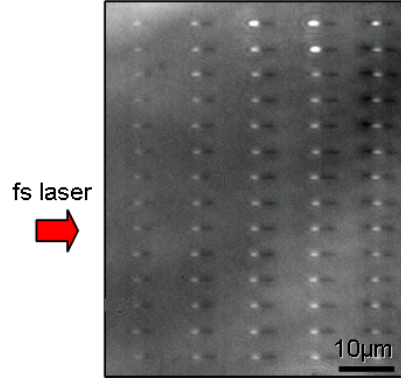


Figure 5.11: Example of an array of dots written in fused silica in the depicted photowriting regime. Each line was written from a single pulse irradiation. The main damage is situated on the right and is not shown.

linear propagation, an interesting perspective regarding the control of their position with optimized spatial modulation is currently under study.

We also succinctly report on an interesting phenomena which can presumably lead to efficient data storage applications with the write/erase and rewrite flexibility from the same femtosecond source. Data storage by femtosecond irradiations in transparent materials was achieved more than ten years ago in fused silica without however, the possibility to erase and rewrite the data points [GMH⁺96]. Taking advantage of photoinscription regimes where birefringent structures based on nanoscale material self-arrangement, Hnatovsky *et al* demonstrated the possibility to erase and write over the same data point by changing its birefringent properties with the ultrashort irradiation [THS08]. Nevertheless, the number of possible re-writing processes is limited due to a gradual degradation of the nano-structures upon successive irradiations. Here we present the first set of investigations we obtained in BK7 glass in Fig. 5.12. The writing procedure simply consists of static irradiations with 10^5 pulses at 20 mW and 100 kHz with $NA=0.45$ ($NA_{eff} \approx 0.41$). Erasing is carried out with transversal scanning of the sample under more energetic irradiation (≈ 100 mW at $\approx 100 \mu\text{m/s}$). As shown in the successive images in Fig. 5.12, it is possible to rewrite data points and to repeat the whole write/erase sequence. Interestingly enough, the aspect of the bulk modification in the region of previous erasure is very similar to that of the irradiation of a fresh area as visible on the left image where two femtosecond and two picosecond exposure are presented. These results need obvious improvement, but it is expectable that adapted spatio-temporal tuning of the irradiation with the help of self-improving loops can lead to smoother erasure. For example, by purposely adding spherical wavefront distortions, the lengthening of the intensity distribution generates a smoother and larger erasing beam (not shown). Moreover, the maximum number of write-erase cycles has to be experimentally investigated.

The perspectives offered by the process can be extended to the writing and erasing or modification of full embedded optical components (e.g, modification of photowritten waveguide connec-

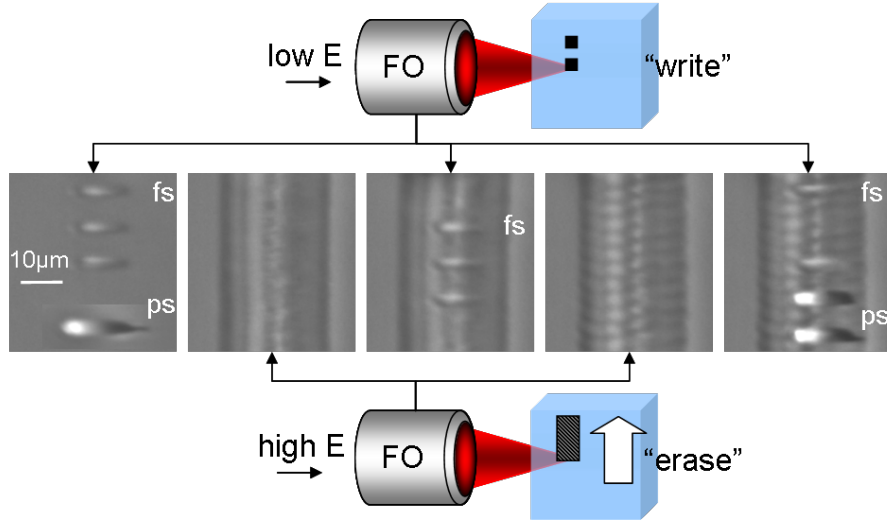


Figure 5.12: Successive write/erase/write... operation in BK7 glass illustrated by PCM pictures. The morphology of the femtosecond (fs) and picosecond (ps) structures is preserved in the previously erased zone.

tions...).

5.2.4 Spherical voids with single pulse in borosilicate glass (D263)

The quality of the laser induced structure is naturally of prime importance for bulk photoinscription. Here we report on a single pulse photowriting regime that generates voids with a very high sphericity. The interest of achieving purely spherical modification is mainly found in data storage applications where the challenge is to preserve the data bit volume as small as possible. Of course other applications can be of interest, particularly for photowriting embedded micro-lenses and so on. Interestingly enough, 3D data storage with femtosecond bulk writing was first addressed in 1996 [GMH⁺96], the same year as the first waveguide writing demonstration. There, the performance of the reported photowritten bits in fused silica is remarkable as the spatial extent in the x, y plane (z being the laser propagation axis) is measured to be only 200 nm⁸. However, if the structures were obtained with single 100 fs pulses, they suffer from a prohibitive extent in the z -axis, more than 12 times their transversal dimension. It is therefore a challenge to generate purely spherical voids while keeping small dimensions. This was achieved with the help of bursts of low energetic ultrashort pulses at MHz repetition rate in tight focusing conditions [SBGM01]. In this regime of high heat accumulation, the laser spot acts as a point-like heat source [EZN⁺08] and it was shown in soda lime glass that the temporal separation between the pulses as well as the length of the burst offer a control on the size of resulting spherical voxel [GCM06]. This efficient pho-

⁸measured by scanning electron microscopy and atomic force microscopy after sample cutting

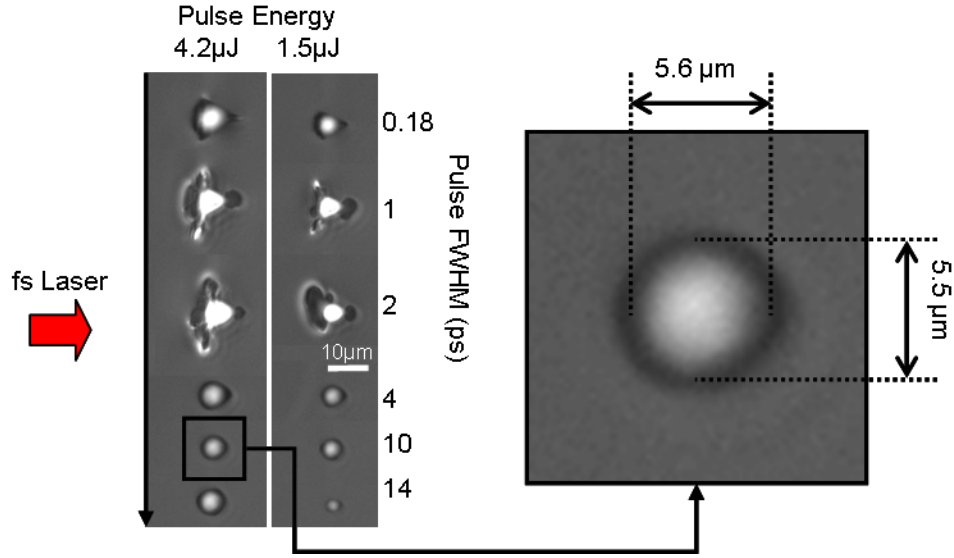


Figure 5.13: PCM pictures of single pulse irradiation in D263 borosilicate glass for various pulse energy and duration. The laser comes from left and the focusing objective associated with an index-matching oil provided a numerical aperture of 1.25. The inset shows a quasi-spherical voxel where the no elongation along the laser propagation axis takes place. the depth of the structures is $130 \mu\text{m}$ with respect to the surface.

towriting regime can be operated directly from the output of an femtosecond oscillator. However, tens of thousands of pulses are usually required for each voxel meaning that one modification lasts at least 1 ms at 1 MHz and that a perfect immobility of the sample is needed during this time which can be a constraint for industrial applications.

We present a regime of single pulse irradiation capable of generating voxels with clean spherical symmetry in borosilicate glass D263. Voids having a circular symmetry around the laser propagation axis under single pulse irradiation were already demonstrated in sapphire [JNT⁺06], however, they suffer from an elongation in the laser propagation axis. Fig. 5.13 presents single pulse irradiation outcome for a set of pulse lengths ranging from 180 fs to 14 ps with two different pulse energies. Interestingly enough, the desired spherical shape is found for pulses longer than 3 ps where a clean spherical symmetry is obtained without elongation along the z -axis.

The physical reasons for this behavior are linked to the reduced sets of nonlinearities (especially plasma defocusing) in the case of picosecond irradiation. More precisely, there are three questions that arises from observations on Fig. 5.13 that can be well-explained.

First, why is it possible to obtain clean spheres from single pulse irradiation longer than 4 ps? To understand this behavior, one has to keep in mind the highly tight focusing condition ($\text{NA}=1.25$). This means that the cone of processing light has an enormous half angle of 75° . In the absence of nonlinear propagation, the laser focal volume is therefore very close to a perfect sphere. To obtain a spherical modification from such an intensity distribution seems logical, provided that:

the light pulse is long and/or weak enough to undergo negligible nonlinear distortions and preserve a quasi-spherical intensity distribution; and of course that the pulse intensity is enough to trigger sufficient photoionization leading to permanent damage smaller than the confocal region (the modification is still a nonlinear process). This explains the fact that the spheres are associated with long pulses at low energy. As an additional argument, lower energy investigations confirmed the possibility to obtain spherical voxels for pulses as short as 1 ps.

Second, why is the femtosecond trace not spherical? The high peak intensities reached with femtosecond pulses unavoidably leads to a certain onset of nonlinear propagation, even when employing energies just above the modification threshold. Therefore, we think that mainly self-focusing and plasma defocusing are responsible for distortions leading to a less confined focal intensity distribution with obvious topological consequences on the permanent damage. In fact, we investigated femtosecond irradiation until detectable modification under our microscopy set up, and all the traces presented the same distorted shape.

Third, what is the reason for the cracks appearing just at the intermediate pulse durations (1 – 2 ps)? As we have just mentioned, picosecond irradiation at moderate pulse energies follow an almost linear propagation. While avoiding a strong plasma defocusing effect, the energy deposition is therefore more confined than for femtosecond exposure potentially leading to cracks. Thus, there is an optimality in concentrating the energy. When augmenting further the pulse duration, the chances of triggering the first seed electrons through multiphotonic ionization are reduced, implying a latter start as well as a smaller area for the avalanche ionization to take place. Thus, an increased part of the pulse does not participate in feeding the electronic gas. Consequently, the laser-induced plasma is weaker and the cracking regime unattained. The effect is similar when diminishing the pulse energy and we experimentally verified the possibility to generate spheres with a 1 ps pulse at $0.15 \mu\text{J}$. As we will show in the next chapter, this behavior (that augmenting the pulse duration from a hundred femtoseconds to tens of picoseconds leads to an increase followed by a decrease of energy coupling) is exactly followed by the amplitude of the transient pressure wave subsequent to the laser irradiation.

As a word of conclusion for this paragraph, it is interesting to see the increase of processing flexibility that temporal shaping offers. The technique allowed us to evidence a photoinscription regime where spherical smooth voids are formed with a single picosecond pulse at low energy without the need of a burst of pulses. The size of the voxel is controllable from less than a micrometer up to $7 \mu\text{m}$ by pulse length and/or energy tuning. Again, we would have kept with the shortest available pulse duration, this regime would still be unexploited. We mention here that we were able to obtain voxels with a diameter beneath the micrometer when working at lower energies.

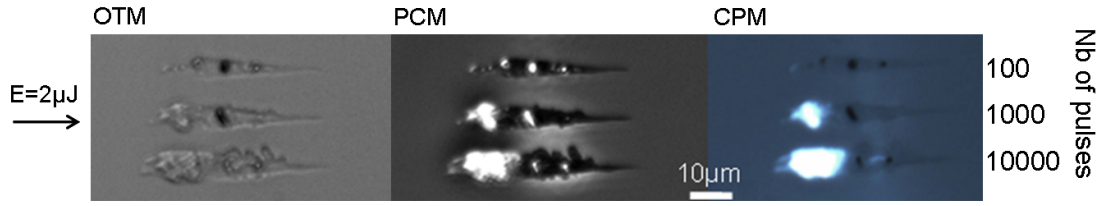


Figure 5.14: Cumulative study in fused silica at 200 μm deep observed with optical transmission microscopy (OTM), phase contrast microscopy (PCM) and cross polarizers microscopy (CPM). The appearance of birefringent structures after a few hundreds of pulses is denoted by the bright area in CPM. $\text{NA} = 0.45$ and $\text{NA}_{eff} = 0.42$

5.2.5 Application of laser-induced birefringence in fused silica

At higher energy inputs in fused silica, the irradiation outcome is accompanied by laser-induced birefringence. We use a this photowriting regime in order to process a polarization-sensitive waveguide. The presence of self-organized nanoscale arrays is evidenced with scanning electron microscopy pictures of the bulk waveguide after sample cutting.

Background and state of the art

In the context of energetic interactions in glass materials we indicate that laser-induced birefringence is possibly obtained in bulk isotropic glass materials [BSPA02, YBG⁺04, PSF⁺03, YWNI03]. It has been shown that the onset of birefringence surrounding the laser focusing cone is a signature of laser-induced stress in the glassy matrix [PSF⁺03]. Another type of stronger laser-induced birefringence was reported having the particularity to be situated within the interaction volume [SFPM99, BKK04, BBS⁺08]. As an illustration, Fig. 5.14 shows permanent modifications in fused silica for different number of linearly polarized irradiating pulses at 1 kHz under PCM, OTM and crossed polarizers microscopy (CPM). It is noticeable that after a few hundreds of pulses, a regime of strong laser-induced birefringence is attained. It was shown that in this particular photowriting regime, the birefringence properties are correlated with the presence of self-organized nano-arrangements inside the laser traces [SKQH03, BSR⁺06, WGBH08]. While under our PCM apparatus, these structures are well-below the spatial resolution, their presence is noticeable has their overall contribution to the refractive index is negative (see the white zones in the PCM image in Fig. 5.14). However CPM is more adapted to reveal the birefringence regions (in chite) which correspond to the principal white zones in PCM (but not all). The resulting layered structures are oriented perpendicular to the electric field vector, leading to birefringence values in the range of $\delta_{oe} = 5 \times 10^{-3}$ at 633 nm wavelength. While the physical origin of these nano-organization is still under discussion, the following scenario is commonly admitted. First, the ultrashort irradiation

triggers essentially electronic polarization effects while keeping the molecular reorientation low. Second, the accumulation dose supports a positive feedback response for stimulating the growth of the organized sub-wavelength structures. Both aspects indicate a driving electronic mechanism of self-organization, with modulated energy transfer to the glass matrix. The proposed models [SKQH03, BSR⁺06] involve collective electronic oscillations and local changes in polarizabilities which lead to the formation of a rippled structure in volume. The resulting gratings consist in narrow layers of lower index, oriented perpendicular to the laser electric field with an interlayer period of approximately $\frac{\lambda}{2n}$, n being the refractive index and λ the writing wavelength. The modulated structures also show noteworthy structural and optical properties; among these, a preferential concentration of oxygen-deficiency centers in the layers [SKQH03], and peculiar optical scattering [KIM⁺99, QKS⁺00] or reflection properties [MKBB02]. Remarkably, an efficient photowriting regime for bulk nano-gratings in fused silica was employed to generate polarization sensitive data points and gratings being sensitive to the polarization of the observing light [THS08]. Channels with enhanced etching properties due to the nano-planes were also evidenced.

Our contribution here lies in the photowriting of waveguides taking advantage of the polarization-sensitivity of the laser-induced structures in this processing window.

Polarization-sensitive type II waveguides

Naturally, the formation of birefringent regions based on nanoscale self-organization in fused silica is dependent on the irradiation regime [SFPM99, KS08, THS08]. It is practical to divide the achieved structures with the corresponding energetic requirements. As already mentioned at the beginning of this section, low irradiation levels usually induce isotropic positive changes of the refraction index, they are here denoted type I structures. Higher energy doses initiate the so-called type II structures characterized by birefringent material modifications [SFPM99]. The formation of self-organized nanoscaled arrays was associated with type II structures [KS08, THS08].

Fig. 5.15 depicts examples of type I (upper part) and type II (bottom part) laser-induced longitudinal traces for linear polarization together with near-field modes of guided 800 nm light. Type I traces show normally a smooth type of modification as noticeable in the PCM traces, with weak index changes in the range of 10^{-4} – 10^{-3} (depending on the scan velocity), indicated by the shallow dark color in the left upper panel of Fig. 5.15. The tracks were subsequently injected with polarized 800 nm light. No noticeable polarization sensitivity was observed (Fig. 5.15 top right), both \uparrow and \leftrightarrow orthogonal polarizations being guided (see figure). The type II traces show as well an overall axial positive refractive index change (dark colors in PCM), bordered by narrow rougher edges of negative index change or scattering zones (white colors in PCM). The index increase is significantly higher as for the type I guide, reaching up to a factor of ten in magnitude depending on the writing conditions. Upon injection with 800 nm light we have observed a remarkable behav-

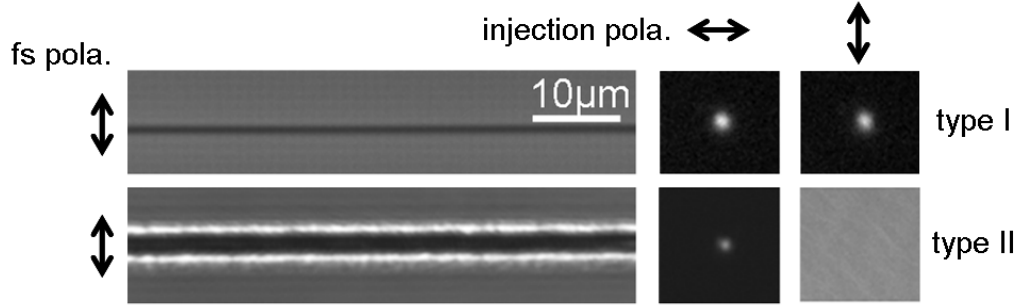


Figure 5.15: Polarization dependent optical guiding in various types of longitudinal waveguides in a-SiO₂ written by linearly polarized 800 nm femtosecond laser radiation with $NA = 0.42$ and $NA_{eff} = 0.31$. Images in the left frame show top view PCM pictures of photowritten waveguides with a linear polarization indicated on the left side. The upper part depicts a type I trace while a type II is represented in the bottom part. The right frame shows near-field modes for injected 800 nm radiation; the polarization of the injection laser is depicted on the top of the right frame. All the structures are written by 33 mW (type I) and 195 mW (type II), 100 kHz laser pulses at the speed of 10 μm . The length of all waveguides is 7.3 mm.

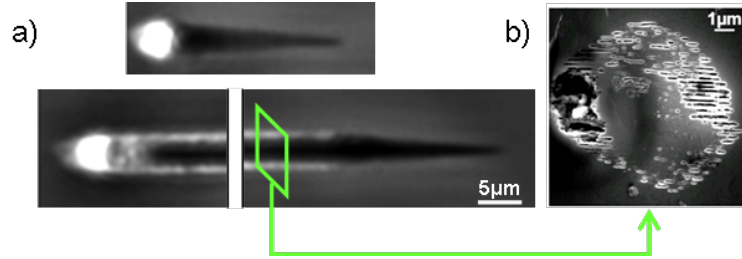


Figure 5.16: Morphological details on the type II waveguide: a) PCM pictures of the extremities of type II structure written at 150 mW, 50 kHz and 10 μm compared with a static trace (1 s irradiation), b) scanning electron microscopy picture of the waveguide cross section after transverse cutting, polishing and etching showing the nano-gratings perpendicular to the writing laser polarization.

ior. Type II traces indicate light guiding properties only for injected light with the electric vector perpendicular to the initial writing beam vector; a different polarization being scattered away. This observation holds essentially for injected 800 nm; the polarization sensitivity being visibly reduced for injected 633 nm. Considering that nano-arrays are formed in the trace as previously reported [SKQH03, BSR⁺06], they allow light transport for polarizations aligned along the planes (TE with respect to the structure), orthogonal to the polarization of the writing beam. Note also the strong confinement of the field mode as a result of the higher index contrast, however the optical losses are significantly increased by the orders to several dB/cm. No guiding modes were observed for circular writing polarization due to the reported presence of less ordered scattering nano-structures within the trace [TSH08].

Fig. 5.16 b) shows scanning electron microscopy (SEM) pictures of cross sections of the type II waveguides showed in Fig. 5.15 with indication of the femtosecond laser polarization state. The sample were cut, polished and etched before SEM investigations. The nano-arrays are oriented at 90° with respect to the oscillations of the electric field with a period close to $\frac{\lambda}{2n}$ as already reposted [THS08]. Interestingly enough, the nano-gratings are present in regions corresponding to the white areas on the borders of the longitudinal structures on the PCM side-pictures. The waveguide core, appearing black under PCM, can be unequivocally correlated to the central zone of the SEM image (Fig. 5.16 b)) which does not show any rippled formation.

5.3 Conclusion

After these various examples of laser-induced permanent modifications and their interest in potential applications, it is obvious that the femtosecond bulk writing technique is still far from reaching its full potential. First, the need of a dedicated characterization tool is a main issue and heavily depends on the desired irradiation outcome. Among various refractive index profiling techniques, we showed that phase contrast microscopy is a well-adapted method for refractive index qualitative characterization. The interest of the Abel transform to correct Quantitative phase contrast microscopy pictures has been underlined from experimental measurements of BK7 laser-written waveguides. Different photoinscription regimes were shown in fused silica and BK7 glass with the emphasis on a high energetic case where regularly spaced dots preceding the focal plane are formed. We demonstrated that these modifications precisely matches areas of higher exposure predicted from Fresnel propagation simulations taking into account beam truncation and the effect of the air-glass interface. The regime is characterized by the simultaneous photowriting of multiple regular structures. Using high numerical aperture, we also present the formation of spherical voids under single pulse irradiation in borosilicate D263 glass under a regime of purposely reduced nonlinearities involving picosecond pule duration. Finally, we demonstrate the possibility to induce polarization-sensitive waveguides taking advantage of a birefringent photowriting regime in fused silica.

Given the variety of the permanent modifications presented in this chapter, it is expectable that femtosecond bulk processing is appropriate to answer most of the challenges of integrated optics. We saw however that materials have specific reactions to the laser passage (e.g the wide difference between irradiated fused silica and BK7 glass). As their dynamical changes are most likely to differ as well (see next chapter), a method for tailoring the laser tool to the material is required in order to obtain a certain processing flexibility. We recall here the example of the possibility to obtain spherical voxels in D263 glass with a single pulse. Without the capacity to temporally stretch the pulse, this interesting regime would still be unknown. This is just a little example of

the potential of adding spatio-temporal controlling tools to ultrashort irradiations, the leitmotiv of this work. The rest of this report adds to this point with time-resolved picturing of the transient dielectric state of the glass after a temporally shaped femtosecond pulse (see Chap. 6), spatial and/or temporal phase optimization for deep femtosecond writing, and spatial tailoring for parallel processing in the bulk (see Chap. 7).

Chapter 6

Time-resolved imaging of transient bulk modifications

An impressive research effort is being conducted to understand the dynamics and processes leading to bulk modification after the ultrashort irradiation as a way to inspect the true nature of the phenomena. If the perspective of being able to predict the material response for arbitrary exposure conditions seems a long lasting challenge, one cannot deny the significant recent progresses in identifying the ionization processes, their respective contribution to the formation of a hot electronic plasma and the main scenarios for energy relaxation to form a permanent change on longer timescales. Naturally, an improved understanding of the physical phenomena implies a potentially finer control of the laser-induced modification process. As the light structuring tool is on ultra short time scales, the need of probing the material in this temporal range is indispensable to apprehend the physics of the interaction. This chapter is thus dedicated to time-resolved imaging and characterization of the material from sub-picosecond to an hundred of nanosecond delays after the bulk excitation. After a brief overview of 'classic' pump-probe arrangements and the particularities of our experimental apparatus, we present time-resolved mapping of the free electronic gas and of the matrix. From electronic density N_e calculations on OTM pump-probe images, we compare the order of excitation between femtosecond and picosecond pulse in fused silica and discuss the relative role of MPI, avalanche and saturation effects above the modification threshold in the presence of non linear distribution of the intensity. For the first time, the density topology of the transient electronic gas around the focus is evaluated for both pulse durations, showing the more dense and confined character of the picosecond-generated plasma. While both free-electronic and matrix contributions are mingled in the OTM and PCM pictures, we describe a new method allowing for their separation and involving the calculation of N_e . The microscopic topology of the bulk free carrier density and lifetime is equally investigated. A set of investigations is thus conducted in fused silica and BK7 glass, revealing the axial modulation of the free carrier lifetime which lasts

longer in the zones of permanent modification. The energy relaxation is followed, culminating with heating and launching of pressure waves which are characterized for various glasses (fused silica, BK7, TeO₂ and SF57 heavy metal oxide glass). We also investigate on an ultra-short time scale two photoinscription regimes producing similar permanent modifications but implying very contrasted dynamics, namely picosecond and double pulses. Finally, time-resolved measurements are conducted in a regime close to the type II waveguide writing regime. The dynamics of energy coupling is analyzed in a regime of accumulation of numerous pulses, giving insights to the formation of the nano-structured regions.

6.1 Introduction

6.1.1 State of the art

The major interest of femtosecond light pulses has been the possibility to use them as ultrashort flashes to follow chemical reactions and other physical processes with an unequaled temporal resolution¹. The so-called pump-probe experiments take advantage of this property by employing a seed light pulse to trigger the investigated physical process and a probe pulse to optically probe the area of interest, yielding precious information concerning lifetimes, species proportions and so on. In the field of femtosecond processing, the same laser beam is optically split to serve as pump and probe. Their relative delays is adjusted by managing the length of the optical path. Experimentally, delays longer than 100 ns (i.e an optical path of ≈ 30 m in the air) becomes difficult to achieve with this method. For investigations of the transient material properties under femtosecond irradiation, a wide range of various experimental set-ups were designed [Cal00, SLFE87, SvdL00]. More precisely, when the detection of the dynamic absorption and refractive index is of prime importance, techniques employing collinear pump and probe beams have been successfully employed [DFG⁺03, CXW05, ST05, MSZR05, WBS⁺06]. In these cases, a major advantage lies in the fact that the time resolution usually corresponds to the minimum pulse length available from the femtosecond source. However, the absorption and refractive index variations (i.e the electronic density estimation) are integrated all along the laser propagation axis for the entire sample thickness. These investigations are therefore conducted on thin samples in loose focusing conditions to be able to the excitation uniform as the Rayleigh volume is in the order or surpasses the sample thickness [WBS⁺06].

An efficient variation of this technique utilizes an off-axis pump pulse and collect two collinear probe pulses that interfere in the spectral domain enabling for a fine detection of the transient optical properties [ADS⁺94, QGM01]. However, the spatial resolution stays inadequate for in-

¹ 1999 Nobel Prize in Chemistry to Pr. A. H. Zewail, California Institute of Technology, Pasadena, USA

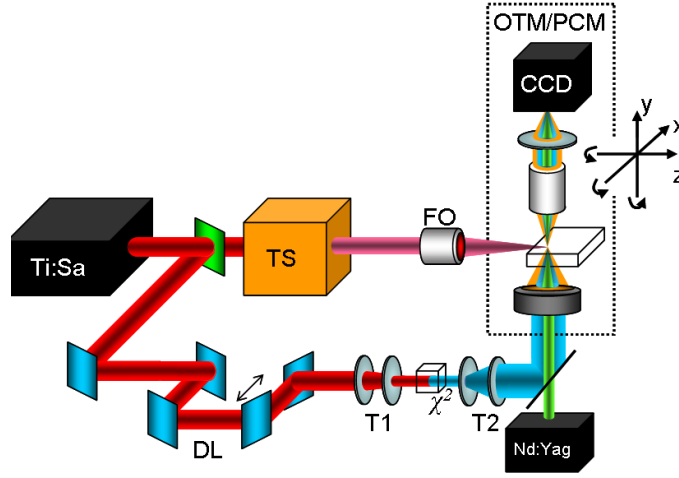


Figure 6.1: Illustration of the experimental set up for time-resolved studies. TS: temporal shaper. FO: focusing objective. OTM-PCM: Optical transmission and phase contrast microscopy for sample modification investigation. χ^2 : Frequency doubling crystal. DL: delay line. T1: Telescope reducing the femtosecond laser beam size before second frequency doubling crystal. T2: Telescope magnifying the beam before entering the microscope illumination path. the additional laser source labeled Nd:Yag emits nanosecond pulses at 532 nm.

vestigations in focusing conditions as tight as discussed in this report, and the variations are also integrated along the z-axis. The transient lens method developed by Sakakura and Terazima [ST05] is an efficient answer to the need of better spatial resolution. The excited area by the pump acts as a dynamic lens affecting the propagation of the probe pulse. Again, this method can not take into account the topology of excitation along the axis of laser propagation.

Pump probe techniques where the pump and the probe beams propagate perpendicularly in the investigated volume have emerged [SJL⁺05a, Hor03, KHP05, HKP04, PZT07]. The pump-probe technique proposed by Sun et al. in [SJL⁺05a] permits measurements of the real and imaginary parts of the refractive index with the help of interferential imaging and time-resolved shadowgraphs recording with good spatial resolution. Horn and coworkers [Hor03, KHP05, HKP04] showed an efficient time-resolved microscopy setup with the possibility to use the Nomarski configuration down to nanosecond scales. As already mentioned in Chap. 5, Nomarski microscopy is sensitive on refractive index gradients only.

6.1.2 Experimental details

Here we use a technique which allows time-resolved observations in optical transmission microscopy and phase contrast microscopy with a spatial resolution limited only by the characteristics of our microscope, and a sub-picosecond temporal resolution. The major improvements conducted

during this work lies in the possibility to temporally shape the pump while keeping the probe to the shortest available pulse duration and in the addition of a nanosecond laser for probing delays above the microsecond. Some characteristics of the corresponding experimental apparatus were already described in details [Mer07]. Precisions on the equipment are provided in Chap. 4. Here, we briefly underline the principle of operation illustrated in Fig. 6.1. A 4-f temporal shaper is installed on the pump beam after splitting the beam into the pump and probe arms. The probe is frequency-doubled and directed to the illumination path of a microscope permitting transmission and phase contrast microscopy. Switching from 400 nm probe illumination to white light or 532 nm probing is easily achievable with a set of flip mirrors (not shown). Therefore, this experimental set up allows for probing the dynamics of the bulk modification subsequent to temporally shaped ultrashort irradiation for a wide range of delays from sub-picoseconds to microseconds. The time resolution was also greatly improved by changing the optics of the microscope and turning to critical illumination in order to diminish the amount of traversed glass for the probe. The temporal response was evaluated by picturing the irradiated region of a boro-sulfate glass for a set of negative delays of a few tens of femtosecond in the phase contrast mode (not shown). The pump pulse propagation is clearly observable with dark concentric regions in front of the focal region, corresponding to the electronic gas and/or the n_2 variation generated by the pump and seen by the probe pulse. Therefore, the extent d of these areas along the propagation axis can be used to evaluate the temporal resolution $\Delta t = \frac{nd}{c}$, n being the refractive index. We found ≈ 200 fs for a 160 fs pulse duration at the output of the laser, which is a significant improvement of the 640 fs of the former set up. The main challenge of this set up is linked to Speckle artifacts that considerably affect the contrast of the images. An association of diffusers is therefore placed in the probe path and for each time delay. Additionally, at least twenty acquisitions (i.e 20 shots in the sample) are conducted to average the Speckle effect. In order to have each pulse interacting with a fresh area of the glass, the sample is slowly translated perpendicularly to the laser propagation axis. A careful and rigorous sample alignment procedure permits to keep constant the processing depth *and* the microscopy observing plane during the entire process.

6.2 Method for mapping the free electronic density and of the ionic contribution

6.2.1 Calculation of the free electronic density from OTM images

Here, we first briefly describe the method for the calculation of the free electronic density N_e from optical transmission microscopy pictures with the help of the results of Chap. 3. Under the Drude model, we expressed the total dielectric constant $\tilde{\epsilon}_{tot} = \epsilon_1 + i\epsilon_2$ of a free electronic gas with

damping in a solid (see Eq. 3.16) where ϵ_1 and ϵ_2 are easily identifiable). The complex refractive index $\tilde{n} = n + ik$ is defined as the square root of the total dielectric constant, which gives the following relations for n and k .

$$n = \sqrt{\frac{1}{2} \left(\sqrt{\epsilon_1^2 + \epsilon_2^2} + \epsilon_1 \right)} \quad \text{and} \quad k = \sqrt{\frac{1}{2} \left(\sqrt{\epsilon_1^2 + \epsilon_2^2} - \epsilon_1 \right)} \quad (6.1)$$

We recall here that k is referred to as the extinction coefficient linked to the absorbance α by $\alpha = \frac{4\pi k}{\lambda}$. By considering that the intensity levels of optical transmission microscopy pictures denote the transmission $T = \frac{I}{I_{bkgd}}$ of the electronic gas, the absorbance α map of the irradiated area is obtained with the Beer Lambert law (see Eq. 3.8) yielding:

$$\alpha = -\frac{1}{L} \ln \left(\frac{I}{I_{bkgd}} \right) \quad (6.2)$$

With L the thickness over which the absorption is integrated to yield the contrast of the microscopy transmission picture. This integration takes place along the microscope optical axis (perpendicular to the laser propagation axis) with L corresponding to the depth of field ($\approx 2 \mu\text{m}$). As this distance is inferior to the transverse size of the observed analyzed structures, L is supposed constant in the entire region of interest (see Chap. 5 for the discussion on the Abel inversion). Replacing k in Eq. 6.1 while supposing $\epsilon_2 \gg \epsilon_1$ for simplicity, the map (r, z, t) of the electronic density normalized to the critical density N_{cr} reads:

$$\frac{N_e(r, z, t)}{N_{cr}} = -\ln \left(\frac{I(r, z, t)}{I_{bkgd}} \right) \frac{\lambda}{2\sqrt{2}\pi L} \frac{1 + (\omega\tau)^{-2}}{(\omega\tau)^{-1}} \quad (6.3)$$

This equation was employed in the following to calculate the free electronic density after the ultrashort pulse passage assuming a constant Drude scattering time of $\tau = 3.7 \text{ fs}$ [SPG⁺07] (see Chap. 3). All of these computations were carried out under Labview. We underline here that, taking into account the fact that the electronic densities attained are within 10% below half of the critical density, the reflectivity remains negligible in front of the absorption (see Fig. 3.3 and [SJL⁺05a]). In order to minimize the effect of illumination derivation associated with picturing various part of the sample, a pre-processing of the image is integrated to the calculation code enabling the correction of the background and its standard deviation.

6.2.2 Method to unveil the transient matrix state

A new method is proposed to annihilate the free electronic contribution in time-resolved pictures of the irradiated area, thus revealing the 2D mapping of the matrix behavior after the passage of the ultrashort sequence. The main calculation steps are summarized in Tab. 6.1 where the main hypothesis are recalled. We showed that, under the Drude theory, the contribution of the

Table 6.1: Proposed method to unveil the matrix dynamics by canceling the free electronic contribution

Step	Hypothesis
OTM and PCM transient picture (< 1 ps)	
Calculation $\frac{N_e}{N_c}$ from OTM	Absorption mainly due to electronic gas
Calculation of the free-electronic $\Delta n_{x,z}$	
Adjust q to retrieve the PCM picture from $\Delta n_{x,z} \times q$	PCM mostly sensitive to phase
PCM - $\Delta n_{x,z} \times q$ yields the matrix phase	
Other delays, same steps with q constant	

free electrons can be directly linked to the contrast of optical transmission time-resolved pictures especially in the first moments of the interaction or more precisely while the majority of the free carriers have not yet recombined. At this time, it is reasonable to state that any optical transmission or phase contrast observation is exclusively due to the electronic sub-critical plasma. The previous sections outlines how the electronic density can be estimated from OTM pictures. From the thus-obtained $\frac{N_e}{N_c}$ 2D-map, the corresponding spatial variation $\Delta n_{x,z}$ of the real part of the refractive index n can be obtained combining Eq. 6.1 with Eq. 3.16).

Assuming that phase contrast microscopy pictures are mostly reporting phase variations ², it is therefore possible to withdraw the contribution of the free electronic plasma to the contrast of the PCM time-resolved images by simply subtracting the calculated $\Delta n_{x,z}$ to the PCM picture. Having in mind the the PCM response is not linear for big phase variations [NK92] and that the sample illumination is sensitively different from OTM, an adjustable factor q is tuned to force the subtraction result to zero for sub-picosecond delay. This factor is constant on the entire picture. That way, the electronic answer deduced from OTM image completely explains the PCM picture at delays (< 1 ps) where the free electronic gas can be considered to be the only source of contrast in both PCM and OTM. For longer delays, when progressive electronic decay takes place (with a characteristic duration depending on the material), the PCM pictures are corrected following the same method based on the corresponding OTM images and keeping the same q . Hence, the matrix contribution only is qualitatively retrieved. Fig. 6.2 depicts an example in BK7 glass which is discussed hereafter. Note the quasi-non existent matrix deformation at the zero delay and its major role at delays above 30 ps. We now discuss the relative importance of the assumption of the PCM being sensitive to phase-only variations. It is well-known that absorption and refractive index variations are usually mingled in PCM images and that additional techniques are required to separate them [NK92]. However, this does not pose a problem in our case since the q factor is employed as an adjustable multiplying constant to completely retrieve the PCM image from

²although the proposed method works despite of this restrictive hypothesis as discussed later

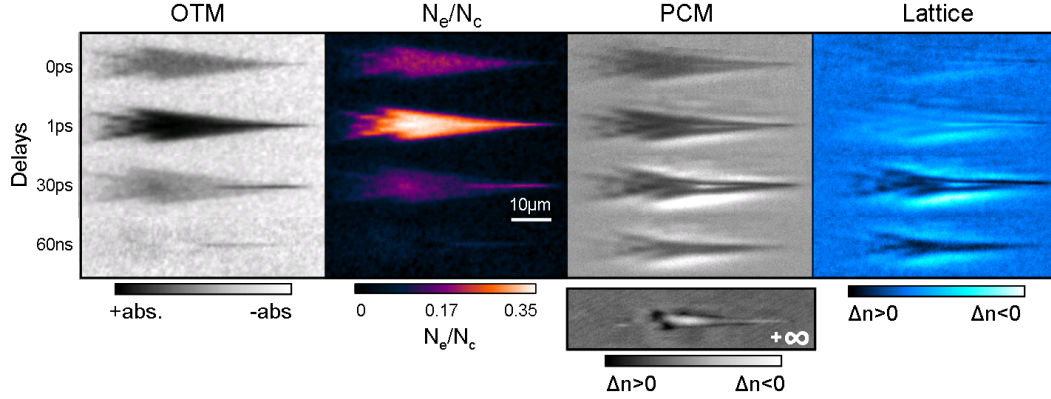


Figure 6.2: Illustration of the steps of the proposed calculation method to extract the matrix phase variations from time-resolved pictures of BK7 glass at various delays in the high energetic regime of photoinscription ($4.3 \mu\text{J}$, 150 fs pulse focused at $\text{NA} = 0.45$ and $\text{NA}_{\text{eff}} = 0.42$). The maximum detectable absorption under OTM was found at 1 ps . From left to right: OTM picture; calculated $\frac{N_e}{N_c}$; PCM picture; subtraction of the PCM picture with the $\Delta n_{x,z}$ calculated from the $\frac{N_e}{N_c}$ map. See text for details.

the calculated $\frac{N_e}{N_c}$ 2D-map. If the PCM image carries absorption variations, these are taken into account anyway by finely tuning q factor. This obviously does not affect the subtraction of the free carriers contribution at longer delays as the electronic decay is obtained from the OTM pictures. More important is the assumption that the OTM pictures deliver just the electronic contribution, an hypothesis that gradually loses its validity for delays surpassing the free carrier recombination time. However, we precise that in the imaging conditions related to the pump probe investigations, the permanent damage were most of the time undetectable in the OTM configuration for the pulse energies treated in this chapter. In the following, we thus consider that the OTM pump-probe images presented hereafter denote the free electronic variations only (unless differently specified).

6.3 Influence of the pulse length on the free carrier generation above the modification threshold

The differences between femtosecond and picosecond irradiations of bulk dielectric materials were already investigated from their respective permanent modifications [SFH⁺96b, BBS⁺07, MBM⁺08, MMR⁺08]. In fused silica, a stronger energy confinement leading to more contrasted and compact bulk modifications in the case of picosecond pulses was reported and verified by NLSE simulations [BBS⁺07]. For the first time, these observations are correlated with the transient free electronic density deduced from time-resolved microscopy images.

Fig. 6.3 a) presents the $\frac{N_e}{N_{cr}}$ map for pulse energies ranging from 0.12 to $4.4 \mu\text{J}$ for a 150 fs

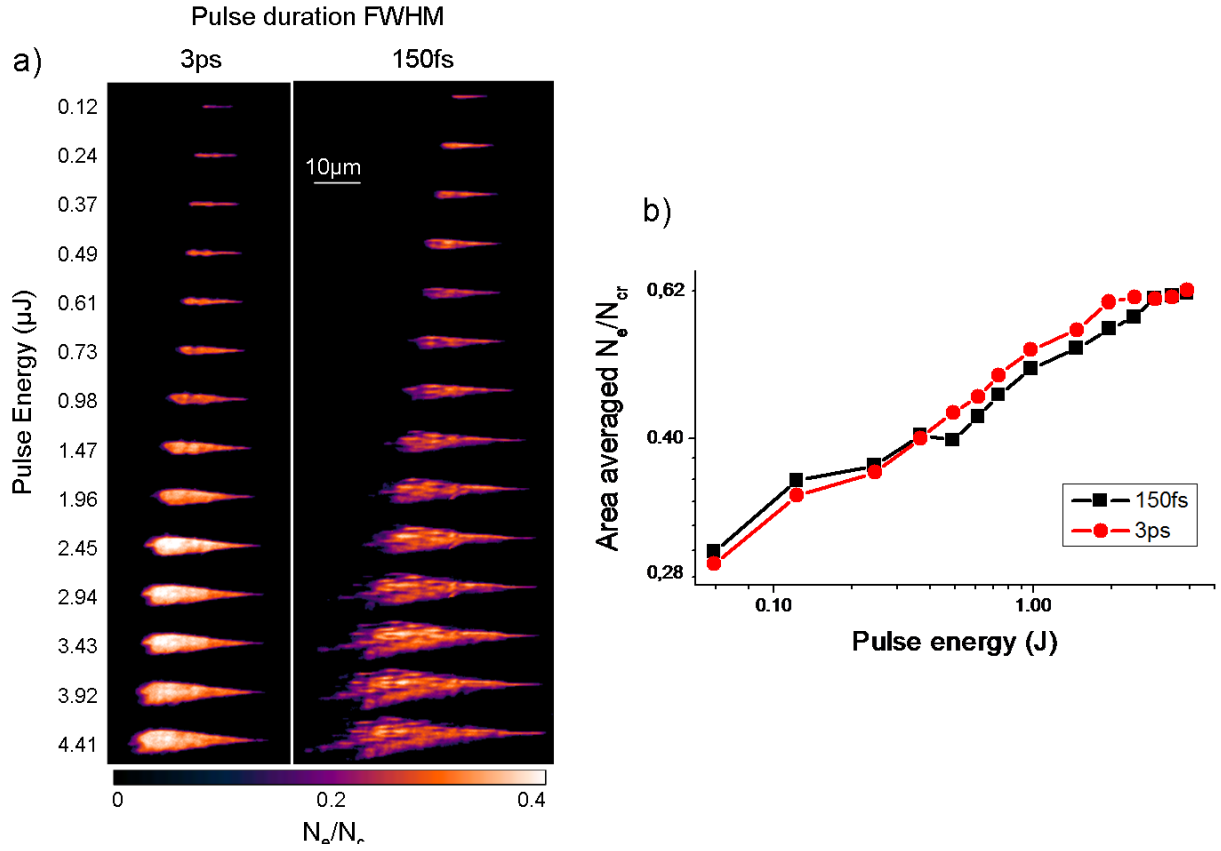


Figure 6.3: Intensity dependence of the transient electronic density N_e normalized to N_{cr} for femtosecond and picosecond pulse at $NA = 0.45$ and $NA_{eff} = 0.38$. a) Side $\frac{N_e}{N_{cr}}$ mapping from optical transmission microscopy pictures following Eq. 6.3. The laser comes from left. b) Averaged $\frac{N_e}{N_{cr}}$ versus the pulse energy over an identical volume for picosecond and femtosecond cases on logarithmic scales.

pulse and a 3 ps pulse at 200 μm deep in fused silica. Pixels belonging to the background ³ were set to 0. We mention here that for energies above 0.5 μJ , the permanent modification is much smaller than the pictured electronic gas for the femtosecond pulse as already reported in detail in [Mer07]. It is also the case for the picosecond pulse but on a much smaller scale. The optical delay was set to maximum absorption for the femtosecond pulse, corresponding the pump and probe overlapping. It is assumed that at this moment, only electronic excitation takes place. This delay was kept constant for the picosecond investigation as we experimentally checked that both pulses arrive synchronously. The pulse energy was varied using a polarizer and a half wave plate to ensure constant optical delay of the pump. The first aim of this study was to identify the main photoionization channels for the generation of the electronic plasma. As already mentioned in Chap. 3, a typical signature of multiphotonic ionization is the scaling of N_e with the n-power of the pulse intensity I , n being the smallest number of required 'simultaneous' photons to surpass the bandgap (n= 6 at 800 nm for fused silica). The avalanche mechanism is believed to imply an exponential [DLK⁺94, SFH⁺96a] dependence between I and N_e .

The identified photoionization channels in fused silica were clearly shown to be vastly dominated by multiphotonic ionization for fluences below permanent modification and in loose focusing conditions [QGM01, TSZ⁺06]. To be able to compare with these results which were obtained assuming an uniform excitation along the laser propagation axis, we averaged the electronic densities on identical volumes for the femtosecond and picosecond cases. The variation of $\frac{N_e}{N_{cr}}$ with the pulse energy is plotted in Fig. 6.3 b) on logarithmic axis. The slope of the curves indicate a similar dependency of the electronic density with the laser intensity $\propto I^{\frac{1}{2}}$ for both pulse durations which is obviously much slower than the expected $\propto I^6$ for MPI and $\propto e^{\alpha I}$ for avalanche ionization. While it is reported that femtosecond pulses rely more on a multiphotonic ionization process than longer pulses [JLS⁺03, TSZ⁺06], the present data does not show any preferential photoionization mechanisms between femtosecond and picosecond irradiations. In fact, both temporal shapes are characterized here by a much slower dependency with the laser intensity. This result is far from being contradictory with previous reports as the pulse energies investigated here are well above the modification threshold. We could not find a regime below the modification threshold with a detectable plasma at this NA= 0.45 where obviously less nonlinear propagation effects would take place. The reasons are probably related to our tighter focusing conditions than in [QGM01, TSZ⁺06]. However, the investigations were carried out at NA= 0.45 as we employed this focusing conditions for writing waveguides and other optical components (see Chap. 7). The reasons for the slower dependency of $\frac{N_e}{N_{cr}}$ with I are related to strong onset of nonlinear propagation effects (see end of Chap.2) that govern the efficiency of the energy transfer. We also have to mention the saturation of the available valence electrons as a possible cause for this behavior, how-

³i.e being closer than 10% to the background mean gray level value

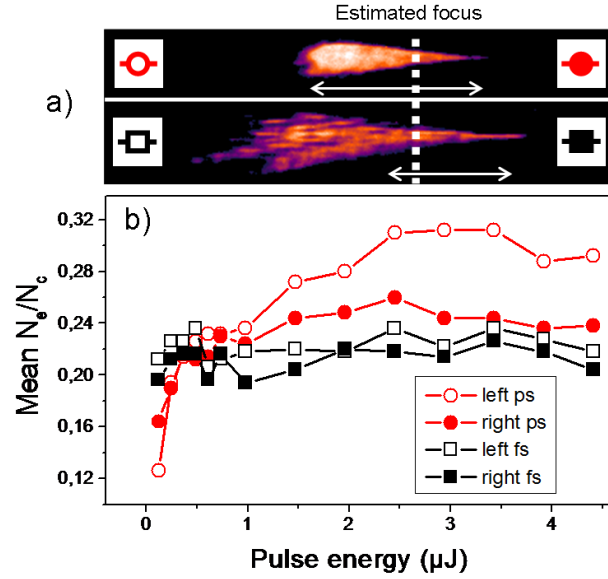


Figure 6.4: Intensity dependence of the electronic density map N_e normalized to N_{cr} for femtosecond and picosecond pulse in fused silica. a) Examples of transient $\frac{N_e}{N_{cr}}$ with indication of the estimated focal plane (dashed line) for femtosecond (bottom) and picosecond (top) irradiation. $\frac{N_e}{N_{cr}}$ was averaged on the left (empty) and on the right (solid) of the focal plane for femtosecond (circles) and picosecond (squares) and plotted vs the pulse energy in b). An overall saturation of the electronic density is clearly observable for the shorter pulse, whereas the picosecond irradiation permits a significant increase of the electronic density before the focal plane.

ever, the sub-critical densities estimated here tend to position this effect in a secondary position. Other mechanisms possibly participating in this saturation are discussed in Chap. 3.

The 2D-mapping of the electronic density along the laser propagation axis is the main interest of these experimental results. An exciting question would be: How correct is the hypothesis of an uniform excitation along the z-axis [QGM01, TSZ⁺06]. Fig. 6.4 provides interesting answers to this question. There, the electronic density is averaged for two parts of the plasma, one being in front of the estimated focal plane (called here "the head") and the other one ("the tail") being after as illustrated in Fig. 6.4 a). In the femtosecond case, the head and the tail know a relatively similar averaged electronic density despite of the pulse energy except on a small area in the head corresponding to the permanent white void where $\frac{N_e}{N_{cr}}$ is slightly higher as already observed in [MBR⁺09]. While the volume occupied by the electronic cloud incessantly increases (see Fig. 6.3 a) right), its density remains constant and identical in the head and in the tail as plotted with the black curves (Fig. 6.4 b)). Reasons for this behavior are linked with the efficient plasma generation that occurs soon in the pulse propagation. Note that the starting point of the plasma for femtosecond pulses is always positioned before the picosecond irradiation on the z-axis. This

plasma generation extents further as well. As explained in Chap. 3, the optical properties of the free carrier cloud are dominated by an increased absorption and a lower refractive index. The latter has a defocusing effect on the laser pulse. Thus, the region of main beam concentration is pushed further as the beam propagates and loses intensity due to the plasma absorption. Consequently, the zone of interaction is elongated with a quasi-constant electronic density.

On the contrary, picosecond sequences permit an increase of the electronic density with the pulse energy mainly in the head of the plasma (see Fig. 6.4 b)). The picosecond envelope induces a retarded, low density, and spatially modulated plasma. This creates a smaller negative shift for the incoming energy and less defocusing, helping thus to concentrate the energy. Additionally, the nonlinearity of excitation diminishes, allowing efficient absorption only in a restricted region.

These time-resolved experimental results are the first to experimentally evidence in details the wide difference of energy deposition between femtosecond and picosecond pulses above the modification threshold from 2D-mapping of N_e . This was already predicted by NLSE simulations [BBS⁺07]. We show that the zone of higher electronic density in the case of picosecond pulses is situated in front of the focal plane with a low variation in volume while femtosecond pulses tend to generate a quasi-uniform plasma over volumes increasing with the pulse energy.

6.4 Mapping of the transient free electronic density and the matrix phase in BK7 and fused silica

In this section, we employ the method previously described to characterize both the transient electronic density and matrix phase in BK7 and fused silica glass. The process enables an advanced and original topological study of these entities along the propagation axis, showing distinct mechanisms of energy deposition during a single pulse interaction. As an illustration, Fig. 6.5 presents examples of OTM and PCM images from which the transient electronic density and matrix phase are numerically extracted (see Sec. 6.1 and Chap. 3). The results are discussed in the following. The photoinscription regime investigated is that of the higher energetic range described at the beginning of Chap. 5 where thermo-mechanical processes dominate the energy relaxation pathways. Precisely, the irradiation conditions are $4.3 \mu\text{J}$, 150 fs , $\text{NA} = 0.45$ and $\text{NA}_{eff} = 0.42$ for both BK7 and fused silica in this section.

6.4.1 Topology of the free carrier density and lifetime in BK7 glass

The possibility to draw the 2D-map of the electronic density in a plane comprehending the propagation axis is a fairly new possibility offered by our experimental set-up. It has evident interests for considering the linear and non linear light propagation effects and to understand the nature of

6.4. Mapping of the transient free electronic density and the matrix phase in BK7 and fused silica

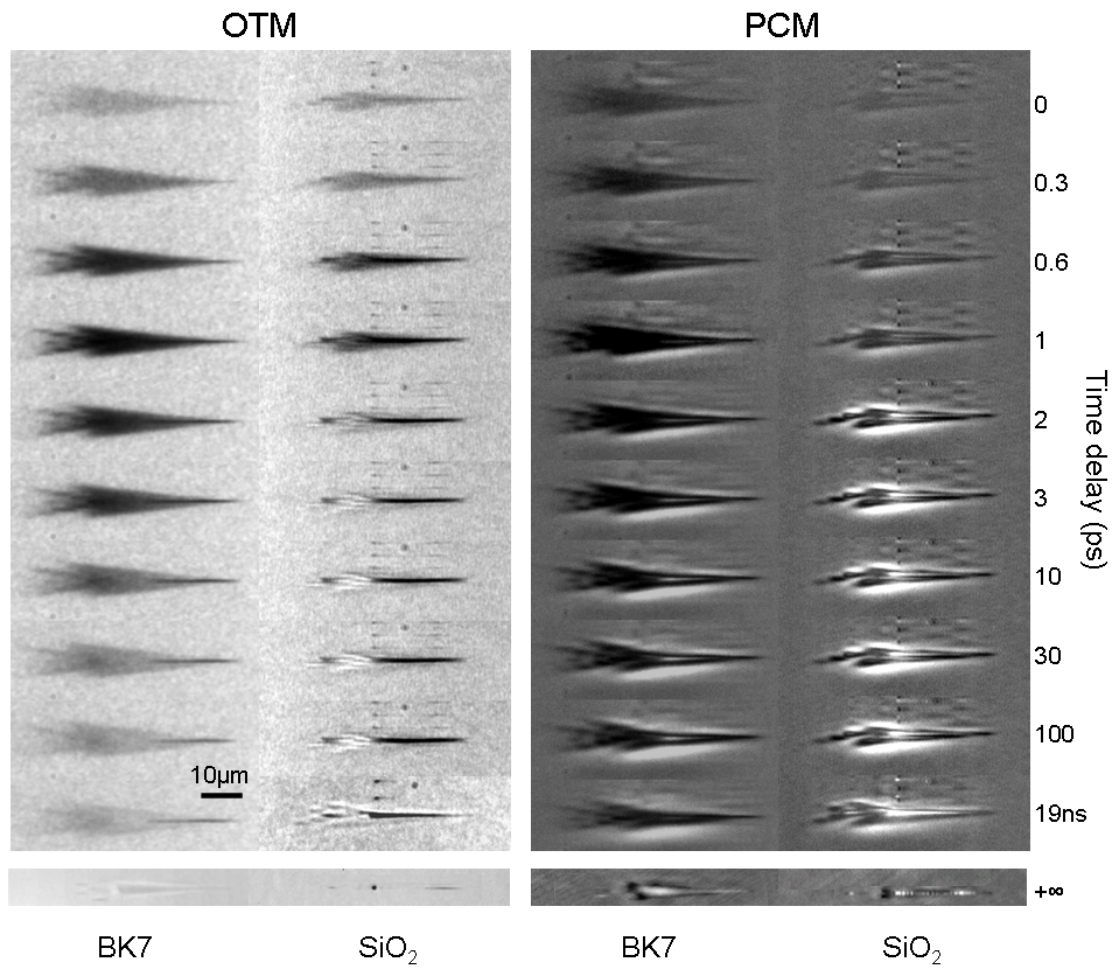


Figure 6.5: Selected time-resolved images with OTM and PCM in fused silica and BK7 glass in the energetic regime of photoinscription, $4.3 \mu\text{J}$, 150 fs , $\text{NA} = 0.45$ and $\text{NA}_{\text{eff}} = 0.42$.

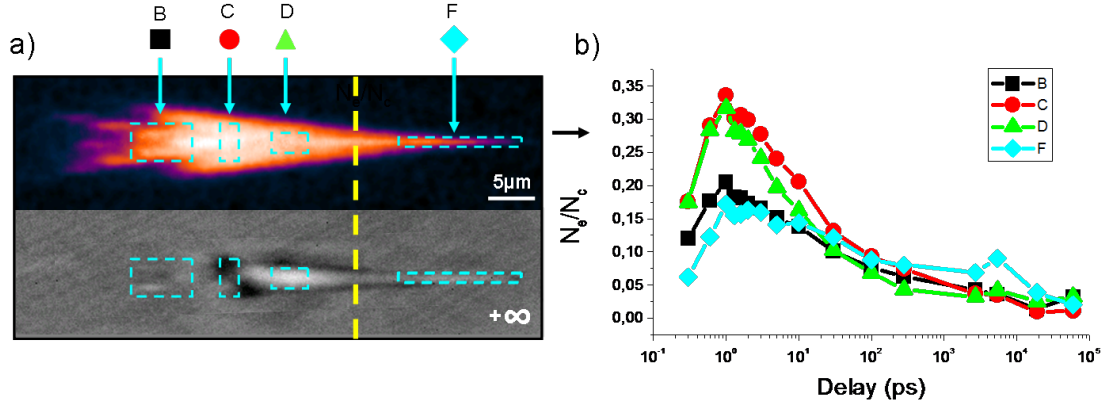


Figure 6.6: Electronic densities as a function of the optical delay for various regions of the irradiation volume in BK7. The conditions are the same as Fig. 6.2. a) $\frac{N_e}{N_c}$ map at 1 ps (top) with a PCM picture of the permanent modification (bottom) at the same scale. Areas of interest are designated by the letter B,C,D,F for which the decay is plotted in b). The dashed line represents the estimated geometrical focus.

the energy deposition along the z -axis. We try to exploit in the following the rich set of informations from these pictures. Fig. 6.6 shows the electronic density as a function of time and space in BK7 glass under the same conditions as in Fig. 6.2. The temporal electronic decay was calculated from a first order exponential fit of the data showed in Fig. 6.6 b). The electronic lifetime in B, C and D regions is respectively 13 ps, 12.5 ps and 9 ps which is close to values recently reported on the zone of non-permanent modification (8 ps-[Mer07]). Interestingly enough, the area of the tail (F) unambiguously shows a much longer recombination time of 30 ps. This tendency is confirmed when mapping the lifetime along the z -axis as shown in Fig. 6.7.

First of all, the electronic density is quite low in the left region [B] where very little modification take place. The corresponding pre-dots are discussed in the previous chapter. Higher electronic densities are associated with the central white area [D]. From there, the free carrier density decreases until the tail of the modification while the electronic recombination time grows by a factor of almost three as compared to the rest of the trace (see left data of Fig. 6.7). This observation is the signature of a difference in the modification processes in the central part [D] and in the tail of the laser-induced structure [F]. A temperature elevation scenario followed by thermal elasto-plastic deformation succeeds in explaining the central white region of lower density surrounded by a compressed layer (darker) [MBM⁺08]. From the time-resolved $\frac{N_e}{N_c}$ map, this main region is associated with the highest electronic density and the quicker recombination time. The quick energy transfer to the matrix thus provokes the strongest local increase of the temperature of the interaction zone. Having in mind the small softening point of BK7, a phase transition is likely to occur in this area followed by a movement of the heated material from the high energy density

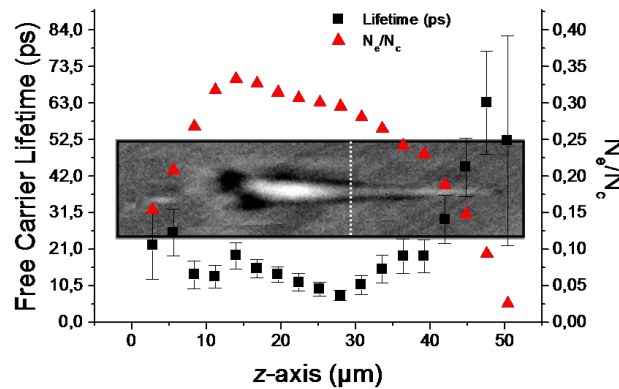


Figure 6.7: Electronic densities and free carrier lifetime along the laser propagation axis in BK7 . The PCM picture of the corresponding permanent modification is shown to scale in background. Irradiation conditions: $4.3 \mu\text{J}$, 150 fs , $\text{NA} = 0.45$ and $\text{NA}_{eff} = 0.42$

region to the interface with the cold bulk, confined by the internal pressure of the cold material.

This "thermal" model [SB02, MBM⁺08] is thus associated here with the white region which clearly dominates the permanent modification. It is therefore reasonable to state that thermo-mechanical mechanisms prevail in the BK7 response to the laser excitation. At the end of the tail [F], the electronic density is lower while the recombination time is longer, which tends to show that the mechanisms in play are different in this region with presumably less thermodynamics. It is known that a lower electronic density possibly triggers a softer modification based on relatively rarefied defect generation (or colored-center model discussed in [SB02]) with the generation of mostly boron oxygen hole centers. In fact, when an electron leaves the valence band, an exciton may be formed from the binding of an electron and a hole by Coulomb attraction [MQG⁺04] (see also Chap. 3). This entity creates an intermediate energy level in the band gap which in turn possibly opacify, depending on the energy value, the probing light and the density of defects. Given the wide variety of species forming the BK7 glass, it is reasonable to expect sufficiently opacifying excitons to be detected on the OTM transient pictures. Consequently, the recombination time of the excitons presumably affects and elongates the observed electronic lifetimes in the tail region. If this explanation sounds satisfying, it also tends to explain the dilemma between the thermal and the colored center models discussed by Streltsov *et al.* [SB02] as both mechanisms occurring in distinct areas are observed. We now turn to the matrix investigations.

6.4.2 matrix dynamics after ultrashort irradiation in BK7 glass

The new procedure to extract the matrix contribution was employed to obtain the data presented in Fig. 6.8 in the same irradiation conditions. Again, we chose a few regions of interest to better

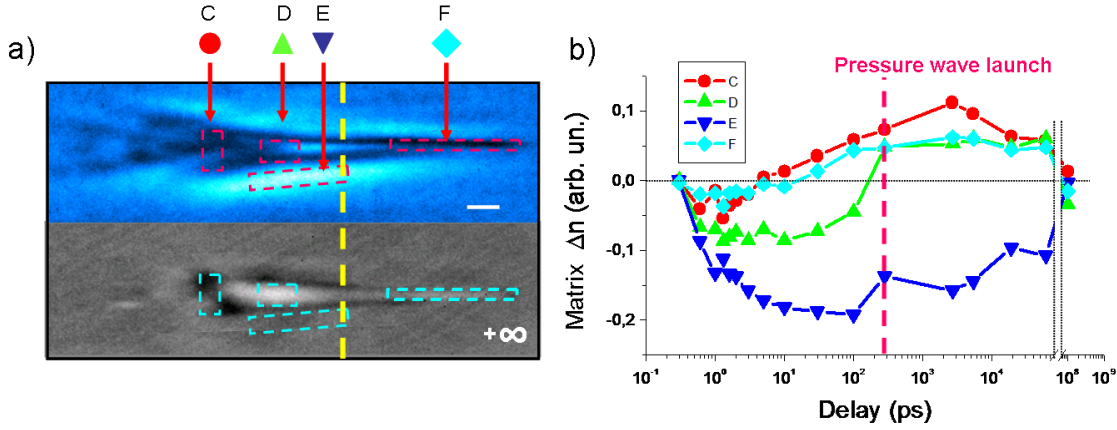


Figure 6.8: BK7 matrix qualitative phase mapping of the interaction region on ultrashort time scales. a) matrix map at 30 ps (top) with a PCM picture of the permanent modification (bottom) at the same scale. Areas of interest are designated by the letters D and F for which the transient variations are plotted in b). The horizontal line in b) shows the background level.

illustrate the following discussion. Let first consider the area labeled 'D' which corresponds to the main white zone of the permanent modification. Following its dynamics in Fig. 6.8 b), we can note a quite rapid decrease of its refractive index during the first few picoseconds [Mer07]. This presumably lower density region then knows a sudden increase of the refractive index (or density) at 300 ps, the precise moment where we observed a strong spherical pressure wave launched from the laser-induced structure [STS⁺07]. This compression wave is discussed in the following paragraphs. As already pointed out from the electronic density mapping, the material experiences a temperature elevation in this area involving a mechanical constraint. This results in a deformation beyond the elastic limit launching a pressure wave accompanied in an sudden variation of the transient local density (Fig. 6.8 b)). The dynamics confirm the synchronism of this brutal change of the matrix density with the pressure wave launch. However, the reasons for a density increase after the pressure wave launch are more difficult to address. In fact, a shockwave is normally followed by a rarefaction wave which is expected to brutally leave the material in a lower density state [JNT⁺06, MBM⁺08]. Here the inverse phenomena is observed which can supposedly be caused by a reflection of the pressure wave on the cold matrix surroundings, given the high energetic conditions of this photoinscription regime. Then, the 'D' area is slowly driven to a lower density state surrounded by a compressed shell upon cooling owing to the strong thermal expansion coefficient of BK7 [MBM⁺08]. A different scenario is envisaged for the zone labeled 'F' belonging to the tail where lower electronic densities are attained. Contrary to the 'D' zone, the release of the pressure wave apparently does not affect this area. After a slight decrease of the refractive index, the index variation turns positive above 10 ps, which is consistent with the formation of sufficient excitons

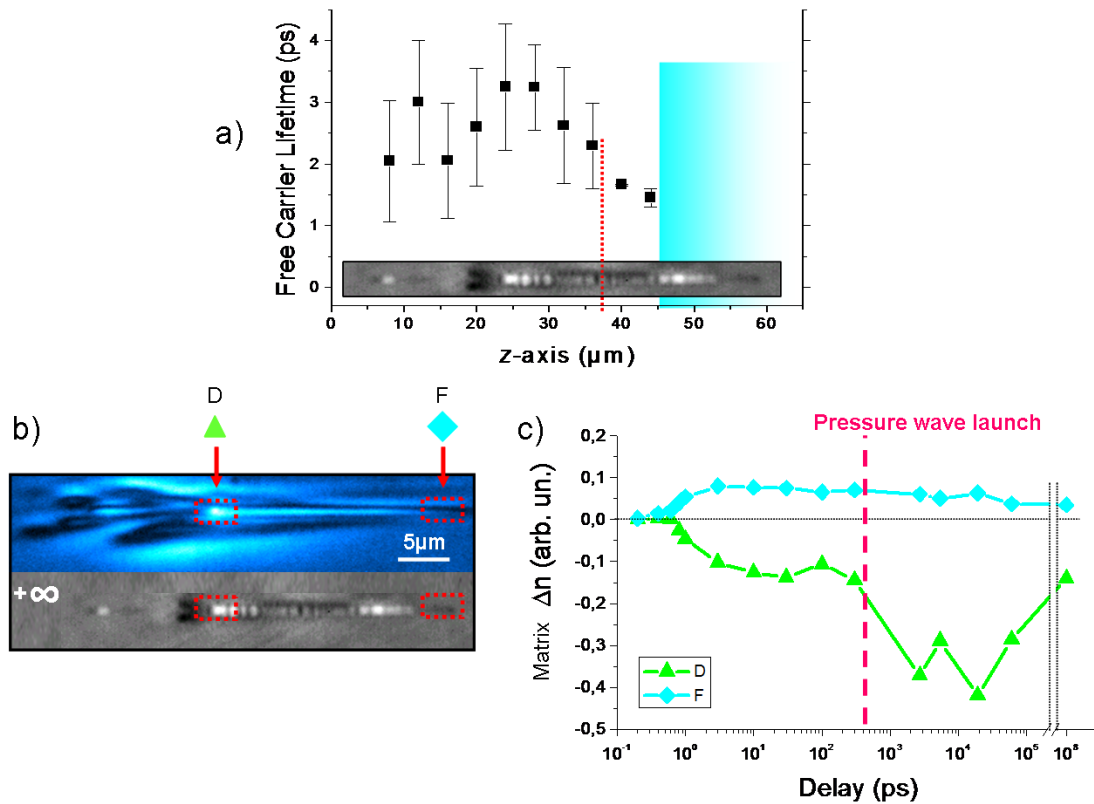


Figure 6.9: Electronic density and matrix variations in fused silica. a) Free carrier lifetime along the laser propagation axis in fused silica. The PCM picture of the corresponding permanent modification is shown in background. b) matrix map at 30 ps (top) with a PCM picture of the permanent modification (bottom) at the same scale. Areas of interest are designated by the letters D and F for which the transient variations are plotted in c). The horizontal line in c) shows the background level. Irradiation conditions: $4.3 \mu\text{J}$, 150 fs, $\text{NA} = 0.45$ and $\text{NA}_{\text{eff}} = 0.42$

and less thermo-dynamical mechanisms.

6.4.3 Free carrier density and matrix changes in SiO_2 glass

The same procedure is applied to study the case of fused silica under the same irradiation conditions. The results are represented in Fig. 6.9. The electronic lifetime along the z -axis is depicted in Fig. 6.9 a). We underline here that the recombination time in fused silica is around 150 – 170 fs for fluences below the modification threshold [PDGM97, SJL⁺05a], a duration inferior to the temporal resolution of our set up. Therefore, the lifetime results shown in Fig. 6.9 a) are to be taken with caution. Regarding the electronic lifetime in the tail of the structure (blue area in Fig. 6.9 a)), we precise that its estimation from OTM pictures employing the described method may lead to

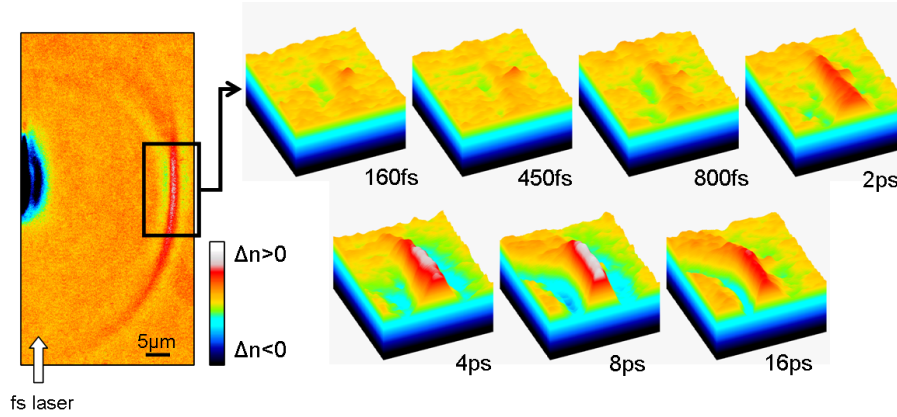


Figure 6.10: Pressure wave picturing from PCM images for various pulse duration in fused silica at constant pulse energy. ($4.3 \mu\text{J}$, 150 fs , $\text{NA} = 0.45$ and $\text{NA}_{\text{eff}} = 0.42$)

wrong ideas as permanent damages are detectable in the OTM images. It is therefore disputable to suppose that only the free electrons are responsible for the contrast of OTM pictures. We underline however that the decrease of transmittivity in the tail lasts at least one hundred of picosecond (as observed in [CXW05, Mer07]). In the high energetic regime studied here, the hot laser-induced electronic bath alters the overall capacity of the material matrix to participate in the free carrier recombination because of a drop of the matrix deformation potential. Thus, the free carriers experience a very long recombination time. More insights can be obtained from the matrix transient phase estimation (Fig. 6.9 b, c)). The matrix phase variations observed in the regions labeled 'D' and 'F' are in perfect agreement with previous measurement [Mer07] indicating the onset of thermomechanical phenomena in 'D'. There, the launch of the pressure wave is again clearly linked with a sudden change of the density.

6.5 Pressure wave characterization in glass

Usually, upon energy relaxation, the temperature increase induces a corresponding pressure increase which relaxes via thermal expansion and shock generation. In the following paragraphs, we present PCM transient pictures showing the launch of a pressure wave (PW) subsequent to the laser irradiation. We show that the PW amplitude is a good indicator of the nature of the energy transfer from PW characterization in fused silica under various pulse lengths. We report on the launch of a secondary weaker PW in fused silica a few ns after the first one. We then qualitatively compare the pressure wave aspect in fused silica, BK7, TeO_2 and SF57 glass.

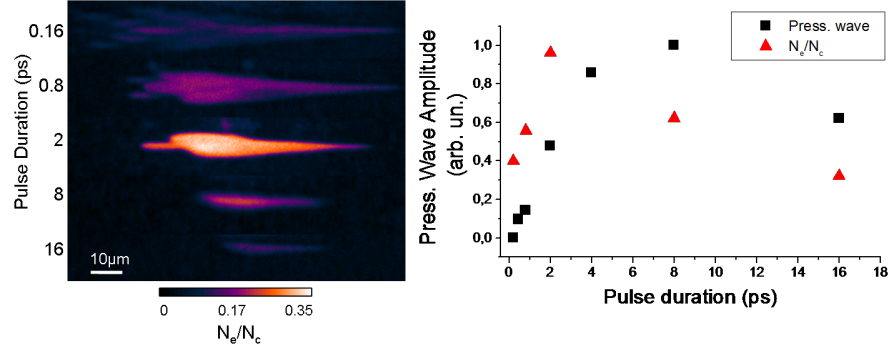


Figure 6.11: Comparison of the $\frac{N_e}{N_c}$ and the PW amplitude for femtosecond to picosecond pulse durations in fused silica. a) $\frac{N_e}{N_c}$ map calculated from OTM pictures. b) Comparison of the $\frac{N_e}{N_c}$ (triangles) and the PW amplitude (squares). Pulse energy: $4.3 \mu\text{J}$, $\text{NA} = 0.45$ and $\text{NA}_{eff} = 0.42$

6.5.1 The pressure wave as an energy transfer indicator in fused silica

Fig. 6.10 shows the qualitative amplitude of the generated PW for various pulse duration in fused silica in the same high energetic thermo-dynamic regime. As already reported [HKP04], the PW has a spherical shape. The refractive index variation associated with the traveling wave is supposed small enough to remain within the linear response of the PCM measurement ([NK92] permitting the comparison of their amplitude. The general observation of a stronger PW in the case of picosecond pulse sequence has already been made [HKP04], however the present results allow to precisely find the optimal pulse length to obtain the largest PW amplitude (here 8 ps). Remarkably, the launching moment is identical for all the pulse durations involved here, denoting a similar energy coupling mechanism differing mostly in its efficiency and not in its chronology. We correlate these PW amplitudes with the corresponding free electronic densities at the delay of maximum absorption in Fig. 6.11.

In agreement with our previous investigations on the transient electronic densities versus the pulse duration (see the beginning of the chapter), the picosecond sequence is characterized by an enhanced energy confinement leading to a stronger pressure wave. Apparently, the optimum pulse duration maximum electronic density does not corresponds to the maximum amplitude of the PW, however, this observation has to take into account the temporal window over which the electronic density is estimated. More precisely, for a pulse longer then this temporal resolution, the electronic density is naturally underestimated if calculated from a single optical delay which explains the discrepancy. Hence, the measurement of the amplitude of the PW constitutes a choice indicator of the energy coupling as it does not suffer from this temporal slicing.

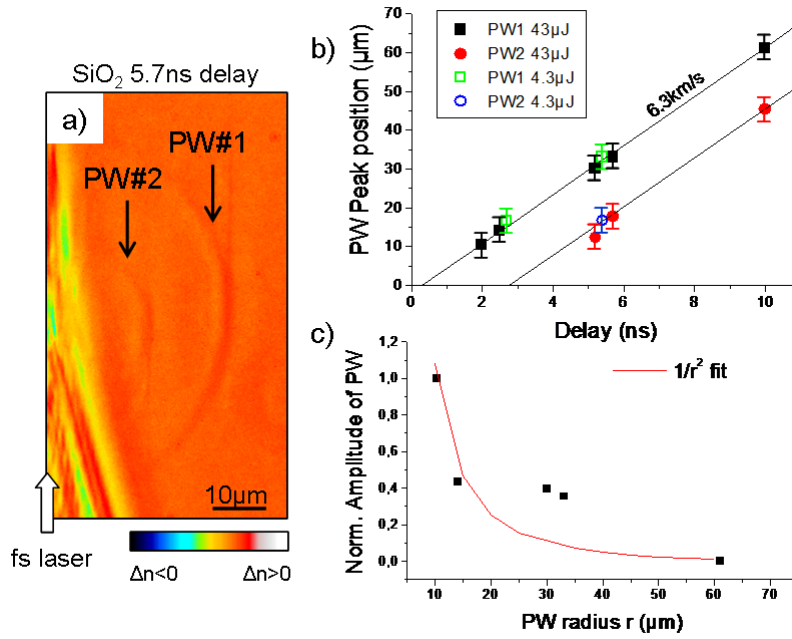


Figure 6.12: Evidence of two pressure waves from a single femtosecond pulse irradiation in fused silica from a transient PCM picture a). b) Determination of the traveling speed. c) Amplitude decay of PW1 as a function of radius. Pulse energy: 40 μJ , NA= 0.45 and NA_{eff} = 0.42

6.5.2 Double pressure wave generated in fused silica

We could observe the launch of a secondary weaker pressure wave in fused silica glass for sufficiently short pulse durations (below 500 fs) only. Interestingly enough, we could not detect this behavior in the other investigated glasses (BK7, TeO₂, SF57). This secondary PW has a quasi-identical shape as the first main PW, however its center seems a little ahead on the propagation axis, closer to the permanent white region and its amplitude is $\approx 30\%$ lower. Fig. 6.12 a) presents the corresponding picture for a 43 μJ , 150 fs pulse with NA= 0.45 and NA_{eff} = 0.42. This high energy regime ease the PW detection, however, they are also detectable around the modification threshold. In that case, the PW are concentric. Interestingly enough, the dense shock front is followed by a rarefaction wave [JNT⁺06]. Fig. 6.12 b) shows the PW radius variation with the temporal delay for both waves. A sonic speed of 6.3 km.s⁻¹ is found from linear regression for both PW and the launch of the first PW is estimated below the nanosecond time delay. This event occurs during the sharp density change of the matrix underlined in the previous section, indicating their close relation. The second PW is released 1 \sim 2 ns after the first one and is presumably due to local rupture of the material following the rarefaction wave coming after the first shock release [JNT⁺06]. As expected, the amplitude decay of the PW scale with $\frac{1}{r^2}$ with r being the PW radius [DZF⁺91].

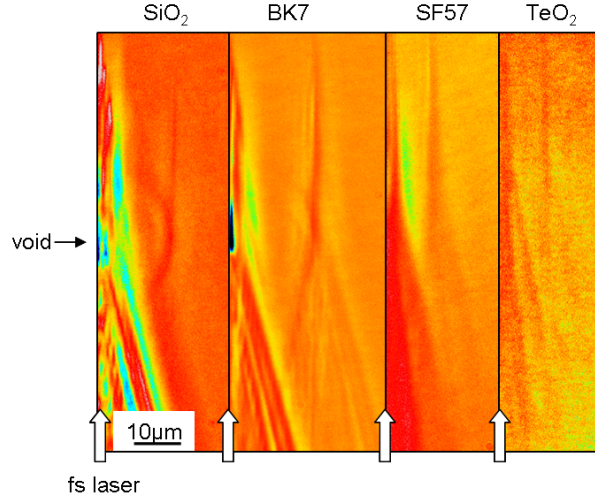


Figure 6.13: PCM pictures of the pressure wave of (left to right) fused silica, BK7, SF57 and TeO₂ glass resulting from a femtosecond pulse irradiation at NA= 0.45 and NA_{eff} = 0.42.

6.5.3 Morphology of pressure waves in other glasses

We found that the morphology of the pressure wave in fused silica is very specific to this material. The quasi-spherical morphology even at high fluences was not retrieved in the other glasses involved in this study. Fig. 6.13 illustrates this with PW from fused silica, BK7, SF57 and TeO₂ glass. Note the particular PW form in the BK7 case. Surprisingly, the topology of the focusing cone is precisely reproduced in the traveling PW while a spherical component remains. As the amplitude of the PW depends on the initial temperature increase and on the material mechanical properties [STS⁺07], it is understandable that the ensemble of regions with a sufficient temperature increase and high enough thermal expansion coefficient (as for BK7 glass) participate in the formation of the PW. In fused silica, the reduced thermal expansion coefficient restricts the PW source regions to a restricted volume yielding a quasi-spherical PW. In SF57 and TeO₂ glass, the observed PW has a comparable contrast as the permanent modification region. This is explained by their very high thermal expansion coefficient. as a general comment, the PW morphology tends to reflect the growth of the heat source.

6.6 Time-resolved investigations of temporally shaped pulses

Temporal shaping has been shown to offer increased flexibility in material processing [ERH⁺07, SBT⁺03]. In particular, third order temporal phase masks were employed to improve the irradiation outcome on surfaces where the main issue concerned the generation of dense enough electronic plasma on nanoscales at surfaces [ERH⁺07]. If the physical mechanisms to be controlled

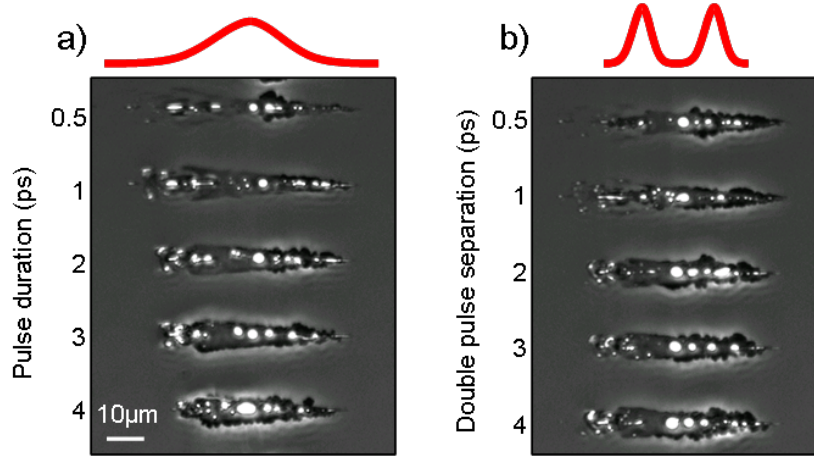


Figure 6.14: PCM pictures of permanent modifications in fused silica associated with a) picosecond irradiation with various pulse length and b) double pulse sequence with various temporal separation. The total pulse energy is $20 \mu\text{J}$ and $\text{NA} = 0.45$ and $\text{NA}_{\text{eff}} = 0.42$.

were logically identified, investigations on the transient plasma were not yet conducted for temporally shaped pulses. However, the need of time-resolved measurement of the electronic gas remains highly desirable as experimental proofs of the invoked physical phenomena and also to extent the technique of temporal shaping to a wider class of material processing.

Taking advantage of the possibility offered by the set-up to temporally shape the pump pulse, we carried time-resolved investigations for femtosecond, picosecond and double pulse irradiations in fused silica. Fig. 6.14 compares the outcome from picosecond and double pulse irradiation (each pulse masting $\approx 200 \text{ fs}$). Note the similarities in the permanent modifications for pulse lengths of $2 - 3 \text{ ps}$ and double pulse separations of $2 - 3 \text{ ps}$. The following question arises: how different ultrashort temporal envelopes can lead to quasi-identical bulk modifications? Hence, we conducted time-resolved investigations employing OTM on these particular pulse shapes. The free electronic density map was calculated from these images as previously explained. Fig. 6.15 presents an overview of the corresponding results.

The maximum electronic density is plotted versus time for the three pulse temporal shapes. We first remark the rather low free carrier density after $3 - 4 \text{ ps}$ associated with the femtosecond pulse. Before that, however, the electronic density experiences a peak to $0.4 \times \frac{N_e}{N_c}$ at the passage of the ultrashort pulse. This relatively high density quickly decreases as propagation non linearities spreads out the energy delivery. On the contrary, the reduced amount of plasma defocusing for picosecond sequence allows for more confined energy deposition where the major part of the pulse interacts with a free electronic plasma. This renders possible an efficient energy absorption through inverse bremsstrahlung, augmenting the electrons kinetic energy along with the avalanche efficiency. A long-lasting density superior to $0.4 \times \frac{N_e}{N_c}$ is thus obtained.

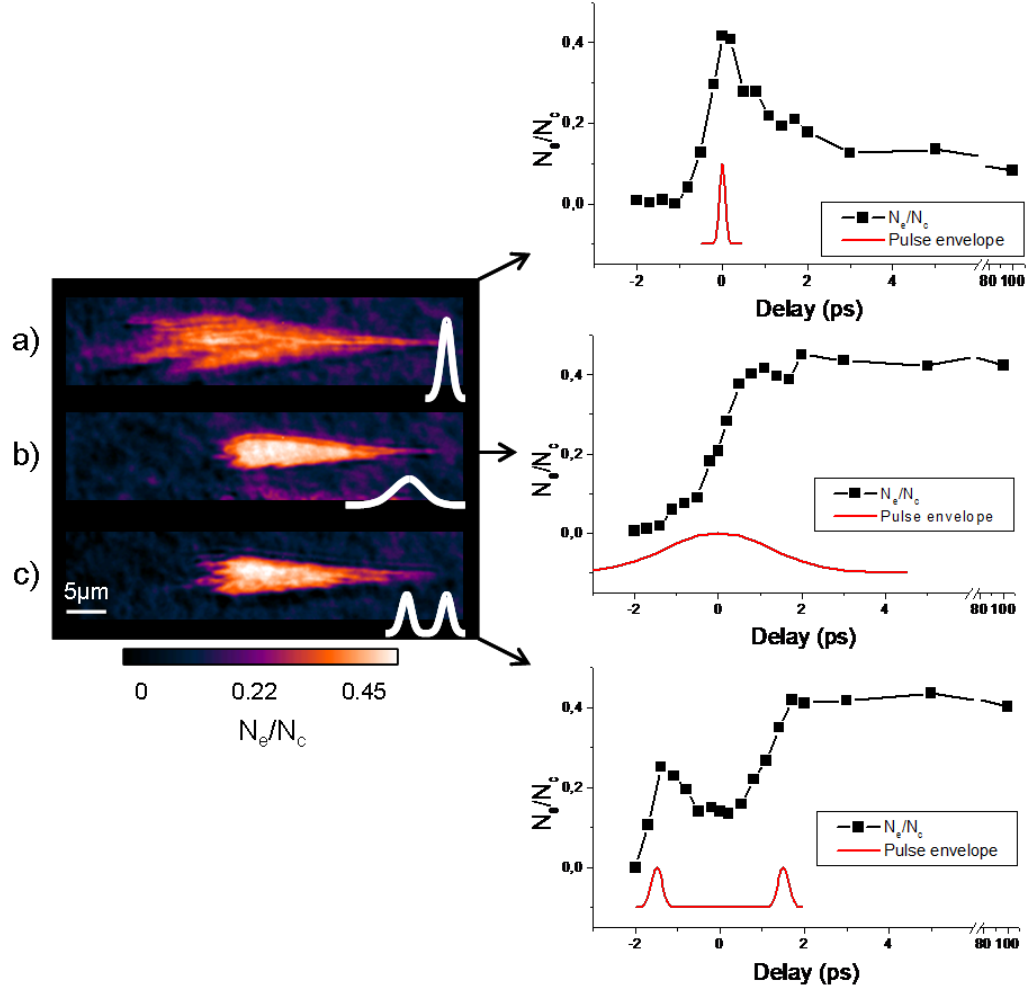


Figure 6.15: Calculated transient $\frac{N_e}{N_c}$ for single irradiation with a) a 150 fs pulse, b) a 3 ps and two pulses separated by 3 ps. Each irradiation sequence carries an energy of $6 \mu\text{J}$. Left column: example of the $\frac{N_e}{N_c}$ 2D map corresponding to the delay of maximum free carrier generation. Right column, Temporal evolution of the maximum $\frac{N_e}{N_c}$ with indication of the irradiation envelope. Picosecond and double pulse sequences generate a $\frac{N_e}{N_c}$ three times higher than the femtosecond case. $NA = 0.45$ and $NA_{eff} = 0.38$.

The time resolved mapping of $\frac{N_e}{N_c}$ in the case of the double pulse sequence permits to unequivocally account for the similarities between the corresponding permanent modification and the picosecond one. Fig. 6.15 c) left shows that the electronic density experiences two successive increases synchronized with each of the light pulse. The significant phenomena concerns the effect of the second pulse which interacts with a still hot electronic gas, even though a certain decay has already taken place. Thus, the energy of second light pulse is efficiently absorbed through inverse bremsstrahlung by the free electrons. There, the electronic density is multiplied by a factor three to surpass $0.4 \times \frac{N_e}{N_c}$. Note that the cloud is almost as confined as for the picosecond pulse (Fig. 6.15 b)).

6.7 Pump-probe picturing in type II waveguide writing regime in fused silica

Extending the pump probe investigations to the multipulse regime is an unavoidable step to take when aiming at understanding the physics of waveguide writing for example. A number of exciting interrogations can be addressed, among those is found the question of the effect on the energy deposition of an already present laser-induced modification. In Chap. 5, a processing window for writing of polarization sensitive waveguides in fused silica is discussed. The structures are obtained with the accumulation of hundreds of pulses and present highly birefringent rippled structuration on the nanoscale revealed by SEM and appearing white under PCM. While the production of these kind of ultrafine structures in the bulk is already mastered and trigger an increasing interest for applications [THS08], the physical phenomena leading to the formation of this well-ordered nanosheets are still vastly discussed. Taylor *et al.* propose the so-called nanoplasmonic model where the notion of field enhancement at the edges of the nanoplasmas is the corner stone. In short, randomly laser-induced hot-spots due to localized inhomogeneous nonlinear multiphoton ionization at defects or rugosity evolve towards nanoplasmas after several pulses owing to a augmentation of the ionization rate due to the memory of a previous ionization [RGS⁺06]. At the boundary of these growing nanoplasmas, field enhancement takes place resulting in an asymmetric growth perpendicularly to the laser polarization via field-induced polarization and deformation. The growth eventually leads the initially spherical nanoplasmas toward an arrangement of nanosheets whose spacing is dictated by the lowest order optical mode whose field distribution reinforces the growth of the nanoplanes (no closer to each other than half of laser period). As a main experimental result supporting the theory, the transition from nano-ellipsoids to nanoplanes with increasing number of accumulated pulses was reported from post-mortem sample analysis [THS08].

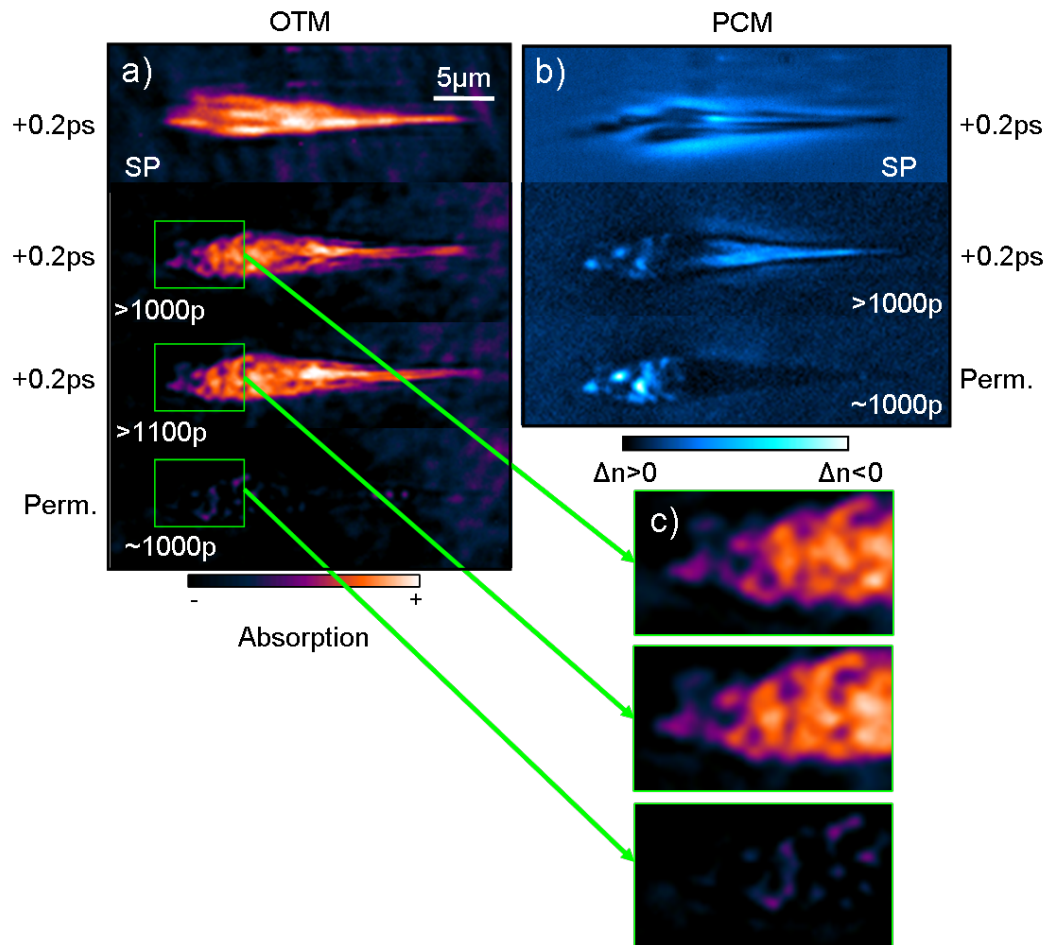


Figure 6.16: Time-resolved OTM (left) and PCM (right) pictures in single and cumulative regime corresponding to type II waveguide writing i.e 180 fs, 1000 pulses, $1.5 \mu\text{J}$ at $\text{NA} = 0.45$ and $\text{NA}_{\text{eff}} = 0.42$. 'Perm.' refers to permanent modification.

Quite evidently, the possibility for time-resolved investigations in this cumulative regime may play a decisive role in validating the nanoplasmonic model. More precisely, the field enhancement phenomena should lead to a detectable variation visible on transient OTM and/or PCM images. Therefore, we placed ourselves close to the type II waveguide writing regime in fused silica where the rippled nanostructures are inevitably formed. Fig. 6.16 presents pump probe PCM and OTM pictures in single pulse (SP) and after 1000 pulses in fused silica. Neither the calculation of the electronic density nor the matrix phase separation were conducted here because the presence of the permanent modification strongly affects the contrast and therefore the $\frac{N_e}{N_c}$ and matrix phase calculations. However, the transmission and phase contrast pictures are sufficient to support the following discussion.

We first note the similitudes between the SP regime and the cumulative regime on the OTM pictures (Fig. 6.16 a)). Interestingly enough, the area of the detected transient electronic cloud in SP matches perfectly the permanent modification region. We mention here that a much higher number of pulses (1000) leads to a relatively little size increase of the laser-induced transient structure (see Fig. 5.14) showing that a certain saturation occurs after a sufficient number of pulses in the region of the electronic cloud. In fact the transition from 100 to 1000 pulses brings the most significant change in the head which turns to white under PCM and start to show birefringence (see Fig. 5.14). Looking more precisely to the transient absorption at the head of the trace in Fig. 5.14 c) evidences a very interesting phenomena. After 1000 or 1100 pulses, the random topology of the absorption remains identical and shows precise morphological resemblance with the permanent modification. Noteworthy, this topology strongly differs from the SP absorption map whose topology is mainly governed by Fresnel propagation⁴. Thus it appears that the pre-existing bulk modification governs the energy deposition cartography and the consecutive absorptive plasma spatial distribution. This observation pleads in favor of a local reinforcement of preexisting structures which tend to confirm the mechanisms of field enhancement proposed by the nanoplasmonic model. However, the micrometric spatial resolution offered by the microscope can not totally confirm this behavior on the nanograting scale. Therefore, this reasoning has to be considered prudently but the perspective of conducting this time-resolved investigations with a sub-micrometer spatial resolution becomes highly promising. We add that the overall absorption level is significantly reduced after 1000 pulses when compared to the SP regime. This is an evident consequence of light scattering and diffraction due to the already-present bulk modification, particularly on the nano structures present in the head. In fact, the corresponding scattered signal shows a relatively strong generation and diffraction of third harmonic light during multipulse irradiation [CMM⁺09].

From the PCM pictures shown in Fig. 6.17 b), it is interesting to compare the transient picture with the permanent modification. First, the head appears less bright on the transient picture than

⁴Note the appearance of pre-dots in the plasma. See Chap. 5

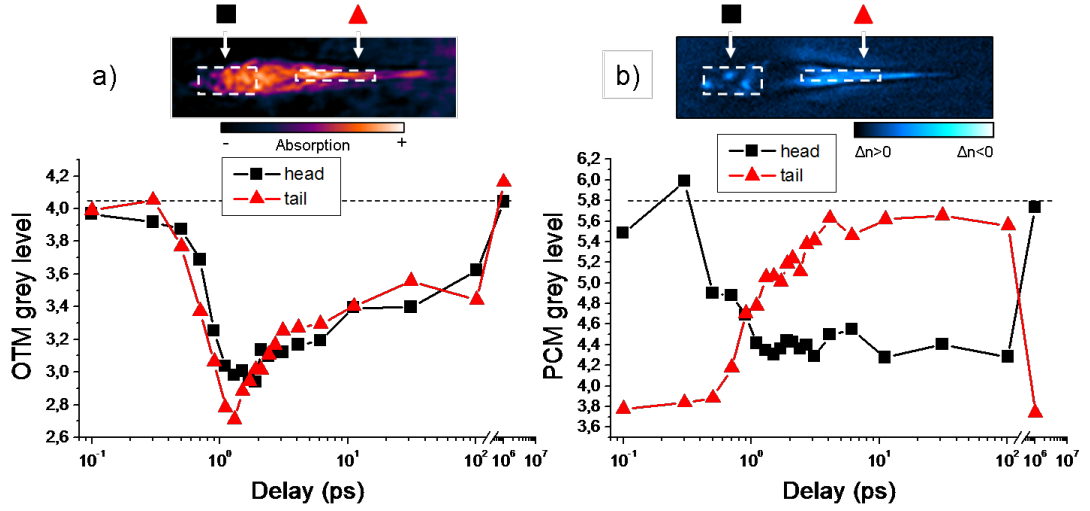


Figure 6.17: Details of the temporal evolution of the laser modification after 1000 pulses from OTM a) and PCM b) pictures. The mean gray level of the head (square) and the tail (triangle) of the trace is plotted versus time delay.

on the permanent structure due to the presence of the absorptive electronic cloud. Again the head topologies are similar. The tail transient imaging shows a bright area which appears dark on the permanent structure. In order to better understand the involved physical phenomena, the temporal evolution of the OTM and PCM signals is reported in Fig. 6.17.

We first mention the very similar absorption level and temporal variations for the head and the tail observed in OTM where no areas of significantly decreased transmittivity can be detected. The dynamic study (plot of Fig. 6.17 a)) shows a rapid increase of the absorption, witness of the generation of an electronic plasma at the pulse passage. Then a decay on the order of a few picosecond (as for SP regime) is observed evidencing the lengthening of the electronic recombination time and the creation of transient intermediate energy levels in the bandgap probably associated with excitons. As no changes were observed on the permanent modification before and after the 1001^{th} pulse, neither for the 1100^{th} , we believe the interaction area is beyond saturation which implies that the generated excitons relax without the creation of additional defects.

The PCM investigations (Fig. 6.17 b)) are now discussed. We mention here that this area corresponds to the 'D' area of the SP regime whose dynamics are reported on Fig. 6.9 c). As for the SP regime, the region shows a rapid increase of the refractive index at the pulse passage. If the dynamics after a few nanoseconds were not yet conducted to check on the sudden refractive index increase on the nanosecond associated with the pressure wave as observed in SP case, a significant indication of a similar behavior is found in the fact that this region most of the time shows one or a few permanent voids pleading for the onset of thermo elastic processes (see Fig. 5.14). The

reason for the non-systematic presence of voids in that region seems linked to the strong light scattering occurring on the trace head. This undoubtedly drops the amount of coupled energy in the tail and reduces the chances of sufficient mechanical constraint to drive the material beyond its elastic limit there. Besides, this limit may be altered in the tail of the permanent modification. Concerning the head of the trace experiences a slower increase of refractive index and/or absorption which stagnates at least over 100 ps. The corresponding gray level is darker than for the permanent modification while keeping the same random morphology. This denotes the presence of absorptive plasma in that region as already discussed above. It could also be due to a loss of birefringence upon electronic excitation which in turn averages the refractive index differences between the nanosheets. Time-resolved experiments with polarization-sensitive microscopy are in preparation.

Whereas the present results are not sufficient to entirely support the nanoplasmonic model proposed in [THS08] but they undoubtedly reinforce it. More precisely, we observed that the pre-existing modification governs the cartography of the transient electronic gas toward the permanent change topology. Therefore, the concept of field enhancement is verified in the region of nanostructures on the micrometric scale. Further investigations involving sub-micrometer spatial resolution as well as birefringent sensitivity are required to bring about a clearer conclusion.

6.8 Conclusion

In this chapter, an efficient experimental apparatus for time-resolved 2D microscopic mapping of the interaction area was presented allowing for temporally shaped irradiation. A new method to estimate the free electronic density as well as the matrix changes from the microscopic images is reported. The microscopic topology along the propagation axis of the bulk free carrier density and lifetime is reported for the first time. In fused silica, we demonstrate the more dense and confined character of the transient electronic plasma generated by a picosecond irradiation than a femtosecond one. Single pulse interaction regimes in fused silica and BK7 glass are studied and the free carrier lifetime cartography along the laser propagation axis reveals zones of longer recombination time associated with permanent modification. We show that the dynamics of the matrix changes temporally match the launch of a pressure wave which is studied in various glasses (fused silica, BK7, TeO₂ and SF57). In fused silica, the transient electronic density generated from femtosecond, picosecond and double pulse is calculated showing and explaining the more efficient free carrier generation and heating in the two latter cases. Finally, time-resolved measurements are conducted in type II waveguide writing regime where the accumulation of numerous pulses generates the formation of self induced nano gratings. The measured transient absorption is shown to follow the topology of the pre-existing structure which tends to confirm the field enhancement phenomena invoked by the nanoplasmonic model.

Chapter 7

Spatio-temporal laser beam control for bulk functionalization

This chapter presents demonstrative experimental results illustrating the main theme of this report i.e the benefits of laser spatial shaping and temporal pulse tailoring bringing about a significant breakthrough in the ultrafast laser bulk processing field. We first relate the possibility offered by temporal pulse shaping to ameliorate the energy coupling upon evolutionary optimization of the irradiation pulse in conditions of deep focusing. Then, spatial beam forming powered with self-improving learning algorithms is employed to overcome well-known limitations in longitudinal waveguide writing. Finally, we present a technique permitting multispot bulk processing through spatial phase modulation and the corresponding achievement of diverse embedded photonic devices (2D and 3D light dividers, light couplers, wavelengths demultiplexers).

7.1 Temporal tailoring for improved energy deposition

In this section, the evolutionary optimization loop is employed in connection with the pulse temporal shaping unit on the LRR laser system. Therefore, the optimization strategy focuses on tuning the relative delay of the femtosecond pulse spectral components in order to meet a desired bulk modification outcome. Here, the processing plane is intentionally positioned deep in a fused silica sample. Consequently, the intensity distribution is stretched along the z-axis with detrimental consequences on the irradiation outcome as already illustrated in Chap. 5. The adaptive loop is again utilized to counteract this elongation effect acting this time on the tailoring of the temporal shape of the pulse. If the scope appears similar as in Sec. 7.2, the technique relies here on the ability to influence propagation non linearities through temporal shaping.

Adaptive control of pulse temporal forms was recently used to control filamentary propagation

in nonlinear environments.[HKCL06, ASL⁺06] The location and the spectral properties of the ionization region were shown to be modulative. The key factor is the intensity feedthrough which determines the competition between self-focusing and ionization. Breakdown probability and shock waves generation were also observed to be controllable via temporal envelopes [SGYH06]. At surfaces, manipulation of pulse frequencies indicated sensible variations in the damage threshold [LHP⁺05]. Cubic chirp, spectral interferences, and asymmetric intensity envelopes have also shown surprising reduction in the damaged area, below the diffraction limit [ERH⁺07]. The balance between photo and collisional ionization mediates the localized formation of a hot electron population, taking into account the different process dependencies on intensity and radiation wavelength. All these observations indicate flexibility in manipulating nonlinear propagation, ionization, and energy gain events generated by ultrashort laser pulses in nonlinear environments. Intensity adjustment is a powerful control knob for directing the overall course of the laser-matter interaction. With a focus on refractive index modification processed in optical materials we address below some aspects generating spatial confinement of energy and structural modification in dielectric environments when the illuminated zone is elongated due to spatial wavefront distortions. An adaptive technique is used relying on programmable temporal pulse manipulation and feedback derived from optical microscopy observation of laser-induced structures in the presence of aberrations.

7.1.1 Experimental details

Single pulses from the LRR system (see Chap. 4 of $1\ \mu\text{J}$ were focused inside parallelepipedic fused silica ($\alpha\text{-SiO}_2$) samples at various depths by a microscope objective (numerical aperture $\text{NA}=0.45$ and $\text{NA}_{\text{eff}}=0.42$). Detection of the relaxed structures is realized in-situ by the above-mentioned positive optical phase-contrast microscope.

The self-learning feedback loop[JR92] connects the microscopy detection and the temporal shaping control unit, guided by an adaptive evolutionary algorithm. Exploring the search space, the algorithm manipulates spectral phase patterns, varying in turn the temporal pulse envelope. An objective functional is defined by analyzing the axial morphology of the photo-inscribed phase object. The maximization of the functional defines the success of the irradiation sequence.

7.1.2 Results and discussion

Static and dynamic bulk photo-induced changes

Phase-contrast observations of permanent structures induced by a short laser pulse (160 fs and $1\ \mu\text{J}$) are presented in Fig. 7.1(a) for different working depths. These are accompanied by corresponding

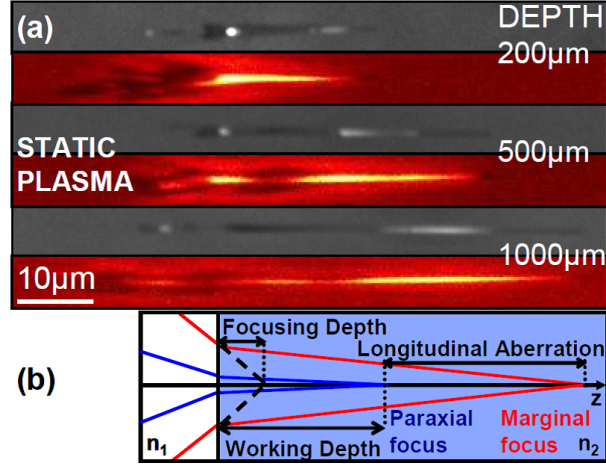


Figure 7.1: a) PCM images of static permanent structures and transient plasma observations induced by single short pulse in bulk irradiated $a\text{-SiO}_2$ for various depths. Irradiation parameters: 160 fs and $1\text{ }\mu\text{J}$. The laser pulse is coming from left. The plasma images are taken 1 ps after the pulse excitation. b) Schematic view of spherical aberration.

phase contrast images of plasma excitation taken 1 ps after the laser pulse in the pump-probe setup (see Chap. 4). The plasma images are affected by the continuum emission at high excitation densities.

As mentioned in Chap. 5, the permanent traces show a refractive index modulation which transpires the axial variation of excitation. We recall here that the white domains were identified with regions of maximum energy deposition, [BBS⁺07, SJM04], where material is likely to suffer expansion. The left-side white dot was indicated as a self-focusing effect [BBS⁺07]. The black, positive index region involves a complex mixture of thermomechanical phenomena and defect generation. The structure length increases quasi-linearly with the working depth from approximately $25\text{ }\mu\text{m}$ at a depth of $200\text{ }\mu\text{m}$, to $43\text{ }\mu\text{m}$ at $500\text{ }\mu\text{m}$, and then to a size of $65\text{ }\mu\text{m}$ at $1000\text{ }\mu\text{m}$. If the spatial index modulation accentuates with the depth, the domain of modulation appears to be defined by the longitudinal aberration (Fig. 7.1(b)), [HSM⁺07]. The self-focusing displacement [SFPM01] in the present experimental conditions is of several microns. Apart from nonlinear spectral effects, the spatial distortion of the pulse front may also lead to a pulse broadening of up to 200 fs at $1000\text{ }\mu\text{m}$ depth [DR06].

Temporal optimization for energy confinement

Preserving positive index changes, we have attempted to reduce the spatial extent of the white regions using the shaping strategy. The objective functional was defined accordingly. The microscopy image analysis determines the area of positive (negative) index change by summing the

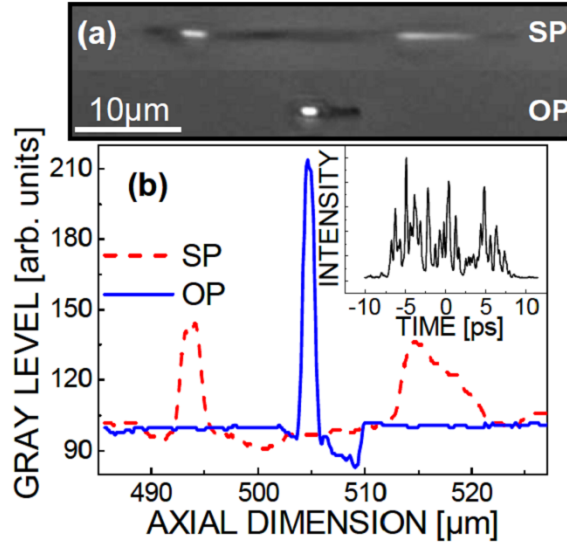


Figure 7.2: a) Short pulse (SP) and optimal pulse (OP) induced structures at a depth of 500 μm and 1 μJ input energy. b) The corresponding axial cross-sections. The inset shows the optimal pulse shape.

number of black (white) pixels detectable on the PCM image within an narrow axial region. The optimization functional or 'fitness' F is defined by the ratio $F = \frac{n_B}{n_W}$ between the number of black and white pixels, respectively n_B and n_W . We have applied the automated feedback loop with the purpose of maximizing the index ratio. The optimization result is an intensity shape that has produced refractive index patterns with maximum contrast. The results of the optimal pulse (OP) compared to short pulse (SP) irradiation are shown in Fig. 7.2 for an input energy of 1 μJ .

The optimal sequence takes the form of a structured intensity envelope extending on a picosecond scale. This particular sequence provides an almost three times increase for the objective functional. The control parameter appears to lie in the extended envelope. At the same time, a drastic decrease in the size of the structure is noticeable, while keeping the negative index region to a minimum. The consequences of a ps envelope are twofold [BBS⁺07]. Firstly, the ps envelope induces a retarded, low density, spatially-modulated plasma. This creates a smaller negative shift for the incoming energy and less defocusing, helping thus to concentrate the energy in the region of best focus. The intensity defines in this case the moment of free electron production and subsequent acceleration. Secondly, the nonlinearity of excitation diminishes, allowing efficient absorption only in a restricted region around the geometric focal point.

Landscape of the space search

The material response defines the topology of the solution space. In order to gain insights into the propagation and modification factors we have attempted to simplify the control landscape by

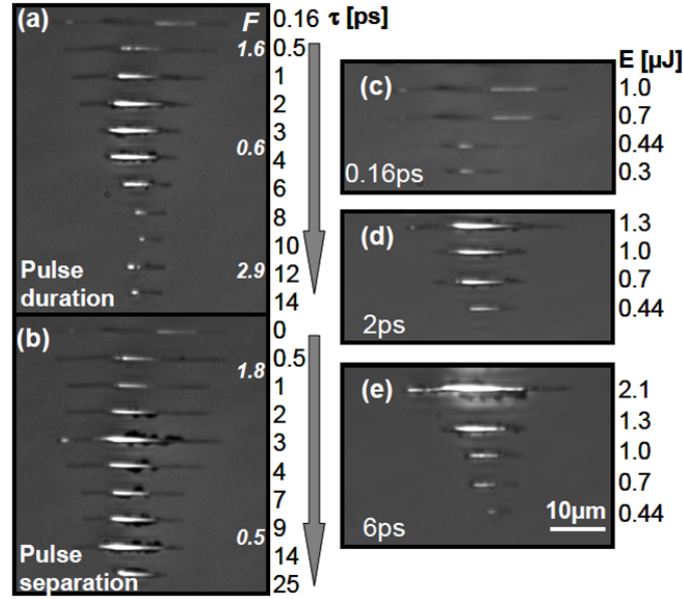


Figure 7.3: Structures induced by pulses with different pulse durations a) or double pulse sequences with various pulse separations b) at $1 \mu\text{J}$. Energy effects for pulses with selected durations; short 0.16 ps pulse c), 2 ps pulse d), and 6 ps pulse e). All structures are induced at a depth of $500 \mu\text{m}$.

using less complex pulse shapes, namely temporally broadened pulses and double pulse sequences with variable separation times. The irradiation energy was varied as well. The results are given in Fig. 7.3. The systematic variation of pulse duration at $1 \mu\text{J}$ (Fig. 7.3(a)) indicates the following behavior. For moderate stretching, below 6 ps, the energy concentrates very efficiently, leading to the onset of a hot spot in the central area. The main modification is a negative index change due to presumably fast heating and thermal expansion. However, beyond a value of 6 ps the behavior changes. The positive index change takes over, with a gradual reduction of the low index region. Similar results were obtained for up- and down-chirped pulse which indicates that the temporal shape is the dominant control factor and not the frequency succession in the pulse. The double pulse result in Fig. 7.3(b), less sensitive to pulse separation due to a leveling of the optical response [CXW05], shows essentially the rarefaction effect at high energy concentration.

The subsequent question relates to the physical factor for reducing the modification size, despite the geometrical spread of the focal area. The imposed dispersion generates a complex temporal pulse shape at the focus which cannot be determined accurately. We therefore concentrate on qualitatively observing the experimental results. This brings interesting clues for explaining the partial filamentation control and proposing probable bulk excitation paths. Following the wave-front distortion, the laser beam is first focused at the paraxial location (closer to the surface). If a low density plasma is formed, a small defocusing effect is induced, shifting the energy depo-

sition further away from the interface. Additionally, the lower intensity ensures that ionization takes place on a reduced scale, with a change in morphology at low excitation densities. We have subsequently reduced the energy [Fig. 7.3(c–e)] for pulses with different durations. An increase of the modification threshold was observed, ranging from approximately $0.09 \mu\text{J}$ for the short pulse to $0.6 \mu\text{J}$ for 14 ps pulse (not shown). This indicates the increasing energy costs for longer pulses as a consequence of reduced absorption nonlinearity. Structures with dominant highly-contrasted positive index changes at low energies can be obtained for the short pulses or for pulses exceeding a duration of 6 ps in a large energy domain around the modification threshold. This particular aspect shows that the threshold criterion by itself is not sufficient to explain the optimization results and that the plasma mediates spatially the energy deposition process. This allows to distribute the input energy in precise doses in the spatial and temporal domains.

In conclusion, adaptive temporal shaping induces spatio-temporal pulse behaviors able to localize energy on limited spatial scales, determining as well a dominant region of positive refractive index change. The decreased nonlinearity and the lower ionization efficiency assist the energy confinement while reducing the structure ellipticity. Refractive index tunability may have beneficial consequences for 3D processing of waveguide components. In the following, we present a more 'natural' technique to counteract energy spreading based on spatial wavefront adaptative tailoring.

7.2 Aberration counteraction in longitudinal waveguide writing in BK7 glass

We pointed out throughout this report that the nonlinear aspect of the laser-matter interaction in the femtosecond regime enables energy deposition on a micrometer scale [DMSH96, GMH⁺96, KMJM01]. The consecutive material structural modifications therefore take place in the laser focal volume [JNT⁺06] with an accompanying change in the material optical properties [IWNS06], leading to local alteration of birefringence, absorption and refractive index [SFPM99, BKK04]. When a local increase of the refractive index predominates, simple translation of the laser spot in the bulk permits to photowrite light guiding structures in the three dimensions [NWBT03] with the possibility to realize various photonic devices [IWNS06, WAY⁺03, VTO⁺07].

7.2.1 Wavefront aberrations in longitudinal writing

By replicating the laser-induced structures over large distance, efficient waveguides are potentially achievable. This waveguide writing can take place along or perpendicularly the propagation axis and is then referred to as longitudinal and transversal waveguide writing respectively. Nevertheless, the air-dielectric interface encountered in bulk focusing can be at the origin of significant

wavefront degradations of the femtosecond beam. The associated spatial phase alterations augment with the depth of the processing spot, the refractive index contrast at the interface and the numerical aperture of the focusing lens. As pointed out with Fourier propagation calculations in Chap. 2, this results in a detrimental axial spreading of the focal intensity distribution along the propagation with the consequence of a reduced energy density. Fig. 7.4 schematically exemplifies this focal volume elongation on the basis of geometrical optics. The air dielectric interface causes paraxial and marginal rays to focus at distinct sample depths (respectively shorter and longer). The related wavefront modulation is principally spherical aberration and implies a peak intensity drop increasing linearly with the focusing depth [HSM⁺07]. Moreover, the axial intensity distribution is also modulated with dramatic aftermaths on the bulk modifications [BNW98, HTS⁺05]. Therefore, it is quite understandable that if narrow waveguide processing windows are available at shallow depths, the effect can virtually close them when focusing more profound in the material. In particular, the formation of the phase object is accompanied with morphology and homogeneity alterations [MMJ⁺03, SJL⁺05b, LLA⁺06] which lead to additional losses, inhomogeneous refractive index and non guiding regions [DSS06]. If longitudinal waveguide writing has evident advantages with the intrinsic circular symmetry of the photowritten structures as compared to transverse writing, the spherical aberrations restrict its applications to shallow depths or, in other words, to very short waveguides. Wavefront correction is thus necessary to overcome these limitations by keeping a distortion-free spatial phase regardless of the processing depth. Dynamic tailoring of the spatial phase thus permits energy deposition while keeping the focal intensity distribution sufficiently free of spatial dispersion.

The interest is twofold. Firstly, by preserving alike excitation conditions for the ensemble of the machining depths, an increased uniformity of the photowritten structures is reachable. This highly desirable feature was until recently restricted to low numerical aperture focusing apertures [MQI⁺97, HWG⁺99, KO04]. However, the associated looser focusing augments the focal volume with the consequences of lower achievable fluences and is also prone to hardly manageable filamentation phenomena. Secondly, as it will be shown below, sufficient energy density can be kept over long distances in order to trigger specific mechanisms of positive index modifications. The consecutive photowritten longitudinal waveguides present an increase in homogeneity reducing optical losses and enhancing the light guiding region, a significant breakthrough in the field of femtosecond bulk machining.

The influence of spherical aberration in ultrafast laser material processing was recently analyzed via depth-dependent material modification thresholds and aspect-ratio measurements [MMJ⁺03, SJL⁺05b, LLA⁺06]. Microscope objectives equipped with adjustable collars can offer compensation of spherical aberration to preserve the modification size in bulk optical materials [HTS⁺05]. Adaptive optics were employed to achieve corrective functions in order to minimize depth-dependent

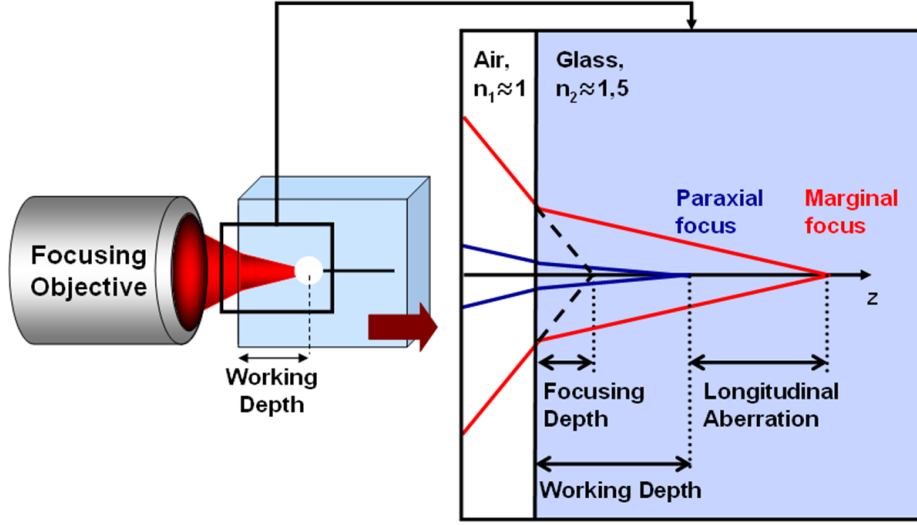


Figure 7.4: Illustration of longitudinal waveguide writing with the associated wavefront distortions upon deep focusing [HTS⁺05]. Insert: Description of spherical aberration due to refraction at air-dielectric interfaces and the subsequent elongation of the focal area. The longitudinal aberration depends on the index contrast between the two media and increases with the numerical aperture and the focusing depth.

aberrations [BSW⁺06] for data storage and microscopy applications. The consequences for quality waveguide writing were already indicated [HTS⁺05, LLA⁺06]. We propose here a time-varying wavefront tuning procedure capable to dynamically counteract the varying wavefront distortions in longitudinal waveguide writing. The technique rely on programmable spatial phase retardation integrated in adaptive closed loops. A global optimization strategy is employed to gradually define the wavefront modulation in accordance to a feedback resulting from the laser action. While spherical aberration correction can be achieved analytically using wavefront polynomial decomposition, a precise calibration of the spatial shaping system along with meticulous correspondence of the phase shaping plane and the entrance pupil of the focusing objective are indispensable. We tend to show here that that global search algorithms [HKCL06] represent an effective calibration-free technique, able to significantly improve the structuring process. Moreover, it can be applied without complete knowledge of the overall wavefront deformations that may include inherent beam aberrations and distortions associated with nonlinear propagation. The feedback utilized by the optimization loop can be directly linked to the material processing result [CTE⁺07] with evident advantages for material structuring applications. In addition, the proposed method includes pulse spectral frequency dispersion control as a supplementary factor to optimize nonlinear contributions to energy deposition.

After rapid precisions regarding the experimental choices, we describe the detrimental effect of spherical aberration with notably the departure from the waveguide writing regime at high depths.

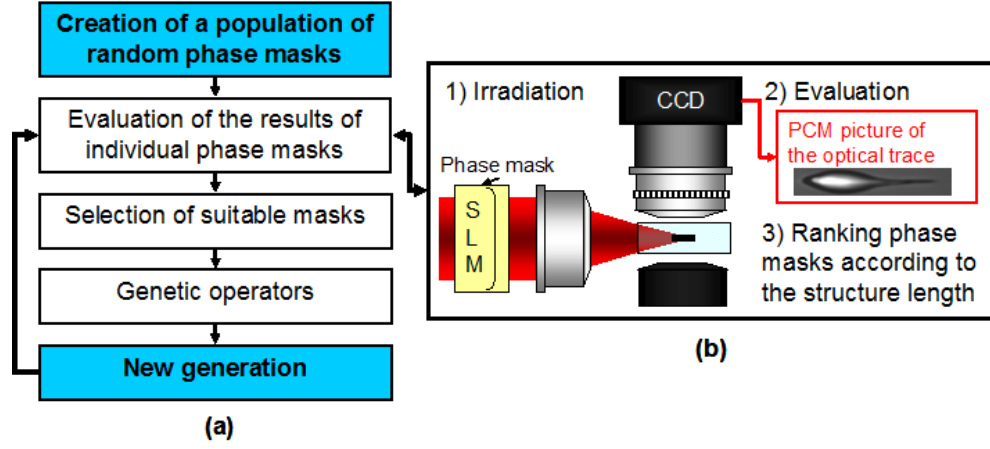


Figure 7.5: The feedback loop diagram. a) Schematic representation of the optimization procedure, emphasizing the main steps of the self-improvement approach. The strategy involves applying, testing and comparing each phase mask according to its ability to achieve user-defined bulk modification, (here restricted axial elongation of the structure). b) Phase-mask fitness attribution sub-steps: irradiation of the sample with the tested phase mask, estimation of the corresponding trace length and ranking of the phase mask.

The adaptive strategy success in preserving the desired photoinscription conditions is then experimentally demonstrated with punctual irradiations and the achievement of a corrected longitudinal waveguide.

7.2.2 Experimental details

Schott BK7 borosilicate crown glass was chosen not only as a model material due to potential applications in optics and microfluidics, but also for its narrow laser processing window for positive refractive index changes [BSC⁺05]. It is therefore the ideal medium for the demonstration of precise energy density preservation at arbitrary depths. The HRR laser system is employed (described in Chap. 4) to irradiate polished BK7 parallelepipedic samples $10 \times 20 \times 3$ mm. We recall here that it is equipped with a optically addressed spatial shaping unit and a temporal shaping apparatus. The laser beam is focused inside the target by the long working distance microscope objective mentioned in Chap. 4. To preserve a high energy throughput, the size of the beam at $1/e^2$ is adjusted to the objective aperture. Detection of the laser-induced structures is carried out with the transmission microscope employed in the phase contrast mode (see Chap. 5), thus realizing a qualitative 2D side-mapping of the relative refractive index variation subsequent to the femtosecond pulses passage. Thus, the axial extent of the damage can be precisely evaluated for different laser focusing depths.

A feedback loop drives the microscopy detection and the pulse spatial control unit, guided by

an adaptive optimization algorithm based on an evolutionary strategy. The beam tailoring unit sequentially modulates the spatial phase and the detection delivers the quantitative evaluation of the laser action under the tested wavefront modulation. For each phase mask, the 2D map of the photoinscribed phase object is numerically treated to evaluate the laser-induced structure axial size. More precisely, a note (*fitness*) is attributed related to the root mean square difference between the gray-level axial cross section of the current trace and of a non-aberrated trace obtained at shallow depths. The minimization of the RMS difference defines the success of the phase modulation to counteract the aberration-induced axial spreading. A schematic representation of the optimization strategy is depicted in Fig. 7.5. A set of random phase patterns is initially applied on the optical modulator and evolves in through genetic propagators (see Chap. 4) towards an optimal solution. In order to significantly reduce the space search, the spatial phase information was encoded on a 64 pixels string which was then radially replicated to fill the laser pulse aperture as spherical aberration follow this circular symmetry. This encoding procedure allows to represent a potential phase solution by a string of real numbers corresponding to a radial section of the mask. The discrete string containing phase retardation values determines the pattern, its performance, and the genetic dowry of the phase mask. We use 64 genes, one gene corresponding to two addressing point values. The mechanism of optimization is the following [JR92, Bar02, Mer07]. After the testing of each phase mask of the initial random population, the most effective modulations are utilized to give birth to a new generation through crossover and mutations (see Chap. 4). The procedure reiterates for a few tens of generations until an acceptable solution is found.

7.2.3 Results and discussion

Static and dynamic BK7 photoprocessing

In order to quantify the effect of laser irradiation under optimal focusing conditions, we evaluate the results of laser structuring in the vicinity of the surface, where the influence of spherical aberrations is minimal. Fig. 7.6 shows the result of irradiation of 150 fs pulses (measured before the focusing objective) at a working depth (the physical position of the paraxial focus in the material) of $200\ \mu\text{m}$ for two different input average powers, 125 mW and 80 mW. Fig. 7.6 a) and b) show the static refractive index modifications produced by 10^5 pulses. The femtosecond irradiation induces a dominant refractive index decrease denoted by the white color. In case of the high energy static structures, a shallow region of positive index change (black color) surrounds the low index core, terminating with an elongated trace of high index material at the structure tip. The low energy preserves somehow the topology with the region of surrounding compression being drastically reduced. An axial cross-section through the index contrast of the structures is depicted as well (Fig. 7.6e)).

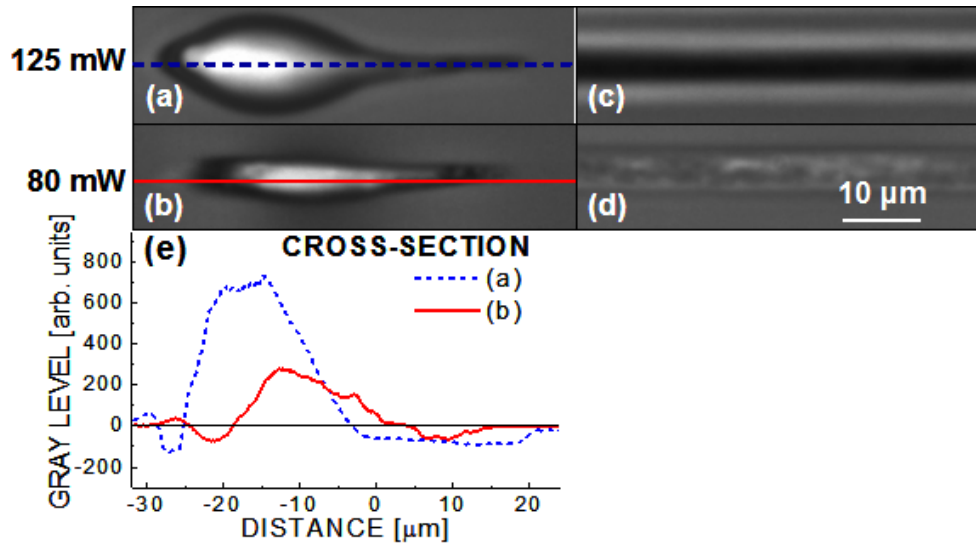


Figure 7.6: Static (left, (a,b)) and dynamic, longitudinally-written (right, (c,d)) material modifications induced in BK7 by ultrafast laser radiation at different input powers with $\text{NA} = 0.45$ and $\text{NA}_{\text{eff}} = 0.41$. The static irradiation corresponds to 10^5 pulses/site while the dynamic structures are made at a scanning speed of $1 \mu\text{m/s}$. Laser pulses are incident from the left and scanned towards the laser source. The structures are localized at $200 \mu\text{m}$ depth with respect to the air-dielectric interface. Waveguide writing conditions are achieved only at high powers (see text for details). e) Axial cross-section through the laser written structures in conditions a) and b). The axial cross-sections correspond to the relative change in the refractive index.

A scenario regarding the specific topology of the irradiation outcome has been reported in Chap. 5. As main remark, an energy threshold appears to trigger the desired compaction regime for longitudinal photoinscription of waveguides. However, with increasing processing depth, the problematic of optical distortions renders difficult the preservation of sufficient energy density. Indeed, a quasi-linear increase of the modification threshold energy with the working depth was previously observed [MMJ⁺03, LLA⁺06]. In order to observe the consequence for a dynamic regime of photoinscription and to create guiding elements, the focal point was translated along the irradiation axis in a spatial region located around the working depth of 200 μm . The scan direction was towards the laser beam, with the starting point into the bulk. The Fig. 7.6 parts c) and d) indicate structures written longitudinally at a scanning speed of 1 μm , corresponding to the situations a) and b). For the high power longitudinal line, a contrasted region of positive index change is visible at high energies, denoted by the intense black color, bordered by narrow lines of decreased index. This structure shows a high and homogeneous index contrast. The low energies correspond mainly to a negative refractive index change represented by the dominant white color. The index variation is not uniform and positive and negative changes alternate. Important for guiding applications, it appears from the figure that a uniform region of positive refractive index change occurs during translation only when a critical density of energy was transported at the interaction place. This indicates the achievement of a high temperature in the interaction region, followed by the onset of the surrounding compressed region. The longitudinal translation at high repetition rates leads to a high density trace upon scanning in the direction of the laser pulse. To reach this regime of dynamic positive index change, a transition power threshold of approximative 90 mW was found necessary in our experimental conditions. The transition power depends as well on the scan velocity. Below this value moderate thermal expansion and subsequent rarefaction upon cooling determine to a large extent the material response, inducing a dominant low index phase canceling waveguiding. Inevitably, upon irradiation at different depths, the energy density decreases due to spherical aberration and limits the possibility to trigger the positive index regime far from the air-glass interface. Consequently, we have attempted to correct the spatial phase distortion using the above-mentioned optimization loop in order to preserve a high energy density.

Adaptive correction and processing solutions

We noted above that high energy, low density structure replication via scanning delivers a positive refractive index change. This may be connected to the presence of the surrounding high index, compressed region. It indicates as well that dynamic regimes of photoinscription should take into account the effects of a moving heat source. Pointing to this behavior we will focus below on the possibility to restrict the energy spread by spatial phase adjustments. In order to reach the compressive regime at arbitrary depths, it is imperative that the energy delivery remains concentrated to

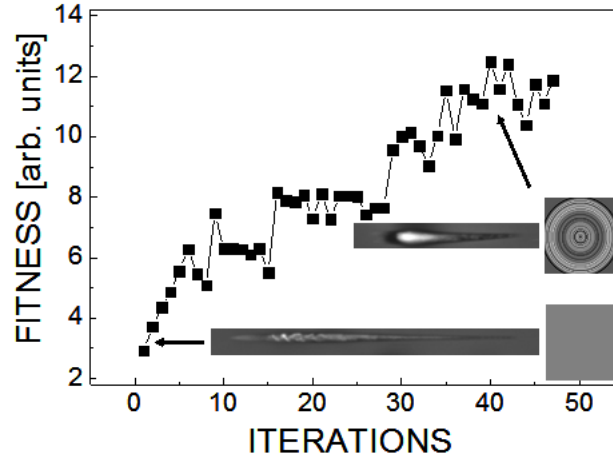


Figure 7.7: Evolution of the trace fitness during the optimization run at the depth of $2500\ \mu\text{m}$. Example of traces and corresponding gray-level phase masks at different moments of optimization are given as well.

the narrowest region. This was achieved by adaptively determining the corrective phase masks in the microscopy-based feedback loop presented before. We recall that the success of the operation was related to the minimization of the damaged region. An example of the iterative improvement during the optimization run is given in Fig. 7.7.

Similar optimization runs were effectuated at different depths from $500\ \mu\text{m}$ to $3000\ \mu\text{m}$ in steps of $500\ \mu\text{m}$. Whereas the objective working distance is usually the limiting factor, the maximum reachable depth was also restricted by the condition that the excitation beam is not clipped at the front surface. Fig. 7.8a) shows the results of the optimization procedure for photoinscription as compared to the effect of the uncorrected beam for different depths into the glass material. For completeness, part b) shows axial cross-sections through the index change in relative units at $200\ \mu\text{m}$ and $3000\ \mu\text{m}$. If the structures induced by the uncorrected pulse show a threefold length increase (Fig. 7.8 left), the correction procedure has stabilized the structure length at almost the initial size (Fig. 7.8 right). We mention that the optimal results show a slightly more effective size reduction as compared to theoretically calculated masks using Zernike-polynomial decomposition (Fig. 7.9). This demonstrates the efficiency of the loop, the relatively low non-linear effect contribution for this specific material, and the fact that the adaptive strategy is suitable for more complex aberration correction problems, including wavefront distortions due to nonlinear effects. The reason for the slightly lower effectiveness of the theoretical corrections may also be connected to a small mismatch between the effective entrance pupil diameter of the microscope objective and the radial extension of the phase map displayed on the spatial phase modulator.

Nevertheless, if the structure size is kept at a constant level, the energy density is slightly de-

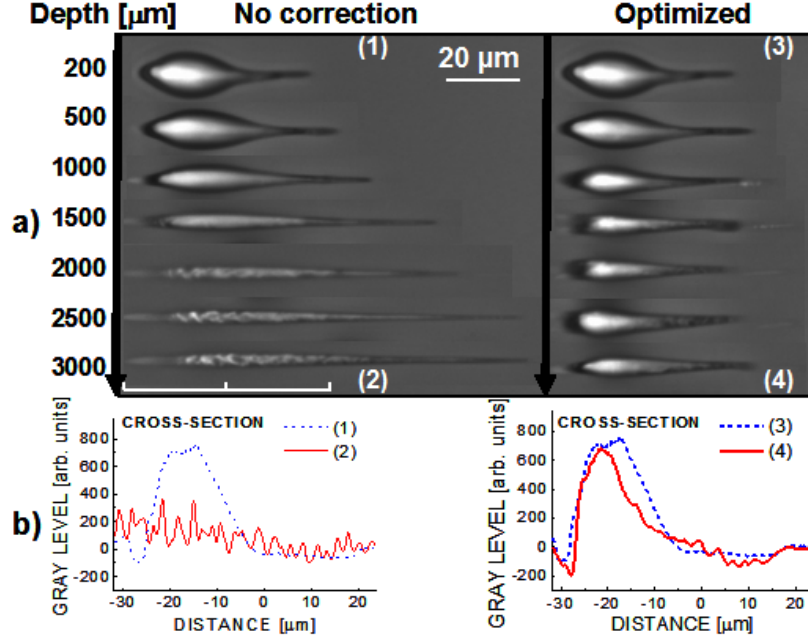


Figure 7.8: a) Non-corrected (left) and spatially-corrected (right) static structures induced at different depths with respect to the sample surface $NA_{eff} = 0.41$. The working depth was defined in Fig. 7.4 as the position of the paraxial focus. The structures are induced by 10^5 pulses of 150 fs duration at 100 kHz and 125 mW average power. b) Axial cross-sections through some laser written structures. Note the discrepancies in the spatial scales in a) and b).

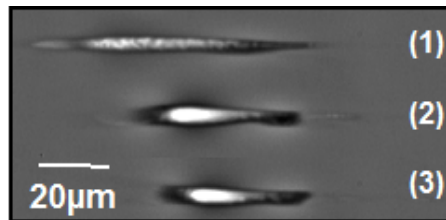


Figure 7.9: Comparison between the effect of theoretical and optimized correction phase masks for 125 mW input power. Static laser structures induced at 2000 μm depth without correction (1), with theoretical correction (2), with adaptive correction (3). $NA = 0.45$ and $NA_{eff} = 0.41$

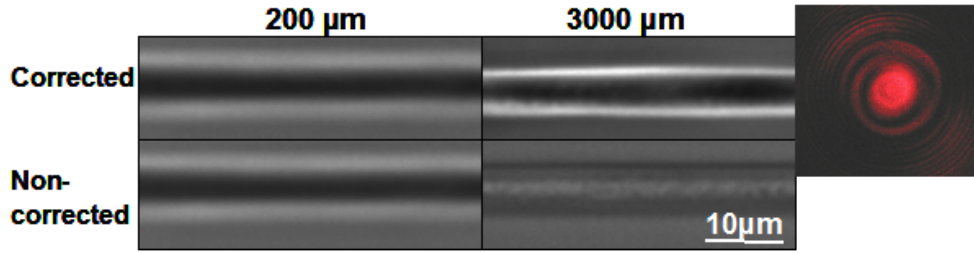


Figure 7.10: Longitudinal structures at different working depths in corrected (top) and non-corrected (bottom) cases. The corrections enable a positive refractive index change over a distance of 3 mm. Scanning speed is $1 \mu\text{m}$ at 125 mW average power. Right, far-field pattern of the guided mode at 633 nm for the corrected guide.

creased as compared to the unaberrated structures, as indicated by the level of the white color (Fig. 7.8 right a),b)). Consequently, the excitation density in the bulk is below the threshold for inducing a positive refractive index change during the longitudinal writing in the profound regions. Since the laser source has limited energy output which is just above the transition threshold, only 10% size variation with respect to the unaberrated trace decreases the energy density below the critical value. To compensate for this slight deviation with respect to the unaberrated structure and due to the limitations in the input laser power in our case, additional corrective solutions are required. A complementary technique for increasing the energy density deposited within the material is represented by pulse linear temporal chirping for the following reason. We have discussed above that ultrafast irradiation focused with moderate to high NAs results in structures where self-focusing is dominated by light defocusing on self-induced electron-hole plasmas. To minimize the effect of light spreading due to defocusing, the moment of reaching the maximum plasma density has to be delayed with respect to the beginning of the laser pulse. A longer temporal intensity envelope and a retarded plasma formation produces a less effective defocusing, allowing the energy to be concentrated efficiently in the irradiated region.

The success of the operation is verified by effectively writing longitudinal guiding structures. Combining the spatial correction with a gradual increase in pulse duration with depth (up to 2.7 ps at 3 mm by programmable second order dispersion) allows writing waveguiding structures as long as 3 mm. To avoid catastrophic damage during the longitudinal scan towards the front surface, the pulse was continuously compressed, reaching the shortest value at a depth of just below 1 mm. A positive quadratic dispersion coefficient was found to be slightly more effective in obtaining the positive index change regime. The spatial phase correction masks were as well applied in synchronization with the advance of the structure inside the glass material. The optimization run offered spatial solutions for depths located at: $500 \mu\text{m}$, $1000 \mu\text{m}$, $1500 \mu\text{m}$, $2000 \mu\text{m}$, $2500 \mu\text{m}$, and $3000 \mu\text{m}$. The maximum optimization depth was restricted due to technical limitations of the

microscopy system. Linear interpolation was used to generate patterns for intermediary depths by dividing $500\text{ }\mu\text{m}$ domains in 30 steps. The newly generated pattern were applied in five seconds tact at the scan speed of $1\text{ }\mu\text{m/s}$. We mention that, in the hypothesis that spherical aberration is the main distortion factor, the number of optimization solutions could be decreased due to the linear dependence. The photoinscription outcome is depicted in the top part of Fig. 7.10 which synthesizes the result of the dual corrective procedure. Both ends of the longitudinal structure are shown. A uniform dark structure is becoming visible indicating a positive index change all along the guide length. Microscope inspection showed good homogeneity for the corrected trace. This indicates that the spatio-temporal correction enables the generation of a uniform cylindrical waveguide with a high positive index contrast for a length superior to standard irradiation and which allows symmetric guiding. By evaluating the numerical aperture of the generated guide at 633 nm , an index increase of approximately 5×10^{-3} was estimated. For comparison, the uncorrected trace is shown as well in the bottom part of Fig. 7.10. In this former case, the guiding region is restricted to 1 mm , the rest of the trace showing a negative index change.

This experimental achievement constitutes a clear evidence of the higher flexibility offered by spatio-temporally shaped femtosecond laser beam. The decisive breakthrough obtained by the depicted method withdraws significant limitations that reduced the field of ultrafast bulk photomachining applications to shallow depths. It is also noteworthy to underline the fact that an a priori knowledge of the nonlinear propagation can have a decisive impact on achieving particular irradiation outcome.

7.3 Wavefront modulation for parallel photoinscription

If the previous section beam tailoring permitted to overcome well-known limitations met deep bulk machining, we report here on a novel possibility offered by spatial shaping improving the irradiation efficiency [MCH⁺09]. Before entering into the subject, we briefly recall that other irradiation parameters and their influence on the excitation outcome were intensively investigated. More precisely, with the constant scope of improving various properties of the laser written structures, techniques based on controlling the aspect of the focal region at different repetition rates and polarization regimes emerged [EZN⁺08, LAD⁺08]. Among the main characteristics of interest are found the amplitude of the refractive index increase [WRG07, EZN⁺08], propagation losses [ZEH06], cylindrical symmetry [CSM⁺03, OTM⁺03] and compensation of the wavefront distortion during the photoinscription process of deep structures [MMH⁺08, MMR⁺08]. Whereas the three-dimensional photoinscription access constitutes a clear advantage over multilayer lithographic techniques, the single laser focal spot must undergo potentially complicated movements with respect to the sample in order to draw the whole photonic structure. This single spot opera-

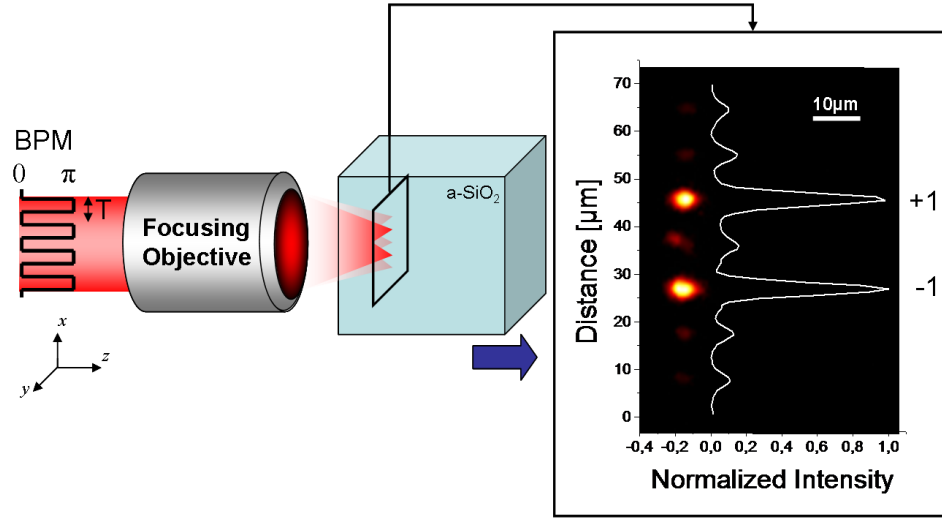


Figure 7.11: Scheme of double spot operation. BPM: Binary phase mask. Insert: Double spot intensity profile inside the sample at the focus of the objective generated by a simple step grating phase at very low power captured by direct imaging on a CCD camera. The blue arrow shows the direction of motion of the sample for longitudinal photoinscription.

tion (SSO) may involve long processing times when the writing of several complex structures is envisaged.

A binary phase mask, when placed at the object plane of a focusing lens, enables the generation of multiple laser spots [LYZT08]. Multispot machining of glass relying on this technique was recently reported [HHN06, SSS⁺09]. We present in the following a time-saving method giving access to dynamic multispot operation (DMSO) with variable and reconfigurable patterns and we successfully apply it to the parallel fabrication of light guiding structures in the bulk. Dynamic multispot operation based on laser wavefront modulation constitutes a step forward as it enables the simultaneous processing of several embedded structures, thus lowering the process time and reducing the complexity of the mechanical support. The paper is organized as follows. After a brief analytical outline pointing out the DMSO through spatial phase modulation, details of the experimental apparatus will be given. Then, the demonstration of parallel longitudinal writing of waveguides is presented followed by examples of photonic structures based on DMSO in the two and three dimensions (2D and 3D).

7.3.1 Description of dynamic multispot operation

In the object plane of a focusing objective, an optically addressed spatial light modulator (SLM) imprints a binary phase-only mask (BPM) $\phi(x)$ of period T and amplitude $\Delta\phi$ on the laser wavefront as shown on Fig. 7.11. For simplicity, it is considered infinite in the x direction and invariant

in the y direction, z being the laser propagation axis. In the frame of the Fraunhofer approximation and supposing that the SLM reproduces perfectly the BPM, the diffraction efficiency η of the m -th order is given by [Goo05] :

$$\eta_{m \neq 0} = \frac{1 - \cos(\Delta\phi)}{2} \text{sinc}^2\left(\frac{\pi m}{2}\right) \quad (7.1)$$

And for the 0-th order:

$$\eta_0 = \frac{1 + \cos(\Delta\phi)}{2} \quad (7.2)$$

For the ideal binary grating, the even orders disappear regardless of the phase step value $\Delta\phi$. Moreover, when $\Delta\phi = \pi$, not only does no diffraction occur at the 0-th order but the first order efficiency becomes much higher than the other orders, thus constituting two available laser spots for laser processing. In that case, adding the positive and negative first order efficiency shows that these two peaks gather 82% of the incoming light. By varying the period T of the BPM, the separation of the two spots becomes an accessible parameter to be controlled during photoinscription through the SLM.

From the experimentally-obtained double spot beam profile depicted in Fig. 7.11(insert), it is worth noting that the spots corresponding to the $+1$ and -1 orders show an expected circular symmetry. As foreseen, these two peaks widely surpass other diffracted orders. Evaluating the relative portion of power contained in these two processing spots by summing the corresponding intensity levels permits to realize that approximately one third of the total power is left into the non-processing orders. This additional spreading out of usable power compared to the above-mentioned 18% is inherent to the incapacity of the continuous liquid crystal layer of the SLM to reproduce perfectly the sharp steps of the desired BPM[YPK⁺04]. These losses can be reduced through the design of more complex phase masks with iterative optimization algorithms [LYZT08]. However, in view of the nonlinear response of the interaction, only the high intensity peaks contribute to the structuring process and in the frame of the present work, the simple step grating phase mask is sufficient for the DMSO demonstration purpose. Moreover, this phase modulation offers a straightforward way to control the position of the two spots by varying its period; a feature more difficult to obtain in the case of more complex phase masks.

7.3.2 Experimental precisions

The choice of fused silica glass is motivated by its numerous potential applications in the fields of integrated optics and microfluidics. Moreover, this well-known material has been thoroughly investigated in order to identify several femtosecond waveguide writing regimes [DMSH96, ZEH06, GFD⁺07]. Polished fused silica parallelepipedic samples are irradiated with HRR laser system (see Chap. 4) used at 10 kHz, the system delivers an usable power of 30 mW. A long working

distance microscope objective from Mitutoyo ($20\times$, numerical aperture $NA=0.3$) is employed to focus the femtosecond beam in the silica glass. The diameter D_b of the beam at $1/e^2$ is 1.5 mm and is adjusted with respect to the objective aperture diameter $D_a = 3$ mm resulting in a truncation ratio T of 0.5.

The above-presented spatial light modulator (see Chap. 4) is imaged on the entrance pupil of the focusing objective and performs user-defined spatial phase modulation of the processing femtosecond beam. This versatile tool [SHA⁺05, MMH⁺08] is used to produce two processing laser spots of controllable separation as described in the previous section.

7.3.3 Results and discussion

We mention here that all the photowritten structures presented below were achieved in the longitudinal configuration(see Fig. 7.11). One of the main advantages of this technique is found in the cylindrical symmetry of the photoinscribed structure while transverse waveguide writing generally requires additional strategies to preserve this symmetry [OTM⁺03, CSM⁺03]. However, the major challenge to be faced in the longitudinal configuration concerns the spherical aberrations due the air-glass interface as widely underlined in the previous section. We recall that the subsequent degradation of the intensity profile at the focus becomes more important when high NAs and deep focusing are considered. Using the formalism depicted in [HTS⁺05], it is possible to estimate the decrease of the focused spot peak intensity with the depth of the spot in the sample for a given NA. In our case, the relatively low effective $NA_{eff} = 0.21$ resulting from the small beam truncation of $T = 0.5$ preserved 84% of the non-aberrated axial peak intensity at 8 mm deep spot in the bulk, allowing us to write longitudinal structures of similar size without prohibitive optical degradation. In addition, it is of interest to point out that, at constant sample velocity, the accumulated spatial rate of deposited energy remains constant during longitudinal writing regardless of the position of the spot in the sample. Those considerations plead in favor of a rather restricted spherical aberration influence in the photowriting conditions presented in this work. Even though the devices depicted hereafter were achieved in the longitudinal configuration, it is worth noting that the extent of the DMSO technique to the transversal case for bulk parallel waveguide writing is straightforward.

Processing window for parallel longitudinal waveguide writing

To demonstrate the capability of the DMSO to generate similar bulk photoinscribed devices as SSO, longitudinal waveguides were written using both techniques in a regime which usually delivers smooth and nonbirefringent traces. A first set of SSO investigations were carried out with various scan velocities for the glass sample at a power level of 8 mW (measured after the objective) with a repetition rate of 10 kHz (see Fig. 7.12a)) i.e; slightly below the single pulse modification

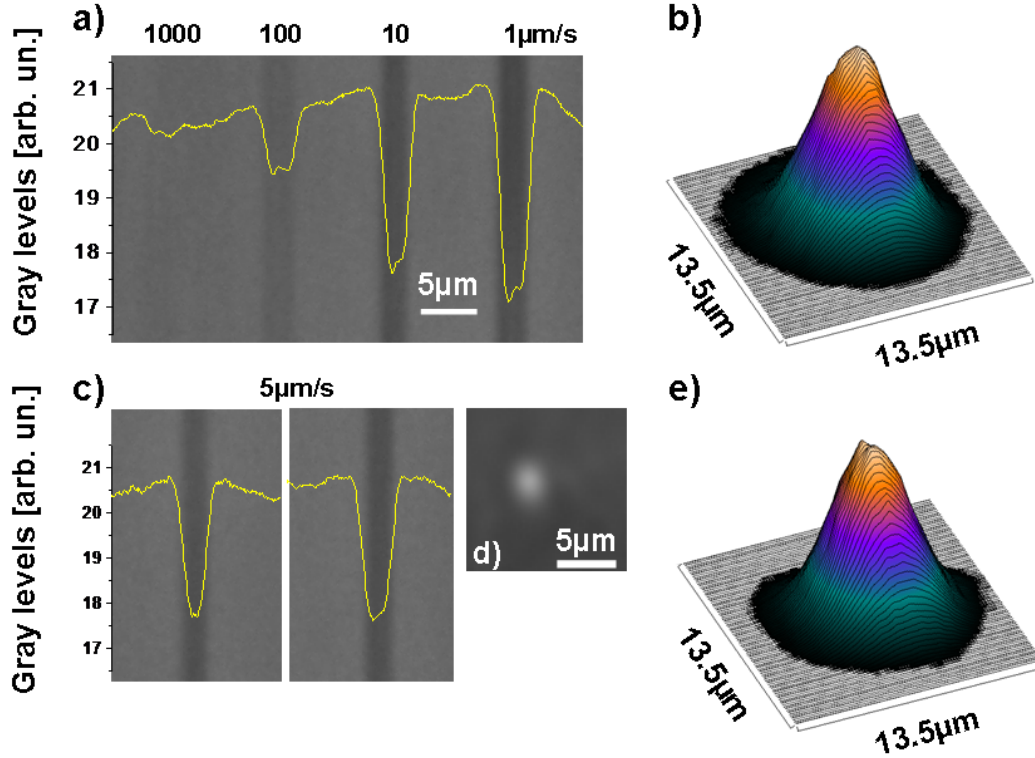


Figure 7.12: Comparison between single and double spot longitudinal photoinscription of waveguides in fused silica. Up: Single spot operation, down double spot operation. a) Side view PCM picture of SSO photowritten waveguides written at different translation speeds at 10 kHz, 8 mW, superposed with transversal cross section of the relative gray scale decrease indicating a positive change of the refractive index (see text body). b) corresponding nearfield profile of 633 nm injected guide written at 5 $\mu\text{m/s}$, 10 kHz, 8 mW in single spot operation. c) PCM picture of two simultaneously photowritten waveguides through double spot operation at 5 $\mu\text{m/s}$, 10 kHz, 24 mW. d) Optical transmission microscope picture of the cross section of one of the waveguides in c) in white light illumination. e) nearfield profile of one of the waveguides pictured in c) at 633 nm. $\text{NA} = 0.32$ and $\text{NA}_{eff} = 0.21$.

threshold. The PCM side image along with its gray scale cross section denotes a relative gray scale decrease after the passage of the femtosecond laser for translation speeds below $10 \mu\text{m/s}$. These darker structures under positive PCM mainly indicate an increase of the refractive index. They are not readily detectable under normal transmission microscopy (not shown) and present light guiding properties when injected with HeNe radiation at 633 nm. These type of waveguides belong to the type I structures characterized by a smooth isotropic positive change of refractive index. We mention here that in those scanning conditions, moving away from this relatively soft interaction regime by using higher laser power results in strongly scattering structures with poor or no guiding property. Based on this processing window, several 8 mm-long buried waveguides were written at $5 \mu\text{m/s}$ with 8 mW for characterization. Fig. 7.12b) depicts a typical nearfield mode under HeNe laser injection at 633 nm imaged on a CCD camera with a 20x objective associated with a 200 mm positive lens. The light is guided along the center of the modified area and the nearfield mode presents a size of $7 \mu\text{m}$ at $1/e^2$, larger than the transverse dimension of the structure ($3.5 \mu\text{m}$) evaluated at $1/e^2$ on the PCM image. The averaged amplitude of the refractive index change was estimated to be of approximately $\Delta n = 1.6 \times 10^{-4}$ through the waveguide NA measurement in the farfield. This rather low value [IWNS06] was confirmed using a mode solving software assuming a step index profile. The guides show an excellent cylindrical symmetry, visible on the nearfield mode and the structure itself. Using the method reported in [WSHM07], propagation losses of less than 0.7 dB/cm were evaluated, which approaches the best values reported so far for bulk photowritten waveguides in fused silica [IWNS06].

Using the DMSO, identical light guides were simultaneously photoinscribed by pairs in one pass. Taking advantage of the two spots available at the focus of the objective, dual structures with a separation of $s = 56 \mu\text{m}$ were achieved in a single motor scan at $5 \mu\text{m/s}$ under the full available power of 24 mW, after the focusing objective. For this purpose, a step grating phase mask of π amplitude at 800 nm with $\nu = 14$ periods across the clear aperture of the objective was displayed with the SLM during the sample displacement. Imaging the focusing plane on a CCD camera, the linear relationship between ν and s was experimentally determined. The PCM side image and nearfield mode of the waveguides are pictured in Fig. 7.12c) and Fig. 7.12e), respectively. The amplitude of the refractive index change as well as the propagation losses were found to be identical to the SSO written waveguides at 8 mW, same speed (Fig. 7.12b)), verifying our estimation of the power spread in the other diffraction orders mentioned in Section 2. The clean cylindrical symmetry is also observable on the nearfield mode as well as on the cross section microscope image (Fig. 7.12d)). These results clearly demonstrate the possibility to write buried photonic devices in parallel with a very simple phase function. Observing the processing conditions and comparing them to the available output of the laser, it appeared necessary to restrict the DMSO to two spots in our case in order to preserve enough energy to trigger the proper waveguide writing regime in

fused silica. However, there is no a priori restriction to increase this number to higher values in the absence of this limiting factor. Having identified this processing window for parallel photoinscription, efforts were carried out in order to achieve more complex photonic devices based on this principle.

2D photonic components

Embedded waveguide arrays have been recently investigated pointing out novel behavioral aspects [CLS03] when light propagates in discrete propagation spaces due to the evanescent light coupling between neighboring guides. In particular, linear effects such as Bloch oscillations [PDE⁺99], light localization, and quasi-incoherent propagation [SDH⁺07] were theoretically predicted and experimentally verified in femtosecond photowritten waveguides arrays. Nonlinear behaviors in the form of spatial solitons were underlined as well in such structures [SBB⁺05] indicating the possibility of obtaining new-types of nonlinear components written by femtosecond lasers. Impressive image reconstruction was recently demonstrated in segmented arrays photowritten in glass [SDH⁺08]. We aim to demonstrate here that complex 2D and 3D arrays and matrices of light guiding structures can be efficiently written using DMSO. In the following, examples of 2D photonic devices relying on evanescent coupling achieved with DMSO are presented, performing various optical functions. Evanescent coupling between parallel waveguides is supported by a precise formalism [Yar91] and has been recently studied in the case of transversal waveguides written in fused silica by femtosecond optical irradiation [SDP⁺07]. Due to the relative asymmetry of such waveguides, investigations were carried out underlining the coupling efficiency variations between two waveguides when their relative position changes. Using an additional static beam shaping technique, transverse waveguides with rotational symmetry were achieved fully counteracting this asymmetry feature [SDP⁺07]. In the longitudinal configuration for waveguide writing, the resulting guides keep the circular symmetry of the irradiation beam permitting to set aside those considerations when the processing spot is aberration-free. It is therefore justified to adopt in a first approach the formalism proposed by Yariv [Yar91] for planar waveguides to design embedded light dividers based on evanescent coupling. Several main concepts are given below.

In this frame, when only one of a pair of parallel and homogeneous identical waveguides is injected with light, the coupling length l_c after which the light is entirely evanescently coupled in the adjacent waveguide writes (also known as the half beat length):

$$l_c = \frac{\pi}{2\kappa} \quad (7.3)$$

κ being the coupling coefficient defined by:

$$\kappa = \frac{2h^2p \times \exp(-ps)}{\beta(w + 2/p)(h^2 + p^2)} \quad (7.4)$$

In the above expression, the parameters can be written as

$$\begin{aligned} h &= (n_1^2 k_0^2 - \beta^2)^{1/2} \\ p &= (\beta^2 - n_0^2 k_0^2)^{1/2} \\ \beta &= k_0 n_{eff}. \end{aligned} \quad (7.5)$$

n_0 and n_1 being respectively the refractive index of the surrounding medium and of the guides, n_{eff} the effective index of the guided mode which obeys $n_0 < n_{eff} < n_1$. w is the waveguide width, s the separation distance between the two parallel waveguides, k_0 the wave number of the injected light and β the propagation constant. The coupling coefficient κ was experimentally evaluated for several waveguide pairs using the method described in [SDP⁺07]. Having access to all the other terms of Eq. 7.5, the effective index n_{eff} could then be estimated.

In the case of a cylindrical guide surrounded by N other identical waveguides having equal distance to the main one at vertices of a polygon [Sny72], the coupling coefficient κ_N for the light to be transmitted to the surrounding structures reads:

$$\kappa_N = \kappa \sqrt{N} \quad (7.6)$$

The corresponding coupling l_{cN} length is then:

$$l_{cN} = \frac{l_c}{\sqrt{N}} \quad (7.7)$$

In that case, the maximum power transfer F between the center and the surrounding waveguides writes:

$$F = \begin{cases} 1 & \text{if } 1 \leq N < 3, \\ \left[1 + \left(\frac{\kappa_{ss}}{\kappa_{cs} \sqrt{N}} \right)^2 \right]^{-1} & \text{otherwise.} \end{cases} \quad (7.8)$$

where κ_{ss} is the coupling coefficient between the adjacent external waveguides and κ_{cs} from the central waveguide to one of the surrounding ones.

For example, in the case of two parallel waveguides with the above-mentioned characteristics ($\Delta n = 1.6 \times 10^{-4}$ and $w = 3.5 \mu\text{m}$), the coupling length l_c becomes 1.6 mm for a separation s of $9 \text{ unit} \mu\text{m}$ and 633 nm light injection. Similarly, an excited waveguide placed in between two identical guides generates a coupling length l_{c2} of 1.1 mm; $s, w, \Delta n$ and k_0 being the same. In these two cases, we have $F = 1$, meaning that all the light is evanescently coupled after the coupling length. Based on these results, it is then possible to design the concept of a light divider reposing on a successive combination of parallel waveguides with defined lengths and separation

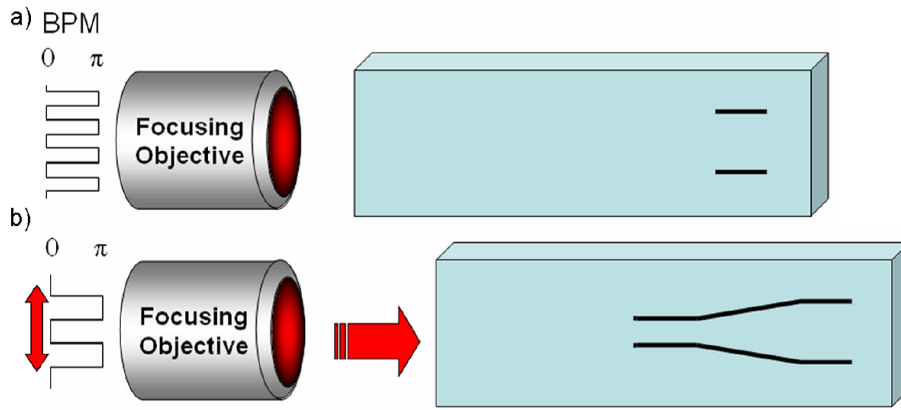


Figure 7.13: Illustration of the main steps of the photowriting of a light divider based on evanescent coupling in a single sample scan. The period of the binary grating is increased at a certain moment during photoinscription in order to draw closer the two processing foci, thus machining the light divider according to the desired shape.

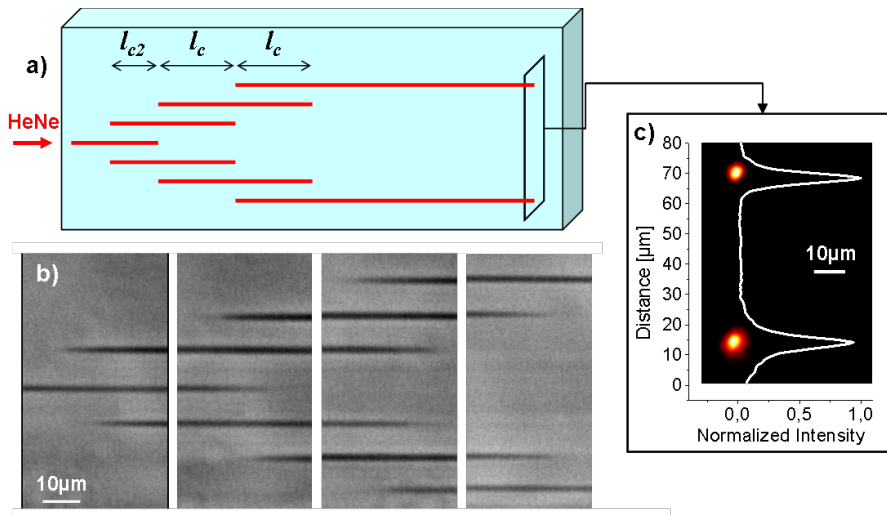


Figure 7.14: Bulk photowritten light divider based on evanescent coupling of injected waves in partial arrays achieved through double spot operation at 24 mW total power and 5 $\mu\text{m/s}$ scan velocity: a) schematic view of the structure: The conditions followed by l_c and l_{c2} enabling evanescent coupling from the central to the external guides are given in the text. b) Assemblage of PCM side-pictures of the device, its total length is 8.2 mm and the lateral separation between tracks is 9 μm . c) Nearfield profile under HeNe injection at 633 nm.

allowing evanescent coupling from a seed waveguide to two or more output waveguides. The DMSO technique appears as an ideal processing solution as it offers the flexibility to photoinscribe a pair of coupled waveguides simultaneously.

Figure 7.14 presents an example of a structure achieved by this technique. This device was photoinscribed in five subsequent steps under the irradiation conditions announced in the experimental section (24 mW, 5 $\mu\text{m/s}$). A single uniaxial motion control is sufficient to achieve the whole divider. A first 5 mm-scan of the sample under femtosecond laser exposure generated the two external waveguides. During this first move, the SLM was imprinting the above-mentioned $[0 - \pi]$ phase mask on the femtosecond laser beam with a high cycling frequency. Lowering the number of periods ν , two subsequent scans were performed to write the two other waveguide pairs of lower separation. Then the central waveguide was written at lower power 8 mW without any wavefront modulation. An assemblage of PCM side-images of the structure is depicted in Fig. 7.14b) to illustrate the result; the slight asymmetries are presumably due to unwanted beam wavefront distortions caused by SLM imperfections. The divider nearfield profile is presented in Fig. 7.14c) when 633 nm radiation is coupled into the central waveguide. With a splitting ratio of approximately 1:1, the light dividing operation is clearly verified. Moreover, further investigations put into light the absence of nearfield mode at the output of the intermediate waveguides, thus confirming light dividing through total evanescent coupling. Losses of the device, apart from the propagation losses, were evaluated to be approximately 30% expectedly mostly related to machining imperfections.

Considering a pair of identical waveguides injected in only one arm, a variation of the exciting wavelength modifies the coupling coefficient and length according to Eq. 7.4 and Eq. 7.5. More precisely, for a given structure, increasing the wavelength shortens the coupling length. In the case of two available wavelengths λ_1 and λ_2 with $\lambda_1 > \lambda_2$, it is possible to create a device for which the coupling length $l_{c\lambda_2}$ for λ_2 is twice as big as the coupling length $l_{c\lambda_1}$ for λ_1 . Then, if the total overlapping length l_o of the waveguides verifies $l_o = l_{c\lambda_2} = 2 \times l_{c\lambda_1}$, exciting one arm with both λ_1 and λ_2 generates total evanescent coupling of the λ_2 light in the other arm whereas the λ_1 excitation is back coupled to the initial arm demultiplexing the input frequencies.

Figure 7.15 shows a device performing the wavelength-division demultiplexing (WDD) operation. The entire device was photowritten with DMSO in a single motor scan in similar exposure conditions as already described. At the beginning of the irradiation, the laser beam was spatially modulated with a BPM having $\nu = 20$ periods resulting in two 84 μm separated spots. The number of periods ν was dynamically decreased while the sample was moving thus lowering the separation to $s = 16 \mu\text{m}$ in synchronization with the photoinscription procedure. At 633 nm, the coupling length for this separation is $l_{c633} = 4.5 \text{ mm}$. For injection with 800 nm CW laser radiation, the length becomes $l_{c800} = 2.4 \text{ mm}$. To take into account the weak coupling in the non-parallel part

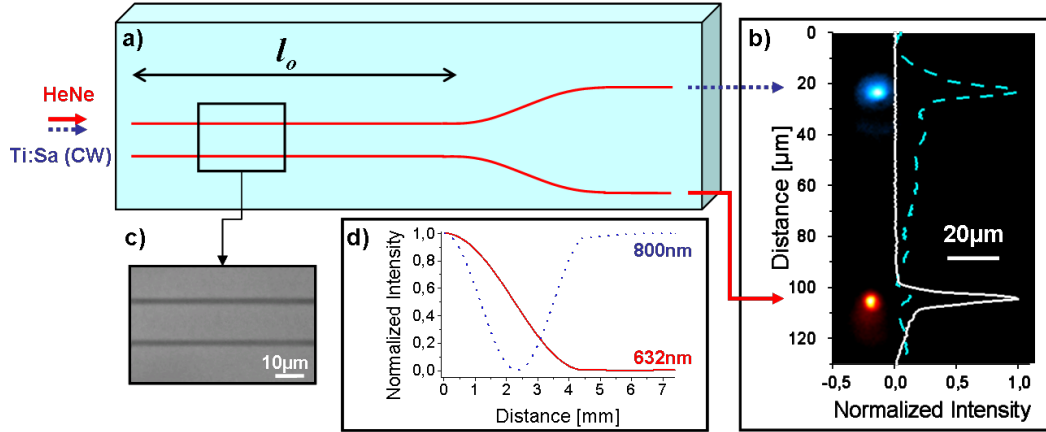


Figure 7.15: Bulk photowritten WDD device achieved through double spot operation at 24 mW total power and $5 \mu\text{m/s}$ scan velocity. a) Schematic view of the structure (condition followed by l_o is given in the text). b) Nearfield profile under 633 nm (solid) and 800 nm (dashed) simultaneous injection in the top arm. c) PCM side-image of the overlapping region. d) Theoretical prediction of the 633 nm (solid) and 800 nm (dashed) intensity variations in the excited waveguide according to [Sny72, MS74] taking into account the wavelength dependance of the coupling coefficient. The total length of the structure is 7.4 mm.

of the structure, we used the formalism proposed by McIntyre and Snyder [MS74] for non-parallel structures. Consequently, the overlapping length $l_o = 4,4 \text{ mm}$ is slightly smaller than l_{c633} . Calculation results for the structure are depicted in Fig. 7.15d) showing clean WDD between 633 nm and 800 nm. The experimental nearfield modes of the excited device at 633 nm and 800 nm are presented in Fig. 7.15b), in agreement with the expected behavior.

3D photonic components

Riveting developments in the design and machining of 3D bulk SSO written structures with puzzling diffraction properties were recently reported [GP10]. We tend to show in the following that the MSO technique presented here appears as a choiced solution to enable easy access to the 3D space. In order to underline further three-dimensional capabilities as well as the high flexibility of the DMSO technique, two optical components are presented hereafter. First, a simple twisted X-coupler is depicted on Fig. 7.16 where a structure rotation from the vertical to the horizontal plane occurs. This device was photowritten in a single scan of the sample during which the wavefront was continuously controlled in order to draw simultaneously the two arms of the structure. At the beginning of the move, the spatial phase mask was driven the same way as for the above-mentioned WDD device i.e by changing the BPM cycling frequency. Then, it was gradually rotated by 90° during the writing of the central part (Fig. 7.16b)). Finally, the number ν of periods was increased to augment the separation of the two arms. The structure dimensions (separation,

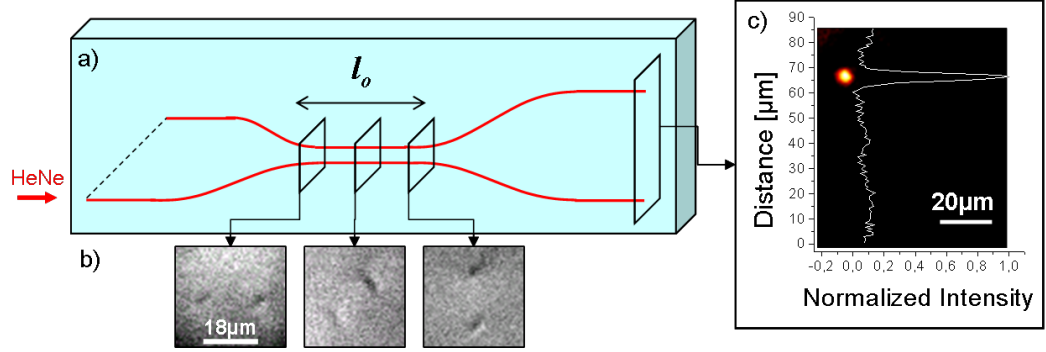


Figure 7.16: a) Schematic view of a bulk photowritten twisted X coupler achieved through DMSO in a single scan. b) Optical transmission microscopy pictures of the central region, showing 90° rotation. c) Nearfield profile at the output of the top arm under 633 nm injection in the bottom waveguide.

overlapping length l_o) were designed with the help of the above-mentioned formalism in order to transmit the totality of the 633 nm light injected in the bottom arm to the top one. Fig. 7.16c) depicts the experimentally obtained nearfield mode at the output of the device.

The second device realized with DMSO is a one to four light divider. Three processing steps were necessary to achieve the optical component. The two first scans were performed imprinting a high cycling frequency phase mask on the laser beam generating two widely separated spots. The mask was rotated by 90° after the first pass. Then the central track was drawn at low power without any wavefront modulation. The structure was designed in order to fulfill $l_{c4} = \frac{l_c}{\sqrt{4}}$ according to Eq. 7.7. The one to four light division is visible on the experimentally obtained nearfield profile (Fig. 6(a)) when the central guide is injected with HeNe. The third structure of interest achieved by DMSO consists of a hexagonal light divider for 633 nm (Fig. 7.17). Hexagonal waveguide arrays written by femtosecond SSO were recently achieved and light propagation in such structures was investigated [SBB⁺06]. The light divider presented here was photoinscribed taking advantage of the flexibility and the 3D access of DMSO. Four sample scans were necessary to achieve the device in similar exposure conditions as already described. We recall here that DMSO was restricted to two processing spots in order to preserve sufficient enough energy to trigger the proper photowriting regime in fused silica. First, the sample was irradiated with the wavefront modulated laser beam offering two processing spots separated by $30 \mu\text{m}$. The two subsequent scans were performed with the same mask rotated by an angle of 60° and 120° , successively. Finally, the central guide was photowritten without any wavefront modulation at lower power. The distance s_{AA} between two adjacent guides equals the separation s_{CA} between the central guide and the six others having $s = 15 \mu\text{m}$, the whole structure forming a regular hexagon.

In order to obtain optimal coupling, the overlapping length l_{c6} (Fig. 7.17) verifies $l_{c6} = 1.5 \text{ mm}$ obtained from Eq. 7.7. Having $s_{AA} = s_{CA}$, it is straightforward to show that $\kappa_{ss} = \kappa_{cs}$. Thus, using

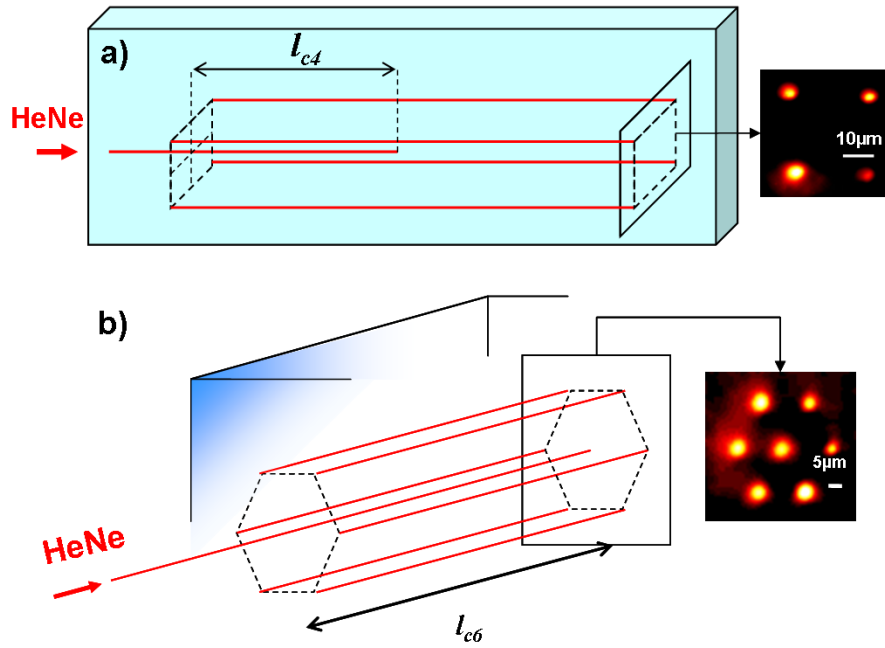


Figure 7.17: Schematic view of bulk photowritten 3D light dividers achieved through DMSO. a) One to four light divider. b) One to seven hexagonal light divider. The conditions followed by l_{c4} and l_{c6} are given in the text. Inserts: Nearfield profile under 633 nm injection in the central waveguide. Schematic view of a bulk photowritten 3D hexagonal light divider achieved through DMSO. Inserts: Nearfield profile under 633 nm injection in the central waveguide.

Eq. 7.8, it is expected to obtain $F = 0.85$, meaning that 85% of the injected light is theoretically retrieved at the output of the six external guides ($\sim 14\%$ per guide), the rest remaining in the seed waveguide. In other words, each of the seven outputs is expected to have the same nearfield mode peak intensity. The insert of (Fig. 7.17) depicts the experimental nearfield intensity distribution, being in good agreement with the foreseen distribution.

As a conclusion, spatial beam shaping permits to extent the domain of femtosecond bulk machining to parallel processing. This innovative technique is demonstrated to photoinscribe optical 3D devices in the bulk of transparent materials using spatial ultrafast beam shaping. The parallel photowriting technique uses time-evolutive modulation of femtosecond laser wavefront, producing two laser processing spots for parallel photoinscription of light guiding structures. Naturally, provided that sufficient energy is available, the technique can be scaled up to a higher number of machining foci. Several devices are demonstrated in the longitudinal writing configuration, thus underlining the high processing flexibility of this technique easily applicable for more demanding photowritten optical components. Examples are given emphasizing waveguide arrays where parallel processing appears as a natural choice. Two and three dimensional photonic structures relying on evanescent coupling were achieved with this method performing functions of light coupling, division and wavelength demultiplexing.

7.4 Conclusion

We presented efficient means of preserving the energy deposition on a reduced scale, with the help of adaptive temporal pulse shaping or spatial wavefront tailoring. Keeping then energy confinement at an efficient level even in presence of linear and nonlinear propagation distortions is a step forward in femtosecond bulk processing, with consequences on the irradiation outcome flexibility. Pioneering results in parallel bulk photowriting of optical devices were obtained relying on dynamic wavefront modulation, opening new perspectives for efficient femtosecond machining of integrated components. The challenge is to extent the technique to the writing of periodic and aperiodic patterns while counteracting detrimental propagation errors. From a general point of view, the pulse spatio-temporal profile ($I(r, t)$) is an efficient factor to control energy deposition in designed patterns for a time-effective, flexible and improved interaction.

Chapter 8

Conclusion and perspectives

While the contribution of the present report to the field of ultrafast laser processing of transparent materials has several aspects, the key point concerns the interest of spatial and temporal shaping of the ultrashort radiation. We showed that with this additional flexibility, the present challenge of machining speed can be solved by parallel photoinscription that uses multiple laser spots with reconfigurable patterns. The method uses a periodical binary phase mask to spatially modulate the wavefront of the laser beam. By varying the period (cycling frequency) of the binary phase, we show that a simple grating phase mask and therefore dynamic double-spot operation can be achieved allowing for rapid parallel photowriting of waveguides, light couplers, light dividers and wavelength division demultiplexers in fused silica glass with 3D extension.

Another significant breakthrough we achieved with spatial shaping concerns the domain of deep bulk photowriting of optical components. This method was usually restricted to shallow processing depths to keep the optical distortions associated with the air glass interface at a low level to preserve a sufficiently confined energy deposition. We indicated that the processing depth can be extended to deep focusing despite of the associated optical distortions. While we verified that the use of a corrective phase mask calculated from geometrical optics considerations can answer this problematic, a more general strategy based on global optimization tools was successfully employed. There, the optimization of the corrective phase mask was carried out from the evaluation of the laser-induced structure without any calculations of the optical distortions in play rather relying on the efficiency of the evolutionary loop. The strategy can therefore be extended to the counteraction of artifacts related to nonlinear propagation in a self-corrective manner. The result of the optimization showed a slightly better correction than the theoretical correction, showing that the robustness of the method as well as its applicability. With the help of the thus-obtained corrective phase masks, homogeneous longitudinal waveguides were photoinscribed deep in BK7 glass.

The preservation of the deposited energy density to arbitrary depths critical to obtain mechanical compaction regimes was shown to be achievable with temporal tailoring of the ultrashort light

pulse. The intensity profile is the key factor in establishing the excitation timing and propagation behavior. With the help of the same evolutionary optimization tool, the laser temporal profile was adjusted to trigger confined bulk modification in fused silica while preserving high energetic deposition. The optimized profile follows a picosecond temporal envelope which are known to propagate with a reduced set of non-linearities.

Our investigation efforts have led us to unveil a new photoinscription regime were regularly spaced dots preceed the region of main beam concentration in fused silica and BK7 glass. We showed that the position of this dots does not depend on the pulse energy neither temporal profile but is predicted by Fresnel linear propagation calculations, provided that the too often dismissed beam truncation is taken into account.

The fabrication of purely spherical voids in the 3D upon single pulse irradiation is reported here for the first time. This new photoinscription regime requires the possibility to employ picosecond pulses here obtained by temporal shaping of the femtosecond pulses. We also indicated a new regime of photoinscription of polarization-sensitive waveguides in fused silica where the formation of self induced nano-gratings occurs that can span a number of interesting developments.

In all the processes involving index changes one of the key question related to the nature of the transformation refers to its dynamics. By using an efficient pump probe set-up based on optical transmission and phase contrast microscopy, we investigated the dynamics of the energy coupling to the glassy matrix for various temporal pulse profiles. We confirm the better energy confinement in the case of picosecond pulses with characterization of the transient electronic gas and of the subsequent pressure wave in various glasses. We developed a method based on the Drude model to differentiate the electronic and matrix contributions to the contrast of the microscopy images, allowing to temporally map the free carrier density and lifetime variations in the interaction zone as well as the matrix changes. Investigations were conducted on fused silica and BK7 glass showing the dependency of the recombination time on the region of the laser-induced modification. As a general result, this recombination time tends to last longer in areas of permanent modifications.

We pointed out the interest of following the transient material state on an ultrashort time scale to understand how distinct temporal pulse profiles (namely picosecond pulse and double pulses) can lead to quasi-identical modifications. There, the transient excitation scenarios is drastically different in the first picoseconds but both lead to the formation of a dense, hot and long-lasting plasma. By monitoring the electronic density, we evidence that the second pulse of the double pulse sequence is efficiently absorbed by the plasma generated from the first pulse. From that aspect, the energy deposition resembles the picosecond case where the majority of the pulse has 'time' to interact with an absorptive plasma.

Innovative time-resolved investigations are conducted in the type II waveguide writing regime in fused silica characterized by the accumulation of numerous pulses and the appearance of nanograt-

ings self-arrangements. As a main result, we show that the pre-existing laser-induced structure has on one side, a light scattering effect thus lowering the deposited energy and, on the other side, a strong influence on the plasma formation which is compelled to follow the topology of the former structure.

We also discussed the importance of precisely controlling the focusing conditions and indicated regimes of photoinscription mainly governed by thermodynamical mechanisms in fused silica and BK7 glass. There, we identified a variety of irradiations outcomes strongly related to the weight of non linear propagation effects. The need of increasing the interaction efficiency appears mandatory to attain sufficient flexibility to promote femtosecond bulk machining to the industrial market. Particularly, the possibility offered by self-improving loops to effectively orientate the beam spatio-temporal profile towards a desired in-volume modification is a very promising concept which undoubtedly makes the ultrashort laser an uncommonly flexible bulk machining tool.

As a main conclusion, it is clear that spatio-temporally tailoring of the ultrashort pulses allows for a drastic increase of the processing flexibility while being an efficient tool to investigate the physical phenomena involved in the laser interaction with the material. On the applicative point of view, the possibility to multiply the number of processing points is evidently a great step ahead that potentially answers the industrial demands in terms of processing speed. It has to be underline that the control of tens of laser spots in the three dimensions was recently demonstrated in the field of optical tweezers, consequently the transfer to femtosecond machining should not pose any major problem provided a rather thin spectral bandwidth (i.e pulse longer than ≈ 100 fs). On the other hand, given the variety of the permanent modifications achievable with temporally shaped light pulses, it is expectable that femtosecond bulk processing will be a solution to answer most of the challenges of integrated optics. The condition however, is to dope this method with spatio-temporal tailoring tools fed with global optimization algorithms.

From a more fundamental point of view, while the present work reports on significant advances regarding the understanding of the physical processes leading to a bulk modification, questions are still to be addressed such as, e.g the temporal variation of birefringence and the quantitative variation of the refractive index. While we presented a method allowing for electronic density estimation from single wavelength images with however a number of assumptions (e.g arbitrary Drude scattering time...), the use of other probing frequencies could determine these densities unequivocally. For this, the use of a more powerful ultrashort source yielding shorter pulses could allow for spectrum broadening through filamentation for the probe while ameliorating the temporal resolution. This would play a significant role, particularly for investigations in fused silica where the recombination time can be short.

The observation means have also to be pushed up to the state of the art for refractive index determination and spatial resolution. While the first could confirm the measured electronic density,

the second would be helpful to follow the formation of nanogratings which obviously requires submicrometric resolution. The challenge though is to employ high numerical apertures lenses for probing while keeping sufficient working distance and low optical distortions. A thorough work on Speckle cancellation while keeping femtosecond flashes should also be conducted to reduce the number of required acquisitions.

Bibliography

- [ADS⁺94] P. Audebert, Ph. Daguzan, A. Dos Santos, J. Gauthier, J. Geindre, S. Guizard, G. Hamoniaux, K. Krastev, P. Martin, G. Petite, and A. Antonetti. *Space-Time observation of an electron gas in SiO₂*. Phys. Rev. Lett. **73**(14):1990–1993 (1994).
- [AGZT04] S. Akturk, X. Gu, E. Zeek, and R. Trebino. *Pulse-front tilt caused by spatial and temporal chirp*. Opt. Express **12**(19):4399–4410 (2004).
- [AH88] J. Arndt and W. Hummel. *The general refractivity formula applied to densified silicate glasses*. Phys. Chem. Min. **15**(4):363–369 (1988).
- [AHHM82] P. Aubourg, J. P. Huignard, M. Hareng, and R. A. Mullen. *Liquid crystal light valve using bulk monocrystalline Bi₁₂SiO₂₀ as the photoconductive material*. Appl. Opt. **21**(20):3706–3712 (1982).
- [AKNO94] B. E. Allman, A. G. Klein, K. A. Nugent, and G. I. Opat. *Refractive-index-profile determinations by using lloyds mirage*. Applied Optics **33**(10):1806–1811 (1994).
- [AKOT03] S. Akturk, M. Kimmel, P. O’Shea, and R. Trebino. *Measuring pulse-front tilt in ultrashort pulses using GRENOUILLE*. Opt. Express **11**(5):491–501 (2003).
- [AMSW05] M. Ams, G. Marshall, D. Spence, and M. Withford. *Slit beam shaping method for femtosecond laser direct-write fabrication of symmetric waveguides in bulk glasses*. Opt. Express **13**(15):5676–5681 (2005).
- [AP83] W. T. Anderson and D. L. Philen. *Spot size measurements for Single-Mode Fibers-A comparison of four techniques*. J. Lightwave Technol. **1**(1):20–26 (1983).
- [Ash03] J. B. Ashcom. *The role of focusing in the interaction of femtosecond laser pulses with transparent materials*. PhD thesis Harvard University (2003).
- [ASL⁺06] R. Ackermann, E. Salmon, N. Lascoux, J. Kasparian, P. Rohwetter, K. Stelmaszczyk, S. Li, A. Lindinger, L. Woeste, P. Bejot, L. Bonacina, and J.-P. Wolf. *Optimal control of filamentation in air*. Appl. Phys. Lett. **89**(17):171117–3 (2006).

- [Bar02] A. Bartelt. *Control of Wave Packet Dynamics in Small Alkali Clusters with Optimally Shaped Femtosecond Pulses*. PhD thesis Freie Universitaet Berlin (2002).
- [BBN02] E. D. Barone-Nugent, A. Barty, and K. A. Nugent. *Quantitative phase-amplitude microscopy i: optical microscopy*. J. of Micro. **206**(3):194–203 (2002).
- [BBS⁺07] I. M. Burakov, N. M. Bulgakova, R. Stoian, A. Mermillod-Blondin, E. Audouard, A. Rosenfeld, A. Husakou, and I. V. Hertel. *Spatial distribution of refractive index variations induced in bulk fused silica by single ultrashort and short laser pulses*. J. Appl. Phys. **101**(4):043506–7 (2007).
- [BBS⁺08] Y. Bellouard, E. Barthel, A. A. Said, M. Dugan, and P. Bado. *Scanning thermal microscopy and raman analysis of bulk fused silica exposed to low energy femtosecond laser pulses*. Opt. Express **16**(24):19520–19534 (2008).
- [BHS⁺09] J. Baumgartl, G. M. Hannappel, D. J. Stevenson, D. Day, M. Gu, and K. Dholakia. *Optical redistribution of microparticles and cells between microwells*. Lab Chip **9**(10):1334–1336 (2009). PMID: 19417896.
- [BKK04] E. Bricchi, B. G. Klappauf, and P. G. Kazansky. *Form birefringence and negative index change created by femtosecond direct writing in transparent materials*. Opt. Lett. **29**(1):119–121 (2004).
- [BKK⁺05] T. Baumert, F. Kannari, F. Korte, J. Koch, and B. Chichkov. *Influence of spatiotemporal coupling induced by an ultrashort laser pulse shaper on a focused beam profile*. Appl. Opt. **44**(6):1092–1098 (2005).
- [BNPR98] A. Barty, K. A. Nugent, D. Paganin, and A. Roberts. *Quantitative optical phase microscopy*. Opt. Lett. **23**(11):817–819 (1998).
- [BNW98] M. J. Booth, M. A. A. Neil, and T. Wilson. *Aberration correction for confocal imaging in refractive-index-mismatched media*. J. of Micro. **192**(2):90–98 (1998).
- [Boo06] M. Booth. *Wave front sensor-less adaptive optics: a model-based approach using sphere packings*. Opt. Express **14**(4):1339–1352 (2006).
- [Bor88] Z. Bor. *Distortion of femtosecond laser pulses in lenses and lens systems*. Jour. of Mod. Opt. **35**(12):1907 (1988).
- [Bor89] Z. Bor. *Distortion of femtosecond laser pulses in lenses*. Opt. Lett. **14**(2):119–121 (1989).

- [Boy80] R. W. Boyd. *Intuitive explanation of the phase anomaly of focused light beams*. J. Opt. Soc. Am. **70**(7):877–880 (1980).
- [Boy08] R. W. Boyd. *Nonlinear Optics*. Academic Press Inc 3rd edition (2008).
- [BS96] B. Di Bartolo and K. Stamatios. *Spectroscopy and dynamics of collective excitations in solids*. NATO ASI series New York (1996).
- [BSB05] Y. Bellouard, A. Said, and P. Bado. *Integrating optics and micro-mechanics in a single substrate: a step toward monolithic integration in fused silica*. Opt. Express **13**(17):6635–6644 (2005).
- [BSC⁺05] V. R. Bhardwaj, E. Simova, P. B. Corkum, D. M. Rayner, C. Hnatovsky, R. S. Taylor, B. Schreder, M. Kluge, and J. Zimmer. *Femtosecond laser-induced refractive index modification in multicomponent glasses*. J. Appl. Phys. **97**(8):083102–9 (2005).
- [BSPA02] N. F. Borrelli, C. M. Smith, J. J. Price, and D. C. Allan. *Polarized excimer laser-induced birefringence in silica*. Appl. Phys. Lett. **80**(2):219 (2002).
- [BSR⁺06] V. R. Bhardwaj, E. Simova, P. P. Rajeev, C. Hnatovsky, R. S. Taylor, D. M. Rayner, and P. B. Corkum. *Optically produced arrays of planar nanostructures inside fused silica*. Phys. Rev. Lett. **96**(5):057404 (2006).
- [BSW⁺06] M. J. Booth, M. Schwertner, T. Wilson, M. Nakano, Y. Kawata, M. Nakabayashi, and S. Miyata. *Predictive aberration correction for multilayer optical data storage*. Appl. Phys. Lett. **88**(3):031109–3 (2006).
- [BW99] M. Born and E. Wolf. *Principles of Optics: Electromagnetic Theory of Propagation, Interference and Diffraction of Light*. Cambridge University Press 7th edition (1999).
- [Cal00] J. P. Callan. *Ultrafast Dynamics and Phase Changes in Solids Excited by Femtosecond Laser Pulses*. PhD thesis Harvard University (2000).
- [CBD99] E. CuChe, F. Bevilacqua, and C. Depeursinge. *Digital holography for quantitative phase-contrast imaging*. Opt. Lett. **24**(5):291–293 (1999).
- [CCK⁺08] S. Chin, Y. Chen, O. Kosareva, V. Kandidov, and F. Thberge. *What is a filament?* Las. Phys. **18**(8):962–964 (2008).
- [CDG⁺96] R. Conde, C. Depeursinge, B. Gisin, N. Gisin, and B. Groebli. *Refractive index profile and geometry measurements in multicore fibres*. J. Eur. Opt. Soc. A **5**(3):269–274 (1996).

- [CHRK01] J. W. Chan, T. Huser, S. Risbud, and D. M. Krol. *Structural changes in fused silica after exposure to focused femtosecond laser pulses*. Opt. Lett. **26**(21):1726–1728 (2001).
- [CK07] P. B. Corkum and F. Krausz. *Attosecond science*. Nat. Phys. **3**(6):381–387 (2007).
- [CKT⁺08] T. Cizmar, V. Kollarova, X. Tsampoula, F. Gunn-Moore, W. Sibbett, Z. Bouchal, and K. Dholakia. *Generation of multiple bessel beams for a biophotonics workstation*. Opt. Express **16**(18):14024–14035 (2008).
- [CLJ⁺09] F. Courvoisier, P.-A. Lacourt, M. Jacquot, M. K. Bhuyan, L. Furfaro, and J. M. Dudley. *Surface nanoprocessing with nondiffracting femtosecond bessel beams*. Opt. Lett. **34**(20):3163–3165 (2009).
- [CLS03] D. N. Christodoulides, F. Lederer, and Y. Silberberg. *Discretizing light behaviour in linear and nonlinear waveguide lattices*. Nature **424**(6950):817–823 (2003).
- [CMM⁺09] G. Cheng, K. Mishchik, C. Maclair, E. Audouard, and R. Stoian. *Ultrafast laser photoinscription of polarization sensitive devices in bulk silica glass*. Opt. Express **17**(12):9515–9525 (2009).
- [Cor93] J. Cordingley. *Application of a binary diffractive optic for beam shaping in semiconductor processing by lasers*. Appl. Opt. **32**(14):2538–2542 (1993).
- [CSF⁺05] A. Couairon, L. Sudrie, M. Franco, B. Prade, and A. Mysyrowicz. *Filamentation and damage in fused silica induced by tightly focused femtosecond laser pulses*. Phys. Rev. B **71**(12):125435–125446 (2005).
- [CSM⁺03] Y. Cheng, K. Sugioka, K. Midorikawa, M. Masuda, K. Toyoda, M. Kawachi, and K. Shihoyama. *Control of the cross-sectional shape of a hollow microchannel embedded in photostructurable glass by use of a femtosecond laser*. Opt. Lett. **28**(1):55–57 (2003).
- [CTE⁺07] S. Campbell, S. M. F. Triphan, R. El-Agmy, A. H. Greenaway, and D. T. Reid. *Direct optimization of femtosecond laser ablation using adaptive wavefront shaping*. J. Opt. A **9**(11):1100–1104 (2007).
- [CTH⁺07] S. Campbell, R. R. Thomson, D. P. Hand, A. K. Kar, D. T. Reid, C. Canalias, V. Pasiskevicius, and F. Laurell. *Frequency-doubling in femtosecond laser inscribed periodically-poled potassium titanyl phosphate waveguides*. Opt. Express **15**(25):17146–17150 (2007).

- [CXW05] I. H. Chowdhury, X. Xu, and A. M. Weiner. *Ultrafast double-pulse ablation of fused silica*. Appl. Phys. Lett. **86**(15):151110–3 (2005).
- [DD96] L. Douillard and J. P. Duraud. *Swift heavy ion amorphization of quartz – a comparative study of the particle amorphization mechanism of quartz*. Nucl. Instr. Meth. Phys. Res. Sec. B **107**(1-4):212–217 (1996).
- [DFG⁺03] C. Daniel, J. Full, L. Gonzalez, C. Lupulescu, J. Manz, A. Merli, S. Vajda, and L. Woste. *Deciphering the reaction dynamics underlying optimal control laser fields*. Science **299**(5606):536–539 (2003).
- [dlCFG⁺09] A. Ruiz de la Cruz, A. Ferrer, W. Gawelda, D. Puerto, M. G. Sosa, J. Siegel, and J. Solis. *Independent control of beam astigmatism and ellipticity using a SLM for fs-laser waveguide writing*. Opt. Express **17**(23):20853–20859 (2009).
- [DLK⁺94] D. Du, X. Liu, G. Korn, J. Squier, and G. Mourou. *Laser-induced breakdown by impact ionization in SiO₂ with pulse widths from 7 ns to 150 fs*. Appl. Phys. Lett. **64**(23):3071–3073 (1994).
- [DMSH96] K. M. Davis, K. Miura, N. Sugimoto, and K. Hirao. *Writing waveguides in glass with a femtosecond laser*. Opt. Lett. **21**(21):1729–1731 (1996).
- [DR06] J.-C. Diels and W. Rudolph. *Ultrashort Laser Pulse Phenomenon: Fundamentals, Techniques, and Applications on a Femtosecond Time Scale*. Academic Press Inc. 2nd edition (2006).
- [Dru06] P. Drude. *Zur Elektronentheorie der Metalle*. Harri Deutsch Verlag (2006).
- [DSLL09] H. T. Dai, X. W. Sun, D. Luo, and Y. J. Liu. *Airy beams generated by a binary phase element made of polymer-dispersed liquid crystals*. Opt. Express **17**(22):19365–19370 (2009).
- [DSS06] V. Diez-Blanco, J. Siegel, and J. Solis. *Waveguide structures written in SF57 glass with fs-laser pulses above the critical self-focusing threshold*. Appl. Surf. Sc. **252**(13):4523–4526 (2006).
- [Dys50] J. Dyson. *An interferometer microscope*. Proc. Roy. Soc. Lond. A **204**(1077):170–187 (1950).
- [DZF⁺91] A. G. Doukas, A. D. Zweig, J. K. Frisoli, R. Birngruber, and T. F. Deutsch. *Non-invasive determination of shock wave pressure generated by optical breakdown*. Appl. Phys. B **53**(4):237–245 (1991).

- [EBGR05] R. El-Agmy, H. Bulte, A. H. Greenaway, and D. Reid. *Adaptive beam profile control using a simulated annealing algorithm*. Opt. Express **13**(16):6085–6091 (2005).
- [ECK⁺02] J. Endo, J. Chen, D. Kobayashi, Y. Wada, and H. Fujita. *Transmission laser microscope using the Phase-Shifting technique and its application to measurement of optical waveguides*. Appl. Opt. **41**(7):1308–1314 (2002).
- [Efr94] U. Efron. *Spatial Light Modulator Technology*. CRC Press 1st edition (1994).
- [EGA02] O. M. Efimov, L. M. Glebov, and H. P. Andre. *Measurement of the induced refractive index in a photothermorefractive glass by a Liquid-Cell shearing interferometer*. Appl. Opt. **41**(10):1864–1871 (2002).
- [EKW⁺04] D. Ehrt, T. Kittel, M. Will, S. Nolte, and A. Tnnermann. *Femtosecond-laser-writing in various glasses*. J. N-Cryst. Sol. **345-346**:332–337 (2004).
- [ERH⁺07] L. Englert, B. Rethfeld, L. Haag, M. Wollenhaupt, C. Sarpe-Tudoran, and T. Baumert. *Control of ionization processes in high band gap materials via tailored femtosecond pulses*. Opt. Express **15**(26):17855–17862 (2007).
- [ES03] A. E. Eiben and J. E. Smith. *Introduction to evolutionary computing*. Springer 1st edition (2003).
- [EZN⁺08] S. M. Eaton, H. Zhang, M. L. Ng, J. Li, W.-J. Chen, S. Ho, and Peter R. Herman. *Transition from thermal diffusion to heat accumulation in high repetition rate femtosecond laser writing of buried optical waveguides*. Opt. Express **16**(13):9443–9458 (2008).
- [FSL02] C. H. Fan, J. Sun, and J. P. Longtin. *Plasma absorption of femtosecond laser pulses in dielectrics*. J. Heat Transfer **124**(2):275–283 (2002).
- [FSWN02] T. Feurer, N. Stoyanov, D. Ward, and K. Nelson. *Direct visualization of the gouv phase by focusing phonon polaritons*. Phys. Rev. Lett. **88**(25) (2002).
- [FZT05] U. Fuchs, U. Zeitner, and A. Tuennermann. *Ultra-short pulse propagation in complex optical systems*. Opt. Express **13**(10):3852–3861 (2005).
- [GCM06] R. R. Gattass, L. R. Cerami, and E. Mazur. *Micromachining of bulk glass with bursts of femtosecond laser pulses at variable repetition rates*. Opt. Express **14**(12):5279–5284 (2006).

- [GFD⁺07] R. Graf, A. Fernandez, M. Dubov, H.J. Brueckner, B.N. Chichkov, and A. Apolonski. *Pearl-chain waveguides written at megahertz repetition rate*. Appl. Phys. B **87**(1):21–27 (2007).
- [GM97] E. N. Glezer and E. Mazur. *Ultrafast-laser driven micro-explosions in transparent materials*. Appl. Phys. Lett. **71**(7):882–884 (1997).
- [GMH⁺96] E. N. Glezer, M. Milosavljevic, L. Huang, R. J. Finlay, T.-H. Her, J. P. Callan, and E. Mazur. *Three-dimensional optical storage inside transparent materials*. Opt. Lett. **21**(24):2023–2025 (1996).
- [Goo05] Joseph W. Goodman. *Introduction To Fourier Optics*. Roberts & Company Publishers 3rd edition (2005).
- [Gou90] L. G. Gouy. *Sur une propriete nouvelle des ondes lumineuses*. C. R. Acad. Sc. Paris **110**:1251–1253 (1890).
- [GP10] T. D. Gerke and R. Piestun. *Aperiodic volume optics*. Nat. Photon. **4**(3):188–193 (2010).
- [GS72] R. W. Gerchberg and W. O. Saxton. *A practical algorithm for the determination of the phase from image and diffraction plane pictures*. Optik pages 237–246 (1972).
- [GST03] D. J. Griffiths, M. P. Soroka, and W. Throop. *Introduction to Electrodynamics*. Pearson Education (US) 3rd edition (2003).
- [GWN⁺03] T. Gorelik, M. Will, S. Nolte, A. Tuennermann, and U. Glatzel. *Transmission electron microscopy studies of femtosecond laser induced modifications in quartz*. Appl. Phys. A **76**(3):309–311 (2003).
- [HBT⁺07] L. Hallo, A. Bourgeade, V. T. Tikhonchuk, C. Mezel, and J. Breil. *Model and numerical simulations of the propagation and absorption of a short laser pulse in a transparent dielectric material: Blast-wave launch and cavity formation*. Phys. Rev. B **76**(2):024101–12 (2007).
- [HHN06] S. Hasegawa, Y. Hayasaki, and N. Nishida. *Holographic femtosecond laser processing with multiplexed phase fresnel lenses*. Opt. Lett. **31**(11):1705–1707 (2006).
- [HKCL06] J. Hahn, H. Kim, K. Choi, and B. Lee. *Real-time digital holographic beam-shaping system with a genetic feedback tuning loop*. Appl. Opt. **45**(5):915–924 (2006).

- [HKP04] A. Horn, E.W. Kreutz, and R. Poprawe. *Ultrafast time-resolved photography of femtosecond laser induced modifications in BK7 glass and fused silica*. Appl. Phys. A **79**(4):923–925 (2004).
- [HKY⁺06] K.-H. Hong, S. Kostritsa, T. J. Yu, J. H. Sung, I. W. Choi, Y.-C. Noh, D.-K. Ko, and J. Lee. *100-kHz high-power femtosecond ti:sapphire laser based on downchirped regenerative amplification*. Opt. Express **14**(2):970–978 (2006).
- [HMG⁺08] A. Horn, I. Mingareev, J. Gottmann, A. Werth, and U. Brenk. *Dynamical detection of optical phase changes during micro-welding of glass with ultra-short laser radiation*. Meas. Sc. Tec. **19**(1):015302 (2008).
- [Hor03] A. Horn. *Zeitaufgelöste Analyse der Wechselwirkung von ultrakurz gepulster Laserstrahlung mit Dielektrika*. PhD thesis Fakultät fuer Maschinenwesen der Rheinisch-Westfälischen Technischen Hochschule Aachen (2003).
- [HSA07] N. Huot, N. Sanner, and E. Audouard. *Optimization of the focal volume in programmable spatial beam shaping*. J. Opt. Soc. Am. B **24**(11):2814–2820 (2007).
- [HSL06] G. Heck, J. Sloss, and R. J. Levis. *Adaptive control of the spatial position of white light filaments in an aqueous solution*. Opt. Comm. **259**(1):216–222 (2006).
- [HSM⁺07] N. Huot, R. Stoian, A. Mermillod-Blondin, C. Mauclair, and E. Audouard. *Analysis of the effects of spherical aberration on ultrafast laser-induced refractive index variation in glass*. Opt. Express **15**(19):12395–12408 (2007).
- [HTS⁺05] C. Hnatovsky, R. S. Taylor, E. Simova, V. R. Bhardwaj, D. M. Rayner, and P. B. Corkum. *High-resolution study of photoinduced modification in fused silica produced by a tightly focused femtosecond laser beam in the presence of aberrations*. J. Appl. Phys. **98**(1):013517–5 (2005).
- [HUA⁺92] D. Huang, M. Ulman, L. H. Acioli, H. A. Haus, and J. G. Fujimoto. *Self-focusing-induced saturable loss for laser mode locking*. Opt. Lett. **17**(7):511–513 (1992).
- [Hum04] R. E. Hummel. *Electronic Properties of Materials*. Springer-Verlag New York Inc. 3rd edition (2004).
- [HW93] N. Hodgson and H. Weber. *Influence of spherical aberration of the active medium on the performance of Nd:YAG lasers*. IEEE J. Quant. Electron. **29**(9):2497–2507 (1993).

- [HWG⁺99] D. Homoelle, S. Wielandy, A. L. Gaeta, N. F. Borrelli, and C. Smith. *Infrared photosensitivity in silica glasses exposed to femtosecond laser pulses*. Opt. Lett. **24**(18):1311–1313 (1999).
- [IWNS06] K. Itoh, W. Watanabe, S. Nolte, and C. B. Schaffer. *Ultrafast processes for bulk modification of transparent materials*. MRS Bull **31**:620–625 (2006).
- [JBC⁺89] S. C. Jones, P. Braunlich, R. T. Casper, X.-A. Shen, and P. Kelly. *Recent progress on laser-induced modifications and intrinsic bulk damage of wide-gap optical materials*. Opt. Eng. **28**:1039–1068 (1989).
- [JLS⁺03] A.P. Joglekar, H. Liu, G.J. Spooner, E. Meyhoefer, G. Mourou, and A.J. Hunt. *A study of the deterministic character of optical damage by femtosecond laser pulses and applications to nanomachining*. Appl. Phys. B **77**(1):25–30 (2003).
- [JMWB10] A. Jesacher, G. D. Marshall, T. Wilson, and M. J. Booth. *Adaptive optics for direct laser writing with plasma emission aberration sensing*. Opt. Express **18**(2):656–661 (2010).
- [JNT⁺06] S. Juodkazis, K. Nishimura, S. Tanaka, H. Misawa, E. G. Gamaly, B. Luther-Davies, L. Hallo, P. Nicolai, and V. T. Tikhonchuk. *Laser-Induced microexplosion confined in the bulk of a sapphire crystal: Evidence of multimegabar pressures*. Phys. Rev. Lett. **96**(16):166101 (2006).
- [JR92] R. Judson and H. Rabitz. *Teaching lasers to control molecules*. Phys. Rev. Lett. **68**(10):1500–1503 (1992).
- [KD03] S. O. Kucheyev and S. G. Demos. *Optical defects produced in fused silica during laser-induced breakdown*. Appl. Phys. Lett. **82**(19):3230–3232 (2003).
- [Kel65] L. V. Keldysh. *Ionization in the field of a strong electromagnetic wave*. Sov. Phys. JETP **20**:1307–1314 (1965).
- [KGV83] S. Kirkpatrick, C. D. Gelatt, and M. P. Vecchi. *Optimization by simulated annealing*. Science **220**(4598):671–680 (1983).
- [KHP05] E.W. Kreutz, A. Horn, and R. Poprawe. *Electron excitation in glasses followed by time- and space-measuring tools*. Appl. Surf. Sc. **248**(1-4):66–70 (2005).
- [KIM⁺99] P. G. Kazansky, H. Inouye, T. Mitsuyu, K. Miura, J. Qiu, K. Hirao, and F. Starrost. *Anomalous anisotropic light scattering in Ge-Doped silica glass*. Phys. Rev. Lett. **82**(10):2199 (1999).

- [KKK09] T. Kozacki, R. Krajewski, and M. Kujawinska. *Reconstruction of refractive-index distribution in off-axis digital holography optical diffraction tomographic system*. Opt. Express **17**(16):13758–13767 (2009).
- [KL66] H. Kogelnik and T. Li. *Laser beams and resonators*. Appl. Opt. **5**(10):1550–1567 (1966).
- [KMH08] S. Kanehira, K. Miura, and K. Hirao. *Ion exchange in glass using femtosecond laser irradiation*. Appl. Phys. Lett. **93**(2):023112–3 (2008).
- [KMJM01] T. Kondo, S. Matsuo, S. Juodkazis, and H. Misawa. *Femtosecond laser interference technique with diffractive beam splitter for fabrication of three-dimensional photonic crystals*. Appl. Phys. Lett. **79**(6):725–727 (2001).
- [KNKL08] S. Kim, J. Na, M. J. Kim, and B. H. Lee. *Simultaneous measurement of refractive index and thickness by combining low-coherence interferometry and confocal optics*. Opt. Express **16**(8):5516–5526 (2008).
- [KO04] M. Kamata and M. Obara. *Control of the refractive index change in fused silica glasses induced by a loosely focused femtosecond laser*. Appl. Phys. A **78**(1):85–88 (2004).
- [Koe06] W. Koechner. *Solid-state Laser Engineering*. Springer-Verlag New York Inc. 6th edition (2006).
- [Kro08] D.M. Krol. *Femtosecond laser modification of glass*. J. N-Cryst. Sol. **354**(2-9):416–424 (2008).
- [KS08] P. G. Kazansky and Y. Shimotsuma. *Self-assembled sub-wavelength structures and form birefringence created by femtosecond laser writing in glass: properties and applications*. Jour. Cer. Soc Jap. **116**(1358):1052–1062 (2008).
- [KSQ⁺05] S. Kanehira, J. Si, J. Qiu, K. Fujita, and K. Hirao. *Periodic nanovoid structures via femtosecond laser irradiation*. Nano Lett. **5**(8):1591–1595 (2005).
- [LAD⁺08] D. J. Little, M. Ams, P. Dekker, G. Marshall, J. M. Dawes, and M. J. Withford. *Femtosecond laser modification of fused silica: the effect of writing polarization on Si-O ring structure*. Opt. Express **16**(24):20029–20037 (2008).
- [LCW94] J. R. Leger, D. Chen, and Z. Wang. *Diffractive optical element for mode shaping of a Nd:YAG laser*. Opt. Lett. **19**(2):108–110 (1994).

- [LHP⁺05] E. Louzon, Z. Henis, S. Pecker, Y. Ehrlich, D. Fisher, M. Fraenkel, and A. Zigler. *Reduction of damage threshold in dielectric materials induced by negatively chirped laser pulses*. Appl. Phys. Lett. **87**(24):241903–3 (2005).
- [LKS⁺98] M. Lenzner, J. Krueger, S. Sartania, Z. Cheng, Ch. Spielmann, G. Mourou, W. Kautek, and F. Krausz. *Femtosecond optical breakdown in dielectrics*. Phys. Rev. Lett. **80**(18):4076–4079 (1998).
- [LLA⁺06] D. Liu, Y. Li, R. An, Y. Dou, H. Yang, and Q. Gong. *Influence of focusing depth on the microfabrication of waveguides inside silica glass by femtosecond laser direct writing*. Appl. Phys. A **84**(3):257–260 (2006).
- [LSK⁺10] J. Lhermite, E. Suran, V. Kermene, F. Louradour, A. Desfarges-Berthelemot, and A. Barthelemy. *Coherent combining of 49 laser beams from a multiple core optical fiber by a spatial light modulator*. Opt. Express **18**(5):4783–4789 (2010).
- [LT02] J. S. Liu and M. R. Taghizadeh. *Iterative algorithm for the design of diffractive phase elements for laser beam shaping*. Opt. Lett. **27**(16):1463–1465 (2002).
- [LYZT08] S. Li, G. Yu, C. Zheng, and Q. Tan. *Quasi-Dammann grating with proportional intensity array spots*. Opt. Lett. **33**(18):2023–2025 (2008).
- [Mal65] I. H. Malitson. *Interspecimen comparison of the refractive index of fused silica*. J. Opt. Soc. Am. **55**(10):1205–1208 (1965).
- [Mar79] D. Marcuse. *Refractive index determination by the focusing method*. Appl. Opt. **18**(1):9–13 (1979).
- [MB83] L. McCaughan and E. Bergmann. *Index distribution of optical waveguides from their mode profile*. J. Lightwave Technol. **1**:241–244 (1983).
- [MBM⁺08] A. Mermillod-Blondin, I. M. Burakov, Yu. P. Meshcheryakov, N. M. Bulgakova, E. Audouard, A. Rosenfeld, A. Husakou, I. V. Hertel, and R. Stoian. *Flipping the sign of refractive index changes in ultrafast and temporally shaped laser-irradiated borosilicate crown optical glass at high repetition rates*. Phys. Rev. B **77**(10):104205 (2008).
- [MBR⁺09] A. Mermillod-Blondin, J. Bonse, A. Rosenfeld, I. V. Hertel, Yu. P. Meshcheryakov, N. M. Bulgakova, E. Audouard, and R. Stoian. *Dynamics of femtosecond laser induced voidlike structures in fused silica*. Appl. Phys. Lett. **94**(4):041911 (2009).

- [MCH⁺09] C. Mauchlaire, G. Cheng, N. Huot, E. Audouard, A. Rosenfeld, I. V. Hertel, and R. Stoian. *Dynamic ultrafast laser spatial tailoring for parallel micromachining of photonic devices in transparent materials*. Opt. Express **17**(5):3531–3542 (2009).
- [Mer07] A. Mermillod-Blondin. *Analysis and Optimization of Ultrafast Laser-Induced Bulk Modifications in Dielectric Materials*. PhD thesis Freie Universitaet Berlin (2007).
- [MJ06] H. Misawa and S. Juodkazis. *3D Laser Microfabrication: Principles and Applications*. Wiley InterScience 1st edition (2006).
- [MKBB02] J. D. Mills, P. G. Kazansky, E. Bricchi, and J. J. Baumberg. *Embedded anisotropic microreflectors by femtosecond-laser nanomachining*. Appl. Phys. Lett. **81**(2):196 (2002).
- [ML74] G. J. Morales and Y. C. Lee. *Ponderomotive-Force effects in a nonuniform plasma*. Phys. Rev. Lett. **33**(17):1016 (1974).
- [MMH⁺08] C. Mauchlaire, A. Mermillod-Blondin, N. Huot, E. Audouard, and R. Stoian. *Ultrafast laser writing of homogeneous longitudinal waveguides in glasses using dynamic wavefront correction*. Opt. Express **16**(8):5481–5492 (2008).
- [MMJ⁺03] A. Marcinkevicius, V. Mizeikis, S. Juodkazis, S. Matsuo, and H. Misawa. *Effect of refractive index-mismatch on laser microfabrication in silica glass*. Appl. Phys. A **76**(2):257–260 (2003).
- [MMR⁺08] A. Mermillod-Blondin, C. Mauchlaire, A. Rosenfeld, J. Bonse, I. V. Hertel, E. Audouard, and R. Stoian. *Size correction in ultrafast laser processing of fused silica by temporal pulse shaping*. Appl. Phys. Lett. **93**(2):021921–3 (2008).
- [MQG⁺04] S. S. Mao, F. Qur, S. Guizard, X. Mao, R. E. Russo, G. Petite, and P. Martin. *Dynamics of femtosecond laser interactions with dielectrics*. Appl. Phys. A **79**(7):16951709 (2004).
- [MQI⁺97] K. Miura, J. Qiu, H. Inouye, T. Mitsuyu, and K. Hirao. *Photowritten optical waveguides in various glasses with ultrashort pulse laser*. Appl. Phys. Lett. **71**(23):3329–3331 (1997).
- [MS74] P. D. McIntyre and A. W. Snyder. *Power transfer between nonparallel and tapered optical fibers*. J. Opt. Soc. Am. **64**(3):285–288 (1974).
- [MSZR05] M. Mero, A.J. Sabbah, J. Zeller, and W. Rudolph. *Femtosecond dynamics of dielectric films in the pre-ablation regime*. Appl. Phys. A **81**(2):317–324 (2005).

- [NB04] K. C. Neuman and S. M. Block. *Optical trapping*. Rev. Sci. Instrum. **75**(9):2787–2809 (2004).
- [NK92] T. Noda and S. Kawata. *Separation of phase and absorption images in phase-contrast microscopy*. J. Opt. Soc. Am. A **9**(6):924–931 (1992).
- [NWB03] S. Nolte, M. Will, J. Burghoff, and A. Tuennermann. *Femtosecond waveguide writing: a new avenue to three-dimensional integrated optics*. Appl. Phys. A **77**(1):109–111 (2003).
- [OCM⁺05] R. Osellame, N. Chiodo, V. Maselli, A. Yin, M. Zavelani-Rossi, G. Cerullo, P. Laporta, L. Aiello, S. De Nicola, P. Ferraro, A. Finizio, and G. Pierattini. *Optical properties of waveguides written by a 26 MHz stretched cavity ti:sapphire femtosecond oscillator*. Opt. Express **13**(2):612–620 (2005).
- [OTM⁺03] R. Osellame, S. Taccheo, M. Marangoni, R. Ramponi, P. Laporta, D. Polli, S. De Silvestri, and G. Cerullo. *Femtosecond writing of active optical waveguides with astigmatically shaped beams*. J. Opt. Soc. Am. B **20**(7):1559–1567 (2003).
- [PBW05] B. Potsaid, Y. Bellouard, and J. Wen. *Adaptive scanning optical microscope (ASOM): a multidisciplinary optical microscope design for large field of view and high resolution imaging*. Opt. Express **13**(17):6504–6518 (2005).
- [PC98] A. Pasquarello and Roberto Car. *Identification of raman defect lines as signatures of ring structures in vitreous silica*. Phys. Rev. Lett. **80**(23):5145–5147 (1998).
- [PDE⁺99] T. Pertsch, P. Dannberg, W. Elfle, A. Braeuer, and F. Lederer. *Optical bloch oscillations in temperature tuned waveguide arrays*. Phys. Rev. Lett. **83**(23):4752 (1999).
- [PDGM97] G. Petite, P. Daguzan, S. Guizard, and P. Martin. *Ultrafast processes in laser irradiated wide bandgap insulators*. Appl. Surf. Sc. **109-110**:36–42 (1997).
- [PDV⁺04] G. Popescu, L. P. Deflores, J. C. Vaughan, K. Badizadegan, H. Iwai, R. R. Gattass, and M. S. Feld. *Fourier phase microscopy for investigation of biological structure and dynamics*. Opt. Lett. **29**(21):2503–2505 (2004).
- [PIDF06] G. Popescu, T. Ikeda, R. R. Dasari, and M. S. Feld. *Diffraction phase microscopy for quantifying cell structure and dynamics*. Opt. Lett. **31**(6):775–777 (2006).
- [PKM⁺09] P. Polynkin, M. Kolesik, J. V. Moloney, G. A. Siviloglou, and D. N. Christodoulides. *Curved plasma channel generation using ultraintense airy beams*. Science **324**(5924):229–232 (2009).

- [PLPA08] B. Poumellec, M. Lancry, J.-C. Poulin, and S. Ani-Joseph. *Non reciprocal writing and chirality in femtosecond laser irradiated silica*. Opt. Express **16**(22):18354–18361 (2008).
- [PRG05] I. Perch-Nielsen, P. Rodrigo, and J. Glueckstad. *Real-time interactive 3D manipulation of particles viewed in two orthogonal observation planes*. Opt. Express **13**(8):2852–2857 (2005).
- [PSF⁺03] B. Poumellec, L. Sudrie, M. Franco, B. Prade, and A. Mysyrowicz. *Femtosecond laser irradiation stress induced in pure silica*. Opt. Express **11**(9):1070–1079 (2003).
- [PWA⁺03] A. Prakelt, M. Wollenhaupt, A. Assion, Ch. Horn, C. Sarpe-Tudoran, M. Winter, and T. Baumert. *Compact, robust, and flexible setup for femtosecond pulse shaping*. Rev. Sci. Instrum. **74**(11):4950–4953 (2003).
- [PZT07] D. G. Papazoglou, I. Zergioti, and S. Tzortzakis. *Plasma strings from ultraviolet laser filaments drive permanent structural modifications in fused silica*. Opt. Lett. **32**(14):2055–2057 (2007).
- [QGM01] F. Quere, S. Guizard, and Ph. Martin. *Time-resolved study of laser-induced breakdown in dielectrics*. Europhys. Lett. **56**(1):138–144 (2001).
- [QHA⁺00] C. Quoix, G. Hamoniaux, A. Antonetti, J. -C. Gauthier, J. -P. Geindre, and P. Audebert. *Ultrafast plasma studies by phase and amplitude measurements with femtosecond spectral interferometry*. J. Quant. Spectro. Rad. Trans. **65**(1-3):455–462 (2000).
- [QKS⁺00] J. Qiu, P. G. Kazansky, J. Si, K. Miura, T. Mitsuyu, K. Hirao, and A. L. Gaeta. *Memorized polarization-dependent light scattering in rare-earth-ion-doped glass*. Appl. Phys. Lett. **77**(13):1940 (2000).
- [QTM⁺06] F. Qur, C. Thaury, P. Monot, S. Dobosz, P. Martin, J.-P. Geindre, and P. Audebert. *Coherent wake emission of High-Order harmonics from overdense plasmas*. Phys. Rev. Lett. **96**(12) (2006).
- [RAB⁺02] A. Roberts, E. Ampem-Lassen, A. Barty, K. A. Nugent, G. W. Baxter, N. M. Dragomir, and S. T. Huntington. *Refractive-index profiling of optical fibers with axial symmetry by use of quantitative phase microscopy*. Opt. Lett. **27**(23):2061–2063 (2002).

- [RCD⁺08] B. Rappaz, F. Charriere, C. Depeursinge, P. J. Magistretti, and P. Marquet. *Simultaneous cell morphometry and refractive index measurement with dual-wavelength digital holographic microscopy and dye-enhanced dispersion of perfusion medium*. Opt. Lett. **33**(7):744–746 (2008).
- [Ret04] B. Rethfeld. *Unified model for the Free-Electron avalanche in Laser-Irradiated dielectrics*. Phys. Rev. Lett. **92**(18) (2004).
- [Ret06] B. Rethfeld. *Free-electron generation in laser-irradiated dielectrics*. Phys. Rev. B **73**(3) (2006).
- [RGS⁺06] P. P. Rajeev, M. Gertsvolf, E. Simova, C. Hnatovsky, R. S. Taylor, V. R. Bhardwaj, D. M. Rayner, and P. B. Corkum. *Memory in nonlinear ionization of transparent solids*. Phys. Rev. Lett. **97**(25):253001 (2006).
- [RN09] S. Russell and P. Norvig. *Artificial Intelligence: A Modern Approach*. Prentice Hall 3rd edition (2009).
- [RRW⁺99] A. Ruffin, J. Rudd, J. Whitaker, S. Feng, and H. Winful. *Direct observation of the gouy phase shift with Single-Cycle terahertz pulses*. Phys. Rev. Lett. **83**(17):3410–3413 (1999).
- [San05] N. Sanner. *Mise en forme programmable de faisceau laser femtoseconde pour le micro-usinage et la photoinscription de guides d’ondes*. PhD thesis Universit Jean Monnet, St-Etienne (2005).
- [SB02] A. M. Streltsov and N. F. Borrelli. *Study of femtosecond-laser-written waveguides in glasses*. J. Opt. Soc. Am. B **19**(10):2496–2504 (2002).
- [SBB⁺05] A. Szameit, D. Bloemer, J. Burghoff, T. Schreiber, T. Pertsch, S. Nolte, A. Tuennermann, and F. Lederer. *Discrete nonlinear localization in femtosecond laser written waveguides in fused silica*. Opt. Express **13**(26):10552–10557 (2005).
- [SBB⁺06] A. Szameit, D. Blmer, J. Burghoff, T. Pertsch, S. Nolte, and A. Tuennermann. *Hexagonal waveguide arrays written with fs-laser pulses*. Appl. Phys. B **82**(4):507–512 (2006).
- [SBDC07] G. A. Siviloglou, J. Broky, A. Dogariu, and D. N. Christodoulides. *Observation of accelerating airy beams*. Phys. Rev. Lett. **99**(21):213901 (2007).

- [SBGM01] C. B. Schaffer, A. Brodeur, J. F. Garcia, and E. Mazur. *Micromachining bulk glass by use of femtosecond laser pulses with nanojoule energy*. Opt. Lett. **26**(2):93–95 (2001).
- [SBM01] C. B. Schaffer, A. Brodeur, and E. Mazur. *Laser-induced breakdown and damage in bulk transparent materials induced by tightly focused femtosecond laser pulses*. Meas. Sc. Tec. **12**(11):1784–1794 (2001).
- [SBT⁺03] R. Stoian, M. Boyle, A. Thoss, A. Rosenfeld, G. Korn, and I.V. Hertel. *Dynamic temporal pulse shaping in advanced ultrafast laser material processing*. Appl. Phys. A **77**(2):265–269 (2003).
- [SC07] G. A. Siviloglou and D. N. Christodoulides. *Accelerating finite energy airy beams*. Opt. Lett. **32**(8):979–981 (2007).
- [Sch01] C. B. Schaffer. *Interaction of Femtosecond Laser Pulses with Transparent Materials*. PhD thesis Harvard University (2001).
- [SD03] S. Sen and J. Dickinson. *Ab initio molecular dynamics simulation of femtosecond laser-induced structural modification in vitreous silica*. Phys. Rev. B **68**(21) (2003).
- [SDH⁺07] A. Szameit, F. Dreisow, H. Hartung, S. Nolte, A. Tuennermann, and F. Lederer. *Quasi-incoherent propagation in waveguide arrays*. Appl. Phys. Lett. **90**(24):241113–3 (2007).
- [SDH⁺08] A. Szameit, F. Dreisow, M. Heinrich, T. Pertsch, S. Nolte, A. Tuennermann, E. Suran, F. Louradour, A. Barthelemy, and S. Longhi. *Image reconstruction in segmented femtosecond laser-written waveguide arrays*. Appl. Phys. Lett. **93**(18):181109 (2008).
- [SDP⁺07] A. Szameit, F. Dreisow, T. Pertsch, S. Nolte, and A. Tuennermann. *Control of directional evanescent coupling in fs laser written waveguides*. Opt. Express **15**(4):1579–1587 (2007).
- [SFH⁺96a] B. C. Stuart, M. D. Feit, S. Herman, A. M. Rubenchik, B. W. Shore, and M. D. Perry. *Nanosecond-to-femtosecond laser-induced breakdown in dielectrics*. Phys. Rev. B **53**(4):1749 (1996a).
- [SFH⁺96b] B. C. Stuart, M. D. Feit, S. Herman, A. M. Rubenchik, B. W. Shore, and M. D. Perry. *Optical ablation by high-power short-pulse lasers*. J. Opt. Soc. Am. B **13**(2):459–468 (1996b).

- [SFPM99] L. Sudrie, M. Franco, B. Prade, and A. Mysyrowicz. *Writing of permanent birefringent microlayers in bulk fused silica with femtosecond laser pulses*. Opt. Comm. **171**(4-6):279–284 (1999).
- [SFPM01] L. Sudrie, M. Franco, B. Prade, and A. Mysyrowicz. *Study of damage in fused silica induced by ultra-short IR laser pulses*. Opt. Comm. **191**(3-6):333–339 (2001).
- [SGYH06] M. Y. Shverdin, S. N. Goda, G. Y. Yin, and S. E. Harris. *Coherent control of laser-induced breakdown*. Opt. Lett. **31**(9):1331–1333 (2006).
- [SHA⁺05] N. Sanner, N. Huot, E. Audouard, C. Larat, J.-P. Huignard, and B. Loiseaux. *Programmable focal spot shaping of amplified femtosecond laser pulses*. Opt. Lett. **30**(12):1479–1481 (2005).
- [She02] Y. R. Shen. *Principles of Nonlinear Optics*. John Wiley & Sons Inc 2nd edition (2002).
- [Sie90] A. E. Siegman. *Lasers*. University Science Books, U.S. 2nd edition (1990).
- [Sie93] A. E. Siegman. *Analysis of laser beam quality degradation caused by quartic phase aberrations*. Appl. Opt. **32**(30):5893–5901 (1993).
- [SJL⁺05a] Q. Sun, H. Jiang, Y. Liu, Z. Wu, H. Yang, and Q. Gong. *Measurement of the collision time of dense electronic plasma induced by a femtosecond laser in fused silica*. Opt. Lett. **30**(3):320–322 (2005a).
- [SJL⁺05b] Q. Sun, H. Jiang, Y. Liu, Y. Zhou, H. Yang, and Q. Gong. *Effect of spherical aberration on the propagation of a tightly focused femtosecond laser pulse inside fused silica*. J. of Opt. A **7**(11):655–659 (2005b).
- [SJM04] C. B. Schaffer, A. O. Jamison, and E. Mazur. *Morphology of femtosecond laser-induced structural changes in bulk transparent materials*. Appl. Phys. Lett. **84**(9):1441–1443 (2004).
- [SKQH03] Y. Shimotsuma, P. G. Kazansky, J. Qiu, and K. Hirao. *Self-Organized nanogratings in glass irradiated by ultrashort light pulses*. Phys. Rev. Lett. **91**(24):247405 (2003).
- [SLFE87] R. W. Schoenlein, W. Z. Lin, J. G. Fujimoto, and G. L. Eesley. *Femtosecond studies of nonequilibrium electronic processes in metals*. Phys. Rev. Lett. **58**(16):1680 (1987).

- [SMB⁺05] R. Stoian, A. Mermillod-Blondin, N. M. Bulgakova, A. Rosenfeld, I. V. Hertel, M. Spyridaki, E. Koudoumas, P. Tzanetakis, and C. Fotakis. *Optimization of ultrafast laser generated low-energy ion beams from silicon targets*. Appl. Phys. Lett. **87**(12):124105–3 (2005).
- [SMD01] Z. Sacks, G. Mourou, and R. Danielius. *Adjusting pulse-front tilt and pulse duration by use of a single-shot autocorrelator*. Opt. Lett. **26**(7):462–464 (2001).
- [SNCV04] A. Saliminia, N.T. Nguyen, S.L. Chin, and R. Valle. *The influence of self-focusing and filamentation on refractive index modifications in fused silica using intense femtosecond pulses*. Opt. Comm. **241**(4-6):529–538 (2004).
- [Sny72] A. W. Snyder. *Coupled-Mode theory for optical fibers*. J. Opt. Soc. Am. **62**(11):1267–1277 (1972).
- [Sol09] J. Solis. Private communication (2009).
- [SPG⁺07] J. Siegel, D. Puerto, W. Gawelda, G. Bachelier, J. Solis, L. Ehrentraut, and J. Bonse. *Plasma formation and structural modification below the visible ablation threshold in fused silica upon femtosecond laser irradiation*. Appl. Phys. Lett. **91**(8):082902–3 (2007).
- [SSB⁺00] Y. Sikorski, A.A. Said, P. Bado, R. Maynard, C. Florea, and K.A. Winick. *Optical waveguide amplifier in nd-doped glass written with near-IR femtosecond laser pulses*. Electron. Lett. **36**(3):226–227 (2000).
- [SSK⁺03] T. Suzuki, L. Skuja, K. Kajihara, M. Hirano, T. Kamiya, and H. Hosono. *Electronic structure of oxygen dangling bond in glassy SiO₂: the role of hyperconjugation*. Phys. Rev. Lett. **90**(18):186404–4 (2003).
- [SSS99] M.D. Skeldon, R.B. Saager, and W. Seka. *Quantitative pump-induced wavefront distortions in laser-diode- and flashlamp-pumped Nd:YLF laser rods*. IEEE J. Quant. Electron. **35**(3):381–386 (1999).
- [SSS⁺09] M. Sakakura, T. Sawano, Y. Shimotsuna, K. Miura, and K. Hirao. *Parallel drawing of multiple bent optical waveguides using a spatial light modulator*. Jpn. J. Appl. Phys. **48**:126507 (2009).
- [ST05] M. Sakakura and M. Terazima. *Initial temporal and spatial changes of the refractive index induced by focused femtosecond pulsed laser irradiation inside a glass*. Phys. Rev. B **71**(2):024113 (2005).

- [STS⁺07] M. Sakakura, M. Terazima, Y. Shimotsuma, K. Miura, and K. Hirao. *Observation of pressure wave generated by focusing a femtosecond laser pulse inside a glass*. Opt. Express **15**(9):5674–5686 (2007).
- [SUB⁺09] N. Sanner, O. Uteza, B. Bussiere, G. Coustillier, A. Leray, T. Itina, and M. Sentis. *Measurement of femtosecond laser-induced damage and ablation thresholds in dielectrics*. Appl. Phys. A **94**(4):889–897 (2009).
- [SvdL00] K. Sokolowski-Tinten and D. von der Linde. *Generation of dense electron-hole plasmas in silicon*. Phys. Rev. B **61**(4):2643–2650 (2000).
- [SW96] K. S. Song and R. T. Williams. *Self-Trapped Excitons*. Springer-Verlag Telos 2nd edition (1996).
- [SWBH10] R. Stoian, M. Wollenhaupt, T. Baumert, and I. V. Hertel. *Pulse shaping in laser material processing*. Sugioka K., Meunier M., Pique A. Eds. (Springer Verlag, Heidelberg, in press) 1st edition (2010).
- [Tan98] C. Z. Tan. *Review and analysis of refractive index temperature dependence in amorphous SiO₂*. J. N-Cryst. Sol. **238**(1-2):30–36 (1998).
- [TBK⁺99] A.-C. Tien, S. Backus, H. Kapteyn, M. Murnane, and G. Mourou. *Short-Pulse laser damage in transparent materials as a function of pulse duration*. Phys. Rev. Lett. **82**(19):3883–3886 (1999).
- [TBR⁺08] R. R. Thomson, A. S. Bockelt, E. Ramsay, S. Beecher, A. H. Greenaway, A. K. Kar, and D. T. Reid. *Shaping ultrafast laser inscribed optical waveguides using a deformable mirror*. Opt. Express **16**(17):12786–12793 (2008).
- [Tho81] K. K. Thornber. *Applications of scaling to problems in high-field electronic transport*. J. Appl. Phys. **52**(1):279–290 (1981).
- [THS08] R. Taylor, C. Hnatovsky, and E. Simova. *Applications of femtosecond laser induced self-organized planar nanocracks inside fused silica glass*. Las. Photon. Rev. **2**(1-2):26–46 (2008).
- [TKO05] E. Toratani, M. Kamata, and M. Obara. *Self-fabrication of void array in fused silica by femtosecond laser processing*. Appl. Phys. Lett. **87**(17):171103–3 (2005).
- [Tra07] F. N. Trager. *Springer Handbook of Lasers and Optics*. Springer-Verlag New York Inc. 1st edition (2007).

- [TRC96] A. J. Taylor, G. Rodriguez, and Tracy Sharp Clement. *Determination of n_2 by direct measurement of the optical phase*. Opt. Lett. **21**(22):1812–1814 (1996).
- [TSH08] R. S. Taylor, E. Simova, and C. Hnatovsky. *Creation of chiral structures inside fused silica glass*. Opt. Lett. **33**(12):1312–1314 (2008).
- [TSZ⁺06] V. V. Temnov, K. Sokolowski-Tinten, P. Zhou, A. El-Khamhawy, and D. von der Linde. *Multiphoton ionization in dielectrics: Comparison of circular and linear polarization*. Phys. Rev. Lett. **97**(23):237403–4 (2006).
- [VLC⁺00] F. Verluise, V. Laude, Z. Cheng, Ch. Spielmann, and P. Tournois. *Amplitude and phase control of ultrashort pulses by use of an acousto-optic programmable dispersive filter: pulse compression and shaping*. Opt. Lett. **25**(8):575–577 (2000).
- [VTO⁺07] G. Della Valle, S. Taccheo, R. Osellame, A. Festa, G. Cerullo, and P. Laporta. *1.5 micrometer single longitudinal mode waveguide laser fabricated by femtosecond laser writing*. Opt. Express **15**(6):3190–3194 (2007).
- [WAY⁺03] W. Watanabe, T. Asano, K. Yamada, K. Itoh, and J. Nishii. *Wavelength division with three-dimensional couplers fabricated by filamentation of femtosecond laser pulses*. Opt. Lett. **28**(24):2491–2493 (2003).
- [WBP⁺05] A. J. Wright, D. Burns, B. A. Patterson, S. P. Poland, G. J. Valentine, and J. M. Girkin. *Exploration of the optimisation algorithms used in the implementation of adaptive optics in confocal and multiphoton microscopy*. Micros. Res. Tec. **67**(1):36–44 (2005).
- [WBS⁺06] S.W. Winkler, I.M. Burakov, R. Stoian, N.M. Bulgakova, A. Husakou, A. Mermillod-Blondin, A. Rosenfeld, D. Ashkenasi, and I.V. Hertel. *Transient response of dielectric materials exposed to ultrafast laser radiation*. Appl. Phys. A **84**(4):413–422 (2006).
- [Wei00] A. M. Weiner. *Femtosecond pulse shaping using spatial light modulators*. Rev. Sci. Instrum. **71**(5):1929–1960 (2000).
- [WGBH08] D. Wortmann, J. Gottmann, N. Brandt, and H. Horn-Solle. *Micro and nanostructures inside sapphire by fs-laser irradiation and selective etching*. Opt. Express **16**(3):1517–1522 (2008).
- [WRG07] D. Wortmann, M. Ramme, and J. Gottmann. *Refractive index modification using fs-laser double pulses*. Opt. Express **15**(16):10149–10153 (2007).

- [WSHM07] Z. Wang, K. Sugioka, Y. Hanada, and K. Midorikawa. *Optical waveguide fabrication and integration with a micro-mirror inside photosensitive glass by femtosecond laser direct writing*. Appl. Phys. A **88**(4):699–704 (2007).
- [Yar91] A. Yariv. *Optical Electronics*. Saunders College Publishing/Harcourt Brace 4th edition (1991).
- [YBG⁺04] P. Yang, G. R. Burns, J. Guo, T. S. Luk, and G. A. Vawter. *Femtosecond laser-pulse-induced birefringence in optically isotropic glass*. J. Appl. Phys. **95**(10):5280 (2004).
- [YKS⁺08a] W. Yang, P. G. Kazansky, Y. Shimotsuma, M. Sakakura, K. Miura, and K. Hirao. *Ultrashort-pulse laser calligraphy*. Appl. Phys. Lett. **93**(17):171109–3 (2008a).
- [YKS08b] W. Yang, P. G. Kazansky, and Y. P. Svirko. *Non-reciprocal ultrafast laser writing*. Nat. Photon. **2**(2):99–104 (2008b).
- [YNC96] G. L. Yip, P. C. Noutsios, and L. Chen. *Improved propagation-mode near-field method for refractive-index profiling of optical waveguides*. Appl. Opt. **35**(12):2060–2068 (1996).
- [YPK⁺04] C. J. Yu, J. H. Park, J. Kim, M. S. Jung, and S. D. Lee. *Design of binary diffraction gratings of liquid crystals in a linearly graded phase model*. Appl. Opt. **43**(9):1783–1788 (2004).
- [YWL⁺04] K. Yamada, W. Watanabe, Y. Li, K. Itoh, and J. Nishii. *Multilevel phase-type diffractive lenses in silica glass induced by filamentation of femtosecond laser pulses*. Opt. Lett. **29**(16):1846–1848 (2004).
- [YWNI03] K. Yamada, W. Watanabe, J. Nishii, and K. Itoh. *Anisotropic refractive-index change in silica glass induced by self-trapped filament of linearly polarized femtosecond laser pulses*. J. Appl. Phys. **93**(4):1889 (2003).
- [ZEH06] H. Zhang, S. H. Eaton, and P. R. Herman. *Low-loss type II waveguide writing in fused silica with single picosecond laser pulses*. Opt. Express **14**(11):4826–4834 (2006).
- [Zen03] Y. Zeng-Guang. *The filtered abel transform and its application in combustion diagnostics*. Final Contractor Report E13773 ASA STI Cleveland, Ohio 44135 (2003).
- [Zer34] F. Zernike. *Beugungstheorie des schneidenverfahrens und seiner verbesserten form, der phasenkontrastmethode*. Physica **1**(7-12):689–704 (1934).

Acknowledgments

Here comes the most challenging paragraph to write at least in my opinion. The simple reason is that words alone, even beautifully arranged, will never transcribe the gratitude I would like to express here. I want to point out that this report is naturally everything but not the result of my own work, carried out alone in a dark laboratory room during nights and holidays. This is true on a very small extent. But the truth is that a combination of motivated beings empowered with uncommon kindness and/or speed of mind and/or administrative influence came to work together somehow to guide me through this unexpectedly wonderful experience.

My first thanks go both sides of the Rhine, to my two advisors and Pr. E. Audouard and Pr. I.V. Hertel. Pr. Audouard is mainly at the origin of my choice of career since my first meetings with him after class hours. His fascination and humility while brilliantly teaching photonics are very contagious and I have to confess him that I got contaminated during his wonderful lecture. I am also deeply impressed by his constant care to force the research advances to become an immediate benefit for the society. I am convinced that this care possibly creates a virtuous circle where applications and research both feed each other with challenges and ideas. I am also very grateful for his sincere attention for the post-thesis period.

Pr. I.V. Hertel welcomed me in his laboratory in a very reassuring and motivating manner. His repeated counsels regarding laboratory work, results analysis and presentation combined with his vast scientific expertise have added coherence to my research efforts without which only a very little portion of the reported results would have been obtained. I would like to thank him also for his help in coordinating the procedures between the French and German universities.

I am very grateful for Pr. L. Wöste who kindly accepted to be my second Gutachter for the Freie Universität. I will never forget my visit to his laboratory where an impressively exciting atmosphere is immediately enjoyable.

Also, I would like to thank Pr. I. Miyamoto who spend a little more than a week with me in the laboratory room. His palpable scientific curiosity coupled to his sense of work and action have deeply influenced me.

How to properly thank Dr. R. Stoian? I sincerely could not have think of a better scientific supervision. He is the kind of person with whom you want to do better all the time. He was able to

create a very friendly atmosphere that constantly fed the desire to answer our questions regarding physics and to "finish the stories" when a unexpected observation would arise. His unwavering patience with my defective memory made him explain some physical concepts at least twenty times, and I am sure that he will take the time to calmly do it again if I need it. He is also the one who taught me the rigorous procedures to follow on the optical table. Thanks again.

Special thanks go to Dr. A. Rosenfeld who supervised my work in Berlin. I am not the only one to think he is the kindest person on earth, but at least this is written now. I remember him welcoming me late at night in Berlin after 1300 km spend in a car with my wife and three kids (at that time). He organized the Kindergarten for us, showed me the Kinderartz and everything we needed for our three stays in Berlin. He was always ready to give a hand in the laboratory or on a scientific question or in an administrative procedure. His 'magic' cupboards always contain the kind of sample you want, or the optical element you need and generally, he was always able to find a solution to any of my problems even to the last lines of this manuscript. Thanks again.

I am also grateful for the help of Dr. I. Mingareev, Dr. D. Wortmann, Dr. J. Gottmann and Dr. D. Mahlmann who warmly welcomed me at the Fraunhofer Institut für Lasertechnik ILT and introduced me to advanced microscopy techniques.

I would like to recognize here the precious collaborations in performing precise characterization of photowritten structures as well as fruitful scientific discussions. Sincere thanks to Pr. J. Solis, D. Little and Dr. A. Crunteanu.

I would like to thank Pr. P. Brouwer Pr. M. P. Heyn from the Physics Department at the FU Berlin for their kind understanding and support all along the thesis submission procedure, as well as Mr. Gibian and Fr. Pasanec.

I am indebted to Dr. N. Huot who helped me a lot on the subject of aberrations at the beginning of my thesis. I am still trying to reach his amazing scientific exactness in Optics.

Dr. A. Mermillod-Blondin deserves special acknowledgments as he played the risky role of the first line soldier in organizing the complex details of the cotutelle procedure. Also, thanks to him I could work on an already-working experiment in Berlin and Saint-Etienne which saved me a considerable amount of time and nerves. More than that, his friendship and interest brought very enjoyable support and motivation while working or spending 'family time' together.

I had the chance to work with Dr. J. Bonse who patiently introduced me on the pump-probe set-up. I really enjoyed his permanent good mood and impressive experimental skills. Next to him, anyone will always feel small.

The best month of my work in Saint Etienne was spend with V. D. Blanco trying to write hundreds of waveguides despite of rather seismologic conditions. I hope I can work again with him somehow in order to improve my spanish which he liked so much...

Whereas our overlapping time was rather short, I am also indebted to Dr. N. Sanner for the

efficient explanations on the spatial shaping apparatus despite of a catastrophic hard drive crash which I am responsible for. I enjoyed the time spend together in the lab or discussing in the office.

Thanks to all the colleagues and friends who made life much more enjoyable in France and Germany, especially Dr. J.-P. Colombier, Dr. C. Liebig, Dr. I. Burakov, L. Ehrentraut, D. Bruneel, B. Dusser, S. Landon, R. Jouglet and Dr. S. Winkler whose flying package is now engraved in our minds.

I am also grateful for all the European citizens whose direct or indirect financial contribution are indispensable for this kind of work. I humbly hope that the results shown in this report will soon have a positive impact on the society through the creation of work opportunities.

The possibility to regularly meet and collaborate with industrial partners was highly profitable for my research work. I would thus like to particularly thank H. Soder and J. Granier from *Impulsion*.

The time comes to thank my family and especially my parents for their constant support and love. Thanks to them, I was taught the eternal principle of hard work which, to my opinion, rendered this adventure fascinating.

None of this would have been possible without the extraordinary patience of my wife Cécile who accepted to see most of the evenings, week-ends and holidays of the last three years ruined in order to bring me to that point. Thank you. My strongest motivation found its source from Olivier, Noémie, David, Thomas and hopefully another one (or two...). Nothing brought more joy to my life than seeing them growing and smiling from day to day.

